Werkstofftechnik

UNIVERSITÄT SIEGEN

Stewart Leith

Development of Novel Superconducting Thin Films for use in Superconducting Radio Frequency Cavities

Schriftenreihe der Arbeitsgruppe
des Lehrstuhls für Oberflächen- und Werkstofftechnologie
im Institut für Werkstofftechnik

Herausgeber: Prof. Dr. rer. nat. habil. Xin Jiang

Band 19

Stewart Leith

Development of Novel Superconducting Thin Films for use in Superconducting Radio Frequency Cavities

Schriftenreihe der Arbeitsgruppe des Lehrstuhls für Oberflächen- und Werkstofftechnologie im Institut für Werkstofftechnik

Impressum
Prof. Dr. rer. nat. habil. Xin Jiang
Lehrstuhl für Oberflächen- und Werkstofftechnologie
Institut für Werkstofftechnik
Universität Siegen
57076 Siegen
ISSN: 2194-0096
Zugl.: Siegen, Univ., Diss., 2021

Development of Novel Superconducting Thin Films for use in Superconducting Radio Frequency Cavities

Von der Naturwissenschaftlich-Technischen Fakultät
der Universität Siegen

zur Erlangung des akademischen Grades eines Doktors der
Ingenieurwissenschaften (Dr.-Ing.)
genehmigte

DISSERTATION

von:	M. Eng Stewart Leith
aus:	Johannesburg, Südafrika
eingereicht am:	18. Mai 2021
Mündliche Prüfung am:	21. Oktober 2021
Referent:	Prof. Dr. rer. nat. habil. Xin Jiang
Korreferent:	Prof. Dr. Jens Knobloch

Zusammenfassung

Dünnschichtbeschichtete Hohlräume für supraleitende Hochfrequenz (SRF) sind ein attraktiver Ersatz für den aktuellen Industriestandard von Bulk-Nb. Daher haben SRF Forschungsgruppen in den letzten Jahren umfangreiche Untersuchungen zur Verwendung von alternativen Materialien und Herstellungstechniken durchgeführt. Diese Dissertation ist Teil dieser Arbeit und präsentiert die Ergebnisse von Experimenten zur Verbesserung der aktuellen Betriebsleistung von SRF-Hohlräumen auf Dünnschichtbasis durch den Einsatz verbesserter Abscheidungstechniken, alternativer Materialien und mehrschichtiger Supraleiter-Isolator-Supraleiter (SIS) Dünnschichtbeschichtungen. Diese Arbeit konzentrierte sich auf die Abscheidung einzelner Nb- und NbN-Dünnfilme sowie mehrschichtiger SIS-Filmbeschichtungen auf sauerstofffreien Cu-Substraten mit hoher Leitfähigkeit (OFHC). Das hier untersuchte SIS-System bestand aus einem Dreischichtverbund aus Nb/AlN/NbN und erforderte eine Optimierung jedes einzelnen Materialsystems. Die Filme wurden sowohl unter Verwendung von Gleichstrom-Magnetron-Sputtern (DC MS) als auch von Hochleistungs-Impuls-Magnetron-Sputtern (HiPIMS) abgeschieden, was einen direkten Vergleich der beiden sowie die Beobachtung der Verbesserungen ermöglichte, die energetische Abscheidungstechniken wie HiPIMS bieten.

Im Rahmen einer Optimierungsstudie zur Oberflächenvorbereitung wurde eine Reihe von Techniken und Verfahren zur Vorbereitung der Cu-Oberfläche untersucht, darunter mechanisches Polieren, chemisches Polieren und Elektropolieren. Die resultierende Topographie der Cu-Probenoberfläche nach Anwendung des optimierten Verfahrens übertraf typischerweise die aktuellen Industriestandards.

Zwei separate Serien von NbN-Filmen wurden unter Verwendung von DC-MS- oder HiPIMS-Techniken auf Cu-Proben abgeschieden. Die Beziehung zwischen den verschiedenen Abscheidungsparametern und den morphologischen, kristallographischen und supraleitenden Eigenschaften dieser Filme wurde untersucht. Die Leistung der NbN-Filme hängt eng mit der Bildung der richtigen kristallographischen NbN-Phase zusammen. Ein Wechselspiel zwischen Abscheidungsdruck, Kathodenleistung und Stickstoff-Gas-Flussrate wurde sowohl für DC-MS- als auch für HiPIMS-Filme beobachtet, wobei die Optimierung dieser Parameter von vorrangiger Bedeutung war. Es wurde festgestellt, dass die Biasspannung eine signifikante Rolle im HiPIMS-Abscheidungsprozess spielt, wobei eine zu hohe Biasspannung zu einer Phasenänderung der NbN-Filme führt. Die Verwendung von HiPIMS führte jedoch zu wesentlichen Verbesserungen sowohl der Dichte als auch der Topographie der NbN-Filme, was

zu einer entsprechenden Erhöhung der supraleitenden Leistung der HiPIMS-NbN-Proben im Vergleich zu den DC-MS-NbN-Proben führte.

DC MS Nb-Beschichtungen leiden typischerweise unter einer schlechten Grenzflächenhaftung und einer geringen Filmdichte. Eine Möglichkeit dies zu verbessern besteht darin, eine energetische Abscheidungstechnik wie HiPIMS zu verwenden. Die morphologischen, kristallographischen und supraleitenden Eigenschaften von mit HiPIMS abgeschiedenen Nb-Filmen wurden hinsichtlich der sich ändernden Abscheidungsparameter analysiert. Es wurde eine signifikante Verringerung der Anzahl von Hohlräumen an der Grenzfläche zwischen dem durch HiPIMS abgeschiedenen Nb-Filmen und dem Cu-Substrat im Vergleich zu DC-MS abgeschiedenen Nb-Filmen beobachtet. In Bezug auf ihre supraleitende Leistung erwiesen sich Nb-Filme, die durch volumenartige kristallographische Eigenschaften gekennzeichnet waren, als weit überlegen. Drei spezifische Abscheidungsparameter: die Substrattemperatur, die Substratvorspannung und die Filmdicke wurden in dieser Hinsicht als die wichtigsten Abscheidungsparameter identifiziert.

Die SIS-Filmbeschichtungen wurden in drei separate Serien unterteilt: DC-MS-SIS-Filme, eine Kombination aus HiPIMS-Nb- und DC-MS-NbN-SIS-Filmen und schließlich HiPIMS-SIS-Filme. Mikrostrukturell waren die Schichten für alle Filme kohärent und epitaktisch gewachsen, wobei morphologische und topographische Verbesserungen sowohl der Nb- als auch der NbN-Bestandteilsschichten durch die Verwendung von HiPIMS erzielt wurden. Das Eintrittsfeld der äußeren Abschirmschicht, in diesem Fall NbN, und die Topographie der Basis-Nb-Schicht erwiesen sich als kritisch für die Leistung der SIS-Filmstruktur. Der Übergang zur Verwendung von HiPIMS sowohl für die Nb- als auch für die NbN-Schicht führte zu signifikanten Leistungsverbesserungen im Vergleich zu DC-MS-abgeschiedenen SIS-Filmen. Diese Ergebnisse liefern Hinweise auf die Wirksamkeit von SIS-Filmbeschichtungen auf Cu-Substraten. Dennoch ist eine weitere Optimierung des SIS-Filmbeschichtungsverfahrens erforderlich, um das Potenzial von SIS-Filmbeschichtungen voll auszuschöpfen.

Diese Studie endet mit der Abscheidung der drei separaten SIS-Filmbeschichtungen auf einer Reihe von QPR-Proben für zusätzliche Vergleiche. Dies lieferte weitere Einblicke in die Verwendung dieser Beschichtungen unter Bedingungen, die denen in SRF-Hohlräumen ähnlicher sind. Die Testergebnisse lieferten wertvolles Feedback und einige vielversprechende Ergebnisse.

Abstract

Thin film coated Superconducting Radio Frequency (SRF) cavities are an attractive substitute for the current industry standard of bulk Nb. As such, the SRF community has, in recent years, engaged in a significant amount of research into the use of alternative materials and fabrication techniques. This dissertation forms part of this body of work and presents the findings of experiments aimed at improving the current operational performance of thin-film-based SRF cavities through the use of improved deposition techniques, alternative materials and multilayer Superconductor-Insulator-Superconductor (SIS) thin film coatings. This work focused on the deposition of individual Nb and NbN thin films, as well as multilayer SIS film coatings onto Oxygen Free High Conductivity (OFHC) Cu substrates. The SIS system studied here consisted of a single tri-layer of Nb/AlN/NbN and required optimisation of each of the individual material systems. The films were deposited using both Direct Current Magnetron Sputtering (DC MS) and High Power Impulse Magnetron Sputtering (HiPIMS) techniques, allowing for a direct comparison of the two as well as observation of the improvements offered by energetic deposition techniques, such as HiPIMS.

An assortment of Cu surface preparation techniques and procedures, including mechanical polishing, chemical polishing and electropolishing, have been explored as part of a surface-preparation optimisation study. The resultant topography of the Cu sample surface, following the use of the optimised process, typically exceeded current industry standards.

Two separate series of NbN films have been deposited onto Cu samples, using either DC MS or HiPIMS techniques. The relationship between the different deposition parameters and the morphological, crystallographic and superconducting properties of these films has been examined. The performance of the NbN films is strictly related to the formation of the correct NbN crystallographic phase. An interplay between the deposition pressure, cathode power and nitrogen-gas flow rate was observed for both DC MS and HiPIMS films, with the optimisation of these parameters of primary importance. The substrate bias was found to play a significant role in the HiPIMS deposition process, with too high a substrate bias resulting in a phase change of the NbN films. Nevertheless, the use of HiPIMS led to substantial improvements to both the density and topography of the NbN films, resulting in a corresponding increase in the superconducting performance of the HiPIMS NbN samples compared to the DC MS NbN samples.

DC MS Nb coatings typically suffer from poor interface adhesion and low film density. One way to improve this is to utilise an energetic deposition technique, such as HiPIMS. The morphological, crystallographic and superconducting properties of Nb films deposited with

HiPIMS were analysed in terms of the changing deposition parameters. A significant reduction in the number of voids at the interface between the HiPIMS-deposited Nb films and the Cu substrate, compared to DC MS-deposited Nb films, was observed. In terms of their superconducting performance, Nb films characterised by bulk-like crystallographic properties were found to be vastly superior. Three specific deposition parameters: the substrate temperature, substrate bias and film thickness were identified as the most significant deposition parameters in this regard.

The SIS film coatings were divided into three separate series: DC MS SIS films, a combination of HiPIMS Nb and DC MS NbN SIS films and finally, HiPIMS SIS films. Microstructurally, the layers were coherent and epitaxially grown for all films, with morphological and topographical improvements of both the Nb and NbN constituent layers provided by the use of HiPIMS. The entry field of the outer shielding layer, NbN in this instance, and the topography of the base Nb layer were found to be critical to the performance of the SIS film structure. The transition to the use of HiPIMS, for both the Nb and NbN layers, led to significant performance improvements compared to DC MS-deposited SIS films. These results provide evidence for the efficacy of SIS film coatings on Cu substrates. Nevertheless, further optimisation of the SIS film coating procedure is required to fully realise the potential of SIS film coatings.

This study culminated in the deposition of the three separate SIS film coatings on a series of QPR samples for additional comparisons. This provided further insight into the use of these coatings in conditions more similar to those found in SRF cavities. The test results provided valuable feedback and some promising outcomes.

Acknowledgements

It goes without saying that this thesis would not have been possible without the help of many special individuals.

I would firstly like to express my gratitude to Prof. Dr. Xin Jiang for affording me the opportunity to work on such an amazing project in his research group – LOT (Lehrstuhl für Oberflächen-und Werkstofftechnologie). He gave me the freedom to conduct my research as I saw fit and provided me with guidance and support when I needed it most. His enthusiasm for research is infectious and helped to motivate me through any difficult stages of my research. I am truly grateful to have been able to complete my research in his group.

I would further like to thank the members of my thesis committee: Prof. Dr. Jens Knobloch, Prof. Dr. Benjamin Butz and Prof. Dr. Carsten Engelhard. Besides agreeing to be a part of my committee, I would also like to acknowledge their willingness to assist me, through the use of different characterisation devices or with informative discussions.

I will be forever indebted to Dr. Michael Vogel for his guidance and assistance during the course of my PhD study. This thesis truly would not have been possible without his help. He was incredibly welcoming and always willing to offer encouragement during the difficult stages of research, while keeping me focused on the positive aspects of my results. I am also extremely thankful for his continuous advice with regards to my scientific writing as well as my presentation skills.

My colleagues at LOT were also absolutely fantastic and I will always remember their willingness to help me as well as the friendly conversations we had with each other. A PhD is often a very solitary pursuit; the smiles in the corridors and the stimulating conversations went a long way during the PhD process and were very meaningful. In no particular order, I would like to acknowledge Ze Jian, Yuning Guo, Jing Xu, Katharina Diehl, Marc Schumacher, Xiu Xiu Han, Qun Jin, Tianxiao Guo, Kevin Suta and Özdem Sezgin. Further colleagues from LOT also deserve a specific mention for their friendliness, assistance and guidance during my thesis: Dr. Thorsten Staedler, Dr. Nianjun Yang, Petra auf dem Brinke, Claudia Kretzer and Thomas Degen. A special thank you to Andrea Brombach, I cannot thank you enough for all the help you gave me, no matter the topic. Your warm smile was also a welcome sight on many days.

I would also like to acknowledge my co-workers from outside of LOT at the University of Siegen, who gave willingly of their time and knowledge during my thesis. Dr. Yilmaz Sakali, Dr. Julian Müller, Dr. Christian Wiktor, Ying Li, Damian Sulik, Markus Hartmann, Sebastian Weitz, Anna Schulte, Ulrike Koch. My unending barrage of questions and requests never seemed to tire them.

A large portion of this work hinged upon the efforts of my dedicated students. Your work ethic and belief in me were inspiring and I am forever grateful for your contributions. I acknowledge Jian Fan, Jiaokun Qiao, Bing Bai, Zeshan Khalil and Aliaa Mohamed.

I was privileged to be a part of two separate EU projects during my PhD. As such, a number of my results stem from the combined efforts of multiple researchers in separate stages of their careers. More specifically, a number of these team members contributed directly to this work through the measurement and analysis of my samples. I would therefore like to thank Dr. Eugen Seiler, Dr. Oliver Kugeler, Rastislav Ries and Dmitry Tikhonov. I would also like to acknowledge the advice and help of Dr. Guillaume Rosaz. To this end, I would like to acknowledge the sources of funding I received during this thesis:

This study forms part of the EASITrain Marie Sklodowska-Curie Action (MSCA) Innovative Training Networks (ITN), which has received funding from the European Union's H2020 Framework Programme under Grant Agreement no. 764879.

The superconducting measurements in this work, conducted by E. Seiler and R. Ries from IEE SAS, form part of the European Union's ARIES collaboration H2020 Research and Innovation Programme under Grant Agreement no. 730871

Being a part of the EASITrain project also allowed me to associate with some of the most amazing, intelligent and driven people I have ever met. I have no doubts that they will all go on to be valuable members of the scientific community and I am forever indebted to them for their friendliness, encouragement and imparting in me a drive to succeed. I am truly grateful to have met all of you. Thank you all so much!

To my friends and family, specifically my parents, your support (mostly from a distance) has been unwavering over these three years and you have been the biggest source of inspiration throughout my time in Germany. Your visits to Europe always left me re-energised and I looked forward to them keenly.

Finally, the most important thank you of all. To my amazing wife, Gabriella. You gave up everything to allow me to pursue this opportunity and have been nothing but supportive throughout the past three years. You have been a never-ending source of encouragement and inspiration and you are the reason why I was able to finish this thesis. I cannot express my gratitude enough.

Siegen, May 2021 Stewart Leith

Preface

Due to the collaborative nature of the projects which this work formed part of, a number of the experiments in this work were performed by project collaborators. Further investigations were also performed by members of the staff at the University of Siegen. It should be noted that the experiments and data acquisition may have been performed by others, but the data analysis and preparation for this thesis was completed by the author. The specific tests performed by others are listed as follows:

- The VSM and AC Susceptometer measurements were completed by E. Seiler and R. Ries at IEE, Slovak Academy of Sciences, as part of the ARIES research program.
- The QPR sample testing was completed by D. Tikhonov at HZB Berlin, as part of the EASITrain and ARIES research programs.
- The RBS measurements were completed by E. Alves and N.P. Barradas at Centro de Ciências e Tecnologias Nucleares, Instituto Superior Técnico, facilitated by R. Valizadeh, as part of the ARIES research program.
- The TEM investigations were performed by Y. Li and C. Wiktor at the University of Siegen.
- The XPS measurements were performed by A. Schulte at the University of Siegen.
- The SIMS measurements were performed by U. Koch at the University of Siegen.

In light of the above, parts of this work have been published in conference papers, deliverable documents and journal papers, often as part of milestone requirements defined for the EU projects of which this work formed part. These are listed here:

- C. Pira *et al.*, "ARIES Deliverable Report D15.1: Evaluation of cleaning process," 2018.
- O. Malyshev *et al.*, "ARIES Deliverable Report D15.2: Evaluation of systems 1 and 2," 2019
- S. B. Leith, A. S. H. Mohamed, Z. Khalil, M. Vogel, and X. Jiang, "Initial results from investigations into different surface preparation techniques of OFHC copper for SRF applications," in *19th International Conference on RF Superconductivity* (SRF 2019), 2019, pp. 941–944.
- S. B. Leith, M. Vogel, X. Jiang, E. Seiler, and R. Ries, "Deposition parameter effects on niobium nitride (NbN) thin films deposited onto copper substrates with DC magnetron sputtering," in *19th International Conference on RF Superconductivity* (SRF 2019) 947–951
- O. Kugeler *et al.*, "ARIES Deliverable Report D15.3: Evaluation of system 3 and SIS," 2020.

- S. Leith, M. Vogel, J. Fan, E. Seiler, R. Ries, and X. Jiang, "Superconducting NbN thin films for use in superconducting radio frequency cavities," *Supercond. Sci. Technol.*, vol. 34, no. 2, p. 025006, Feb. 2021
- S. Leith, M. Vogel, J. Qiao, E. Seiler, R. Ries, and X. Jiang, "HiPIMS deposition of Nb thin films onto Cu substrates", *to be published.*
- S. Leith, M. Vogel, B. Bai, E. Seiler, R. Ries, and X. Jiang, "HiPIMS NbN thin film development for use in multilayer SIS films", *to be published.*
- S. Leith, M. Vogel, X. Jiang, Y. Li, J. Müller, B. Butz, R. Ries, E. Seiler, D. Tikhonov, O. Kugeler, S. Keckert, J. Knobloch, "The Development of HiPIMS Multilayer SIS film coatings on Copper for SRF Applications", *to be published.*

Table of Contents

List of Tables

List of Figures

List of Symbols

Abbreviations

AC	Alternating Current
AFM	Atomic Force Microscopy
ARIES	Accelerator Research and Innovation for European Science and Society
BCC	Body centred cubic
BCS	Bardeen Cooper Schrieffer
CERN	European Organisation for Nuclear Research
CLSM	Confocal Laser Scanning Microscopy
DC	Direct Current
DC MS	Direct Current Magnetron Sputtering
EASITrain	European Advanced Superconductivity Innovation and Training Network
EBSD	Electron Backscatter Diffraction
EDX/S	Energy Dispersive X-Ray Spectroscopy
EM	Electron Microscope
EP	Electrolyte Polishing
FCC	Face centred cubic
FCC	Future Circular Collider
FESEM	Field Emission Scanning Electron Microscope
FIB	Focused Ion Beam
FWHM	Full With at Half Maximum
HiPIMS	High Power Impulse Magnetron Sputtering
HRTEM	High Resolution Transmission Electron Microscope
LHC	Large Hadron Collider
MF	Medium Frequency
MP	Mechanical Polishing
OFHC	Oxygen-Free High Thermal Conductivity
PF	Pole Figure
PL	Pulse Length
PVD	Physical Vapour Deposition
QPR	Quadrupole Resonator
Q-slope	Quality Factor Slope
R-DC MS	Reactive Direct Current Magnetron Sputtering

R-HiPIMS	Reactive High Power Impulse Magnetron Sputtering
RMS	Root Mean Square
RBS	Rutherford Backscattering Spectroscopy
RF	Radio Frequency
RRR	Residual Resistivity Ratio
SAED	Selected Area Electron Diffraction
SEM	Scanning Electron Microscope
SIS	Superconductor-Insulator-Superconductor
TOF-SIMS	Time of Flight Secondary Ion Mass Spectrometry
SRF	Superconducting Radio Frequency
SZD	Structure Zone Diagram
TEM	Transmission Electron Microscope
VSM	Vibrating Sample Magnetometer
XPS	X-ray Photoelectron Spectroscopy
XRD	X-Ray Diffraction

Chemicals

Al	Aluminium
AlN	Aluminium nitride
Ar	Argon
C	Carbon
$C_4H_{10}O$	n-butanol
$C_6H_{14}N_2O_7$	Ammonium citrate
Cu	Copper
CuSO4	Copper sulfamate
H_2O_2	Hydrogen peroxide
H_3NO_3S	Sulfamic acid
HNO_3	Nitric acid
LHe	Liquid helium
N_2	Nitrogen gas
Nb	Niobium
NbN	Niobium nitride
O_2	Oxygen gas
Pt	Platinum

Si	Silicon

Symbols

a_0	Lattice parameter (nm)
C_{peak}	Peak Current
d	Anode to cathode distance (Paschen's Law)
d_{cryst}	Crystal plane spacing
E_{acc}	Accelerating gradient
f_{pulse}	HiPIMS pulse frequency
G	Geometrical constant
H	Magnetic field strength
H_a	Applied magnetic field
H_c	Thermodynamic critical field
H_{c1}	First critical field
H_{c2}	Second critical field
H_{en}	Field of first flux penetration (entry field)
H_{Max}	Maximum measured magnetic field
H_p	Peak magnetic field
H_{sh}	Superheating field
H_{tr}	Trapped magnetic field
J_c	Critical current density
K	Scherrer constant
l	Mean free path
L	Crystallite size
m	Magnetic moment
M	Isotopic mass
P_{cath}	Cathode power
p_{dep}	Deposition pressure
P_{peak}	Peak cathode power
Q	Quality factor
R_a ,R_q	Arithmetic mean and root mean square roughness (line)
R_{BCS}	BCS surface resistance
r_{dep}	Deposition rate
R_{res}	Residual surface resistance

R_s	Surface resistance
S_a , S_q	Arithmetic mean and root mean square roughness (area)
t	Film thickness
t_i	Insulator film thickness
t_s	Superconductor film thickness
T	Temperature
T_c	Superconducting critical (transition) temperature
T_h	Homologous temperature
T_m	Melting temperature
T_s	Substrate temperature
U_B	Substrate bias
V_{acc}	Accelerating voltage
z	Cavity length
ξ	Effective coherence length. Includes effects of mean free path changes.
ξ_0	BCS coherence length. Interaction distance between electrons that form a Cooper pair.
ξ_{GL}	Ginzburg-Landau coherence length. Distance over which the order parameter varies significantly.
Δ	Superconducting energy Gap
κ	Ginzburg-Landau parameter
λ	Effective penetration depth. Includes effects of mean free path and temperature changes.
λ_{GL}	Ginzburg-Landau penetration depth. Equivalent to the London penetration depth (λ_L).
λ_L	London penetration depth
λ_x	X-ray wavelength
ρ_n	Normal state resistivity
θ	Theta, Incident angle of X-ray

Units

°C	Degrees Celsius
Å	Angstrom (1 Å = 0.1 nm)
μm	Micrometre (1 μm = 10^{-6} m)
eV	Electron volt

g	Gram
Hz	Hertz
K	Kelvin, absolute temperature (1 K = - 273.15°C)
mbar	Millibar
min(s)	Minute(s)
ml	Millilitre
mm	Millimetre (1 μm = 10^{-3} m)
mT	Millitesla (1 mT = 10_{-3} T)
MV/m	Megavolt per metre
nm	Nanometre (1 μm = 10^{-9} m)
Oe	Oersted
Pa	Pascal
sccm	Standard Cubic Centimetres per Minute
T	Tesla
V	Volts
W	Watt

1. Introduction

1.1 Introduction

One of the principle tools helping researchers to probe ever further in their quest to understand the underlying principles of physics are high-energy particle accelerators. In order to achieve these high energies, accelerators use accelerating cavities to impart energy to particles travelling through them. This energy is imparted by an electromagnetic field within the cavity, which typically operates at microwave frequencies. Modern particle accelerators make use of superconducting radio frequency (SRF) accelerating cavities in order to benefit from the decreased losses available with the use of superconducting materials, in the case of circular accelerators, or to attain high energies within a short distance, in the case of linear accelerators.

The vast majority of operating SRF accelerating cavities are made from bulk Nb, as it is the elemental material with the highest superconducting transition temperature (T_c = 9.2 K) and highest lower critical magnetic field (H_{c1} ~ 170 mT at 2 K). It is also readily available and relatively easy to form. Typically, bulk Nb cavities are operated at temperatures of 2 K or below, to benefit from the reduced losses at these temperatures. Nowadays, as a result of decades of research and continuous improvements, bulk Nb is approaching its theoretical limits of operation [1], defined by its superheating field (H_{sh} ≈ 220 mT), which is equivalent to an accelerating field of roughly 50 MV/m.

Further improvements to SRF cavities have been explored through the use of thin film coatings. Because of the shallow penetration depth of an RF field into a superconducting material (< 1 μm), it is possible to coat a thin layer of superconducting material, such as Nb, onto the inner surface of an accelerating cavity made of another, often more advantageous material. This has already proved successful at CERN, where Nb-coated Cu cavities have been successfully operated in both the LEP-II and LHC accelerators. The principal benefits with the use of coated Cu cavities are in the form of cost savings, both for construction and operation. This is achieved through the significant material costs saving, the increased thermal conductivity, which allows for operation at 4.2 K instead of 2 K, resulting in lower refrigeration costs, as well as a lower susceptibility to Earth's magnetic field, which decreases the amount of magnetic shielding required.

The main figure of merit for accelerating cavities is the quality factor (Q), which is defined as the stored energy of the cavity divided by the energy lost per RF cycle. One of the most significant issues affecting the quality factor is the surface resistance (R_s) of the accelerating

cavity. Therefore, reducing the surface resistance of the cavities is one of the main avenues for operational improvement.

One significant drawback of current Nb-coated Cu cavities, is the so called Q-slope; the rapid reduction of the quality factor observed with an increase in the magnetic field [2]. This is equivalent to an increase in the surface resistance with increasing field and its existence has limited the operation of Nb-coated Cu cavities to low field values, and by extension, low accelerating fields, e.g., 5.3 MV/m for the LHC [3]. The origin of the Q-slope has been linked to multiple different sources within the thin film coatings: lattice defect density and intra-granular impurities, the surface topography of the material, interfacial voids and the film's grain morphology, to name a few. Many of these issues have been linked to the currently used deposition techniques, an example of which is DC Magnetron Sputtering (DC MS).

Therefore, in order to increase the performance of Nb-coated Cu cavities, the use of new energetic deposition techniques, such as High Power Impulse Magnetron Sputtering (HiPIMS) and Electron Cyclotron Resonance (ECR), has been gaining traction due to the significant improvements afforded to users [4]. Further to this, an alternative approach, which utilises a multilayer structure deposited onto bulk Nb cavities, has been proposed [5] with initial results indicating its potential [6]. The premise of this approach is to deposit a "shielding" superconductor layer (S-layer) on top of the Nb cavity, separated by a thin insulating layer (I-layer), which protects the underlying superconductor from vortex penetration. This approach is purported to allow operation of SRF cavities above the H_{sh} of the underlying superconductor by shielding it from the applied RF field. The use of alternative, higher T_c materials (NbN, Nb_3Sn, etc.) for the shielding layer also leads to a reduction in the BCS surface resistance of the films, due to an increase in the superconducting energy gap Δ [7].

These Superconductor-Insulator-Superconductor structures, colloquially known as SIS structures, were originally intended for use with bulk Nb cavities. Nevertheless, it is foreseeable that if a bulk-like Nb thin film can be deposited onto Cu substrates as a base layer, the SIS film approach would also be applicable to coated Cu cavities.

In summary, the overarching objective of this thesis is to investigate pathways to improve the current operational performance of thin-film-based SRF cavities through the use of improved deposition techniques, alternative materials or alternative methodologies. This is accomplished through the engineering of; HiPIMS-deposited Nb thin films on Cu substrates, DC MS- and HiPIMS-deposited NbN thin films on Cu substrates and DC MS- and HiPIMS-deposited multilayer SIS films on Cu substrates. From this, an understanding of the influence

of different substrate preparation techniques and deposition parameters on the resultant superconducting properties of the samples is determined. Moreover, the efficacy of SIS films deposited onto Cu substrates is also elucidated.

1.2 Thesis Outline

The investigations in this thesis were completed in a staggered fashion, based on the step-wise improvements made to each of the individual material systems. A graphical representation of the chronological order in which the separate investigations were completed, including the corresponding Chapter number, is detailed in Figure 1-1.

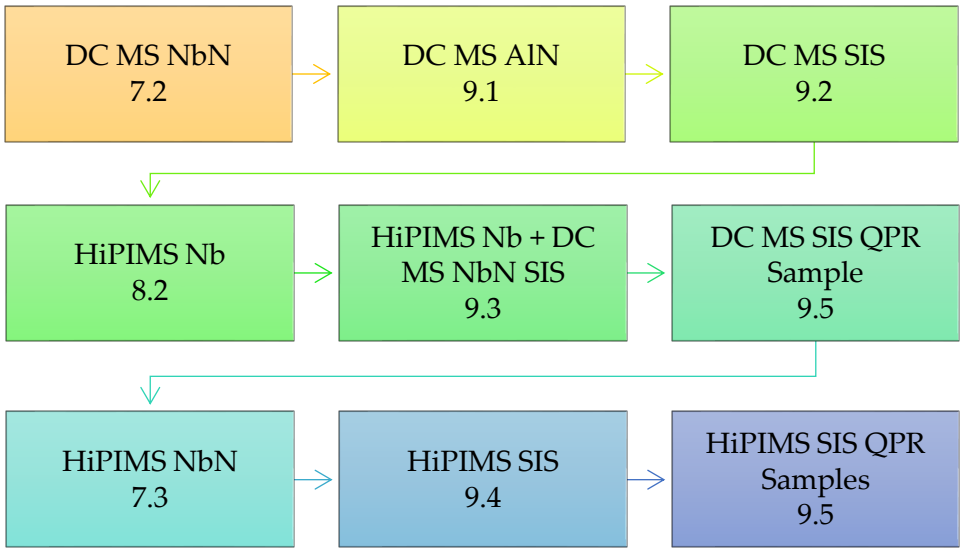

Figure 1-1: Graphical representation of the chronological order of the separate coating series, including relevant chapter numbers.

The experimental results, however, are grouped together based on the material type or the experimental topic being investigated. Thus, this thesis is organised as follows:

- Chapter 2 introduces the basic theories of Superconductivity, allowing insight into some of the decisions made during this work.
- Chapter 3 presents the fundamentals of SRF cavity design and operation, an introduction to the current state of the art for bulk Nb cavities and thin film cavities as well as possible methods for improving cavity performance.
- Chapter 4 details the process of thin film deposition by magnetron sputtering, including different operational approaches such as reactive sputtering and HiPIMS. The physics of film growth and the effects of the deposition parameters on the films are also presented.

- Chapter 5 introduces the surface preparation theory applicable to this work as well as the experiments conducted in order to optimise the surface preparation process used in this work.
- Chapter 6 presents the coating system and the characterisation equipment used in this work.
- Chapter 7 details the results of investigations into reactive DC MS and reactive HiPIMS NbN thin films deposited onto Cu substrates.
- Chapter 8 presents the results of the investigation into HiPIMS Nb thin films deposited onto Cu substrates and a QPR sample.
- Chapter 9 presents the results of a series of investigations into the efficacy of SIS films deposited onto Cu substrates, including the deposition of a few QPR samples.
- Chapter 10 is a summary of the outcomes from the study presented as a series of conclusions, including recommendations for further development.

2. Superconductivity

This chapter serves to provide the reader with a theoretical overview of relevant elements of superconductivity and its application in Superconducting Radio-Frequency (SRF) cavities. This will allow the approaches taken concerning surface preparation and thin film deposition to become more comprehensible with regards to performance optimisation.

2.1 Introduction

Particle accelerators around the world employ radio frequency (RF) cavities to accelerate particles to higher energies for use in experiments. For many applications, the use of cavities constructed with normal conducting material is acceptable. However, when trying to attain higher energies, SRF cavities present an advantage over their normal conducting peers by reducing the surface resistance, and thus cooling requirements of the cavities, while allowing them to reach these higher energies. The reduction in the surface resistance, which implies a lower RF power dissipation, results in an increased quality factor (Q) for SRF cavities over their normal conducting peers by several orders of magnitude (roughly 10^{10} for Nb compared to 10^{4} for Cu) [8]. This is due to the specific traits that materials in the superconducting state possess compared to their normal conducting state.

2.2 Critical Temperature and the Meissner Effect

Superconductivity, and superconducting materials, are characterised by three distinct properties: zero DC electrical resistance, perfect diamagnetism and the quantisation of magnetic flux. The disappearance of DC electrical resistance below a certain temperature, known as the critical or transition temperature (T_c), was first observed in 1911 by H. Kamerlingh Onnes [9] following experiments with the liquefaction of helium. Onnes observed the complete disappearance of electrical resistance in metals such as mercury, tin and lead, within a small temperature range around the critical temperature. This is represented in Figure 2-1 (a). The critical temperature of naturally occurring elements is generally governed by the relationship $T_c \propto 1/\sqrt{M}$, where M is the isotopic mass. However, some of the best-known metallic conductors, such as Au, Cu and Ag are non-superconducting.

The second hallmark of superconductivity, perfect diamagnetism, was later discovered in 1933. On cooling a superconducting material through the critical temperature, while exposed to an externally applied magnetic field, the magnetic field inside the superconductor was

found to be completely expelled. Materials are said to be in the "Meissner state" when the flux is fully expelled. This behaviour is known as the Meissner-Ochsenfeld effect [10] and is illustrated in Figure 2-1 (b).

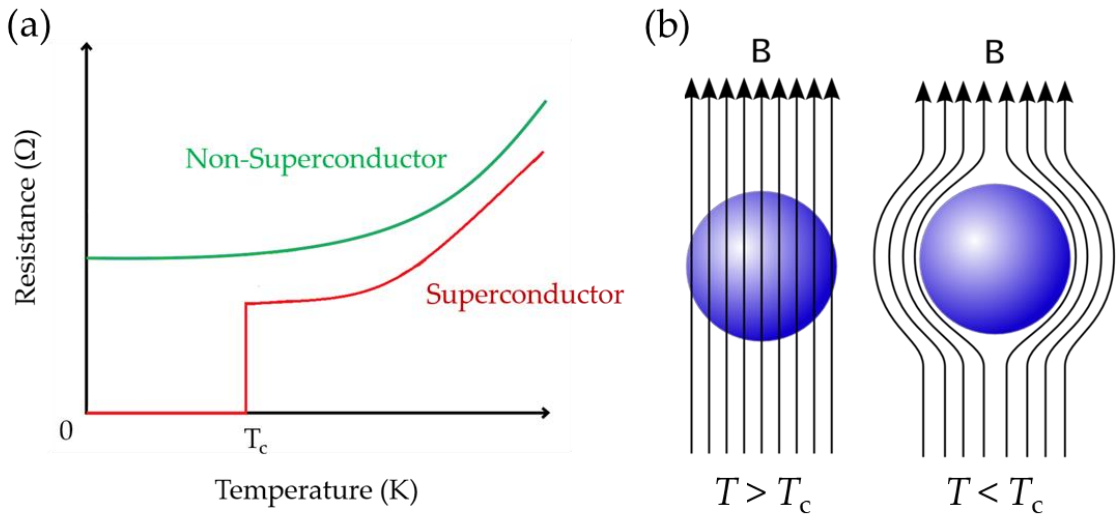

Figure 2-1: (a) Graphical representation of the behavioural difference of the resistance vs temperature of normal conductors compared to superconductors. (b) Illustration of the flux expulsion found in materials cooled below their critical temperature [11]. *This is known as the Meissner-Ochsenfeld effect* [10].

The perfect screening from the external field is enacted by super-currents which circulate within a very small layer at the surface of the material [12]. If a strong enough field is applied however, the screening effect will be overcome and the magnetic field will penetrate the superconductor, driving it into the normal conducting state. This transition point is known as the critical magnetic field (H_c). The critical magnetic field is also temperature dependent and is governed by the following relation:

$$H_c(T) = H_c(0)\left[1-\left(\frac{T}{T_c}\right)^2\right] \tag{2-1}$$

Because of this temperature dependence, a material will only transition between states at $T = T_c$ in the absence of a magnetic field. In the presence of a magnetic field, the superconducting transition temperature will be reduced. These critical parameters: the critical temperature (T_c) and the critical magnetic field (H_c), along with the critical current density (J_c), define the transition point between the normal and superconducting states of a material. A material can thus only display superconducting behaviour when $T < T_c$, $H < H_c$ and $J < J_c$. This will be expanded upon in the discussion of Type-I and Type-II superconductors in Chapter 2.4.

The third hallmark of superconductivity, the quantisation of magnetic flux, was discovered in 1961 by Deaver and Fairbank [13]. This discovery describes how, in the mixed superconducting state, magnetic field penetrates the superconductor in the form of flux vortices. These vortices exist in the form of normal conducting cores, with radius ξ_{GL}, surrounded by a magnetic field, which decays to zero over a distance λ_{GL}. Each of these vortices contains a quantised (minimum) amount of magnetic flux denoted by the flux quantum ϕ_0. The vortices are evenly distributed, usually occurring at either lattice imperfections or elemental impurities called pinning centres. An increasing number of vortices exist in the superconductor as the external field is increased.

2.3 Superconductivity Theory

A clear understanding and theory defining superconductivity and the phenomena which exist because of it, required many years of research. Ultimately, three theories were developed which together, explain how the phenomena of superconductivity are enacted.

The London Theory [14], proposed in 1935, expands upon the two fluid model proposed by Gorter and Casimir [15]. When a material temperature decreases below T_c, a fraction of the electrons will condense, forming a "superfluid" which is in the superconducting state with zero resistance. The remaining electrons stay in the normal conducting state, thereby creating a two-fluid state with the co-existence of a superfluid and a normal fluid [16]. As the temperature decreases further, the percentage of the "superfluid" increases. In an applied DC electric field, the superelectrons flow in parallel without resistance and thus they short out the applied field, leading to zero resistance. This is not the case in an AC field, where the inertia of superelectrons does not allow them to follow the field instantaneously, leading to slight acceleration of the normal electron fluid and a subsequent resistance effect. This effect increases with increasing frequency.

The London theory explains the Meissner-Ochsenfeld effect with the introduction of a parameter known as the London penetration depth (λ_L). The penetration depth is the decay length that the magnetic field penetrates into a superconductor and is dependent on the density, mass and charge of superelectrons. Thus at a depth greater than λ_L, the superconductor is fully in the Meissner state. The London penetration depth is a material property and is calculated using the following equation:

$$\lambda_L = \sqrt{\frac{m_s}{\mu_0 n_s e^2}} \tag{2-2}$$

Where m_s is the mass of the superelectrons, μ_0 is the magnetic constant, n_s is the density of superelectrons and e is the charge. Pippard later expanded on the London theory, detailing the effects of impurities on superconducting characteristic lengths [17]. By adding impurities to a material, the mean free path (l) of normal electrons is reduced, thereby changing the electrodynamic response from the clean ($l >> \xi_0$) to the dirty ($l << \xi_0$) regime. Because of this behaviour, some characteristic lengths are adjusted depending on the electron mean free path. For instance, a decrease in the mean free path results in an increase in the penetration depth of a material. An approximation for this phenomenon is given below:

$$\lambda(l,T) = \lambda_L(T)\sqrt{1+\frac{\xi_0}{l}} \tag{2-3}$$

Here it is necessary to introduce the coherence length ξ_0. The coherence length describes the interaction distance between electrons that form a Cooper pair. Cooper pairs will be further explained below. The coherence length is applicable in BCS theory and is regularly called the BCS coherence length. It is calculated as follows:

$$\xi_0 = \frac{\hbar v_f}{\pi\Delta(0)} = \frac{\hbar v_f}{1.764\pi k_B T_c} \tag{2-4}$$

Where ħ is the reduced Planck's constant, v_f is the Fermi velocity and Δ_0 is the zero-temperature superconducting gap. ξ_0 is the coherence length of a material in the clean regime (see Chapter 2.6.1) and is an intrinsic material property. For impure materials, a second purity dependent coherence length of a material, known as the electromagnetic coherence length, relies on the mean free path of the material and is related to ξ_0 as follows [18]:

$$\frac{1}{\xi} = \frac{1}{\xi_0} + \frac{1}{l} \tag{2-5}$$

Thus as $l \to \infty$, $\xi \to \xi_0$.

The Ginzburg–Landau (GL) Theory [19], proposed in 1950, is a phenomenological theory which uses a thermodynamic description of superconductivity near T_c. The theory describes the effects of the spatial variation of superelectron density e.g. what occurs at the interface between normal conducting and superconducting regions of a material [16]. The theory describes the state of a material using the order parameter ($\tilde{\Psi}$). In the normal conducting state, the order parameter is zero while in the superconducting state; the order parameter is greater than zero. The density of superelectrons is then given by $n_s = |\tilde{\Psi}|^2$.

The theory proposes the Ginzburg-Landau (GL) parameter (κ), which is the relationship between the penetration depth and the coherence length of a material and provides information regarding a material's interface conditions. The GL parameter also details

whether a superconductor is Type-I or Type-II (detailed in Chapter 2.4) and is calculated as follows:

$$\kappa = \frac{\lambda_{GL}}{\xi_{GL}} = \frac{\lambda(T)}{\xi(T)} \tag{2-6}$$

Where λ_{GL} is the Ginzburg-Landau penetration depth, which has the same meaning as the London penetration depth (λ_L) [12] and ξ_{GL} is the Ginzburg-Landau coherence length, which is distinct from the BCS coherence length (ξ_0) and can be defined as the distance over which the order parameter varies significantly. In pure superconductors, at $T << T_c$, ξ_{GL} approaches ξ_0 [12] and can be related to the ξ_0 as follows [18]:

$$\xi_{GL} \approx \frac{\sqrt{\xi_0 l}}{\sqrt{1-\frac{T}{T_c}}} \tag{2-7}$$

Therefore, at $T << T_c$, the GL parameter can also be calculated using $\kappa = \lambda_L/\xi_0$.

The Bardeen Cooper Schrieffer (BCS) Theory [20], proposed in 1957, postulates the formation of Cooper pairs, essentially two bonded electrons, when a material transitions to the superconducting state. The Cooper pairs are formed as electrons pass through a crystal lattice and deform it, creating regions with an intensified positive charge. Due to this, free electrons combine into Cooper pairs, significantly lowering their energy state [16].

As a result, an energy gap (Δ) exists between the base energy of the cooper pairs in the superconducting state and their energy level in the normal conducting state. In order to break a Cooper pair apart, an energy of 2Δ is required. The energy gap decreases with increasing temperature up until the critical temperature where it becomes zero. In other words, above 0 K, a material will contain a mixture of normal electrons and Cooper pairs.

BCS theory also introduces a temperature dependence to the London penetration depth, but this does not alter its physical meaning [21]. The following relation defines the temperature dependence:

$$\lambda_L(T) = \frac{\lambda_L(0)}{\sqrt{1-\left(\frac{T}{T_c}\right)^4}} \tag{2-8}$$

The above relations are applicable in the clean limit, where the mean free path of electrons in the superconducting material is far greater than the coherence length. In the dirty limit, there is an adjustment of the above material properties which can be approximated as follows: $\xi_o \rightarrow \sqrt{\xi_0 l}$ and $\lambda_L \rightarrow \lambda_L\sqrt{\xi_0/l}$ where l is the mean free path of electrons [22].

The above equations were first noted for bulk superconducting materials, but they are generally applicable to thin films of superconducting material as well. However, when the

film thickness, t < λ, fluxoids are said to have a long range interaction force as opposed to the short range interaction force associated with bulk materials [23]. This leads to an increased effective penetration depth in thin films with thickness $t < \lambda$, which is known as the Pearl length and is computed using [24]:

$$\lambda_p = \frac{\lambda^2}{d} \tag{2-9}$$

This is specifically relevant to multilayer films, where the outermost superconducting layer is purposefully deposited with a thickness $t < \lambda$.

2.4 Type-I and Type-II Superconductors

As stated earlier, the critical values of temperature, magnetic field and current density, define a transition surface between the normal conducting and superconducting states of a material. There are, however, two different types of superconducting materials, which behave differently in terms of their transition from their normal to superconducting states. These two types are classified by their GL parameter κ. A division can be made between the two superconductor types based on the following:

$$\kappa < \frac{1}{\sqrt{2}}, \text{ type-I superconductor}$$

$$\kappa \geq \frac{1}{\sqrt{2}}, \text{ type-II superconductor}$$

There are distinct behavioural differences between these two types of superconductors in relation to the applied magnetic field.

Type-I superconductors have two states and transition directly from the Meissner state to the normal conducting state above the critical magnetic field H_c. On the other hand, *type-II* superconductors have three states, with boundaries defined by the lower (H_{c1}) and upper (H_{c2}) critical magnetic fields. Below the H_{c1}, type-II superconductors operate in the Meissner state. Above H_{c1}, it becomes energetically favourable for a vortex to be inside a superconductor [25] and a portion of the applied magnetic field penetrates the superconductor via vortex nucleation. This is known as the mixed state. Once the applied magnetic field reaches the upper critical magnetic field H_{c2}, the material transitions to the normal conducting state. A visual representation of the behavioural differences between the two superconductor types, as a function of applied field and temperature, is shown in Figure 2-2.

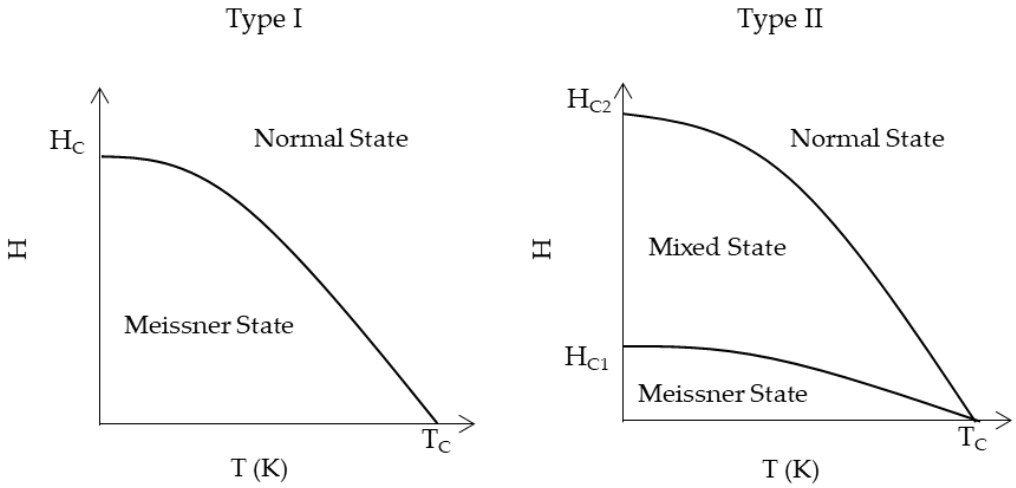

Figure 2-2: Variation of critical fields of type I and type II superconductors. Reproduced from [26].

This can also be understood by investigating a superconductor's reaction (magnetisation) to an applied magnetic field (H). As seen in Figure 2-3, in a type-I superconductor, the magnetic moment increases linearly with the applied field up to the critical magnetic field H_C, where after the superconductor transitions to the normal conducting state. Comparatively, a type-II superconductor also displays an initial linear increase in magnetic moment with the applied field. However, once a type-II superconductor reaches H_{C1}, vortex penetration begins and the superconductor enters the mixed state. In this state, any further increase in the applied field levels leads to a decrease in the magnetic moment, up to H_{C2}, where it again becomes normal conducting.

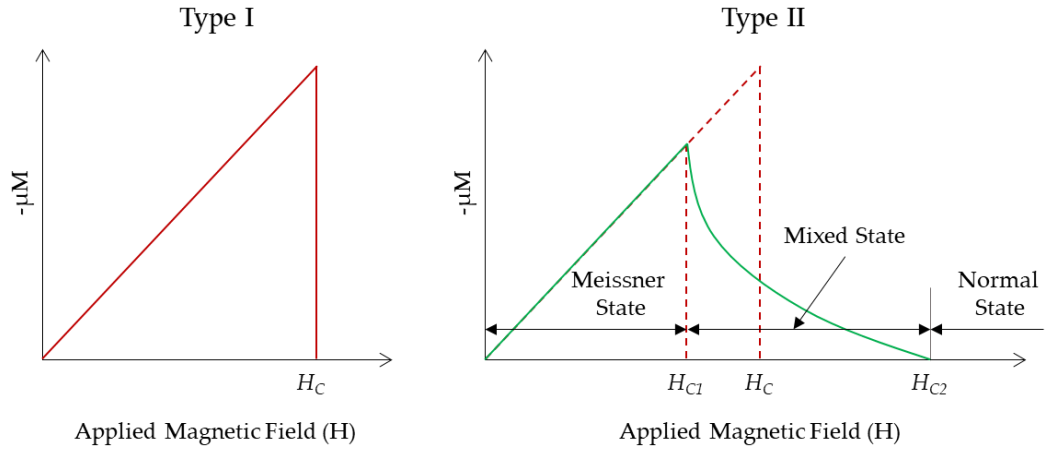

Figure 2-3: Relationship between magnetisation M and the applied field H for type I and type II superconductors. Reproduced from [26].

The mixed (Abrikosov) state is characterised by the presence of flux quanta; normal conducting columns (vortices) where flux has penetrated surrounded by a decaying field in the superconducting medium, as shown in Figure 2-4.

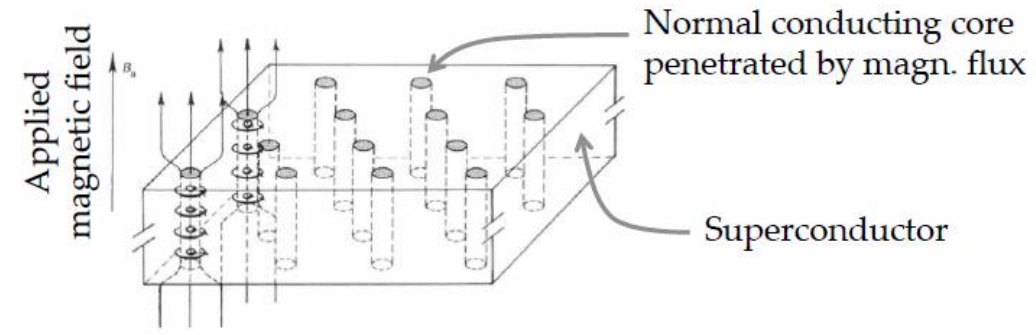

Figure 2-4: Illustration of vortex penetration and flux quantisation in the mixed (Abrikosov) state of type-II superconductors. Reproduced from [27].

As the magnetic field is increased, the number of vortices also increases. Each vortex will carry the same, minimum field possible due to the flux quantisation phenomenon. Thus, as the field increases, the number of vortices will increase to accommodate it [16]. The presence of vortices within the superconducting material can lead to decreased performances in real-world applications. When a current passes across a superconductor in the mixed state, it acts upon the vortices with the Lorentz force, thereby causing vibrations and subsequent heat generation and energy dissipation. The critical fields in type-II superconductors, as defined by BCS theory, are defined by the following equations [8]:

$$H_{c1} = \frac{\phi_0}{4\pi\lambda^2}\left(ln\frac{\lambda}{\xi}+0.5\right) \tag{2-10}$$

$$H_c = \frac{\phi_0}{2\sqrt{2}\pi\lambda\xi} \tag{2-11}$$

$$H_{c2} = \frac{\phi_0}{2\pi\xi^2} \tag{2-12}$$

It is important to note that the behaviour of the critical magnetic fields of deposited thin films is different to that of bulk materials. Nb thin films for instance have a longer London penetration depth, but a reduced electronic mean free path compared to bulk Nb, due to local defects inducing a reduced coherence length. This results in a lower H_{c1} and higher H_{c2} than the bulk material [28]. For the sake of brevity, type-II superconductors will be emphasised in future sections due to their applicability in this work.

2.5 The Superheating Field

For type-II superconductors, the Meissner state is stable up until the lower critical field (H_{c1}). At this point, magnetic flux penetration via vortex nucleation is said to begin. However, the onset of vortex nucleation can be delayed, allowing a superconductor to remain in a metastable Meissner state up until a superheating field H_{sh} [8], where $H_{c2} > H_{sh} > H_{c1}$. This phenomenon, first detailed by Bean and Livingston, is due to the presence of an energy barrier at the superconductor surface, which impedes the penetration of vortices into the superconductor [29]. As a result of this, a type-II superconductor can remain in a non-dissipative state at fields up to the superheating field [30]. Therefore, the maximum accelerating field of a cavity is defined by H_{sh}. At fields greater than H_{sh}, the Bean-Livingstone surface barrier disappears and any further increase in field will result in vortex penetration as the Meissner state becomes absolutely unstable [31]. The surface barrier is negatively impacted by the presence of fluxoid nucleation sites, such as defects and inclusions as well as increased surface roughness. A graphical representation of the superheating field with respect to the previously defined critical fields is shown in Figure 2-5.

Initial investigations to try and determine a theoretical equation for H_{sh} from GL theory resulted in different equations depending on the GL parameter κ as detailed below [8][32][33]:

$$H_{sh} \approx \frac{0.84}{\sqrt{\kappa}} H_c, \kappa \ll 1 \tag{2-13}$$

$$H_{sh} \approx 1.2\, H_c, \kappa \approx 1 \tag{2-14}$$

$$H_{sh} \approx 0.745\, H_c, \kappa \gg 1 \tag{2-15}$$

Due to their dependence on GL theory, these equations are valid at temperatures of $T = T_c$.

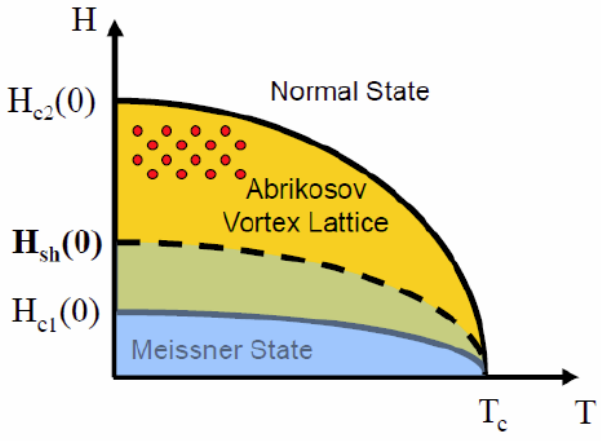

Figure 2-5: Representation of the positioning of the superheating field with respect to the critical fields of Type-II superconductors. The Meissner state can remain metastable at fields greater than H_{c1} up to the superheating field H_{sh}. Reproduced from [21].

A temperature dependence for the superheating field has also been defined for high-κ superconducting materials. Initial calculations by Galaiko showed H_{sh} (T) can be calculated for the temperature range $0 < T < T_c$ in the clean limit with $\kappa >> 1$ using $H_{sh} = 0.84\ H_c$ at $T \rightarrow 0$ and $H_{sh} = 0.745\ H_c$ for $T \rightarrow T_c$. Later research by Catelani and Sethna found a maximum of $H_{sh} \approx 0.843\ H_c$, at operating temperatures of $T/T_c = 0.04$, while also accounting for the decrease in H_c with increasing temperature [29].

Further studies have resulted in a proposal for the use of a critical GL parameter to split the superheating field into two regions; one with 1D perturbations ($\kappa < \kappa_c$) and the other with 2D perturbations ($\kappa > \kappa_c$) [34]. The two regions are split by a critical GL parameter $\kappa_c \cong 1.1495$ and the superheating field can be calculated as follows:

$$\frac{H_{sh}(\kappa)}{\sqrt{2}H_c} \approx 2^{-\frac{3}{4}}\kappa^{-\frac{1}{2}}\frac{1+4.6825120\kappa+3.3478315\kappa^2}{1+4.0195994\kappa+1.0005712\kappa^2}, \quad \kappa < \kappa_c \tag{2-16}$$

$$\frac{H_{sh}(\kappa)}{\sqrt{2}H_c} \approx \frac{\sqrt{10}}{6} + \frac{0.3852}{\sqrt{\kappa}}, \quad \kappa > \kappa_c \tag{2-17}$$

Lin and Gurevich [32] completed a detailed theoretical study on the effects of impurities on the superheating field for SC materials with $\kappa >> 1$ (such as NbN). These impurity levels were determined by a scattering rate factor $\alpha = \pi\xi_0/l$ (nonmagnetic impurities) and $\alpha_m = \pi\xi_0/l_m$ (magnetic impurities). In summation, the value of H_{sh}/H_c is minimally affected by the presence of non-magnetic impurities. In comparison, magnetic impurities significantly decrease H_{sh} in a similar way to the T_c suppression due to the pair-breaking effects of these impurities [35]. There also seems to be no interplay between magnetic and nonmagnetic impurities with the magnetic impurities dominating the effects on the superheating field.

The effect of surface topography on the superheating field is also of great importance, as field enhancement due to surface features is well documented [36]. It is understood that the surface of an RF cavity is covered by structures on multiple length scales, which are fractal in nature [37]. Nano-scale structures are distributed with a higher density than micro- or millimetre sized structures and occur almost continuously throughout the surface. It has also been reported, for Type-II superconductors with a large GL parameter ($\kappa >> 1$), that the superheating field H_{sh} is reduced at each nano-defect. This results in a suppression of the allowable peak surface magnetic field, to a decreased "effective" superheating field [38]. The theory proposes that the effective superheating field is given by $\tilde{H}_{sh} = \eta H_{sh}$, where η is the suppression factor due to nano-sized surface defects and is calculated as follows:

$$\eta = \frac{1}{\alpha}\left(\frac{\Gamma\left(\frac{\alpha}{2}\right)\Gamma\left(\frac{3-\alpha}{2}\right)\alpha\sin\frac{\pi(\alpha-1)}{2}}{\sqrt{\pi}}\frac{\xi}{\delta}\right)^{\frac{\alpha-1}{\alpha}} \tag{2-18}$$

Where the slope angle (α) and the defect depth (δ) are defined in Figure 2-6, which details the model of the nano-defect used in this study. This model provides a good qualitative starting point for detailing the superheating field suppression due to nano-defects.

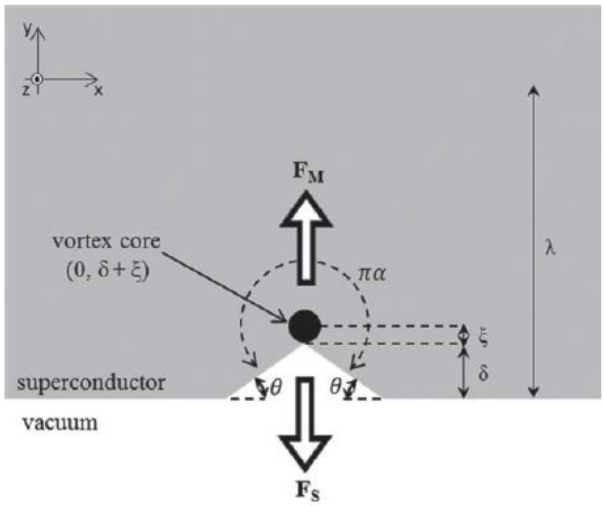

Figure 2-6: Image detailing the model of a nano-defect used for the theoretical calculation of the suppression factor of the superheating field as detailed in [38].

Calculation results for a range of defect shapes show that as the angle (α) and the depth (δ) increase, there is a decrease in the suppression factor, which will result in a decrease in the effective superheating field. It is also evident that the angle (sharpness) of the defect is more relevant to H_{sh} suppression than the defect size.

Recent studies have also suggested that the presence of defects on the surface of a cavity may lead to penetration times of individual vortices (~ 10^{-13} s) which are considerably faster than the RF period (~ 10^{-9} s). This would reduce the point of vortex penetration below the superheating field value and raises questions about the applicability of the vortex nucleation model [39].

Type-II superconductors with $\kappa >> 1$ are known to have very small coherence lengths (e.g. NbN ~ 3 nm). This leads to the increased possibility of vortex nucleation, owing to the higher likelihood of coherence length sized defects, and a resultant decrease in the superheating field. Liarte *et al* however indicated that their use should not be avoided and that the materials should simply be operated at lower levels of H_a/H_{sh} [35].

2.6 Surface Resistance

In a superconductor, DC currents are carried by Cooper pairs (paired electrons) without friction, thereby enabling the system to be lossless at $T < T_c$. In the case of RF currents, the

situation is slightly different. Above $T = 0$ K, not all electrons will form Cooper pairs. Given the fact that most superconducting systems operate above 0 K, there will typically be a mixture of superconducting Cooper pairs and normal conducting electrons present in a superconducting material during operation. Due to the inertial mass of the Cooper pairs of $m = 2*m_e$, a force must be applied to bring about the alternating directions of flow. As such, an electric field will be induced in the London penetration depth λ_L and continuously interact with the normal conducting electrons, leading to a dissipation of power proportional to the square of the frequency [8]. This resistance term is known as the BCS surface resistance and is temperature dependent.

Based on this explanation, one can theoretically expect the surface resistance to fall to zero at $T = 0$ K. However, this is not observed in practice. A certain "residual" surface resistance remains that is seemingly temperature independent. This surface resistance is known as the residual surface resistance and can be further broken down into the trapped flux (fluxon-induced) surface resistance R_{fl}, which is related to magnetic flux trapped in the superconductor during cooldown, and the residual resistance R_{res}, which accounts for the remaining surface resistance. These will be expanded upon below. A simplified equation for the surface resistance is shown below [40], however, the temperature reliance of the trapped flux resistance is debated:

$$R_s(H_{rf}, T, B) = R_{BCS}(H_{rf}, T, 0) + R_{res}(H_{rf}, 0, 0) + R_{fl}(H_{rf}, T, B) \tag{2-19}$$

2.6.1 BCS Surface Resistance

Because of the temperature dependence of the BCS surface resistance, SRF cavities are operated at the lowest economical temperature, in order to reduce it as much as practicable. The value of the BCS resistance is determined by the following equation [1]:

$$R_{BCS} = \frac{Af^2}{T} e^{-\frac{\Delta(T)}{kT}} \tag{2-20}$$

The constant A is dependent on the material properties of the superconductor, namely: the London penetration depth λ_L, the intrinsic coherent length ξ_0 and the electron mean free path l. It can be approximated, based on the Mattis-Bardeen theory, with the following [41]:

$$A \cong \frac{\mu_0^2 \lambda^3 \Delta}{\rho_n k_B} ln \frac{9 k_B T}{4\hbar f} \tag{2-21}$$

Where ρ_n is the normal state resistivity. Manipulation of factors that affect the constant A, such as the electron mean free path, have been successful in reducing the BCS surface resistance. One such example is impurity doping, which has been found to reverse the normal dependence of R_{BCS} on field strength [42].

Depending on the value of the electron mean free path of a superconductor, it is possible to split them into two regimes, the dirty regime and the clean regime. Superconductors with a mean free path $l << 20$ nm are classified as "dirty" [1]. R_{BCS} is found to decrease with increasing l in the dirty regime, reaching a minimum value at $l \sim \xi_0/2$ [43]. With further increase in l above the coherence length, i.e. in the clean regime, the surface resistance is actually found to increase, saturating at $l >> \xi_0$. This relationship is detailed in Figure 2-7, which displays an adapted figure from a study by Benvenuti *et al* [40]. Thus, it can be said that, for a dirty material, R_{BCS} depends on the mean free path and can therefore be adjusted by impurity management; while in contrast, R_{BCS} in the clean regime becomes independent of the material purity. A further parameter $a = \pi\xi/l$ has been defined to define the clean and dirty regimes. With $a \ll 1$, the material is in the clean regime, while $a \gg 1$ leaves the material in the dirty regime.

Thin film coated cavities display a high likelihood of meeting the condition for a minimum in the BCS resistance of $l \sim \xi_0/2$ when deposited onto oxidised Cu. This affords them a lower BCS resistance than bulk Nb cavities, as shown in a study completed by Benvenuti *et al* [40]. The recent integration of nitrogen infusion and nitrogen doping of bulk Nb cavities has produced a significant reduction in the BCS surface resistance [44]. This is believed to be related to adjustment of the mean free path from the clean regime into an area around the coherence length, thereby decreasing the BCS surface resistance of bulk Nb cavities to that of thin film cavities.

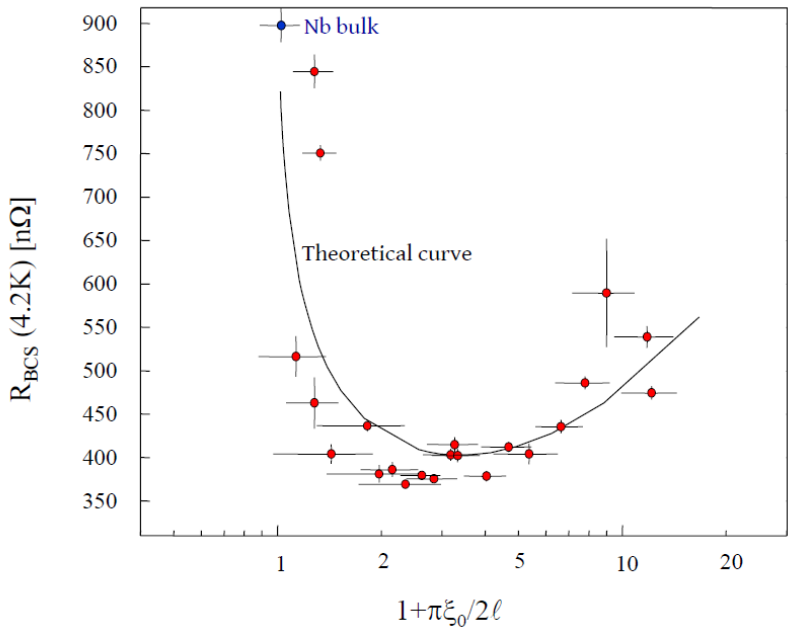

Figure 2-7: The relationship between the BCS resistance and the electron mean free path for Nb/Cu cavities and bulk Nb cavities at 4.2 K. Results were scaled to a T_c of 9.54 K for comparability [45]. *Reproduced from* [40].

2.6.2 Residual Surface Resistance

The residual surface resistance (R_{res}) is temperature independent and still present even at 0 K. The residual resistance is not predicted by the BCS theory and is reliant on a multitude of factors. Moreover, a single all-inclusive equation able to accurately predict the residual resistance term does not exist. Instead, through multiple studies on the subject, the following matters have been identified as playing a role in the residual resistance of superconducting materials:

- Power dissipation and subsequent vortex hotspots caused by oscillating trapped flux vortices under the influence of an RF field. These can dominate the residual resistance at low temperatures and lead to a dependence of R_s on the RF field amplitude [41]. Connected to this is the trapping of noble gas atoms from the process gas. Noble gas contamination arises from backscattered neutral noble gas atoms arriving at the substrate with high energy during the deposition process [46]. The gas atoms then act as pinning centres for magnetic fluxons.
- The formation of metallic hydrides that lead to eddy current losses. Hydrogen is often absorbed during surface preparation processes. This is then able to dissolve or damage the passivating native oxide layer of Nb_2O_5 present on the Nb surface [8].
- The surface roughness plays a significant role, with an increase in surface roughness leading to an increase in residual resistance. As such, the substrate surface roughness and shadow effects on the film also contribute to residual resistance [2].
- Adsorption of gases on the surface of the superconductor. This can be countered with the use of a good vacuum [1], thermal cycling to 300 K or by discharge cleaning initiated by ion/electron bombardment [47].
- Impurities and defects present in the superconductor also affect the residual resistance, with a definite reliance on dimension. It is understood that impurities and defects smaller than the coherence length, only lead to a small decrease in superconducting properties of a metal, such as T_c and Δ, while impurities with dimensions greater than the coherence length can lead to a loss of coherence of the superconducting state, leading to losses which persist even at 0 K [2].
- The residual resistance is proportional to the normal state resistivity ρ_n [48].
- Some authors attribute residual resistance to small grain sizes but no significant correlation between grain size and SRF performance exists. The effects of the grain boundaries themselves is also inconclusive. It is possible for the grain boundaries, due to their size, to be invisible to strong RF currents, however, it is possible for impurities

and precipitates to segregate to grain boundaries, thereby increasing their current blocking potential, leading to an increased resistance [43].

2.6.3 Trapped Flux Surface Resistance

The surface resistance due to the trapping of magnetic flux during the cooldown of superconducting cavities through the transition temperature is often treated as a part of the residual resistance term as a whole. This, however, is not very pertinent for this thesis as it is focused on the material science of thin films and how this influences their superconducting properties. A note of importance is that one of the advantages of using thin film superconductors, such as Nb/Cu, is that their sensitivity to trapped flux residual resistance is extremely low, believed to be due to a reduced mean free path compared to bulk materials [40][49]. Recent studies of a Nb/Cu QWR cavity have, however, yielded a significant increase in the quality factor when the external field was well compensated [50]. A short overview of the trapped flux surface resistance is provided below.

When a cavity enters the Meissner state, the ambient DC field will be expelled. Unfortunately, some of the flux will be trapped in the material at pinning sites (defects) such as grain boundaries, gas inclusions, normal conducting inclusions etc. This leads to additional losses through eddy current dissipation due to the oscillation of trapped flux vortices under the influence of RF fields [51][52]. The trapped flux resistance thus measures the sensitivity of a superconductor to an externally applied magnetic field [53] as the trapped flux surface resistance increases with increasing RF field. A proposal for this phenomenon indicates it might be due to the progressive de-pinning of vortices from their pinning sites with increasing field [40]. The existence of a linear relationship between the residual resistance and the intensity of trapped magnetic flux has also been verified [54]. It is possible to approximate the trapped flux surface resistance using the following formula [55]:

$$R_{fl} = \rho_n \frac{H_{ext}}{2H_{c2}} \tag{2-22}$$

Where ρ_n is the normal state resistivity. From this, it is understandable that, as the mean free path decreases, which leads to an increase in H_{c2}, the sensitivity of the trapped flux surface resistance decreases [42]. The decrease in the mean free path also leads to a possible increase in pinning centre density, which is known to reduce the surface resistance at low fields [41]. However, the best performing Nb cavities have shown a more reasonable pinning defect density ($l >> \xi$) [56].

There is some debate surrounding the effect of the cooling rate of cavities on the proportion of trapped flux and thus, the trapped flux surface resistance. A dressed bulk Nb cavity tested

in a horizontal cavity testing facility indicated a small temperature gradient (slow cooldown across T_c) leads to the most efficient Meissner state and therefore the most efficient flux expulsion, due to thermoelectric current-induced flux created with a large thermal gradient [57]. Other investigations, using bare bulk Nb cavities in a vertical test stand, have found that a large thermal gradient along the length of the cavity (fast cooldown across T_c) leads to the most effective flux expulsion [58]. As with bulk Nb cavities, a fast cooldown rate across the superconducting transition has also been found to decrease the surface resistance of elliptical Nb/Cu cavities [59].

The use of a thermal cycling process has also been reported to improve the trapped flux surface resistance. During this process, the temperature of the cavity is raised slowly to just above T_c, to equalise the temperature across the cavity, and then cooled back down below T_c. Studies indicated that a thermal gradient along a system during superconducting transition generate a thermoelectric current and subsequent magnetic flux which can then be trapped [60]. Recent studies on small Nb samples have indicated no effect of the cooling rate on the flux trapping efficiency [61]. There is therefore some possibility that the cavity environment (dressed vs. undressed) as well as positioning (upright vs. horizontal) during testing could impact the trapped flux and subsequently the trapped flux surface resistance.

3. Radio Frequency (RF) Cavities

This chapter serves to provide the reader with the necessary introduction to radio frequency (RF) accelerating cavities. This will provide insight into their operation requirements, thereby shedding light on the choices made concerning the materials that were studied and the methodologies used for sample production.

3.1 Introduction

One of the most crucial components of modern particle accelerators, especially in the pursuit of higher energies, is the Radio Frequency (RF) Cavity. The RF cavity is an electromagnetic resonator used to impart energy, through a stored electromagnetic field, onto a bunch of charged particles traversing the accelerator structure. More often than not, accelerating cavities are constructed using normal conducting materials, such as Cu, operating near room temperature. Superconducting materials, such as Nb are limited to specific applications, such as a high duty cycle (continuous wave operation), high particle speeds and large accelerating gradients. The main advantage of superconducting materials over normal conducting materials, as detailed in Chapter 2.6, is the substantial reduction in surface resistance offered by superconducting materials in these specific operating regions.

RF cavities are available in a multitude of different designs. The type of RF cavity to be used is often dictated by the type of particle to be accelerated, from electrons to heavy ions, and by the required speed or energy of the particles, which ranges anywhere from a fraction of the speed of light to very close to the speed of light. The speed of the particles is described by the β value, which indicates the proximity of the particle speed (v) to the speed of light (c), $\beta = v/c$. RF cavities are also designed and constructed to operate at a certain fundamental frequency. The frequency requirement is governed by their intended application and affects the final cavity design choice. The different cavity design options available for use in particle accelerators operating at different β and frequency values are displayed in Figure 3-1. Generally, for $\beta > 0.5$, elliptical cavities are preferred and are operated in the Transverse Magnetic (TM) mode, while lower β cavities are generally Quarter-Wave Resonators (QWR) or Half-Wave Resonators (HWR).

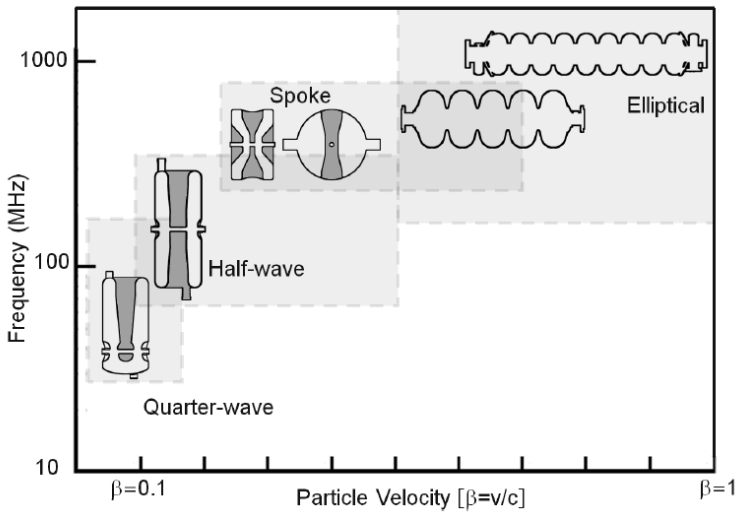

Figure 3-1: Overview of superconducting RF cavity designs for application in particle accelerators operating at different particle speeds and frequencies. Reproduced from [62].

A high-β elliptical cavity will be used as an example in order to describe the main principles of RF cavity operation. A cross-section of such an elliptical cavity is provided in Figure 3-2.

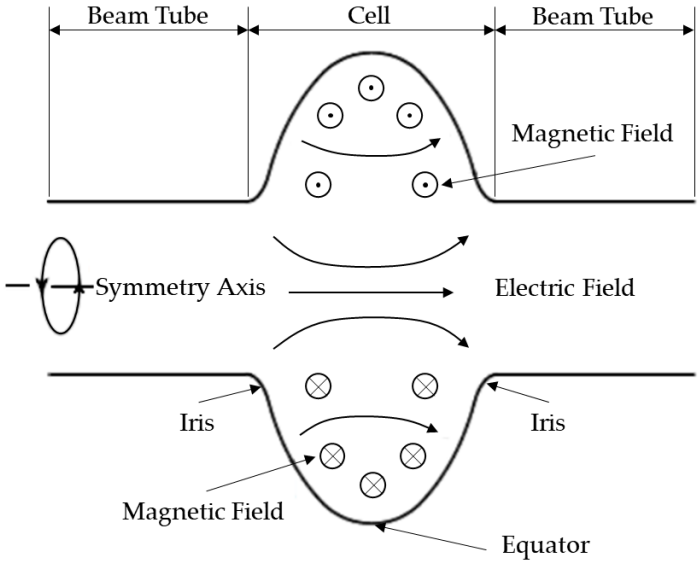

Figure 3-2: Cross-section view of a high β elliptical RF cavity. Reproduced from [63].

The particles enter and exit the cavity via a beam tube attached on either side of the cell, while the electromagnetic field is brought into the cavity using a separate RF coupler attached to the beam tube upstream of the cavity, not shown here. The electromagnetic field exists within the cavity in the form of a standing wave. As such, the entry of the particle bunches needs to be timed to coincide with the leading edge of the RF wave in order to receive the required acceleration in the desired direction. RF cavities involved in particle accelerators are generally operated in the Transverse Magnetic (TM) mode. This results in an electric field oriented in

the longitudinal direction, which has a maximum amplitude at the central cavity axis, while the magnetic field is orientated in the azimuthal direction, and sees a maximum at the cavity walls. During operation, it is possible for the particle beam to excite higher order modes (HOMs) within the cavity. These are extracted by HOM dampers or couplers positioned downstream of the cavity, also not shown here.

In order for superconducting materials to operate as required, they are placed inside what is known as a cryogenic (cryo)-module and are cooled by liquid helium (LHe), which generally circulates at around 2 K. At this temperature, LHe is considered a superfluid, and possesses zero viscosity and is thus able to penetrate and cool all areas of the cavity outer surface. The cooling of the cavities is made all the more important by the fact that the dissipated power scales with the square of the RF field [12].

To measure and compare the performance of different RF cavities, certain figures of merit have been defined which provide a good overview of a cavity's performance.

3.2 Figures of Merit

The accelerating field (E_{acc}), also known as the accelerating gradient due to its typical units of MV/m, is the source of acceleration for charged particles as they traverse an RF cavity. This field is calculated by dividing the acceleration voltage (V_{acc}) by the distance travelled by the particle in the cavity (essentially the cavity length) (z). In order to receive the maximum energy from the cavity, and to ensure the particle always experiences a field pointing in the direction of travel, a particle should traverse the cavity in ½ an RF period (T_{RF}) [64].

$$T_{RF} = \frac{2\pi}{\omega} = \frac{2z}{v} \tag{3-1}$$

$$E_{acc} = \frac{V_{acc}}{z} \tag{3-2}$$

There is a certain limitation to the accelerating field however. The maximum accelerating field for a given cavity depends on the maximum surface fields it can sustain before vortex penetration diminishes its efficiency [7]. It is thus important to minimise the ratios of the peak fields to the accelerating field by selecting a suitable cavity geometry [64]. The maximum surface fields are the peak surface electric field (E_{pk}) and the peak surface magnetic field (H_{pk}). These values are proportional to the accelerating field in a specific cavity operating with a specific field [65].

During operation, the RF field is carried by a thin portion of the cavity walls, due to the London penetration depth limitations, thereby limiting its volume. Seeing as the averaged energy in the electric field equals that of the magnetic field, the total energy stored in the cavity is given by:

$$U = \frac{1}{2}\mu_0 \int_v |H|^2 dv = \frac{1}{2}\epsilon_0 \int_v |E|^2 dv \tag{3-3}$$

Because of the non-zero surface resistance of the cavity, there is a certain amount of power dissipated during operation. The dissipated power, assuming a constant R_s, is calculated over the interior cavity surface.

$$P_d = \frac{1}{2} R_s \int_s |H|^2 ds \tag{3-4}$$

In light of this, an important measure of performance is defined. The quality factor (Q_0) of a cavity is a ratio of the stored energy to the dissipated power. The quality factor can also be multiplied by 2π to obtain the number of RF cycles required for all of the stored energy to be dissipated.

$$Q_0 = \frac{\omega U}{P_d} \tag{3-5}$$

$$\therefore Q_0 = \frac{\omega \mu_0 \int_v |H|^2 dv}{R_s \int_s |H|^2 ds} \tag{3-6}$$

This equation is often simplified as follows:

$$Q_0 = \frac{G}{R_s} \tag{3-7}$$

$$G = \frac{\omega \mu_0 \int_v |H|^2 dv}{\int_s |H|^2 ds} \tag{3-8}$$

Where G is the geometry constant, and is only dependent on the shape of the cavity.

In order to gauge the performance of an accelerating cavity, the quality factor is often measured as a function of the accelerating voltage, generating a Q_0 vs E_{acc} curve. BCS theory predicts a very stable and consistent quality factor for all accelerating fields up until the theoretical limit imposed by a material's critical field. This is not what transpires in reality and will be discussed in Chapter 3.3.

The shunt impedance is a further figure of merit, relating the accelerating voltage to the dissipated power. Ideally, it should be as large as possible for accelerating cavities.

$$R_a = \frac{V_{acc}^2}{P_d} \tag{3-9}$$

Linked to this is another figure of merit, which relates the shunt impedance to the quality factor and describes the power dissipated per unit length at a given accelerating field.

$$\frac{R_a}{Q_0} = \frac{V_{acc}^2}{\omega U} \tag{3-10}$$

One final but crucial figure of merit, which is more reliant on the material quality, is the Residual Resistivity Ratio (RRR). The RRR is an immediate estimate of a material's purity: the higher its value, the purer the material [66]. The RRR value is affected mainly by

impurities, which act as scattering sites for electrons, thereby reducing the RRR. The RRR is defined as the ratio of the normal state resistivity to the superconducting state resistivity as follows:

$$\mathrm{RRR} = \frac{\rho(300\ \mathrm{K})}{\rho(4.2\ \mathrm{K})} \tag{3-11}$$

The RRR value for material used to produce bulk Nb cavities is typically RRR > 300. Nb thin films, even though deposited using a RRR > 300 target, usually have a far lower RRR value. For example, the RRR value for the LEP-II Nb coated Cu cavities was around 11 ± 1 [46], however, recent ECR Nb thin films have reached substantially higher RRR values, in the region of 300 on *a*-sapphire and 587 on MgO [67]. It has been suggested that the RRR is dependent on the electron mean free path *l*, as follows [52]:

$$RRR = 0.38l\ [nm] + 1 \tag{3-12}$$

In terms of cavity choice and comparability, the two most important figures of merit are the accelerating field and the quality factor. The accelerating field determines the number of cavities that will be required to reach the required energy levels. As such, it has a direct influence on the capital costs of an accelerator. The higher the accelerating field, the fewer cavities are required to accelerate the beam. The quality factor helps to predict the amount of cooling power that will be required to maintain the desired operating temperatures and thus determines a large portion of operating costs. A higher quality factor leads to a lower operating cost and is therefore of vital importance for future high energy accelerating structures.

3.3 Superconducting Radio Frequency (SRF) Cavities

Based on the superconductivity principles laid out in Chapter 2, the choice of material for SRF cavities is dependent on a few important characteristics. Firstly, BCS theory predicts that a good candidate for superconductive RF applications must be not only a good superconductor (high T_c), but also a good metal in the normal state (low ρ_n) [68]. Secondly, the superheating field H_{sh}, which is related to the critical magnetic field H_c, should also be high, with a GL-parameter κ as small as possible [69]. With these limitations, there are only a certain number of materials from which to choose. An overview of these materials is shown in Table 3-1. The two materials of interest during this study, Nb and NbN, have been highlighted.

Table 3-1: Superconducting properties of materials suitable for SRF applications. Reproduced from [48].

Material	T_c (K)	ρ_n (μΩcm)	H_c (0) (T)	H_{c1} (0) (T)	H_{c2} (0) (T)	λ (nm)	Δ (meV)	ξ (nm)
Nb	9.23	2	0.2	0.18	0.28	40	1.5	35
NbN	16.2	70	0.23	0.02	15	200-350	2.6	3-5
NbTiN	17.3	35		0.03	15	150-200	2.8	5
Nb_3Sn	18	8-20	0.54	0.05	28	80-100	3.1	4
V_3Si	17	4	0.72	0.072	24.5	179	2.5	3.5
Nb_3Al	18.7	54			33	210	3	
MgB_2	40	0.1-10	0.43	0.03	3.5-60	140	2.3/7.2	5

Nb has been the material of choice in the construction of SRF cavities for the past few decades. This is due to it having the highest transition temperature (T_c = 9.2 K) of pure metals and the highest lower critical magnetic field (H_{c1} ≈ 180 mT @ 2 K) of all superconductors [48]. It is also readily available and relatively easy to machine. However, due to the significant advancement made by the SRF community over the past few decades, the operating point of Nb cavities are approaching their upper limit ~ 50 MV/m. Coupled to this, Nb is a poor thermal conductor, which means it requires substantial cooling systems to operate. Nb cavities are also expensive and involve the use of hazardous chemicals, such as HF, during preparation [70]. As such, alternative materials, as well as alternative methodologies have been gaining traction in recent years, due to the possibility of improving the accelerating field beyond the fundamental limit of bulk Nb cavities. The boundaries overcome for bulk Nb cavities as well as the alternative materials and approaches mentioned here are detailed below.

3.3.1 Bulk Niobium Cavities and Principal Cavity Limitations

Even though Nb presents very attractive characteristics for SRF applications, multiple unforeseen issues have been encountered over the past few decades. These issues are best understood when looking at their effect on a quality factor vs. accelerating field curve, as shown in Figure 3-3. Each of these phenomena have been carefully studied and overcome by the SRF community. A summary of the issues and the methods used to overcoming them are presented [1].

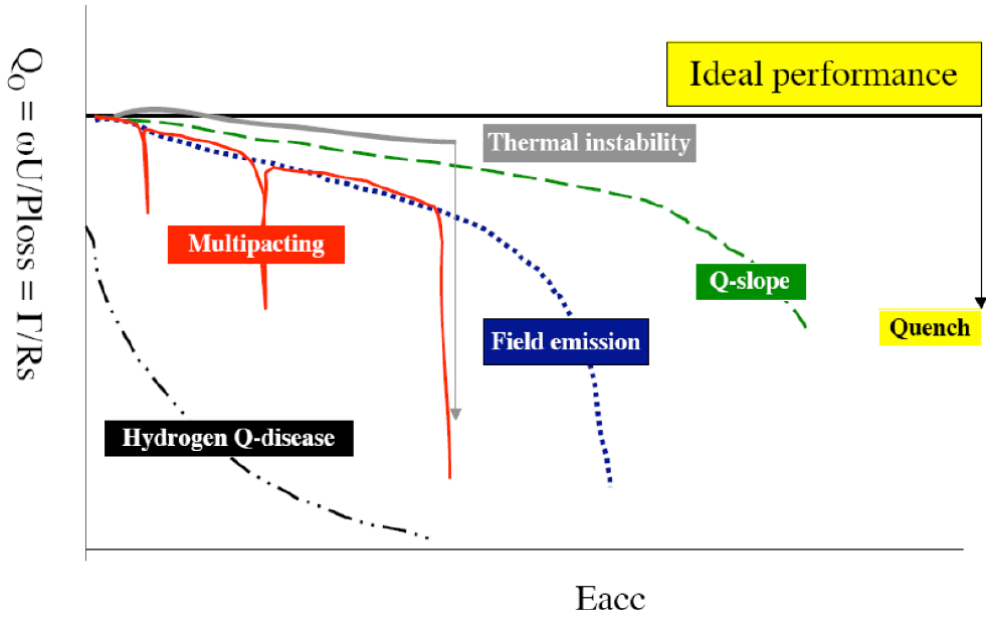

Figure 3-3: Quality factor vs. accelerating field for bulk Nb cavities, indicating the ideal performance and the effects of different issues encountered in SRF cavities [1].

The Hydrogen Q-Disease:

In the 1980's and 1990's, cavities which had passed their vertical acceptance tests and were subsequently placed in a cryomodule for operation, were suddenly found to have a decreased quality factor that further decreased with an increase in the magnetic field. The reason for this was found to be the precipitation of hydrogen in islands near the surface region of the cavity. During cooldown, hydrogen moves within the Nb and forms Nb-hydrides, which are weak superconductors. This problem was found to be worse in high purity Nb. In low purity Nb, the defects act to bind the hydrogen in place preventing it from forming precipitates. To prevent this, a high temperature bake and a fast cooldown to 100 K to "freeze" hydrogen in place was implemented. Nowadays, the use of nitrogen doping is also thought to trap further hydrogen, allowing bulk Nb cavities to operate at even higher fields.

Electron Multipacting:

During cavity operation, a sudden drop in the quality factor of a cavity is often indicative of multipacting. Multipacting is due to secondary electron emission from impacts of stray electrons with the cavity surface. The emitted secondary electrons are further accelerated by the cavity, thereby absorbing energy, and make impact with the surface of the cavity. If the accelerated secondary electron repeatedly impacts the same cavity area, the absorbed impact energy heats the surface and forms a local hot spot. If more than one secondary electron is emitted for every impacting electron, multipacting occurs. Multipacting was found to be

mainly related to cavity geometry, but also related to the secondary electron yield of the cavity material. Sometimes multipacting can be processed away, this is known as a soft barrier, but following this, a hard barrier is typically always encountered. Modern elliptical cavities, due to their field configuration, have all but eradicated multipacting issues.

Thermal Breakdown (Cavity Quench):

Interactions of the RF field with defects on a cavity surface, such as weld defects, drying stains or foreign particles, lead to an increase in the surface temperature due to RF field heating. The thermal conductivity of Nb is not high enough to transport this heat away. As such, the temperature of the localised area around the impurity increases above T_c and becomes normal conducting, which effectively increases the defective area size. This procedure is self-amplifying and quickly leads to a quench of the cavity. This problem is now well understood and measures are in place to help prevent it, e.g.; Nb sheet scanning, chemical etching of the Nb and clean room assembly.

Electron Field Emission:

By 1990, all previous reasons for quality factor reduction had been understood and solutions were in place to decrease their effects. Now that higher accelerating fields were achievable, a new phenomenon was encountered. Electrons were found to be emitted, through a tunnelling mechanism, mostly by micro particles on the cavity surface. This was found at accelerating fields between 10 – 20 MV/m [8] in areas affected by a high surface electric field. The emitted electrons are accelerated by the electromagnetic field and impact another surface of the cavity, where they cause localised heating, (possibly leading to a quench) and x-ray emission. This phenomenon is known as field emission and is found to increase exponentially with the field.

Generally, stringent cleaning techniques and clean room assembly keep cavities particulate free and thus reduce the likelihood of field emission. It is also possible to remove particulates through RF processing, which leads to a permanent recovery of the quality factor. Cavity design optimisation can also combat field emission by limiting the surface electric field at a particular accelerating field by adjusting the E_{pk}/E_{acc} ratio.

Nb cavities are subjected to a well-documented series of processing steps in order to overcome these different issues. These include high pressure rinsing (HPR), which helps to prevent field emission, electropolishing in a solution without hydrogen, for extremely smooth surfaces and no hydrogen precipitation, 120°C baking, to avoid the high-field Q-slope

and most recently discovered, nitrogen doping, which increases the quality factor by reducing the residual resistance [16]. This allows modern Nb cavities to be readily produced with very high performance characteristics. However, Nb cavities are still very expensive and the use of cheaper substrates with higher thermal conductivity, such as Cu, and coating them with a thin film of superconducting material, could provide thermal stability and cryogenic load decreases [21] as well as significant savings in capital expenditure. Because of this, Nb thin film cavities are particularly well suited to operation at low frequencies or for potential operation at 4.2 K.

3.3.2 Thin Film Nb/Cu Cavities

An alternative approach to the use of bulk Nb is to manufacture a Cu cavity and coat the inside surface with a thin film of superconducting material. This is known as a thin film cavity and has already been successfully implemented by CERN for the LEP-II [71], LHC [72] and most recently the HIE-ISOLDE [82][83] accelerating cavities as well as by INFN for the ALPI accelerator [75]. The very shallow penetration depth (40 nm for Nb and 200 – 350 nm for NbN) of radio frequency fields in superconducting materials essentially makes SRF properties a surface phenomenon. Because of this, a material thickness on the order of a few microns is required, thereby enabling the use of thin film coatings [76]. As with anything though, the thin film approach has its advantages and disadvantages, the more pertinent of which are described below.

Low cost

Cu is far less expensive, costing roughly 10% of Nb. This reduces the capital costs significantly. Of equal importance, Cu is easier to machine than Nb, providing a further cost reduction. This is particularly advantageous for large cavities, i.e. those operating at low frequencies.

Thermal stability

The thermal conductivity value of Cu (300 – 1500 W/mK [77]) far surpasses that of Nb (10 – 200 W/mK @ 4.2 K depending on purity (RRR) [78]). Because of this, it is far easier for the Cu cavity to transport any built up heat on the cavity surface to the LHe refrigeration system. The high thermal conductivity of Cu also allows it to be more robust against incidents that locally produce heat in the cavity, such as multipacting or field emission.

Earth magnetic field trapping insensitivity

An added advantage found with thin film cavities over bulk Nb cavities is a large reduction, 100 times lower, in the amount of the earth's magnetic field that is trapped during cooldown [48]. A simple explanation for this is a reduction in the mean free path of thin films, as opposed to bulk Nb, and a high H_{c2} [8]. This leads to a lower surface resistance due to flux trapping and importantly, to far less complex shielding requirements for cryostats that house thin film cavities as opposed to bulk cavities.

Surface quality

Thin films are known to reproduce the structure of the surface onto which they are deposited. Therefore, the substrate surface (roughness, uniformity etc.) has a big influence on the deposited thin film, which in turn greatly influences the performance of the thin film. Large surface roughness values could lead to shadowing during film growth, which results in low-density films and possible porosity within the film. This leads to a decreased level of performance due to weak links [72]. Any foreign material or voids in the interface region between the Cu and Nb could lead to hotspots, due to decreased thermal contact, and therefore decreased quality factors [54]. For this reason, the Cu surface requires a precise series of preparation and processing steps before it is coated with a superconducting thin film. This is detailed in Chapter 5.

Impurities

In any sputtered thin film, the possibility of finding impurities is quite high, due to the nature of the process and the affinity of O_2 and H for Nb. The primary source of impurities is the outgassing of the Nb cathode and the Cu substrate during the deposition process. Impurities are known to have an adverse effect on thin film performance, for instance the dissolved oxygen content decreases the T_c of Nb by about 1 K per atomic percentage [54].

It is also understood that process gas inclusions in thin films are a common occurrence when the atomic mass of the process gas is smaller than that of the cathode material [46]. The extent to which different process gases are included depends on the gas that is being used for the deposition process. The higher the atomic number of the gas species, the lower the possibility of reflection from the cathode and subsequent inclusion in the film. These inclusions will also affect the performance of the films by, for example, acting as flux pinning sites or creating local hotspots due to RF heating. For this reason, a pre-deposition heat cycle is used to reduce the presence of desorbed impurities, such as water, hydrocarbons and oxygen.

Q-Slope

One of the biggest drawbacks facing thin film deposited cavities is the so-called "Q-slope", which limits thin film cavities to operation at relatively low fields. Thin film coatings have a superior quality factor to bulk Nb at low fields, possibly due to the lower BCS resistance [72]. However, due to the increase in residual resistance with increasing field, the quality factor of Nb thin film cavities decreases at a far quicker rate than bulk Nb cavities [72]. A representative graph showing a Q-slope comparison between the two is provided in Figure 3-4.

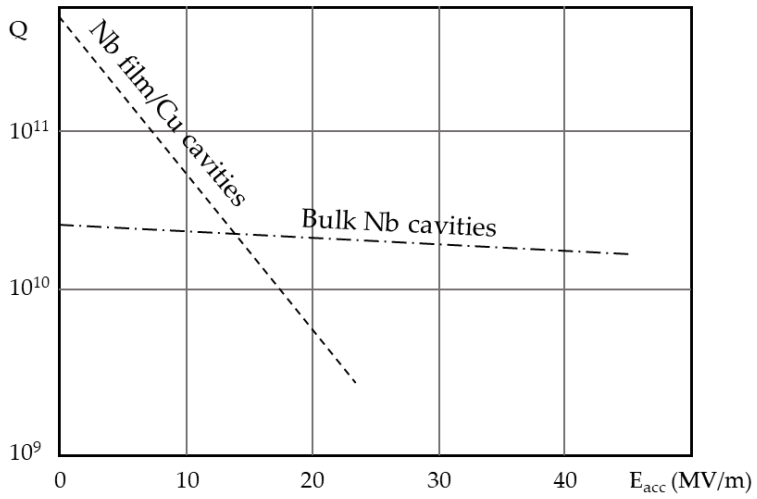

Figure 3-4: Comparison of the typical Q-slope for bulk Nb cavities vs thin film Nb/Cu cavities. Reproduced from [79].

There are multiple effects reported as possible causes of the Q-slope, with a very good synopsis provided by Palmieri and Vaglio [49]. The overarching theme is seen to be the stronger increase in the residual resistance with increasing field for thin films over bulk Nb. This phenomenon is said to be due to Non-Quadratic Losses (NQL) [80]. Unfortunately, a single cause for the Q-slope has not been isolated and all attempts to eradicate the Q-slope through improvements of the film quality have failed [21]. Further research is required to elucidate the reasons behind it.

In order to reduce the effects of some of these disadvantages, Nb coated Cu cavities have been the subject of significant amounts of research and development. In light of this, a short summary of the current state of the art Nb coated Cu cavities is provided below, including the multiple different methods with which the film coatings are completed.

Current state of the art and future research initiatives

For the most part, Nb/Cu cavities have been produced using different sputtering techniques, such as DC magnetron sputtering (elliptical cavities for the LHC at CERN) and DC bias diode sputtering (QWR cavities at INFN and CERN). These techniques rely on the deposition of neutral atoms of Nb material onto the surface of a Cu cavity. Because of this, even though both of these techniques can employ a bias voltage during deposition, they are still not considered as "energetic" deposition techniques and therefore suffer from adhesion issues, non-conformal coatings and lower film density. Energetic deposition/condensation techniques are those that produce a large percentage of target material ions during the deposition process. This allows these types of processes to better utilise a bias voltage to attract the sputtered material towards the substrate surface. The resultant increase in the adatom energy provides significant benefits, such as:

- Improved film adhesion
- Increased film density
- Conformal coatings
- Altered film morphology

Much of the current research is thus focused on the use of energetic deposition techniques. These techniques and suitable references are indicated below:

- *HiPIMS.* This has been applied to elliptical SRF cavities by multiple labs, including CERN [81][82], Jefferson Lab (JLab) [83], Lawrence Berkley National Laboratory (LBNL) [84] and STFC [85] and is currently being investigated for use with the future FCC crab cavities at CERN [86]. As of now, the HiPIMS coated cavities show equal performance to the best DC MS cavities, however, there is room for optimisation [87].
- *Vacuum/Cathodic Arc Deposition.* This technique was implemented at INFN Roma 2 with good results on small samples which were unfortunately not replicated on full cavities [88]. This technique can suffer from the deposition of large macroparticles on the sample surface.
- *Coaxial Energetic Deposition (CED™).* This is a new technique developed in co-operation between the Alameda Applied Science Corporation and JLab [89]. Initial results from cavity deposition were not very successful however.
- *Electron Cyclotron Resonance (ECR).* This technique was developed and studied at JLab and shows significant promise [90][91]. There is a large production of singly charged ions and an absence of macroparticles. The one limitation is the difficulty in constructing a setup suited for a cavity geometry [21].

Further research, being conducted at INFN Legnaro, is focused on the use of thicker Nb films (~ 40 – 70 μm) [79]. This is in an attempt to alleviate hotspot and interfacial void issues by allowing heat to be transported away from the affected zone through the use of a thicker Nb film. Initial results seem promising and a thick Nb film may be a promising future alternative as well [21][92].

In parallel to the ongoing research into Nb coated Cu cavities, a large amount of research into utilising alternative superconducting materials in SRF cavities is also ongoing.

3.3.3 Alternative Materials

As part of efforts to push thin film coated cavities to performance levels equal to or better than bulk Nb at higher fields, the use of alternative materials has been extensively investigated. There are a number of publications of significant importance which contain detailed overviews of possible alternative materials [48][68][69][93]. A shortened list of the materials of interest, including their superconducting properties, is provided in Table 3-1. This list is also visually represented in Figure 3-5, which details the modelled BCS resistance at 4.2 K of alternative superconducting materials at 500 MHz, as a function of T_c and normal state resistivity.

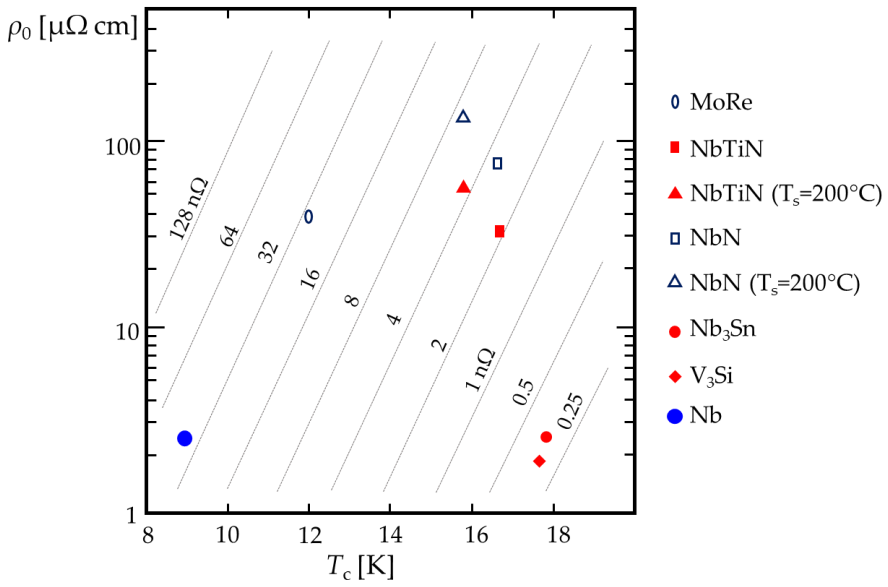

Figure 3-5: BCS resistance of alternative superconducting materials modelled at 500 MHz and 4.2 K as a function of T_c and normal state resistivity. Reproduced from [94].

It is clear that some of these materials perform better than Nb at 4.2 K and are therefore worth researching. The current prime candidates for future accelerator materials include Nb_3Sn and V_3Si, owing to their combined high T_c, low normal state resistivity and low BCS resistance.

The nitrides of NbN and NbTiN are more likely to be implemented in multilayer coatings, due to their high normal state resistivity. For the sake of brevity, only NbN will be described in detail here, as it formed a central part of the investigations covered in this thesis.

Niobium Nitride (NbN)

NbN is a B1 type material system which can occur in a multitude of phases (e.g. β, γ, δ, δ', and ε) depending on the environment in which it is created. The Nb_xN_y phase diagram is detailed in Figure 3-6, albeit for creation using high temperature annealing. Nevertheless, these phases can also be achieved through sputtering, where the phase creation is dependent on the process parameters.

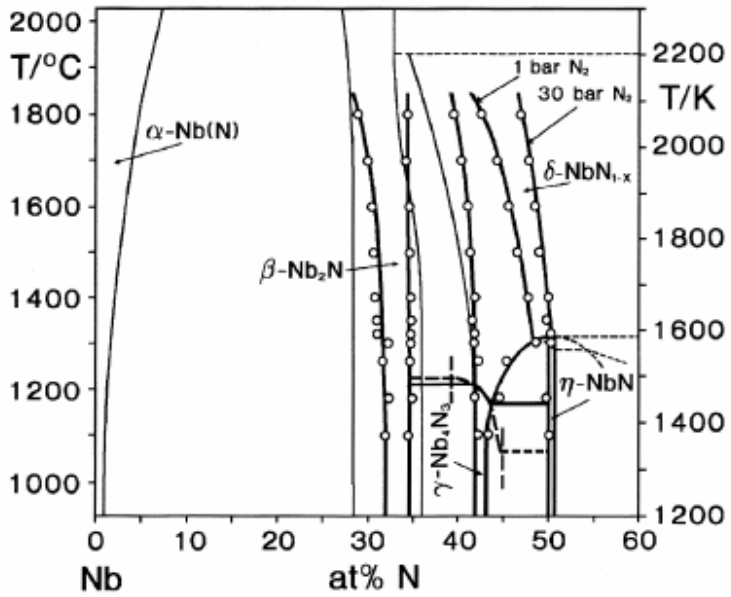

Figure 3-6: Phase diagram of the Nb_xN_y system above 1000°C. The diagram was produced through high temperature annealing of Nb in a nitrogen environment [95].

The phases of Nb_xN_y are reliant upon their respective Nb:N ratios, with the ranges for each phase shown in Table 3-2 [96]. Three of the Nb_xN_y phases are known to be superconducting, with deposited thin film T_c's ranging from 11.6 K for the hexagonal ε-phase [97], 12-15 K for the tetragonal γ-phase [98] and up to 17.3 K for the cubic δ-phase [99]. Films with a Nb/N ratio closer to stoichiometry generally possess better superconducting properties [100]. The creation of NbN thin films with sputtering often results in a mixture of phases present in deposited thin films, which tends to increase the superconducting transition width (ΔT_c) [101].

Table 3-2: Details of the crystal structure, Nb/N ratios and lattice parameter values corresponding to the different Nb_xN_y phases [96][102][103][104].

NbN_x Phase	**Crystal Structure**	**Nb/N ratio range (x)**	**Lattice Parameter (Å)**
α-NbN_x	BCC Nb with interstitial N	0.4 (NbN_x)	a = 3.301 - 3.303
β-NbN_x	Hexagonal, W_2C type	0.39 - 0.5 (Nb_2N)	a = 3.058 c = 4.961 ± 0.001
γ-NbN_x	Tetragonal, Distorted NaCl type	0.75 - 0.8 (Nb_4N_3)	a = 4.380 c = 4.332 ± 0.001
δ-NbN_x	Cubic (FCC), NaCl type	0.88 - 0.98 and 1.015 – 1.062 (NbN)	a = 4.378 – 4.42
ε-NbN_x	Hexagonal, TiP type	0.92 – 1.018 (NbN)	a = 2.958 Å c = 11.273 ± 0.0015
δ'-NbN_x	Hexagonal	0.96 (NbN)	a = 2.94 c = 5.46

Deposited thin films of NbN are known to possess different colours depending on the phase of the film. Mercier *et al* reported that films with a silver colour correspond to the hexagonal phases and those with a gold colour correspond to the cubic phase [105]. Similarly, Benvenuti *et al* reported a yellow colour, corresponding to the cubic and tetragonal phases, and a grey colour corresponding to the hexagonal ε-NbN phase [106]. This provides a visual cue as to the achieved phase of NbN. Interestingly, the addition of impurities has been proposed to stabilise the formation of the superconducting, high T_c δ-NbN phase [107][108]. This has been shown in both NbCN and NbTiN, which both display higher transition temperatures than NbN itself [68].

NbN generally grows in a columnar fashion, often surrounded by voids, normal conducting areas of Nb, Nb-dissolved gas composite phases and other absorbed gases which can extend through the film thickness [109][110]. This is characteristic of a Zone 1 structure as found in the Structure Zone Diagram (SZD), detailed in Chapter 4.4. It is possible to achieve a denser structure in the NbN film, where the film more resembles a Zone T structure, by adjusting the deposition parameters. This was detailed by Westra *et al*, whereby they observed a tight columnar structure for low pressure deposited NbN films and a more open and voided film structure for films deposited at higher pressures [100].

With regards to superconducting applications, one drawback with NbN, is its anomalously high normal state resistivity, which leads to a high surface resistance in the superconducting state and large magnetic field penetration depth [111]. This value is often larger than expected, with values of more than 100 μΩcm often occurring [68]. The formation of normal conducting oxides and oxynitrides as well as the presence of vacancies/voids between NbN

grains is a known problem which affects NbN film performance, and is thought to contribute to the high resistivity [110] and early flux penetration found in NbN films. In relation to this, the effects of nano-scale surface topography of high-κ materials have also been investigated, with the results hinting at a possible explanation for the early flux penetration in NbN films [38]. An increased surface roughness has also been linked to increased flux pinning. However, the scale of surface roughness responsible for flux pinning is associated with the applied field, where high fields are more sensitive to smaller-scale roughness [112]. To counteract this issue, NbN films deposited with thicknesses less than the penetration depth, have also been shown to have enhanced lower critical field values at lower thicknesses [113]. It is of course possible to improve the properties of NbN thin films and one comprehensive study by Wolf *et al* found that lower deposition pressures, with low N_2/Ar ratios in the gas mix and higher deposition temperatures led to superior performing films [114]. Iosad *et al* reiterate the improved performance of NbN films with lower deposition pressure, including decreased film stresses, which they attribute to decreased thermalisation of the sputtered atoms and increased film bombardment by neutral gas atoms [115]. The N_2/Ar gas ratio cannot be too low however, or there will be insufficient N_2 to form stoichiometric NbN films which will lead to the deposition of contaminated Nb films (with a lower transition temperature than regular Nb) [116] or the non-superconducting β-Nb_2N phase. Significant amounts of C were also found in the high T_c films, which gives further weighting to the stabilisation effects of impurities. Further studies have reiterated the deposition parameter choices above which indicated that a lower nitrogen partial pressure [117], lower deposition pressure [118][119] , higher deposition temperature [111] and higher cathode power [120] led to improvements in NbN superconducting properties along with a more bulk like δ-NbN lattice parameter of $a_0 \geq 4.38$ Å [121].

A linear increase in T_c with increasing lattice parameter, was also reported by Beebe *et al* in the range of 4.38 to 4.39 Å [113]. The superconducting properties of NbN films are heavily dependent on the quality of crystallinity of the film [122]. One aspect affecting this crystallinity is the substrate onto which the films are deposited, which makes it difficult to fabricate high quality NbN films on diverse substrates. NbN also possess an inherently low secondary electron emission coefficient [48] which would assist in combatting multipacting in SRF cavities.

There is a well demonstrated correlation between an increase in grain size leading to a decrease in resistivity [123] and an increase in transition temperature [99] and magnetic field penetration [113]. This result lends itself to higher deposition temperatures and lower N_2/Ar

ratios during deposition. Most superconducting properties of NbN thin films, such as T_c and ρ_n, are found to improve with increasing film thickness, becoming constant at a thickness around 200 - 300 nm [118][119][124]. This is the opposite for the magnetic penetration flux (H_{c1}) which is found to increase exponentially for films thinner than the London penetration depth, $\lambda_L \approx 200$ nm [113].

The range of the superconducting properties of NbN have been detailed in Table 3-1. This range can be explained by the variation in the transition temperature and the normal state resistivity, which are both very dependent on the phase formation of NbN and crystallinity. This is observed in the following expression for the effective penetration depth, where the units are in cm [18]:

$$\lambda_{eff} = 1.05x10^{-5}\sqrt{\rho_n/T_c} \tag{3-13}$$

The residual resistivity ratio (RRR) of NbN films is vastly different to pure metallic films such as Nb. For NbN, a good RRR is found to be just > 1, while for Nb films, RRR > 10 is routinely achieved with DC magnetron sputtering. The RRR of NbN has been found to be heavily reliant on both the N_2/Ar ratio during deposition and the absolute pressure as well. This was detailed by Bacon *et al* for ambient temperature deposition, where they showed an increase in RRR with a decrease in N_2 concentration during deposition and a separate increase in RRR with a decrease in the total deposition pressure [118]. Changes to the resistivity of NbN films were also observed due to the erosion of a Nb target. Iosad *et al* show higher resistivities and bigger grain sizes from films deposited with a used Nb target when compared to a new Nb target [125]. This also indicates that the resistivity is not necessarily due to grain boundary interactions. However, there is an increased effectiveness of flux pinning at grain boundaries with a crystalline disorder around the grain boundary on the same order of magnitude of the coherence length ξ [112]. Thin films, with a high grain boundary and disorder density, and by extension low ξ materials display a strong pinning effect.

In light of the above, it is likely that NbN cannot be used as a single layer coating for a coated cavity. However, due to its attractive properties and relative ease of creation, it is well suited for use in multilayer SIS coatings.

3.3.4 Multilayer Coatings

As indicated in Table 3-1, even though the alternative materials proposed for use in SRF cavities possess higher superconducting transition temperatures (T_c) than Nb, all of them have smaller lower critical field values (H_{C1}) than Nb. As a result of this, some research indicates that their use may not allow the attainment of accelerating fields and high-field

quality factors greater than Nb [30]. Fortunately, a new approach to SRF cavities was proposed by Gurevich in 2006 [5]. The proposal utilises multilayer coatings consisting of alternating insulating (I) and superconducting (S) layers, known as SIS structures, which are deposited onto either bulk Nb or Nb-coated Cu cavities. This proposal requires the use of materials with large penetration depths, therefore providing an opportunity to utilise alternative materials. An example of this SIS structure is shown in Figure 3-7 (a), which depicts an insulating interlayer and a superconducting shielding layer deposited onto a bulk superconductor substrate (either bulk Nb or a bulk-like Nb coating).

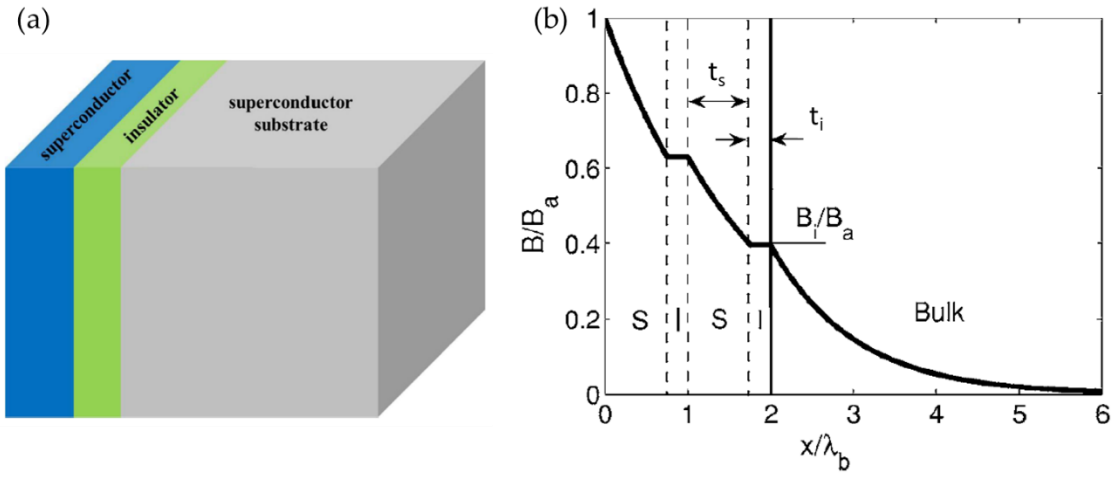

Figure 3-7: (a) Illustration of a multilayer SIS structure deposited onto Nb. Reproduced from [31]. *(b) Variation of the field within a cavity wall when coated with a multilayer SIS structure. In this instance, two SI structures have been coated onto bulk Nb. Reproduced from* [5].

The multilayer structure is essentially used to "shield" the underlying superconductor (film or bulk) from the applied magnetic field, thereby allowing it to operate at higher field values. The shielding acts to increase the field of magnetic penetration (H_{fp}) above the lower critical magnetic penetration field (H_{c1}) of the underlying superconductor, thereby avoiding significant vortex dissipation. This can be visualised in Figure 3-7 (b). The insulating layer and superconducting layers are deposited with thicknesses t_i and t_s respectively. Importantly, the sum of the insulator thickness and the penetration depth of the underlying superconductor ($\lambda > \lambda_{sc} + t_i$) should be smaller than the penetration depth of the superconducting layer [126]. The thin insulating layer, commonly constructed from MgO, AlN or Al_2O_3, is used to inhibit vortex oscillations and prevent global penetration of the vortices into the underlying superconductor [48] and should be large enough to ensure suppression of Josephson coupling between the superconducting layers.

The increase in the penetration field due to this multilayer approach is given by the following equation [5] which is based on initial work by Abrikosov, where ϕ_0 is the flux quantum [127].

$$H_{fp} = \frac{2\phi_0}{\pi d^2} ln\left(\frac{t}{1.07\xi}\right) \text{ , when } d<\lambda_L \tag{3-14}$$

The shielding effect of the multilayer structure is also known to be enhanced through the use of a higher number of SI layers. This effect is governed by the following equation, with N = number of superconducting layers [5]:

$$B_i = B_0 exp\left(-\frac{Nt}{\lambda}\right) \tag{3-15}$$

There is however a trade-off between vortex dissipation reduction and superconductivity suppression at the SI interfaces, which leads to an optimum number of SI layers [48]. The increase in the penetration field is known to lead to a decrease in the surface resistance (R_s) and a subsequent increase in the quality factor (Q).

Results from investigations into the screening effect of SIS coatings were first presented in 2010 and indicated a strong enhancement of the lower critical field and prevention of vortex penetration at fields higher than the lower critical field of Nb [128].

Since the initial proposal of SIS structures in 2006, a great deal of further research has been undertaken, both theoretical and practical, to better understand the deposition characteristics required, as well as to define the equations which describe the behaviour of SIS structures ([31][129][130][131][132]). Optimisation of the different layer thicknesses, in relation to the penetration field, is of critical importance in order to achieve the highest magnetic (accelerating) field possible. In the original paper, the vortex penetration field of the S-layer is given by $B_v = \phi_0/4\pi\lambda\xi$. Subsequently, Kubo *et al* produced the following equation, which takes into account the layer thicknesses and their effects on the vortex penetration field [129]:

$$B_v^{(S)} = \frac{\phi_0}{4\pi\lambda_1\xi_1} \frac{cosh\frac{t_S}{\lambda_1} + \left(\frac{\lambda_2}{\lambda_1} + \frac{t_I}{\lambda_1}\right) sinh\frac{t_S}{\lambda_1}}{sinh\frac{t_S}{\lambda_1} + \left(\frac{\lambda_2}{\lambda_1} + \frac{t_I}{\lambda_1}\right) cosh\frac{t_S}{\lambda_1}} \tag{3-16}$$

This equation reduces to the original equation for a semi-infinite S-layer. Thus, a thin S-layer increases the penetration field, but it cannot protect the underlying bulk superconductor if $t_s << \lambda_1$. The peak surface field without vortex penetration requires consideration of the shielded magnetic field on the bulk superconductor as well. The shielding afforded to the bulk superconductor can be viewed as an attenuation of the applied field. Thus, if the shielded magnetic field seen by the bulk superconductor is less than the vortex penetration field of the bulk superconductor, the bulk superconductor is safely protected. If the shielded magnetic field is larger than the bulk penetration field, the surface magnetic field is limited below the peak values.

As further detailed by Kubo [31], theoretical calculations indicate an optimised thickness of both the insulator and superconductor layers in an SIS structure, which result in the maximum peak surface magnetic field (B_{ML}), while accounting for the effects of both the vortex penetration field at the S-layer and the shielded magnetic field at the bulk superconductor. The plot for a NbN-I-Nb SIS structure is shown in Figure 3-8. These investigations were completed for a thickness independent λ and B_c. When taking into account the thickness dependence of λ and B_c, the resulting plot shows a very similar B_{ML} value with the effects of thickness dependence more pronounced at thicker insulator thicknesses ($\lambda < \lambda_{sc} + t_i$) [126].

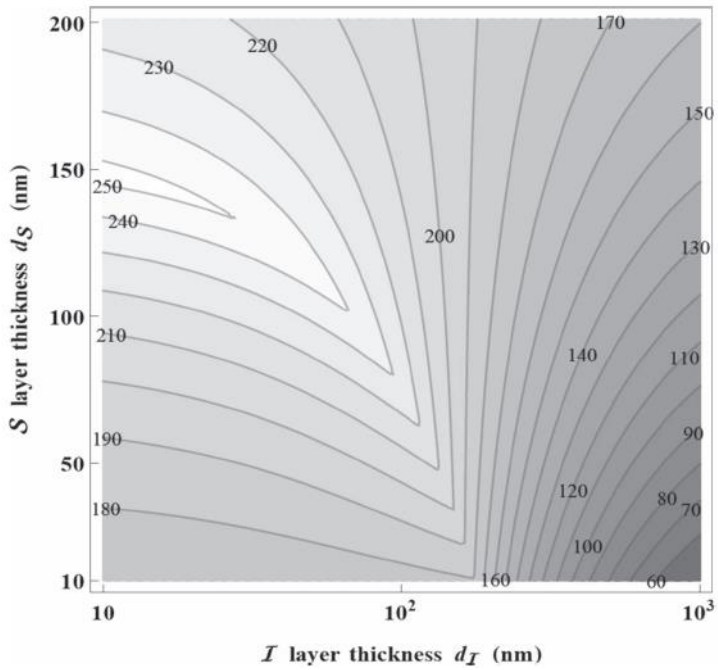

Figure 3-8: Magnetic field limit (B_{ML}) dependence of NbN-I-Nb SIS structures as a function of the respective superconductor and insulator layer thicknesses [31].

The figure indicates an increase in the magnetic field limit compared to bulk Nb, with a peak value of ~ 250 mT. Increasing the insulator layer thickness (d_i) leads to a decrease in B_{ML} due to the rise of the magnetic field attenuation in the S-layer and should thus be kept to a producible minimum. This also limits the effects of the low thermal conductivity and the dielectric losses present in the I-layer.

The plot in Figure 3-8 does not include the effects of surface defects however. Further plots were defined which include the effects of surface defects on the peak magnetic field by using a suppression factor η. The addition of the suppression factor leads to a reduction of the superheating field of the superconductors, $B_{sh} \rightarrow \eta B_{sh}$, which changes the optimum

superconductor and insulator layer thicknesses for peak B_{ML} as well as decreases B_{ML} itself. This can be seen in Figure 3-9 for (a) $\eta = 0.9$ and (b) $\eta = 0.5$, where lower η indicates larger defect presence. Clearly, as η decreases, so too does the optimum S-layer thickness. This is due to the decrease in the field limit of the S-layer, which is compensated for by thinning the S-layer. However, if the S-layer is too thin, it will not provide the protection required by the underlying superconductor.

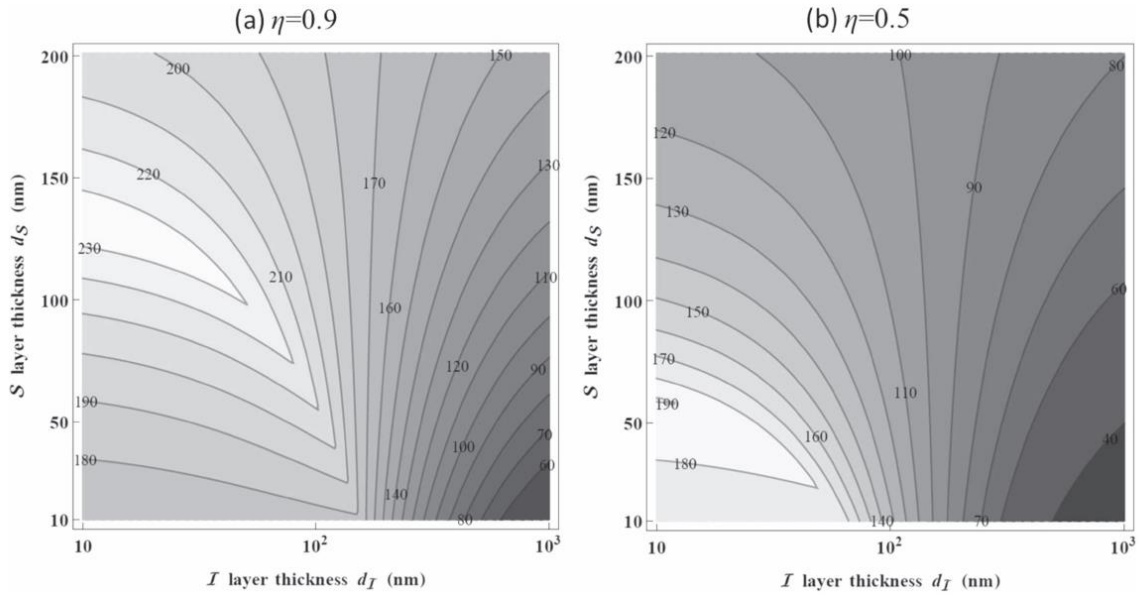

Figure 3-9: Magnetic field limit (B_{Max}) dependence of NbN-I-Nb SIS structures, including the effects of surface defects, based on the superconductor and insulator layer thicknesses [31]. *(a) Plots the results for a high suppression factor of η = 0.9 while (b) plots the results for a decreased suppression factor of η = 0.5.*

It has also been stated that the deposition of multilayer structures can lead to an increase in the surface roughness of the outer film due to the increased roughness of the surface onto which the film is deposited, as opposed to the polished substrate found normally. This can lead to lower critical temperatures of the superconducting layer than if it were deposited onto a polished sample [128][133]. This allows for a further point of optimisation as the resultant roughness is often dependent on the film thickness.

The SIS structure field enhancement has also been applied to SS structures, where the outer S-layer is in the dirty regime. Examples of SS structures include a dirty superconducting layer deposited on top of a clean superconductor, baked bulk Nb or nitrogen doped bulk Nb.

There has been some push back to the possibility of successfully applying SIS coatings in SRF cavities [25] but nearly all indications point to the potential for improved operating

conditions with their use. This can be seen from the large quantity of research which has been completed into a few of the potential materials [7][28][133][134][135][136].

4. The Art of Sputtering

This chapter serves to introduce the deposition techniques used to deposit the thin films studied in this thesis. This includes an introduction to sputtering in general, an overview of DC Magnetron Sputtering (DC MS) and an overview of High Power Impulse Magnetron Sputtering (HiPIMS), both of which are Physical Vapour Deposition (PVD) techniques. The reactive versions of each of these processes, which include the addition of a reactive gas species, are also described. The thin film growth mechanisms are detailed as well as the stresses present in thin films following sputtering procedures.

4.1 Introduction

Sputtering is a type of physical vapour deposition process that has found widespread use in many industries. Thin films of specific materials are deposited onto substrate materials in an attempt to improve their performance by taking advantage of the material properties of both the substrate and the thin film. By depositing a thin film of a specialist material onto a cheaper substrate material, it is also possible to obtain a significant cost saving and still achieve the required performance levels. Sputtered thin films are usually grown in thicknesses ranging from tens of nanometres up to several micrometres, depending on the application. The films deposited in this study were of differing thicknesses; the AlN films were deposited in the range of tens of nanometres (AlN) while the Nb and NbN were deposited from 100's of nanometres up to a few micrometres. One of the prerequisites for sputtering is the generation of a stable plasma.

4.2 Plasma Generation

For explanation purposes, the plasma generation detailed here will focus on DC diode discharges. The sputter discharge mechanisms used in this study, which build off the concepts in DC diode sputtering, will be detailed in the coming sections. Sputtering relies on the generation of a stable plasma, created by ions of the process gas. In order to do this, a large DC field is applied between two electrodes; namely, the cathode, where the target is placed and the anode, where the substrate is placed. These electrodes are positioned inside a deposition chamber filled with a neutral gas species, typically argon. Figure 4-1, acquired from [137], details the electric discharge regimes which typify plasma generation and the changes encountered when increasing the applied field.

The applied field accelerates any background electrons present in the chamber away from the cathode, which then allows for collisions between the electrons and the process gas atoms. If the applied field is large enough, these collisions will generate ions of the gas species. This generation of ions is termed "Townsend Discharge", which is found between points C and E in Figure 4-1. The probability that a collision will result in ionisation is dependent on:

- The mean free path in the gas species, which is determined by the system pressure
- The scattering cross-section of the gas species
- The applied field
- The ionisation potential of the gas species.

These collisions also result in the creation of secondary electrons. With an increase in the applied field, the secondary electrons will also gain enough energy to ionise the process gas. At this point, a collision avalanche occurs which greatly increases the current. The generated gas ions are accelerated towards the cathode where they partake in collisions with the target. The maximum energy an ion can achieve corresponds to the cathode fall, which is equivalent to the difference between the potential of the plasma and the cathode [138].

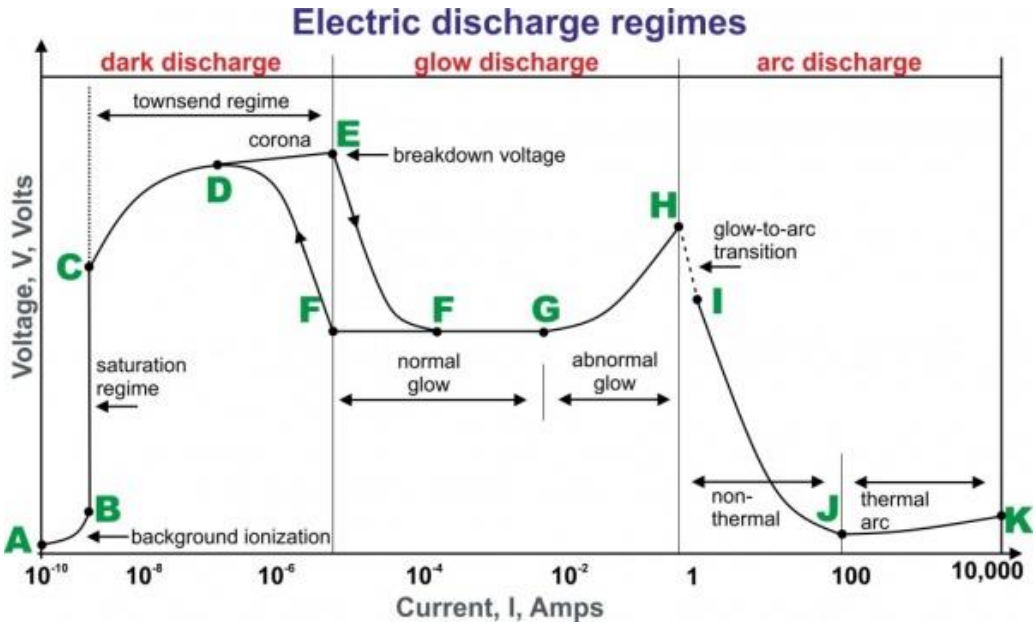

Figure 4-1: Electric discharge regimes in DC sputtering which typify plasma generation [137].

At high enough energies, secondary electrons are also liberated from the target during collisions between the gas ions and the target. This is dictated by the secondary electron emission yield (γ_e) of the target material, which is dependent on the surface condition of the target, the gas (ion) species and the ion energy. The onset of secondary electron emission from the target leads to a sudden drop in the voltage required to sustain the discharge, due to the

increase in charged particle density (discharge current). This is known as Breakdown, shown as point E in Figure 4-1, and is a transition to a self-sustaining discharge and the normal glow regime, characterised by the formation of a plasma [139]. The characteristic glow associated with plasmas is generated by the emission of photons during the recombination of electrons and ions.

During breakdown, sheaths are found to develop on both electrodes, with the electric field concentrated on the cathode sheath. The discharge current of the plasma is then defined by the Townsend equation:

$$i = i_0 \frac{e^{\alpha d}}{1-\gamma_e(e^{\alpha d}-1)} \tag{4-1}$$

Where i_0 is the initial current, γ_e is the secondary electron emission coefficient, d is the distance between the anode and the cathode and α is the Townsend ionisation coefficient, which represents the probability per unit length of ionisation occurring during an electron-atom collision. It is related to the mean free path as follows:

$$\alpha = \frac{1}{\lambda} e^{-\frac{V_i}{qE\lambda}} \tag{4-2}$$

Where λ is the mean free path, V_i is the ionisation potential of the gas species, q is the electron charge and E is the electric field between the anode and cathode. Due to the relationship between the mean free path and the system pressure, the Townsend ionisation coefficient is also dependent on the system pressure. The breakdown voltage can therefore also be described in terms of the system pressure and the electrode spacing with the use of Paschen's law:

$$V_B = \frac{APd}{ln(Pd) + B} \tag{4-3}$$

Where A and B are fitting coefficients which account for the relationship between the mean free path, system pressure and the secondary electron yield of the target. Paschen's law therefore describes two operating extremes: a low value of Pd, indicating a low electron-atom collisions rate, leading to an insufficient secondary electron emission rate and a large value of Pd, indicating frequent collisions, leading to lower particle energies and lower ionisation probability. Consequently, a region exists in between these two extremes where the discharge is self-sustaining.

With a further increase in the field above the normal glow regime, the plasma enters the abnormal glow regime where sputtering typically takes place. This regime is characterised by more stable plasma conditions, conducive to stable sputtering processes. Increasing the field too far however, results in a transition to the arc discharge regime, which typically

results in a decreased sputter yield, the possible deposition of molecules, potential damage to the growing film and potential ion implantation in the target. The cathode is also unable to dissipate all of the applied power anymore and thermionic emission of electrons is also present [21].

4.3 Sputtering

The generation of process gas ions and a subsequent self-sustaining plasma are the first steps in the sputtering process. Sputtering can be considered as a material deposition process, in which material is removed (sputtered) from a target source, in the form of atoms, atom clusters, molecules or ions, as a result of the energy deposited by impacting particles, and deposited onto a substrate typically located at the anode. These impacting particles are the ions of the sputtering gas species, detailed in Chapter 4.2, which originate in the discharge plasma. The explanation below is the basis of all DC sputtering processes.

The onset of sputtering depends on multiple factors, but will only proceed once the energy of the impacting ions exceeds a certain threshold energy. As a rough estimate, once the impacting ions possess an energy greater than four times the heat of sublimation of the target material, sputtering is possible [140]. More accurately though, this threshold energy (E_{th}) is determined by the surface binding energy (E_{SB}) of the material as well as the atomic mass of the incident ions (M_i) and the atomic mass of the target material (M_a). Intuitively, this threshold must be at least as much as the surface binding energy of the target material [141]. It is calculated using [142].

$$E_{th} = E_{SB}\begin{cases}(1+5.7(M_i/M_a))/\Lambda & for\ M_i \le M_a \\ 6.7/\Lambda & for\ M_i > M_a\end{cases} \tag{4-4}$$

Where the energy transfer factor (Λ) is given by:

$$\Lambda = \frac{4M_iM_a}{(M_i + M_a)^2} \tag{4-5}$$

This threshold energy is reached in the normal glow regime, where the plasma is self-sustaining. However, this region is not conducive to depositing good films as the sputtering is very localised with a low sputter yield. Deposition of thin films is conducted in the abnormal glow regime due to the higher sputter yield resulting from increased cathode area usage.

When the ions collide with the target, they liberate (sputter) atoms or molecules from the target, which can then be deposited onto a substrate. The number of atoms liberated from the target per impacting ion is known as the sputter yield and is affected by a number of process parameters. The most significant is the cathode voltage, which determines the kinetic energy

of the impacting ions. As the cathode voltage is increased, the sputter yield will increase up until ion energies reach ~ 10 keV, where after it levels off. Any further increase in ion energy will lead to a decrease in the sputter yield as the ions begin implanting themselves into the target.

The sputter yield is also affected by the atomic mass of the target material, due to the associated change in its surface binding energy, and the atomic mass of the process gas species, where an increase in atomic mass leads to an increased amount of energy being deposited during collisions and a resultant increase in the sputter yield. The sputter yield is also a function of the angle of incidence between the ions and the target, governed roughly by $1/\cos\theta$, where θ is the angle between the ion trajectory and the normal to the target surface. The energy of the sputtered material is found to be independent of the incident ion energy. Therefore, increasing the cathode power increases the sputter yield but does not increase the energy of the sputtered material. The energy of the sputtered material is governed by the Thompson formula [143].

$$Y(E)dE \propto \frac{(1-\sqrt{(U_s + E)/\gamma E_0})}{E^2(1 + U_s/E)^3}dE \tag{4-6}$$

Where E_0 and E are the energies of the incident ions and sputtered atoms, and U_s is the surface binding energy of the target material. The constant $\gamma \equiv 4M_1M_2 / (M_1+M_2)^2$, defines the relationship between the incident ions (M_1) and the target material (M_2). The sputtered particles generally have an energy between 3 – 5 eV, which far exceeds the energies found in evaporation processes, allowing for changes in the resultant film's microstructure. Once removed from the target, the sputtered particles are transported as a vapour and deposited onto a substrate, in the form of adatoms, where a thin film forms over time. There are multiple sputtering techniques available nowadays; those relevant to this work are expanded upon below.

4.3.1 DC Magnetron Sputtering (DC MS)

DC Magnetron Sputtering (DC MS) follows the principles laid out above, albeit with the addition of a magnet, typically a permanent magnet, positioned behind the cathode. DC MS can be utilised with both planar sputtering setups, as was used in this study, as well as with cylindrical sputtering setups, such as is used to deposit the inside of cavities. The setup of a typical rectangular magnetron is detailed in Figure 4-2 (a). The outer (green) magnets will always have an opposite pole to the inner (blue) magnets, as it facilitates the presence of magnetic field lines.

The magnet acts to, essentially, trap the repelled electrons within its magnetic field lines, where the Lorentz force forces them into a gyration motion around the field lines. Consequently, the plasma discharge is localised in front of the cathode, with the chamber essentially acting as the anode. This electron entrapment leads to a higher electron path length at a constant mean free path, thereby increasing the ionisation efficiency compared to regular DC sputtering. The higher ionisation efficiency leads to higher deposition rates and allows for lower deposition pressures (typically 1 Pa or lower) for DC MS compared to conventional DC sputtering (typically 10 Pa or higher) [144]. The localised plasma conditions led to preferential erosion of the target, leading to the well-known "racetrack" erosion and underutilisation of target material. This erosion is found to be more intense in the corners (1.5x higher) than the straight sections [145]. This preferential erosion is shown for a smaller square Nb target used in this study in Figure 4-2 (b).

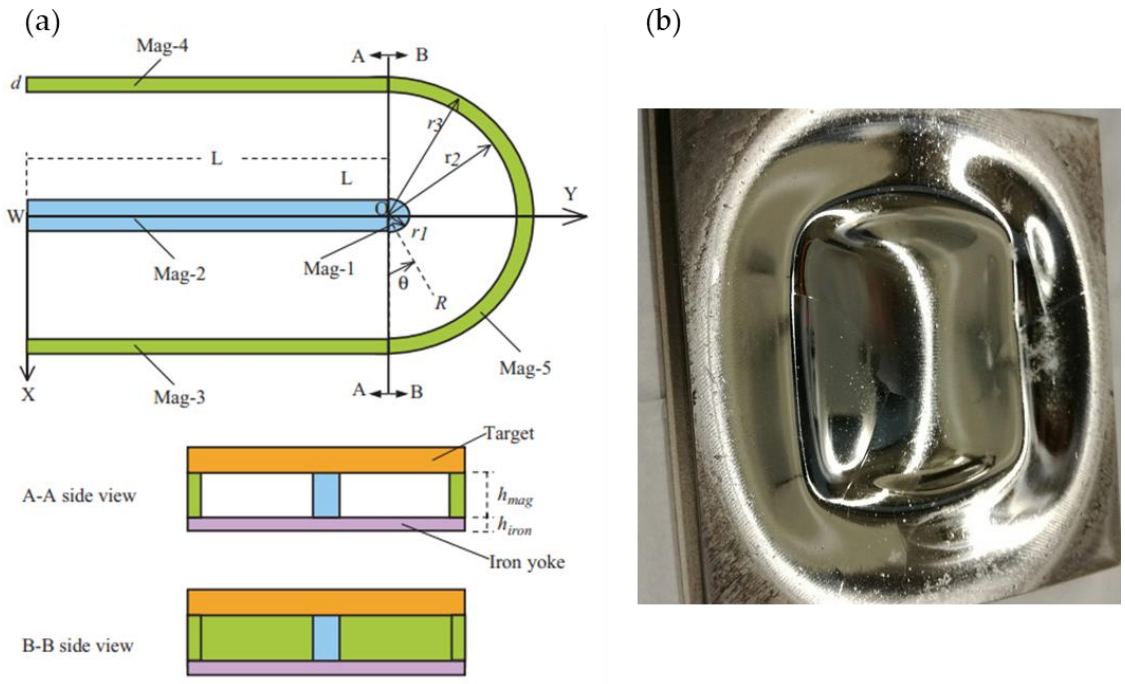

Figure 4-2: (a) Schematic diagram of a portion of a rectangular magnetron cathode detailing the positions of the magnets [146]. *(b) Used Nb target showing the well-worn "racetrack" due to the high ionisation efficiency within the magnetic field lines with magnetron sputtering.*

The erosion of the target is known to impact the properties of the deposited thin film, due to the changes to the sputtering conditions at the target surface. Iosad *et al* completed a series of experiments to determine how to minimise the intrinsic stress levels and changes of Nb and NbN films over the lifetime of the target. For a Nb film, they found that by maintaining a constant power level and constant pressure, the intrinsic stress can be maintained at zero

throughout the lifetime of the target, while the same applies for NbN, with the addition that the nitrogen flow rate must be adjusted proportional to the Nb deposition rate [125]. Aging of the target leads to a progressive drop in the discharge voltage over its lifetime, resulting in a decreasing sputtering rate. For a constant deposition pressure, this results in an effective increase in the number of collisions between sputtered atoms and gas ions. Based on this, the erosion of the target is equivalent to an increase in the target to substrate distance or an increase in the pressure [115].

In DC sputtering, the electrons are affected by the electric field present between the two electrodes. With the addition of the magnet in DC MS, there are now two forces acting on the electrons, the electric field acceleration and the Lorentz force. These forces cause the electrons to move in a spiral motion around the magnetic field lines [21] as well as to drift around the magnet, in the $\boldsymbol{E} \times \boldsymbol{B}$ direction, eventually returning to the position where they started. This motion has been calculated by Fan *et al* for a rectangular target magnetron and is showcased in Figure 4-3 [146].

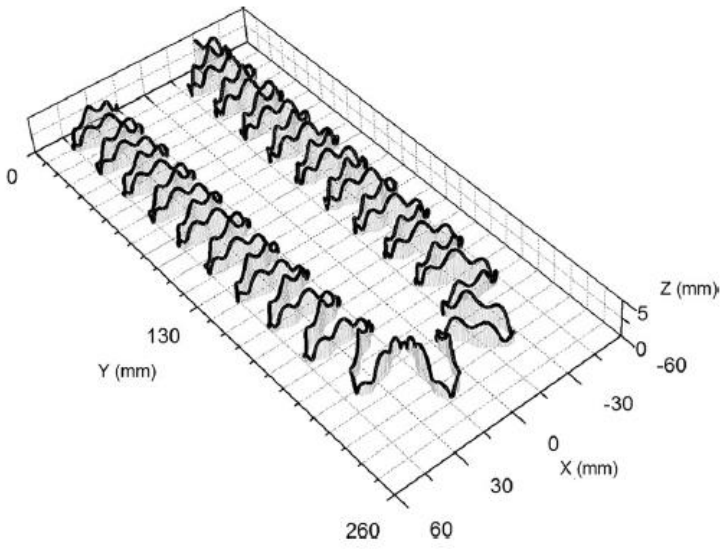

Figure 4-3: Illustration of the calculated electron trajectory above a portion of a rectangular magnetron [146].

The higher ionisation efficiency present in DC MS leads to another phenomenon present in magnetron sputtering known as gas rarefaction. With an increase in cathode power, there is a reduction in the local gas density in front of the cathode, due to the heating of the gas as a result of the increased collision frequency between ejected target atoms and gas ions [147]. This is important with regards to the plasma discharge as it is partially equivalent to locally reducing the gas pressure [148]. It also has implications for stoichiometry control in reactive sputtering.

4.3.2 Reactive DC Magnetron Sputtering (R-DC MS)

Reactive DC Magnetron Sputtering utilises the same principles as regular magnetron sputtering except the thin films are deposited in the presence of a reactive gas added to an inert gas. Some common reactive gases include O_2, N_2, NH_3 and CH_4. The addition of a reactive gas to the process brings about the formation of compound films on the substrate, as well as changes to the dynamics of the sputtering process. This is often easier than creating a compound target with the correct stoichiometry for the chosen applications.

The reactive gas not only reacts with the growing thin film, but also with the target material, where a compound layer is formed on the target surface and any material deposited on the chamber walls. The compound layer can be formed by chemisorption of reactive gas ions on the target surface [149], implantation of previously chemisorbed gas atoms into the target due to ion impingement and direct implantation of reactive gas ions at higher energies [150]. High temperature deposition also leads to diffusion of the reactive gas species into the target, though this can be negated by effective target cooling. The compound layer is thinner in the "racetrack" of the magnetron, as its formation has to compete with the sputtering process. Once the compound layer is fully formed, the target is said to be "poisoned". With changes to the cathode power or reactive gas flow, it is thus possible to have three distinct target states; a fully metal target, a transition state target which is partially reacted and a fully reacted compound (poisoned) state [151].

The formation of the compound layer leads to a decrease in the sputter yield compared to a pure metallic target due to the increased secondary electron yield of the target [151] and increased bond strength of compounds compared to metals. The flow rate of the reactive gas is the main mechanism by which the formation of the compound layer is controlled. There are two methods which can be utilised for controlling the reactive gas flow rate, each with positives and negatives [152]:

- Flow control of the reactive gas is the simplest method; however, this generally leads to sputtering in the poisoned target mode. As a result, the deposition rate is low compared to a metallic target. In addition, the film properties produced by flow control reactive sputtering can be less than optimal. Nevertheless, because the target is poisoned, the process is very stable and reproducible.
- Partial pressure control of the reactive gas is more complex than flow control because it requires active feedback control, but it allows for operation of the process in the transition region. By operating in this region, higher deposition rates compared to

flow control are achieved with improved film properties. However, stability and reproducibility can be sacrificed

It is felt that it is better to operate reactive sputtering in the transition region, between the metal mode and the poisoned mode [144][152]. This is however difficult to achieve in a flow controlled system, as is used for this study.

Reactive sputtering is often associated with the creation of a hysteresis loop. The hysteresis loop is a function of the reactive gas concentration, as indicated in Figure 4-4, and is due to the changing rate of arrival of reactive gas atoms, with a changing reactive gas concentration.

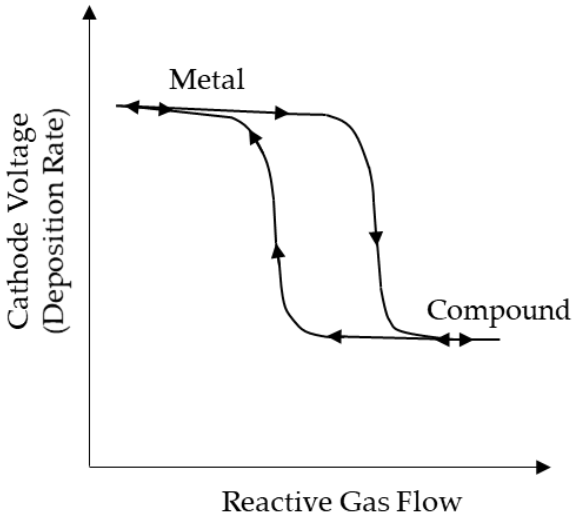

Figure 4-4: Generic hysteresis loop for cathode voltage vs. reactive gas flow rate present in reactive sputtering. Reproduced from [139].

With low arrival rates, the target surface remains metallic (metal mode), as the few target surface atoms, which have reacted, are sputtered away. With increased arrival rates, further compound formation on the target ensues and a point is reached where the compound formation is quicker than its removal (compound/reactive mode). This decreases the sputtering of pure metal from the target, which reduces the reaction rate at the substrate, thus allowing the formation of a compound layer on the target. The formation of a compound layer on the target also leads to a change in secondary electron emission yield. As a result, the partial pressure of the reactive gas increases and the system must find a new equilibrium operating point. If the reactive gas flow is now reduced again, the metal mode will only return once the compound layer has been removed from the target. The removal of the compound layer is the basis for the presence of a hysteresis loop in reactive sputtering. Due to the presence of such a hysteresis, a certain amount of settling time is required for the system to reach a steady state working point. Operation in this hysteresis-affected region is

undesirable as it may result in compound films with different stoichiometry values being deposited due to the existence of two stable operating points.

Berg and Nyberg provided several observations of reactive sputtering hysteresis as well as methods to decrease the hysteresis curve. These are summarised below [153]:

- **Target material:** The sputtering yields for the elemental target material (Y_m) and the compound formed on the target surface (Y_c) are material constants. For materials where $Y_c << Y_m$, hysteresis is normally more pronounced than if Y_c is close to Y_m.
- **Reactive gas type:** Some gases have a higher reactivity to the target material than others do. Normally, O_2 is a more aggressive gas than N_2. However, this may be influenced by, e.g., target/substrate temperatures, surface morphology, etc.
- **System pumping speed**: Hysteresis may be eliminated if the pumping speed is high enough. Unfortunately, the critical value of the pumping speed needed to eliminate the hysteresis is usually unrealistically high.
- **Target to substrate distance:** An increasing collecting area A_c represents an increasing target to substrate distance. Keeping the target to substrate distance small will decrease the hysteresis. The spread of material in sputtering is however unavoidable and the collecting area will always be larger than the target area,

There are some practical considerations to take note of with reactive sputtering as well. If the deposition chamber was opened to atmosphere during sample exchange, it is imperative that it is baked out thoroughly prior to thin film deposition. Opening the chamber to the atmosphere allows water vapour inside the chamber. If not baked out, the water vapour will split into hydrogen and oxygen, and the oxygen will bond with the metal before the nitrogen, due to the higher free energy of formation of oxides over nitrides [152].

The use of a target shutter for pre-sputtering a target will essentially create a smaller collecting area (A_c) than when the shutter is open [152]. Once the shutter is open, A_c will increase appreciably, creating a jump in the process position. This jump will bring about a transition period for the system, while it finds a new operating point. During this time, the composition of the film may vary, leading to variable interfacial and film properties.

One further issue to take cognisance of is gas rarefaction and its effects on compound formation. Rossnagel detailed the decreased arrival rate of reactive species atoms at the substrate surface, due to gas rarefaction, with an increase in cathode power [147]. For this reason, the reactive gas partial pressure should be increased with increasing cathode power to ensure the correct compound formation in the film.

4.3.3 High Power Impulse Magnetron Sputtering (HiPIMS)

High Power Impulse Magnetron Sputtering (HiPIMS) is an adaptation of DC magnetron sputtering which combines pulsed power sputtering and magnetron sputtering. During the process, the power supply stores energy in capacitors during the "off-time" and releases this energy during the "on-time" of the pulses. The relationship between the "on-time" and "off-time" is described by the duty cycle of the process and is affected by both the pulse length and the pulse frequency. The release of the stored energy during a single pulse leads to a peak power, and importantly, a peak current, typically two orders of magnitude higher than the time-averaged power [148]. This results in a significant increase in the plasma density leading to a significant increase of the collision cross-section between sputtered atoms and electrons. The most significant result of this process is that a significant portion of the sputtered target atoms, depending on the ionisation cross-section of the target material and the peak pulse power, can be ionised [154]. This was elucidated by Bohlmark *et al* who utilised optical emission spectroscopy to determine the presence of Ti ions within a HiPIMS plasma [155]. They showed that the ionic contribution in the recorded plasma spectrum was over 90% for high power pulses.

Significant ionisation of the sputtered target atoms can lead to self-sputtering, whereby the newly sputtered target ions are attracted back to the target, where they participate in sputtering the target material. For some high self-sputter-yield materials, such as Cu, the self-sputtering of the target is able to sustain the plasma discharge without a process gas. This phenomenon was initially shown by Hosokawa *et al* and is termed sustained self-sputtering [156]. The condition for sustained self-sputtering is as follows:

$$\alpha\beta\gamma_{ss} \geq 1 \tag{4-7}$$

Where α represents the ionisation probability, β represents the probability that a sputtered and ionised atom will return to the target and γ_{ss} is the self-sputtering yield of the target material. Seeing as $\alpha < 1$ and $\beta < 1$, a self-sputter yield $\gamma_{ss} > 1$ is required but not sufficient for sustained self-sputtering [157]. The self-sputtering process is enabled by the generation of secondary electrons, which essentially transfer energy from the sheath into the plasma, which maintains the high electron temperature required for ionizing collisions. When transitioning from gas sputtering to metal self-sputtering, the decrease in ionisation energy of the metal ions needs to be considered. In order for a material with a low γ_{ss} to maintain the required secondary electron emission, it has been stated that doubly or higher charged metal ions are required for the secondary electron emission necessary for self-sputtering to occur [158].

The possibility of sustained self-sputtering is increased if a longer pulse length is utilised, moving to near millisecond range, because there is an increase in the amount of sputtered atoms and ions in the plasma [158]. Prior to sustained self-sputtering, a transient phase of self-sputtering known as runaway occurs, which involves the sharp increase in the discharge current which is found to occur at a specific threshold power, determined by the applied voltage [158]. The applied voltage also determines the amount of time between the HiPIMS pulse and runaway to sustained self-sputtering operation.

Experiments completed by Anders looking into this phenomenon with a Nb target produced a particularly descriptive graph, which is displayed in Figure 4-5 [148]. It is evident that following a HiPIMS pulse, there is a small peak in the discharge current, which is caused by the ionisation of gas atoms and the generation of secondary electrons, followed by a settling of the discharge current. As the applied voltage is increased towards the runaway threshold, around 570 V, a second peak can be seen, which is caused by the ionisation of target atoms and indicates the onset of self-sputtering. At applied voltages above the runaway threshold of 570 V, the discharge current is seen to increase dramatically up to a higher sustained level due to the significant influence of self-sputtering. An increase in applied voltage is also seen to reduce the time between the pulse and discharge current runaway to sustained self-sputtering.

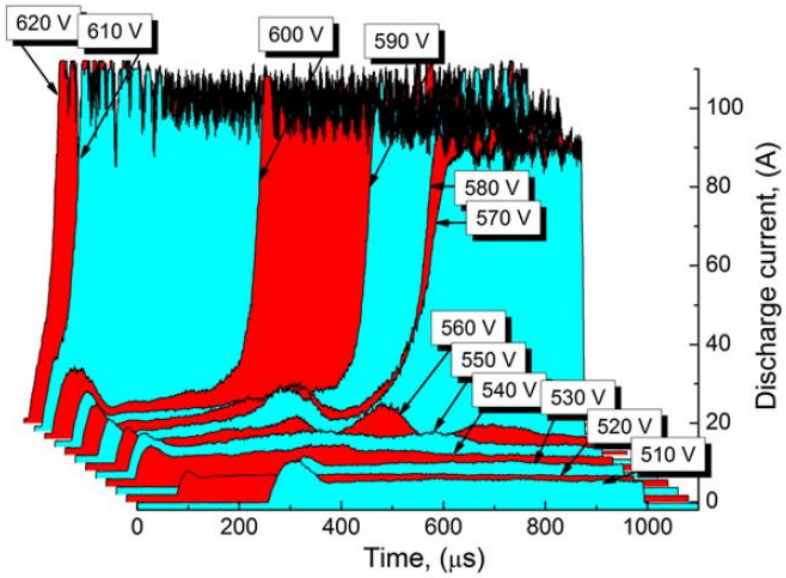

Figure 4-5: Measurement details from Anders showing the effects of the applied voltage pulse on the onset of self-sputtering near the threshold for runaway. Reproduced from [148].

In order to achieve the high power pulses associated with HiPIMS, the duty cycle of the discharge is typically small, around 0.1 to 5%, in order to prevent overheating of the target

and possible damage to the magnets [159]. A typical pulse length is reported to be between 10 – 200 μs. As a result of this low duty cycle, and a few further factors detailed by Anders, the HiPIMS process is reported to have a lower deposition rate (for the same average power) when compared to DC MS [160] and further decreases with increasing pulse length [161]. However, this can change depending on the materials being deposited (sputter yield) and the shape/size of the substrate. The film structure is also very dependent on the specific settings of the HiPIMS power supply, such as pulse frequency and pulse length. The use of short pulse lengths aids in reducing the likelihood of arcing during the process, as the current generally does not reach the maximum value possible for a given voltage [148]. Short pulse times also reduce the likelihood of gas rarefaction and self-sputtering. Changes in the pulse length also affect the time delay; the time between the application of the target voltage and the onset of current at the target.

Terenziani *et al* studied the ionisation efficiency of HiPIMS discharges for a Nb target. They found that the ionisation efficiency increases nearly linearly with current density but increases only slightly with an increase in pulse length [81]. Thus, a short pulse length and high current density led to the highest ionisation efficiency. Due to the nature of the HiPIMS discharge, the ionised species display an evolution with time. Ehiasarian *et al* studied the time evolution of Ti in an environment of inert gas only (Ar) and a reactive atmosphere (Ar + N_2) [162]. They found that the evolution could be split into two regimes. Immediately following the pulse, the discharge consists of mostly inert gas ions with minimal metal ions. The discharge changes as the pulse moves towards the peak discharge current. At this point, the discharge is mainly comprised of metal ions, with the gas ions decreasing due to metal ion creation and gas rarefaction. The metal ion signal then decays after the end of the pulse and the plasma is mainly comprised of gas ions.

One of the main benefits of the ionisation of the sputtered atoms is the ability to influence the kinetic energy of the particles forming the film [84]. This is achieved by applying a bias to the substrate, which can either accelerate particles towards the substrate or reflect particles with insufficient energy. The increased energy of the impacting particles is the basis for the reported improvement of thin films deposited with HiPIMS such as increased density of the films, improved adhesion of the film to the substrate and smoother films [163]. The bias can also improve the directionality of film growth, though this is dependent on the flux of ions reaching the substrate. It has been reported that newly formed ions at the target surface, even after runaway has occurred, have a high probability of returning to the target to act in self-sputtering [157]. This was found to decrease with an increase in the applied voltage beyond

that required for runaway. Thus the flux of sputtered ions at the substrate will increase with an increase in the applied voltage [164].

Kouznetsov *et al* also reported an increased utilisation of the target material due to a broadening of the erosion racetrack in HiPIMS when compared to DC MS. This phenomenon also leads to a more homogeneous film thickness profile from the target centre [154].

4.3.4 Reactive High Power Impulse Magnetron Sputtering (R-HiPIMS)

As has been described for DC MS, the addition of a reactive gas to a HiPIMS discharge also changes the operating conditions of the system and brings about certain complexities for process control. The HiPIMS process operating with a reactive gas is termed R-HiPIMS.

Similar to DC MS, the introduction of a reactive gas leads to the formation of a compound film on the target surface. This compound film leads to a reduction in the sputter yield, as the bond strength of compounds is greater than metals. As a result of this, the target poisoning will result in a reduction in the role of self-sputtering and an increase in the role of gas recycling [165]. The stronger gas rarefaction associated with HiPIMS compared to DC MS could however lead to lower poisoning, due to a reduced flux of reactive gas to the target [166]. Furthermore, the increased gas rarefaction associated with HiPIMS (including the reactive gas) has been linked to the reduction or potential eradication of hysteresis loops when compared to R-DC MS [167]. This decreases the complexity of the sputter process control-system. However, due to the increased role played by the "film pump" in large industrial coating systems, whereby the reactive gas bonds with material sputtered onto the chamber walls, this conclusion may not apply to them. Furthermore, investigations have also revealed how adjusting the R-HiPIMS parameters affects the hysteresis loops, with results indicating that the hysteresis is caused by the same mechanism as in R-DC MS [168]. The process by which the target is poisoned is slightly different in R-HiPIMS when compared to R-DC MS. In R-HiPIMS, there is an increased percentage of the gas, including the reactive gas, which is ionised. Because of this, reactive gas ions arrive at the target with sufficient energy for implantation. Poisoning in R-HiPIMS thus occurs on and below the surface [144].

Changing the parameters of an R-HiPIMS process, as with R-DC MS, leads to changes in the operating regime of the target, metallic vs. poisoned. The issue with a poisoned target, as seen with R-DC MS, is the resultant decrease in deposition rate. Ganesan *et al* studied the effects of pulse length on the level of target poisoning for a Hf target in the presence of Ar and O_2 [169]. They found that with an increase in the pulse length, the target shifts from a fully poisoned state, to a quasi-metallic state. The peak target current was also found to

increase up to a pulse length of 120 μs, where after it decreased again. This indicates an optimum pulse length corresponding to a peak target current for a specific pulse frequency. This has also been described as *duty cycle* effects, where an increase in the duty cycle leads to a gradual shift from a poisoned state to a quasi-metallic state, which leads to an increased deposition rate [170].

Due to the different transport mechanisms at play with R-HiPIMS compared to R-DC MS, a flow rate of reactive gas that gave stoichiometric films for R-DC MS may not result in a stoichiometric film for R-HiPIMS. The bombardment of the growing film by the reactive gas in between R-HiPIMS pulses is said to allow the growth of more stoichiometric films than in the case of R-DC MS [160]. The time evolution of ionised species detailed for HiPIMS is also present for R-HiPIMS, with the ratios of inert gas and reactive gas ions being process dependent.

4.4 Thin Film Deposition

Following the introduction of the different sputtering methodologies, it is now appropriate to describe the process by which thin films grow. Thin films are grown as the material sputtered from the target is deposited onto a substrate, typically located opposite the target. Generally, the film growth process proceeds through the stages shown in Figure 4-6 [139]:

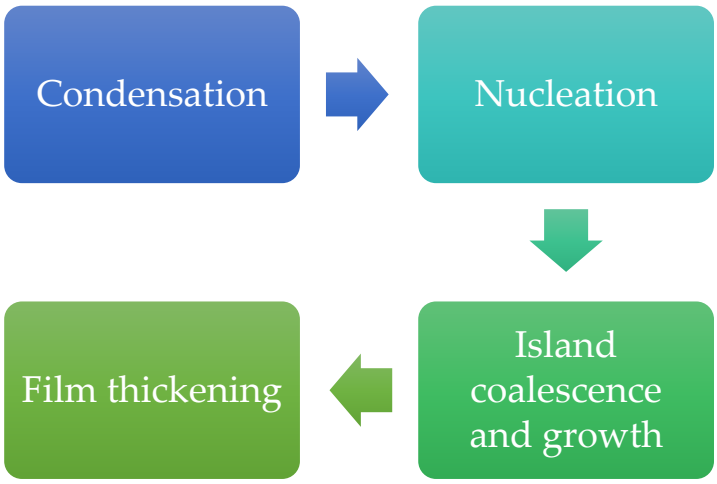

Figure 4-6: Sequence of the stages experienced during the evolution of thin film growth [139].

Condensation is the initial stage of thin film growth and is characterised by the arrival of sputtered atoms onto the substrate surface. Those atoms that stick to the surface are known as adatoms. There are two possible bonding mechanisms between the adatoms and the substrate: chemisorption and physisorption.

Once the adatoms have condensed on the surface, they can desorb from the substrate, diffuse, either along the surface or into the substrate (bulk), or they can remain in place. Typically, diffusion is the sought after result, as it allows adatoms to fill vacancies in the growing lattice and to migrate and add to the growing film structures. Surface and bulk diffusion determine the structural evolution of the film during growth [171] and are greatly affected by the deposition conditions. Diffusion also allows adatoms to find nucleation sites, which are typically defects on the substrate surface, from which they form nuclei; eventually growing large enough where they start to merge with other nuclei, forming a closed surface.
This process of the nuclei meeting and combining with one another is known as coalescence and is the process by which the bulk film is grown. The nucleation and coalescence stages may occur in three different modes, as depicted in Figure 4-7 [139].

- The *Frank van der Merwe* or layer-by-layer growth mode occurs with adatoms which are more strongly bonded to the substrate than each other. Complete layers are formed before the start of another. This is typically found in materials with similar lattice parameters.
- The *Volmer-Weber* or island growth mode occurs with adatoms which are more strongly bonded to each other than the substrate. These islands eventually grow large enough to meet, thereby forming a film. This is typical of materials with a large lattice mismatch or high strain.
- The *Stranski-Krastanov* growth mode is a combination of both of these modes, where the film initially grows in layer form, where after island form takes over as it becomes more energetically favourable. This could be due to the lattice mismatch strain at the interface, which cannot be maintained in the film bulk. This type of growth mode is often found in metal-metal films.

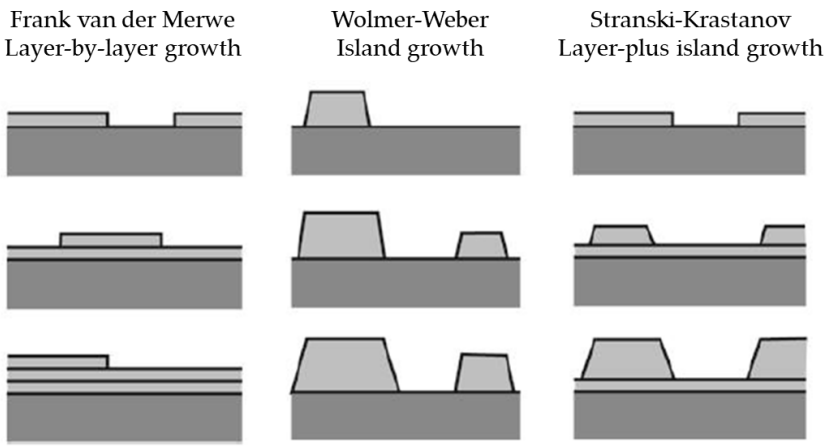

Figure 4-7: Visual depiction of the different thin film growth modes. Reproduced from [172].

The growth mechanism of the thin films will determine the final physical properties of the film and is thus of utmost importance. It is reported that the growth mode during nucleation (initial stages) can affect the ultimate surface morphology, with characteristics whose self-similarity (self-affinity) persists throughout the thickness of the growing thin film [76].

The lattice structure of the substrate and the thin film have an influence on the film through stress and crystal growth effects. The matching of the film lattice to the substrate lattice is termed epitaxy, and will generally prevail in the early stages of film growth regardless of the mismatch between the substrate and the thin film. During these initial phases of film growth, the film will elastically strain to match the interatomic spacing of the substrate [138]. This strain energy will increase as the film thickness increases. However, once the strain energy exceeds some lower possible energy level, the film will decompose to a relaxed structure where a portion of misfit has been relieved by dislocations. It is possible for the lattice of the thin film to be forced into a certain orientation due to the orientation of the substrate, resulting in epitaxial growth.

The microstructure of thin films can be altered with the use of different deposition conditions. As a way of visualising the effects of different deposition parameters, multiple Structure Zone Diagrams (SZD) have been reported over the years, which detail the expected structure of the film based on the deposition conditions used during their creation.

Initial SZDs only detailed the effects of the deposition temperature, through the homologous temperature, $T_h = T_s/T_m$, where T_s represents the substrate temperature during deposition and T_m represents the melting temperature of the target. Movchan and Demchishin proposed the first SZD in 1969 for evaporation coating processes. Thornton later expanded this in 1974 to focus on sputtering processes. The resultant Thornton SZD included the effects of the deposition pressure and the substrate temperature and is perhaps the most well-known SZD. The latest SZD, put forward by Anders and shown in Figure 4-8, includes the effects of particle energies as well [173]. This allows the effects of substrate biasing to be included in the growth models. This is especially relevant, given the current focus on energetic deposition techniques, such as HiPIMS, where a significant difference in ion flux and adatom mobility is seen compared to regular DC MS coatings.

Similar to the Thornton SZD, the Anders SZD includes four designated structure zones. These different structures are known to lead to different characteristics of thin films, with these characteristics often determining the usability of a film. A short breakdown of the zones is provided here:

- **Zone 1 ($T_s/T_m < 0.2$):** The film is comprised of very thin fibres (1-10 nm) often collected into bundles. The grain boundaries are relatively porous while the crystals have a high density of defects. This is often termed fibrous growth and is not subject to high bulk or surface diffusion due to low adatom mobility.
- **Zone T ($0.2 < T_s/T_m < 0.5$.):** The grain structure is found to resemble a strong V-shape. Very fine crystallites grow at the substrate surface, followed by an increase in grain size with increasing film thickness. The grain's size may also normalise at a specific thickness, where after it grows in a columnar structure. Surface diffusion is found to be appreciable in this zone; however, grain boundary migration is strongly limited.
- **Zone 2 ($0.5 < T_s/T_m < 0.8$.):** The grain's structure is homogeneous throughout the thickness of the film and is composed of columns originating at the substrate and extending up to the surface of the film. Surface and bulk diffusion are both present, leading to coalescence and grain boundary coarsening which dissolves the initially small crystallites.
- **Zone 3 ($T_s/T_m > 0.8$):** The grain structure is characterised by three dimensional equiaxed grains. This indicates the crystal growth has been periodically blocked. This zone is dominated by bulk diffusion.

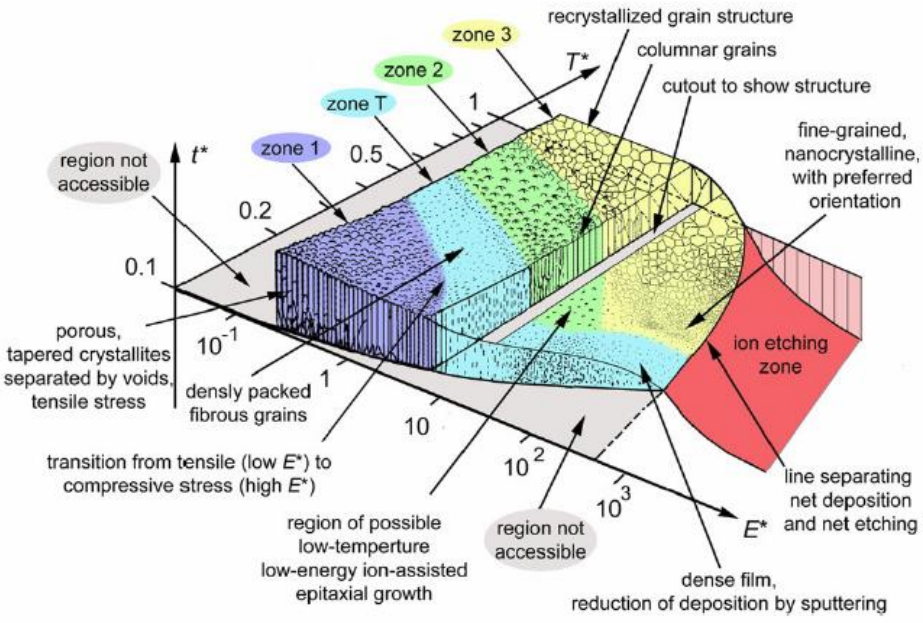

Figure 4-8: Structure zone diagram proposed by Anders applicable to energetic deposition [173].

It is appropriate at this stage to discuss the implications of changing deposition parameters on the growth characteristics of thin films.

4.4.1 Substrate Temperature

An increase in the deposition temperature results in increased adatom mobility. This allows for greater bulk and surface diffusion, due to the higher energy of the adatoms, which will therefore result in increased grain sizes and a densification of the film, although the grain size increase stagnates at roughly 2 to 3 times the film thickness [139].

4.4.2 Deposition Pressure

In sputtering processes, there are two pressure values of interest: the base pressure and the deposition pressure. The base pressure is the pressure of the sputtering system at a specific temperature, often following a bake out and prior to depositing a thin film. A lower base pressure generally results in fewer unwanted impurities (such as oxygen) being present in the sputtering chamber during deposition. As such, a lower base pressure is preferred for when depositing superconducting thin films to limit the amount of unwanted particles. This is however often limited by the sputter chamber size and the pumps employed in the system. A NEG (Non-Evaporable Getter) pump is often employed to assist in reaching very low base values, in the region of 10^{-9} mbar.

The deposition pressure is the pressure of the deposition chamber during the deposition process. This directly affects the kinetics of the particles within the chamber. At low pressure values, there is a higher mean free path or a lower likelihood of collisions between gas atoms and sputtered atoms. As such, sputtered atoms arrive at the substrate with higher energy levels, leading to a higher likelihood of adatom rearrangement and diffusion on the substrate surface. Conversely, at higher pressures values, the sputtered atoms have a lower mean free path leading to a decreased energy level and a shift in their distribution function to much lower energies. It is also more difficult to ignite a plasma at low pressures due to the lower likelihood of secondary electron emission.

4.4.3 Process Gas

Generally, the process gas used in sputtering is a noble gas, such as argon or krypton, but it is possible to utilise reactive gases as well, allowing in-situ reaction between the new thin film coating and the reactive gas to form different materials. The process gas being used during sputtering directly affects the sputter yield and as such, the deposition rate. An increase in atomic mass of the process gas will increase the energy with which they impact the target, thereby increasing the deposition rate. An increase in the process gas mass number also leads to a lower likelihood of gas entrapment in the film due to recoil collisions [46].

Freshly deposited metallic films are known to be strong getters of chemically reactive gases. Unfortunately, this can lead to the formation of contaminants on the film surface. Possible sources of contaminants include [174]:

- Residual and adsorbed gases inside the sputtering chamber
- Vacuum pump, back-streaming and miscellaneous system leaks
- Impure sputtering gases

4.4.4 Substrate Bias

A substrate bias can be utilised in both DC MS and HiPIMS processes with the aim of achieving similar results. In DC MS, a substrate bias is used to accelerate (mostly) ions of the gas species towards the substrate (situated at the anode). This allows increased energy to be imparted by the ions impacting the film surface. This energy is deposited into the film, thereby facilitating surface modification through ion-assisted deposition. These changes can be to the surface roughness, topography, crystallography and texture, grain structure or the stress levels of the film [66].

In HiPIMS, due to the generation of target material ions, the modification of the film structure is not necessarily reliant on energetic bombardment by process gas ions and is instead determined by the ionised target material atoms. The ionisation of the sputtered target material also affords HiPIMS the advantage of achieving more conformal coatings on substrates with difficult structures or topographies due to the attraction imparted by the substrate bias.

The impact of energetic particles on the substrate leads to two competing processes; defect generation and annihilation [173]. An increase in the substrate bias will lead to a reduction in grain size, a change in internal stresses, enhanced film adhesion and increased possibility of noble gas ion incorporation into the film. Increasing the bias too high however, results in resputtering of the already deposited material, although these atoms generally land near to where they were ejected.

4.4.5 Cathode Power

Increasing the cathode power essentially provides higher energy to the gas ions in the plasma, thereby increasing the sputter yield of the process. This results in an increase in the deposition rate and lower levels of process gas entrapment within the film. The increased deposition rate at high cathode power is known to result in kinetically inhibited growth nucleation, which leads to smaller grains due to lower levels of particle diffusion on the

substrate. Changes in cathode power also lead to changes in the film stress. At high power, compressive stress exists while tensile stress exists in films deposited at low power.

4.4.6 Angle of Incidence of Sputtered Material

One further issue to note is the non-perpendicular arrival of atoms at the substrate surface. In the event that sputtered atoms arrive at an oblique angle, shadowing has been found to take place. Shadowing is the build-up of material on the "peaks" of a surface while not reaching the "valleys" [175]. Shadowing is found to worsen with an increasing angle of incidence and results in a rougher textured film as well as a decrease in the RRR value of the film [176]. These effects are significantly decreased through the use of HiPIMS, due to the combined ionisation of the target material and the attractive force of the substrate bias which leads to the perpendicular arrival of atoms at the substrate surface, even on surfaces at 90° to the target [177].

Typically, the deposition of thin films results in a certain measure of stress present in the deposited film. There is no generalisation with regards to the prediction of thin film stresses, however it is clear that the stress in a thin film is a process sensitive property [178]. Manipulation of the above parameters will therefore result in a changing level of stress in a thin film. This will be expanded upon below.

4.5 Internal Stresses in Thin Films

The internal stresses present in deposited thin films are split into two categories: thermal stresses and intrinsic stresses, where the final stress state is the summation of both.

Thermal stresses arise because of the difference in the thermal expansion coefficient between the substrate material and the thin film material. These thermal stresses increase with increasing deposition (substrate) temperature (T_s). This is very relevant for thin film SRF cavities given the fact that the operating temperatures of 2 to 4.2 K are far from the generally used deposition temperatures of 473 – 873 K. The resultant thermal stresses, in the limit where the substrate is much thicker than the film, are given by:

$$\sigma(T) = \frac{(\alpha_s - \alpha_f)(T - T_s)Y_f}{1 - v_f} \tag{4-8}$$

Here, α_s and α_f are the coefficients of thermal expansion of the substrate and film respectively, T_s is the deposition (substrate) temperature, Y_f is the Young's modulus of the film, v_f is the Poisson's ratio of the film and T is the temperature at which the stress is measured.

Intrinsic stresses are due to the "accumulating effect of crystallographic flaws built into the coating during deposition" [175]. These intrinsic stresses also arise due to a mismatch between the lattice parameters of the film and the substrate. In high melting point materials with low values of the homologous temperature ($T_h = T_s/T_m$) such as Nb and NbN, intrinsic stresses tend to dominate over thermal stresses [175]. This is because a high density of defects, which lead to intrinsic stress, can be frozen into the thin film when deposited at low deposition temperature. This can be overcome when $T_h > 0.3$, as this is where the recovery process begins. A diagram depicting the relationship between deposition temperature and thin film stresses for high and low melting point materials is shown in Figure 4-9.

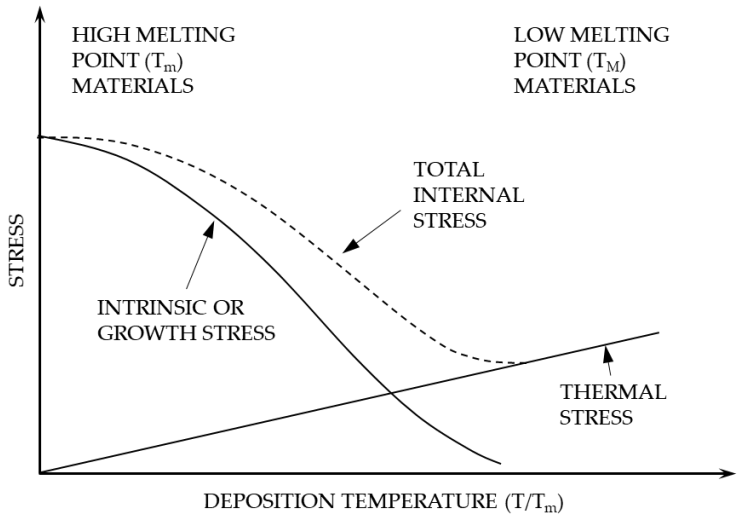

Figure 4-9: Relationship between residual stress and deposition temperature (T/Tm) for high and low temperature melting point materials. Reproduced from [175].

A further relationship between the deposition pressure and the film stress was discovered for Nb films. As can be seen in Figure 4-10, with an increase in deposition pressure, there is a decrease in the compressive film stress up to a specific critical pressure value (~ 1.7 Pa) where the film stress will be zero. Any further increase in pressure will result in a transition to a tensile film stress.

This can be explained as follows: the low gas pressures led to fewer collisions in the gas, which means gas particles can directly peen the substrate surface, thereby compressing it. On the other hand, high gas pressures lead to many scattering collisions, which hinders energetic bombardment of the substrate and tensile stresses arise in the film. Elevated working pressure also facilitates the growth of columnar grains with intercrystalline voids as typified by Zone-1 growth, while lower deposition pressures lead to dense films, as typified by Zone-T growth. Windischmann completed an extensive review of intrinsic stress literature and

established that generally, tensile stresses are observed in Zone-1, porous films due to grain boundary relaxation and compressive stresses are observed in dense, Zone-T films due to the atomic peening mechanism [178].

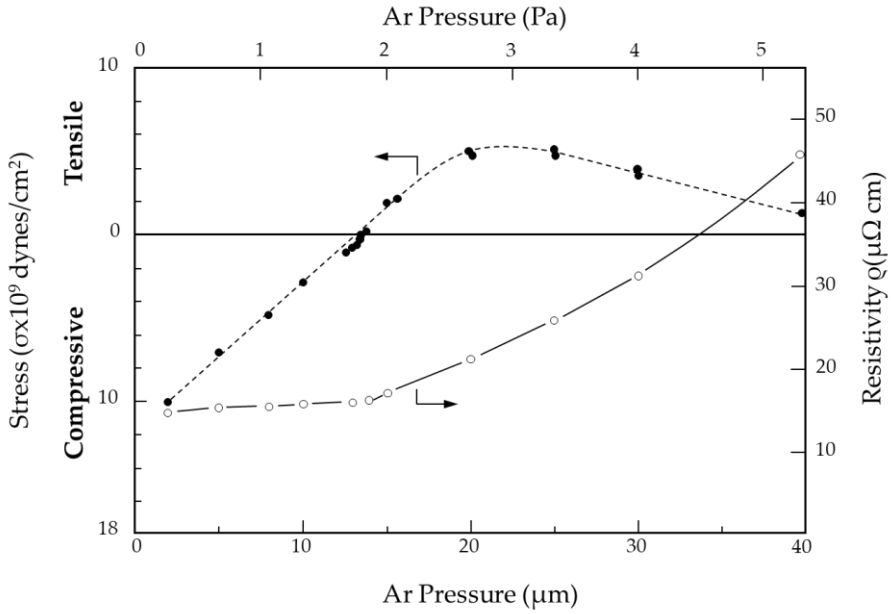

Figure 4-10: Residual film stress vs. deposition pressure for a Nb thin film. A specific critical pressure is shown which leads to a zero stress level and a transition between compressive and tensile stresses within the thin film. Reproduced from [179].

The specific values of the relationship between film stress and pressure depends on the material being deposited, the gas being used and whether or not a substrate bias is used, but the shape of the curve is consistent. Importantly, at high levels of substrate bias, the film will most likely remain in a compressive stress state. This indicates that the stress levels in the film can be adjusted by managing the deposition conditions and thus the film microstructure. A table indicating the effects of different deposition parameters on the film stress was introduced by Hoffman [180] and is reproduced in Table 4-1.

The level of stress present in a deposited thin film will have a significant influence on its adhesion strength and the interface conditions. The required level of adhesion is determined by the final application requirements of the film-coated component. In SRF cavities, the adhesion of the film to the cavity and the quality of contact at the interface will have a large influence on the performance of the cavity due to the thermal boundary resistance model [49]. Optimisation of the deposition conditions will often provide a well-adhered film, while good surface preparation techniques, prior to deposition, will allow for the production of a good interface.

Table 4-1: Relative effects of deposition parameters on the internal stress of deposited thin films [180].

Variable	Compressive Stress	Tensile Stress
Gas pressure	Low	High
Substrate bias	Negative	Positive
Gas atomic mass	Low	High
Target atomic mass	High	Low
Angle of deposition	Normal	Oblique
Angle of emission	Oblique	Normal
Target shape	Cylindrical	Planar
Cathode power	High	Low

There are some specific issues to be aware of and some further mechanisms available for decreasing the film stress effects. The level of intrinsic stress increases with film thickness and thus the likelihood of stress cracking, buckling or poor adhesion can often be observed in thicker films. This effect can be overcome by depositing the film in multiple thinner sections as was shown by Pira [21]. As a mitigation tool, some results indicate the effectiveness of an intermediate (buffer) layer between the substrate and the thin film, or the use of multilayer coatings as effective tools for alleviating some of the stresses brought on by thermal expansion differences or by the lattice mismatch [139][181].

5. Copper Surface Preparation

The Cu cavities used in the production of thin film coated cavities are subjected to a series of surface preparation procedures prior to being coated. This is done in order to enhance the performance of the cavities by improving their surface conditions. This chapter serves to introduce the surface treatments used for the preparation of industry-standard SRF cavities and why these treatments are necessary. The results of the surface treatment investigations undertaken as well as the procedures used to create the Cu samples used in this study are also detailed.

5.1 Introduction

As with most sputter-deposited films, when depositing a thin film of Nb onto a Cu substrate/cavity, the Nb film will replicate the topography of the Cu substrate surface [48]. As such, any features on the surface of the Cu substrate will be evident in the deposited Nb film and will therefore influence the properties of the film. The main purpose behind the employment of surface treatments is to improve the performance of SRF cavities by reducing their surface resistance, thereby improving their quality factor. As detailed in Chapter 2.6, there is no single specific characteristic that can be pinpointed which is responsible for the surface resistance of SRF cavities. However, the surface roughness of the cavity, and therefore of the Cu substrate-thin film system, is known to contribute to it. This relationship between the substrate surface condition and the deposited film's properties allows one to optimise the performance characteristics of the thin film cavities through prior treatments of the substrate surface. This was previously demonstrated by Benvenuti *et al,* who deposited a series of Nb thin films onto substrates with various surface roughness values. The smoother substrate was identified as the main factor behind the noteworthy reduction of the defect density in the deposited film and the superior superconducting performance [2].

The low initial surface quality of SRF cavities stems from the mechanical nature of the initial cavity production and forming processes. A cavity is usually constructed from previously rolled metallic sheets, using methods such as spinning, stamping or hydroforming. These processes all produce a certain amount of microstructural and surface damage, which results in the creation of a damaged layer on the outer surface of the cavity. This damaged layer typically contains surface defects or metallic inclusions as well as a high surface roughness. The raw surface is often initially treated with a mechanical polishing process but this can also result in a damaged surface layer. The severity of the damage decreases with an increase in the fineness of the polish though [182]. A model of the damaged layer is presented in Figure

5-1, which displays the microstructural depth evolution of OFHC Cu abraded by P1200 grade silicon carbide abrasive paper, as described by Turley and Samuels [183].

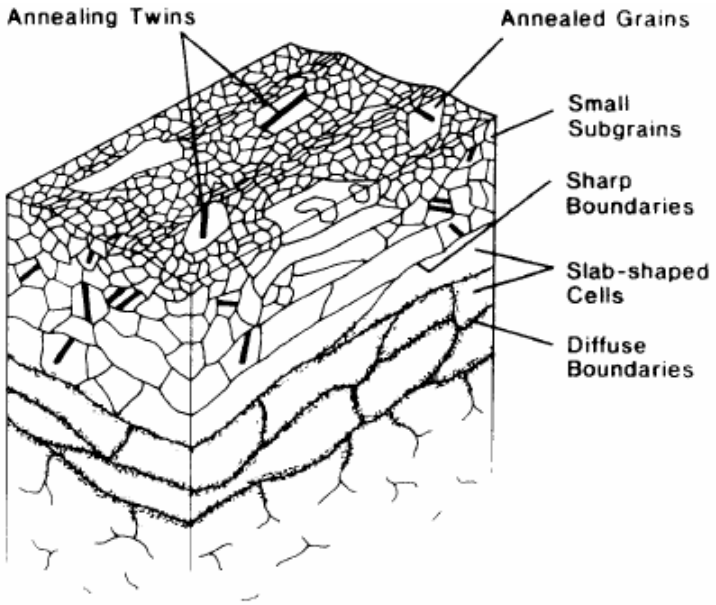

Figure 5-1: Microstructural depth evolution of an abraded OFHC Cu surface [183].

The damaged layer has been reported to have a thickness ranging from 40 to 150 μm, depending on the processes involved in the cavity formation [36][184][185][186]. This layer also contains dislocations, due to the plastic deformation experienced by the cavity. One benefit of this damaged layer is the resultant small grain size, which inhibit the diffusion of Cu into the Nb film better than larger grains [182]. Nevertheless, surface treatments are typically employed to remove this damaged layer.

The vast majority of the research completed on surface treatments of SRF cavities thus far pertains to bulk Nb cavities. Nevertheless, information regarding the effects of Cu surface treatments on the performance of thin film cavities can be gained by studying this research. The surface treatments used with bulk Nb cavities are known to greatly influence their residual resistance and therefore their Q-slope [43][187][188]. It was discovered that bulk Nb cavities, subjected to different surface treatments, with the same amount of trapped flux, display different RF losses. The observed difference is possibly due to a change in the electron mean free path due to the different surface treatments employed [58].

Saito has previously deduced a relationship between the surface roughness and the resultant field enhancement for bulk Nb cavities [36]. It was reported that in order to achieve $E_{acc} > 30$ MV/m, the surface roughness should be less than 2 μm. This can be extended to coated Cu cavities, seeing as it is well known that the surface morphology and topography

of the thin film, closely replicates that of the Cu surface [189]. Put differently, "the roughness of the substrate will dictate the minimum roughness of the film" [7]. One of the more significant impacts of increased surface roughness is an increase in the extent of surface flux pinning within a superconductor, especially thin films, which have a high surface to volume ratio [190]. The extent of flux pinning is, however, field dependent, due to the changing distance between vortices with the applied field. Because of this, the surface roughness length scale to be considered also changes with the applied field [112]. Generally, at higher field values, a cavity is more sensitive to smaller scale surface roughness.

The effects of different surface treatments for thin films coated onto Cu are not as clear as for bulk Nb and considerable research is still required to fully comprehend how the film is affected. Early studies conducted by CERN for both the LEP and LHC cavities pioneered a substantial amount of Cu cavity surface treatment research [184][191]. Multiple further studies have since been completed showing an overarching trend that a reduction of the surface roughness leads to better cavity performance [2][49][53][66][192]. Investigations into the effects of different surface treatments on thin film cavities are still ongoing and the ARIES research program, which this study forms part of, investigated the effects of different substrate treatments on Nb thin film performance [193].

In light of the above, and with the applicability of the results in mind, Oxygen Free High Conductivity (OFHC) Cu (99.95+ %) was used as the focal substrate in this study. The OFHC Cu sheets, supplied by Goodfellow, Germany, were initially cut into 25 x 25 x 1 or 2 mm^3 sample substrates. The samples possessed an RMS surface roughness, prior to any surface treatment, of $S_q = 21.17 \pm 14.19$ nm, as measured by a Halcyonics XE-100 Atomic Force Microscope (AFM) with a scan size of 20 x 20 μm. An example of these AFM scans is shown in Figure 5-2 (a). The image shows a series of linear indentations in the surface. The SEM image captured of the sample surface, displayed in Figure 5-2 (b), also depicts a series of linear markings on the sample's surface, most likely due to the rolling process used during manufacture. This leaves the surface uneven and plagued by scratches and imperfections.

In order to improve the surface of the as-supplied Cu sheets to the levels used in industry, a series of surface treatment procedures were investigated. Samples were treated with individual as well as successive surface treatments to develop an optimised surface treatment procedure. The procedures used for the preparation of the samples used in this study are presented in the upcoming chapters.

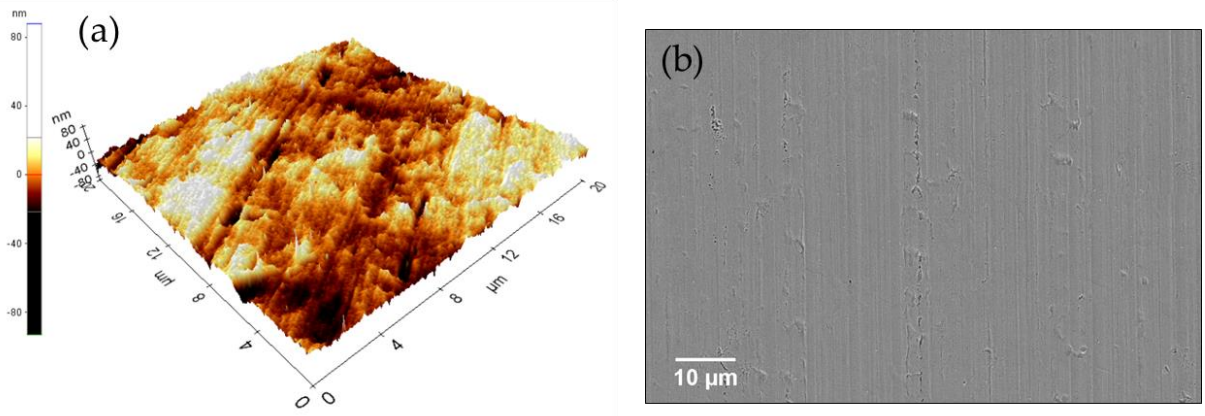

Figure 5-2: Surface characterisation results of the OFHC Cu sample prior to any surface treatment obtained with (a) AFM and (b) SEM.

5.2 Mechanical Polishing

The first step in the surface treatment process is a mechanical polish, which is used to remove any surface imperfections from the forming process and to obtain a homogeneous surface. When working with cavities, some commonly applied mechanical polishing techniques include, rotating wire brush polishing, tumbling and Centrifugal Barrel Polishing (CBP). During tumbling and CBP, the cavity is partially filled with a mixture of different polishing media, ranging from Al_2O_3 cones to coconut shell pieces. The media is typically combined with water and a surfactant, to both cool the cavity and remove material from the surface to allow for further polishing [194]. The cavity is positioned horizontally and rotated slowly (± 100 rpm), with the chips removing some microns of the cavity surface.

During this study, square Cu substrates were mechanically polished using a planar mechanical polishing machine fitted with successively finer grades of sandpaper. The final step of the process used a lapping pad in combination with a polishing fluid containing 1 µm diamond particles in suspension. The resultant RMS surface roughness was S_q = 8.47 ± 0.26 nm, as measured by a series of 20 x 20 µm AFM scans. The results of this process are detailed in Figure 5-3. From both the AFM (a) and the SEM (b) images, it is evident that the surface is now significantly smoother and more homogeneous than the original surface, shown in Figure 5-2. However, the surface still contains scratch lines from the mechanical polishing media as well as surface asperities that could not be completely removed. Following mechanical polishing, the surface typically possesses a mirror finish.

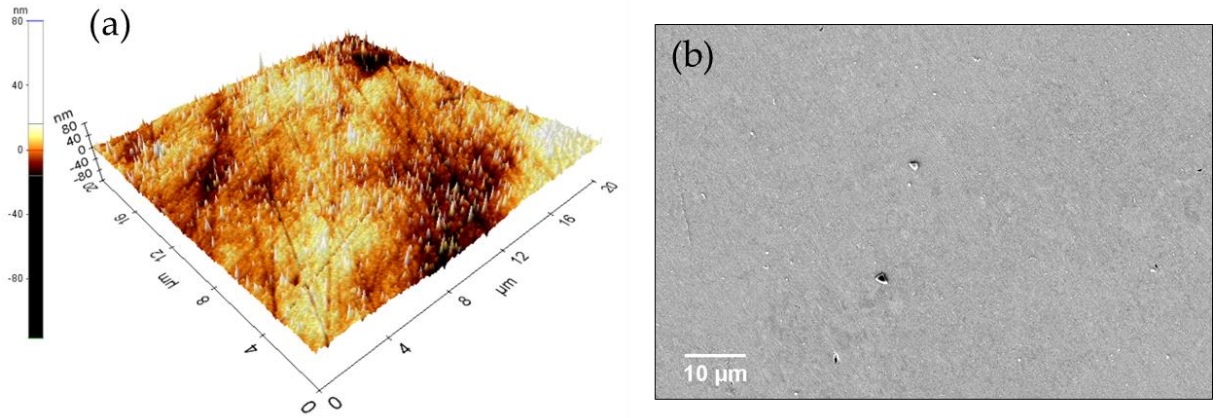

Figure 5-3: Surface characterisation results of the Cu sample following mechanical polishing completed with (a) AFM and (b) SEM.

As detailed in Chapter 5.1, the use of mechanical polishing results in a material layer that exhibits an altered microstructure. The thickness of this layer is determined by the extent of mechanical polishing [182]. The surface will also contain some micro scratches as well as foreign inclusions resulting from the mechanical polishing process even after rinsing. As such, further surface treatments are required to remove this layer, and investigations into their use are detailed next.

5.3 Chemical Polishing

One possible method of removing the contaminated outer layer is to use a chemical polishing process. Chemical polishing processes are relatively simple, as there are no geometrical effects and the process is driven by chemical reactions alone. In this study, two separate chemical treatments were employed. Initially, a chemical etching process using nitric acid was pursued. Following this, trials were made with the CERN-developed SUBU5 chemical polishing mixture.

5.3.1 Nitric acid etch

Prior to the start of this study, chemical polishing of Cu was not employed in the lab. Thus, while the surface treatment optimisation study was ongoing, initial films were deposited onto Cu samples that were prepared with an initial mechanical polish, as detailed in Chapter 5.2, followed by a nitric acid etching process. The samples were placed in a solution of nitric acid (35%) (HNO_3) and distilled water with a 2:3 volume ratio for 30 seconds. Following this, the samples were rinsed with distilled water and placed into the coating chamber.

This procedure resulted in a significantly rougher Cu surface, detailed in the main image of Figure 5-4. The nitric acid etching process also produced a crystallographically faceted surface, which led to a dull surface finish. The resultant RMS surface roughness of the Cu samples following this procedure was $S_q = 108.14 \pm 31.13$ nm as measured by AFM. Additional to the rough Cu surface, the surface of the NbN thin film deposited onto such a sample, shown in the inset of Figure 5-4, also displays a similarly rough surface topography. This is due to the surface decoration phenomenon, whereby defect sites on the substrate's surface, such as grain boundaries, lead to a higher nucleation rate, which leads to them becoming more apparent on the films' surface.

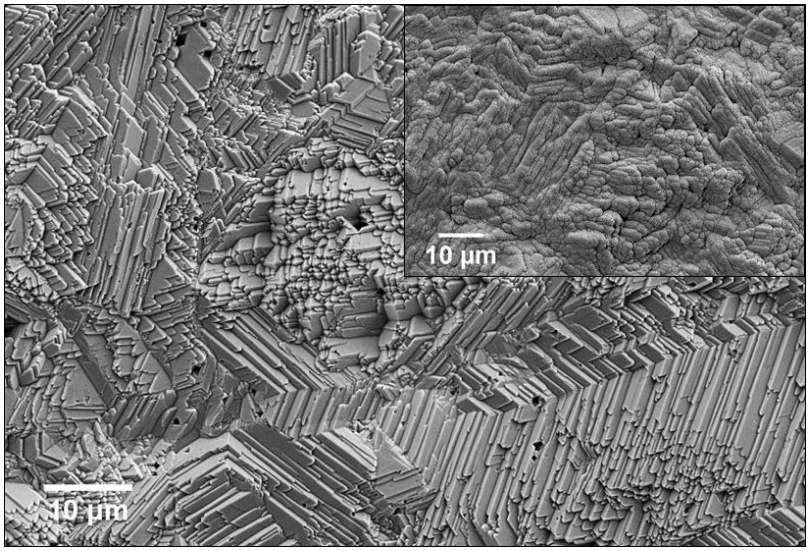

Figure 5-4: SEM images of (Main) Cu sample following nitric acid etch and (Inset) NbN thin film deposited onto nitric acid etched Cu sample.

One of the issues with depositing onto a rough surface is the increased difficulty for the film to conform precisely to the sample topography. This leads to the generation of voids between the film and the substrate during the film growth process, as indicated for NbN films deposited onto nitric acid treated Cu in Figure 5-5. The roughness of the substrate also produces difficulties during film growth, indicated by the presence of voids within the film, shown clearly in the (b). The interface is also noticeably slanted, due to the inhomogeneous etching encountered. All of these issues will decrease the performance of the superconducting thin films. As a result of these issues, the use of nitric acid etching was halted following the NbN screening study detailed in Chapter 7.2.2.

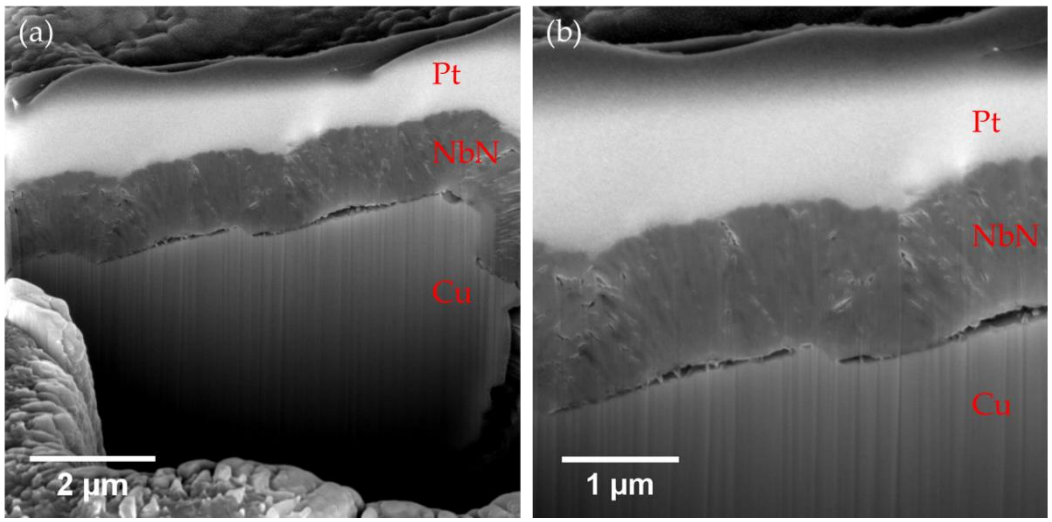

Figure 5-5: SEM images of a FIB prepared cross-section of (a) NbN film deposited onto nitric acid etched Cu samples. (b) Magnified image of the same position.

5.3.2 SUBU5

The chemical polishing agent SUBU5, developed at CERN for LEP II [184] and subsequently used on the LHC cavities, is a mixture of sulfamic acid (H_3NO_3S) (5 g/l), hydrogen peroxide (H_2O_2) 35 % (50 ml/l), n-butanol 99 % ($C_4H_{10}O$) (50 ml/l) and ammonium citrate ($C_6H_{14}N_2O_7$) (1 g/l). During polishing, the mixture is maintained at a working temperature of 72°C. Bath agitation is utilised during polishing to decrease the likelihood of pitting, which is a common issue found in samples following SUBU5 treatment. The stirring also controls the material removal rate [195] by ensuring a viscous layer doesn't form on the Cu surface, which would stop the etching completely [140]. The samples to be polished were hung from a non-reactive wire (stainless steel) and placed in the centre of the solution as shown in Figure 5-6 (a). The SUBU5 process is preceded (5 min) and followed (5 min) by immersion in a sulfamic acid solution (H_3NO_3S) (5 g/l) in order to increase wettability (before) and passivate the Cu surface (after). Transfer of the sample from the polishing mixture to the passivating solution needs to be completed as fast as possible, in order to avoid oxidation of the chemically active surface. Two samples, displaying successful and unsuccessful SUBU5 treatment, are displayed in Figure 5-6 (b) and (c) respectively.

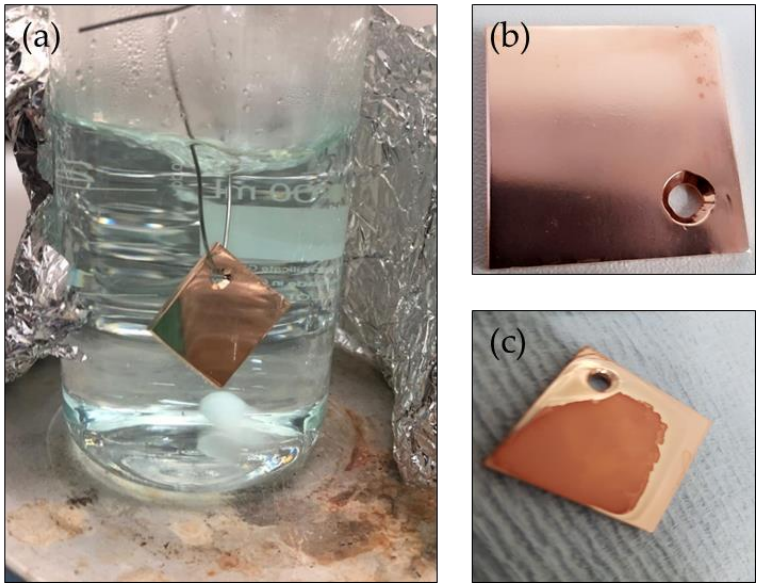

Figure 5-6: (a) Cu sample polishing in SUBU5 chemical mixture. (b) Cu sample following successful SUBU5 treatment. (c) Cu sample following unsuccessful SUBU5 treatment.

The manner in which the chemical polishing with SUBU5 proceeds is detailed in an internal CERN report [191], but a synopsis is provided here. H_3NSO_3 (sulfamic acid), at 72°C, in the presence of an oxidant, H_2O_2 (hydrogen peroxide), reacts with Cu to form $CuSO_4$ (copper sulfamate). H_2O_2 generates active oxygen and dissolves the $CuSO_4$, while the $C_6H_{14}N_2O_7$ (ammonium citrate) prevents the formation of Cu oxides and hydroxides. $C_4H_{10}O$ (n-butanol) is used to moderate the reaction, by limiting the pitting process and bubble production on the surface. The speed of the polishing process goes through a maximum at the beginning of the operation, where after it stabilises for the remainder of the process, resulting in an average etch rate of 0.75 μm/min [74]. The effects of the sample to bath volume ratio are important to note and have an impact on the polishing rate and on the surface finish of the samples.
The results of the surface treatment studies completed using SUBU5 are detailed in Chapter 5.5. Possible adjustments of the chemical formula of SUBU5 were not investigated as this was completed exhaustively in its creation at CERN.

5.4 Electropolishing (EP)

A second method available to remove the damaged surface layer and improve the surface quality of the Cu samples is electropolishing. Electropolishing has the advantages of a reduced waste stream, fewer consumable ingredients and no mechanical stress applied to the substrate [196]. Electropolishing is said to occur through two main mechanisms; 'anodic levelling' (Macrosmoothing) and 'anodic brightening' (Microsmoothing) [197]. Anodic levelling proceeds as a result of the preferential dissolution of surface protrusions due to local

charge differences between peaks and valleys. Anodic brightening proceeds through the suppression of the influence of surface defects and crystallographic orientation on the dissolution process [198][199]. It is possible for one to occur without the other.

Electropolishing has been used for the preparation of Cu cavities for more than 25 years, but has been used in other areas for many years prior to that. Electropolishing essentially comprises an electrolytic cell, where the material to be polished serves as the anode, and is placed at the positive terminal of a DC power supply, with the negative terminal being attached to the cathode [200]. Once the power supply is activated, the anode is oxidised; leading to the removal of material that then diffuses through the electrolyte and is deposited onto the cathode. The anodic reactions, and the amount of material removed in electropolishing mainly depend on the nature of the dissolving metal, the electrolyte composition, the electrolyte temperature, the current density and the degree of electrolyte agitation [182]. The removal of material from the anode leads to two general outcomes: planarisation of the surface, which will be detailed below, and surface brightening. Brightening of the surface occurs as a result of the prevention of crystallographic facet formation found in ordinary anodic dissolution with etching [201]. This was found with the initial nitric acid etched samples, displayed in Figure 5-4.

The most widely studied electrolyte used for the electropolishing of Cu, H_3PO_4, was proposed and systematically studied by Jacquet [202]. Since then, a large amount of research has been completed to optimise the initially proposed ortho-phosphoric acid solution. The electrolyte used in electropolishing generally consists of three components; an acid to ensure oxidation of the material, a reagent to regulate dissolution speed and a substance to promote the viscous state at the solution/metal interface [200]. It is well accepted that during electropolishing, a viscous layer, containing anodic products, is formed on the anode. A more resistive viscous layer improves the planarisation efficiency of the Cu electropolishing system [203]. Multiple interpretations exist for how this viscous layer affects the planarisation of surfaces through electropolishing but the premise is the same. The thickness of the viscous layer is greater above crevices than protrusions and thus the current density at the protrusions is higher than the crevices. For this reason, protrusions dissolve more rapidly than crevices, thereby producing a surface-levelling effect [182]. For features larger than the normal diffusion layer thicknesses (5 – 30 μm), the diffusion layer profile follows the Cu surface profile, and Cu removal is largely conformal [204].

The rate of the reaction is found to be limited by mass transport of ionic species at the anode surface, where diffusion of reaction products is limited and thereby limits the overall reaction

rate [205]. The rate of mass transfer depends on the relative ionic movement, the geometry of the anode and the temperature, type and physical properties of the electrolyte [206]. The rate-limiting step during Cu electropolishing is said to be due to the diffusion of water, which acts as an acceptor species for dissolving ions [207]. The use of surfactants has been found to decrease the limiting current associated with the mass transport limitation by increasing the viscosity of the electrolytic solution, which leads to increased resistance of the diffusion layer to ionic motion. This reduces pitting and the level of defects found on the surface [208]. The current density is found to be inversely proportional to the viscosity of the layer on the anode surface. The presence of a Cu oxide layer, with its own resistance, has been reported to affect the electropolishing outcome as well [209]. Movement of the solution relative to the anode is found to both increase the anode current density and increase the rate of dissolution. Too great a flow rate can lead to etching and a rougher surface finish [8], but the polishing can be restored through an increase in current density [201].

The process of electropolishing can be characterised by the polarisation curve, which plots the current density vs. the voltage during the electropolishing process [189]. A synopsis of a typical polarisation curve can be found in Figure 5-7. This curve can be separated into four zones, each with different resulting surface finishes. Polishing typically transpires in region III where a distinctive current plateau exists, with the best results achieved at higher voltages within region III. The presence of the plateau is associated with the mass transfer limitation. Operating at higher voltages than the plateau leads to the creation of gaseous oxygen bubbles, which are said to be the cause of pitting found at higher voltages in region IV.

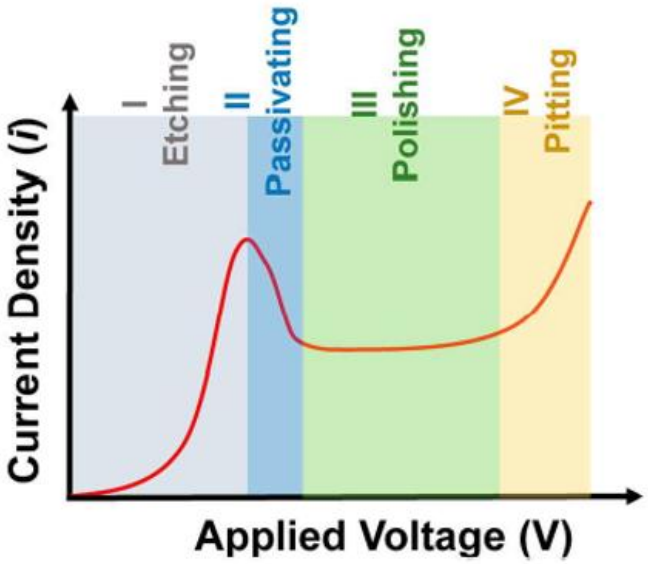

Figure 5-7: Cu electropolishing polarisation curve detailing the current density as a function of applied voltage [200].

The current plateau is also known to change with time, as the current density decreases with the increasing length of electropolishing. The longer processes unfortunately do not necessarily result in a better surface finish though. This is due to the stabilisation of the anodic film which leads to a weaker etching process [210]. Contrary to previous thought, higher temperatures for EP have been found to lead to better finishes of the Cu surface, with a linear decrease in surface roughness for increasing temperature [211]. The higher temperatures also lead to lower levels of pitting due to a decrease in the oxygen density. The two issues most likely to affect the final surface of electropolished Cu samples are pitting, due to oxygen evolution, and trace lines, due to the movement of oxygen bubbles along the surface.

5.5 Surface Treatment Studies

Because of the poor surface finish obtained with nitric acid etching, a series of investigations were completed in order to optimise the surface treatment process used in this study. These experiments utilised individual and a combination of surface treatments to determine the optimum approach to Cu sample preparation. The experiments were conducted as follows:

1. Chemical polish in SUBU5 for 30 min, 60 min, 90 min and 120 min to determine the material removal limits and discern whether it is possible to remove the "damaged layer" following mechanical polishing using SUBU5 alone.
2. Mechanical polishing with either 2000, 3000, 4000 grade or 4000 grade sandpaper plus lapping pad polish with 1 μm diamond particle polishing fluid followed by chemical polish in SUBU5 (30 min). This displays the effective polishing efficiency of SUBU5 based on different starting roughness values.
3. Electropolish at 30 °C and 50 °C for 20 min and 40 min respectively. This was completed to test the effects of higher temperature polishing and to monitor polishing efficiency changes with time.
4. Mechanical polishing with either 2000, 3000, 4000 grade or 4000 grade sandpaper plus lapping pad polish with 1 μm diamond particle polishing fluid followed by electropolish at 40°C for 40 min. This displays the effective polishing efficiency of EP based on different starting roughness values.
5. Electropolish (20/40 min) in phosphoric acid and butanol at ~ 6 A/dm^2 followed by chemical polish in SUBU5 (5/10 min). This was pursued to investigate the efficiency of SUBU5 usage on already smooth surfaces.

The chemical polish was employed for a shorter period for the second set, in order to try to avoid the pitting observed on the surface of the Cu samples following the initial experiments. This is closer to the process used in industry with cavities.

The surface roughness results from the different chemical polishing experiments are displayed in Figure 5-8. The data labels indicate the polishing time (Experiment 1) (blue data), the mechanical polish grade (Experiment 2) (red data) and the time for both the electropolish and chemical polish steps (EP + SUBU5) (Experiment 5) (green data). The surface roughness was measured using an UBM laser profilometer with a scan size of 1 x 1 mm^2.

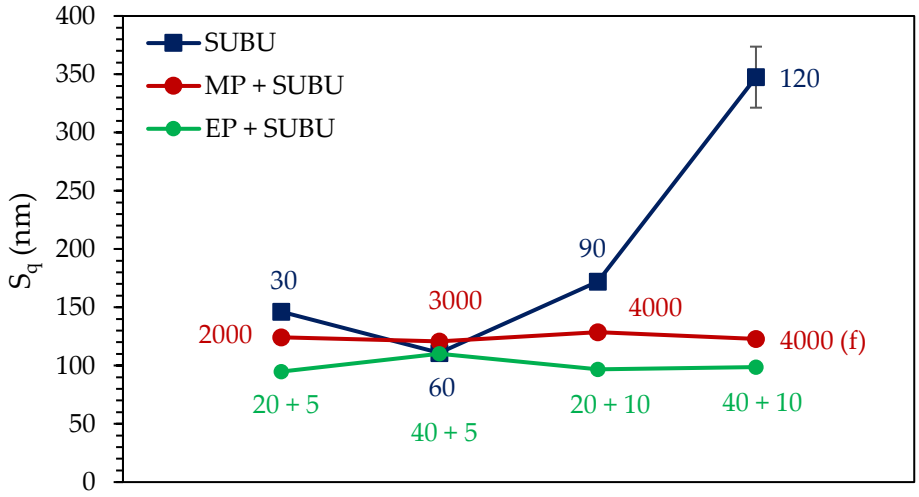

Figure 5-8: RMS surface roughness comparison following different chemical polishing treatments of Cu samples. Blue data indicates results for chemical polish only, red data indicates mechanical polish followed by chemical polish and green data indicates electropolish followed by chemical polish. The (f) specifies the use of 1 µm polishing fluid after 4000 grade MP.

The results indicate that with SUBU5 only, the smoothest surface is reached after 60 min of chemical polish with a S_q = 110.9 ± 1.54 nm. This is a similar result to what was achieved in other labs [212]. Thereafter, the surface roughness increases again, due to increased amounts of pitting, as evidenced in Figure 5-9 (a). This would be detrimental to the performance of any deposited thin films. Samples prepared with various mechanical polish grades followed by an equal chemical polish displayed relatively equal surface roughness values in the region of $S_q \approx 110$ nm. This trend is repeated with the samples subjected to an electropolish followed by a chemical polish. This indicates that the chemical polishing process dominates the resultant surface roughness values, especially at this large scan size. With the large scan size afforded by the laser profilometer, the effects of preferential grain boundary etching, evident in Figure 5-9 (b), become more apparent and are believed to be the reason behind the similar roughness values in experiments 2 and 5.

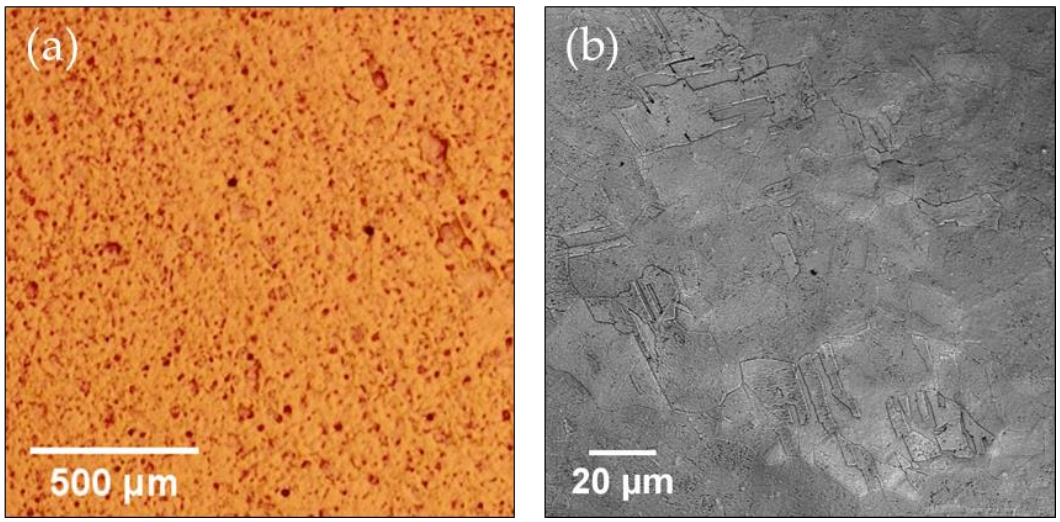

Figure 5-9: (a) Light microscope image of a Cu sample surface following 120 min chemical polish. Large amounts of pitting are clearly visible and would be detrimental to a thin film coating. (b) CLSM image of a Cu sample following 30 min of chemical polishing in SUBU5. Enhanced grain boundary etching is visible.

For the electropolishing-focused experiments, a basic electropolishing setup was designed based on that used at INFN Legnaro for their small samples and utilised a solution of phosphoric acid (85 %) (H_3PO_4) and n-Butanol ($C_4H_{10}O$) in a volume ratio of 3:2 at all times. The Cu substrate, placed at the anode, and the Cu counter electrode, placed at the cathode, were hung from Cu wires. These were attached to power cables leading to a DC power supply, thereby forming an electrolytic cell. Both of the electrodes were immersed completely in the electrolyte. The effective distance between the anode and cathode is known to affect the resistance and thus the degree of polishing [189]. Because of this, the anode and cathode were mounted at equal distances apart from each other at all times, to ensure sample comparability. The electropolishing setup is pictured in Figure 5-10.

Initial samples were polished using a current density of 6 A/dm^2, based on work completed at CERN [184]. The electrolyte was not agitated during polishing. As with the chemical polishing experiments, all electropolishing experiments were preceded (5 min) and followed by (5 min) immersion in sulfamic acid (H_3NO_3S) (5 g/l) in order to increase wettability (before) and passivate the Cu surface (after).

The Cu cathode used for polishing was roughly five times the size of the anode in order to facilitate higher polishing rates as determined during pre-testing. Due to the sheer number of experiments completed, a single electrolyte, where possible, was used to conduct a multitude of tests.

Figure 5-10: Image of the electropolishing setup used for sample preparation. The anode is connected to the red wire while the cathode is connected to the black wire.

The surface roughness results from the different electropolishing experiments, as measured using an UBM laser profilometer with a scan size of 1 x 1 mm², are displayed in Figure 5-11. The blue, purple and orange data represent the electropolish-only results with 30°C, 40°C and 50°C electrolyte respectively. The green data represent the electropolish (40°C) followed by chemical polish results and the red data represent the mechanical polishing followed by 40°C (40 min) electropolish.

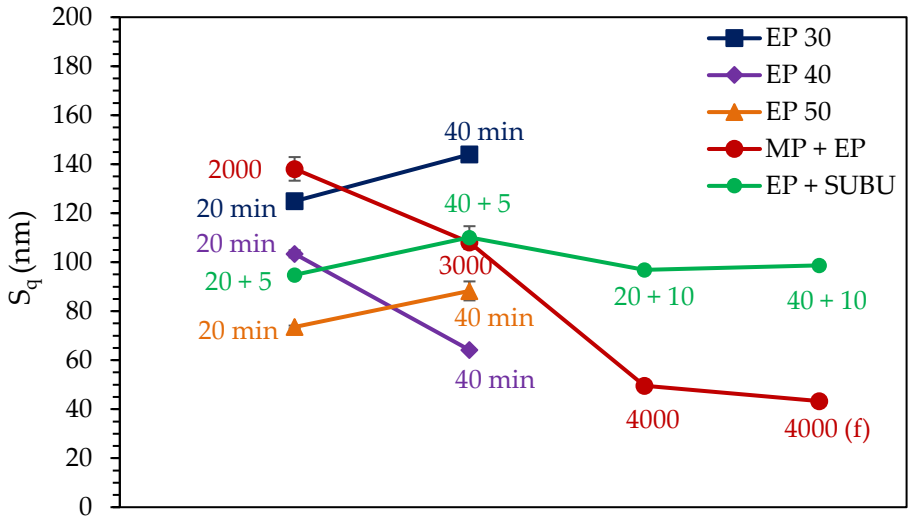

Figure 5-11: RMS surface roughness comparison following different electropolishing treatments of Cu samples. The Blue data indicates 30°C electrolyte, the purple data indicates 40°C electrolyte, the orange data indicates 50°C electrolyte, the Green data indicates electropolish (40°C) followed by chemical polish and the red data indicates mechanical polishing followed by 40°C (40 min) electropolish. The (f) indicates the use of polishing fluid after 4000 grade mechanical polish.

The results indicate a level of reliance on the electrolyte temperature. Following 20 min of electropolishing, the sample surface roughness was found to decrease with increasing electrolyte temperature. This does however change after 40 min of electropolishing, where the sample polished in 40°C electrolyte now possesses the smoothest surface. The material removal rate is increased when using a higher electrolyte temperature, increasing from 0.5 μm/min at 30°C to 2.08 μm/min at 50°C.

The surface roughness of the samples prepared with mechanical polishing and electropolishing steadily decreases as the fineness of mechanical polish increases. The effectiveness of the electropolishing in smoothing the surface is also seen to be greater than that for SUBU5 for all mechanical polish grades except for the 2000 grade sample. The results of the samples prepared by electropolishing followed by SUBU5 are also included for comparison. The smoothest surface was obtained using a combination of mechanical polish, with 4000 grade sandpaper plus lapping pad polish with a polishing fluid containing 1 μm diamond particles, followed by electropolishing at 40°C for 40 min, with a resultant RMS surface roughness of $S_q = 43.3 \pm 1.5$ nm, as measured by a UBM laser profilometer. The Cu surface following mechanical polishing plus electropolishing also displays a more homogeneous finish than samples only prepared with electropolishing, however surface trace lines due to the passage of bubbles along the sample were present. Samples polished at higher current densities displayed more pronounced trace lines following polishing. The material removal rate also showed a marked reliance on the current density, increasing steadily with increasing current density.

Following the initial electropolishing experiments, an electrodynamic sweep experiment was undertaken to determine the optimum current density for the anode-cathode-electrolyte combination. The aim of this experiment was to determine the current plateau position by creating a polarisation curve similar to that shown in Figure 5-7 and is based on the work performed by Jacquet [202]. A three-electrode cell was constructed utilising a saturated calomel reference electrode (SCE) and a Cu counter electrode (cathode) as shown in Figure 5-12. The large amount of Cu wire winding used for the cathode was in an effort to replicate the surface area ratio of the anode and cathode in the normal polishing setup.

Figure 5-12: Images of the three-electrode cell used to perform the electrodynamic sweep of the anode-cathode-electrolyte combination. The anode is placed at the base of the cell, with a small section exposed to the electrolyte. The length of wire employed as the cathode was calculated based on the surface area ratio between the anode and cathode for sample creation.

From this, the optimum current density to be used during the electropolishing process was determined using the current plateau in the polarisation curve presented in Figure 5-13. Testing at the upper plateau value of 18.5 A/dm^2 was unfeasible. Instead, the current density related to the initial dip in the curve at 2.5 A/dm^2 was utilised. The Cu samples polished at this setting displayed an RMS surface roughness of S_q = 59 ± 2 nm (without prior mechanical polishing), as measured by a UBM laser profilometer, and a reduced presence of trace lines. This value was therefore chosen as the new working point and further experiments were focused in this region.

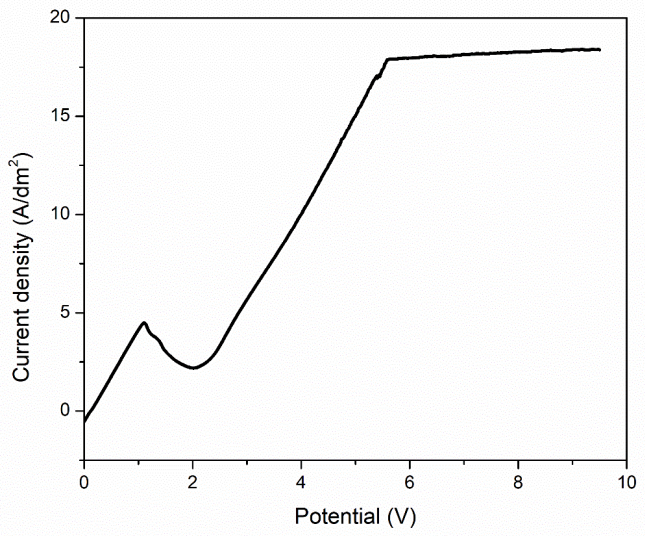

Figure 5-13: Plot detailing the current density vs. the potential for the electrodynamic sweep experiments conducted using the three-electrode cell. The base of the initial dip was utilised as the optimum current density to be used for polishing of the samples.

Due to the presence of trace lines on the samples, further experiments were completed utilising electrolyte agitation during electropolishing. The addition of low speed stirring during electropolishing was found to completely remove any presence of trace lines on the surface, by minimising the contact time of the generated bubbles on the surface and by decreasing the thickness of the viscous layer present on the sample surface. The stirring of the electrolyte also helps to distribute any heat generated during the polishing process.

5.6 QPR Sample Surface Treatment Study

One of the aims of the ARIES research program was to determine which surface treatment is the best option for SRF cavity preparation. Because of this, an initial series of OFHC Cu samples (53 x 53 mm^2) were individually treated at partner institutes, CERN and INFN, with tumbling, SUBU5, EP or a combination of EP+SUBU. These samples were coated, using DC MS, with a 3 μm layer of Nb and subjected to a series of investigations to determine the effects of the different substrate treatments. The results of this analysis showed an improved performance for samples treated with individual SUBU5 or EP treatments [213]. These two surface treatments were therefore chosen for further analysis.

As part of this analysis, four separate QPR samples, consisting of a Nb cylinder and a Cu surface plate [214], were prepared with different surface treatments at INFN Legnaro [215]. Two samples were prepared with SUBU5 and two samples were prepared by electropolishing. Following this, one SUBU5 and one EP prepared QPR sample were each coated with a 3 μm Nb thin film at two different project institutes; the University of Siegen and STFC Daresbury. In order to quantify the effects of the different surface treatments, these four QPR samples were all tested by D. Tikhonov in the QPR system at HZB [215][216], detailed in Chapter 6.2.10.

The deposition process for these QPR samples is discussed in detail in Chapter 8.1. The results of the RF testing showed a consistent trend for the samples coated at the University of Siegen and those coated at STFC; samples prepared with SUBU5 had a higher surface resistance than those prepared with EP. This is shown in Figure 5-14 [218]. Samples B-2 and B-3 were coated at the University of Siegen and were prepared with SUBU5 and EP respectively. Samples B-4 and B-5 were coated at STFC and were prepared with EP and SUBU5 respectively.

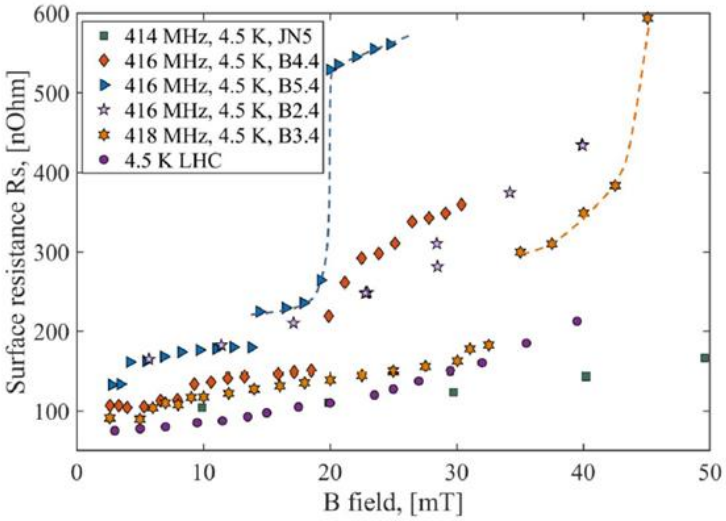

Figure 5-14: Measured surface resistance of QPR samples B-2 to B-5 at ~416 MHz and 4.5 K. Samples were treated with EP and SUBU5 before being coated with a DC MS Nb film. LHC values and the reference bulk Nb sample JN5 are also plotted for comparison. QPR testing and data analysis courtesy of D. Tikhonov (HZB Berlin) [218].

5.7 Conclusions

Based on the results of the series of experiments completed, the following conclusions were made regarding the surface preparation procedure:

The use of chemical polishing as a stand-alone treatment and the introduction of chemical polishing post electropolishing is found to enhance the presence of grain boundaries on the Cu sample. These features are then replicated in the thin film (surface decoration). If chemical polishing is to be used, it should be for a short duration (≤ 5 min) to avoid possible pitting of the surface and grain boundary etching; however, it is not recommended.

The use of a combination of mechanical polishing and electropolishing results in the most homogeneous and smooth surface. The mechanical polish creates a uniform surface from which to start the electropolishing, as it removes any irregular surface abrasions present on the as-received Cu. Sufficient material must be removed following mechanical polishing to ensure the removal of any possible inclusions of abrasive material, foreign particulates as well as the damaged layer created during mechanical processing. Due to the low grade final mechanical polishing step, and based on the values detailed above, a ~ 40 μm thick damaged layer on the Cu surface was estimated. In order to remove ~ 40 μm of Cu, a 60 min electropolish was required. Further to this, electropolishing of the Cu samples for too long resulted in significant step edges between Cu grains of different orientations, due to the differential polishing rate. Therefore, the electropolishing was limited to a maximum of 60 min, to minimise these step edges. The use of the optimal current density, raised

electrolyte temperature and electrolyte stirring allows for a superior surface finish while minimising the presence of trace lines on the surface of the sample.

Based on the testing completed and the conclusions detailed above, the following surface preparation procedure was adopted for the bulk of the samples in this work:

- Mechanical polish of OFHC Cu sample (25 x 25 mm^2) with 4000 grade sandpaper followed by lapping pad polish with polishing fluid containing 1 μm diamond particles in suspension.
- Degrease in acetone in an ultra-sonic bath for 15 min
- Degrease in ethanol in an ultra-sonic bath for 15 min
- 5 min surface activation in a solution of sulfamic acid (H_3NO_3S) (5 g/l)
- 60 min electropolish with low speed (180 - 200 rpm) stirring agitation in a 40°C solution of phosphoric acid (85%)(H_3PO_4) and n-butanol ($C_4H_{10}O$) in a 3:2 volume ratio.
- 1 min surface passivation in a solution of sulfamic acid (H_3NO_3S) (5 g/l)
- Ultra-sonic bath in distilled water for 5 min
- Rinse in ethanol
- Dry with N_2

The state of the Cu sample surface at each stage of the optimised surface treatment procedure is shown in Figure 5-15. The untreated Cu sample is displayed in (a), the sample following mechanical polishing is displayed in (b) and the final sample following electropolishing is displayed in (c). Prior to mechanical polishing, the surface is inhomogeneous and plagued by surface abrasions. Following mechanical polishing, the sample presents a uniform surface with the presence of micro scratches, because of the polishing media used. The surface is also noticeably shinier. These scratches are completely removed during the electropolishing process, resulting in a homogeneous and mirror-like surface.

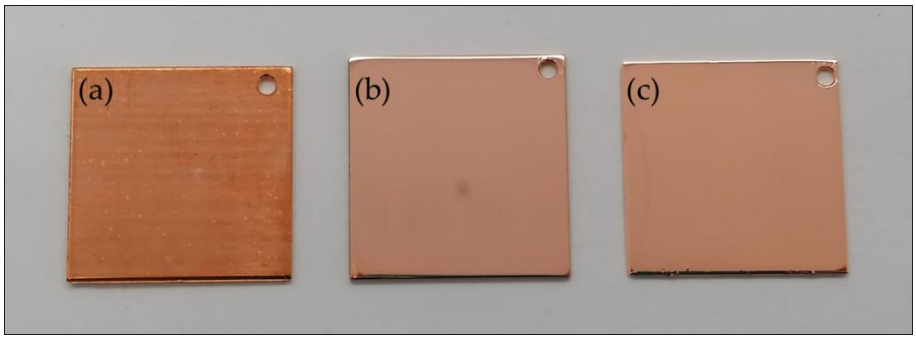

Figure 5-15: Images of the surface of a Cu sample during the optimised surface preparation process. (a) Before surface treatment, (b) after mechanical polishing and (c) after electropolishing.

Further analysis of the resultant Cu surface has also been completed. CLSM, AFM and SEM images depicting the final polished Cu surface are presented in Figure 5-16. The grains of the Cu samples have become clearly visible following the completion of the electropolishing procedure. It is also evident that different grain orientations are polished at different speeds. This leaves a grain boundary step-edge with a maximum value of ~ 20 nm. The final sample surface is characterised by an RMS surface roughness of S_q = 2.58 ± 0.26 nm, as measured by a Halcyonics XE-100 Atomic Force Microscope (AFM) with a scan size of 20 x 20 μm. This value is significantly better than the original surface roughness of S_q = 21.17 ± 14.19 nm.

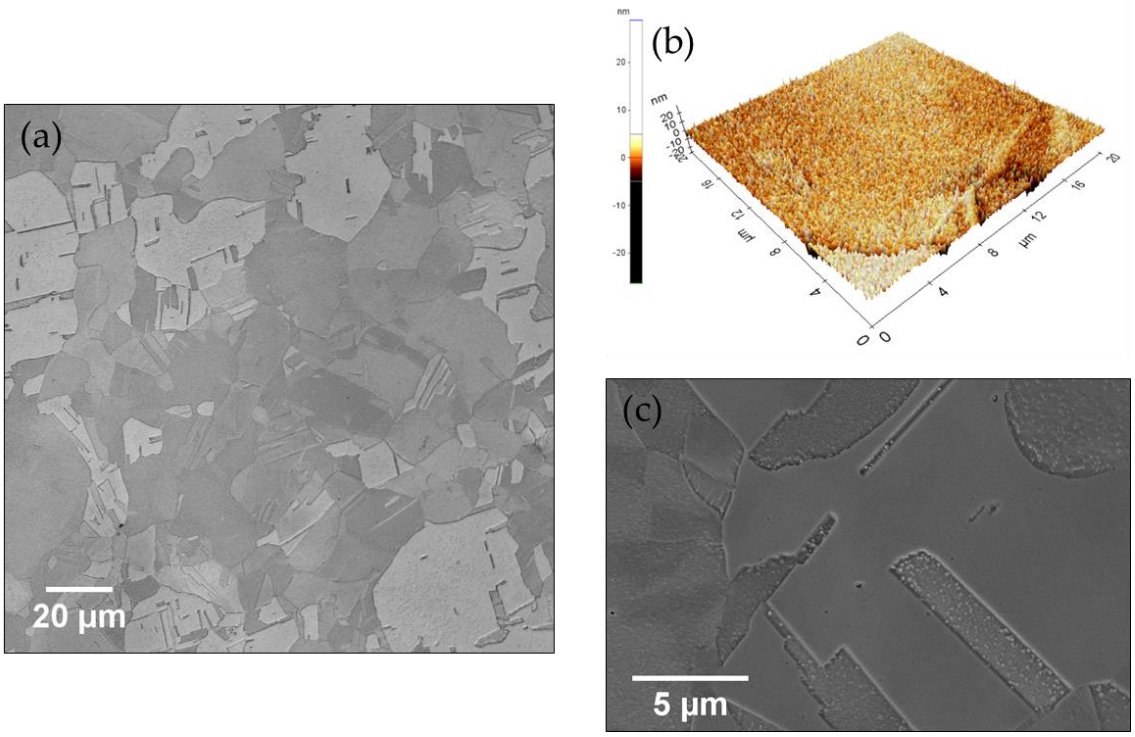

Figure 5-16: Surface characterisation results for the Cu sample following preparation with the optimised surface preparation process obtained using (a) CLSM, (b) AFM and (c) SEM.

Because of the significant reduction in surface roughness, substantial improvements have been made to the interface between the Cu substrate and the thin film. This is detailed in Figure 5-17, which can be compared to the previous nitric acid treated sample shown in Figure 5-5. The interface is visibly flatter and more homogeneous than previous samples, with no presence of voids, leading to improved adhesion between the film and substrate, and superior superconducting performance.

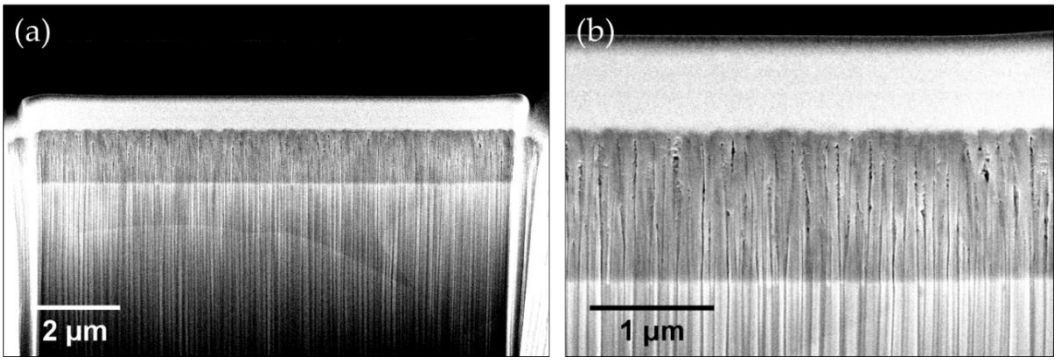

Figure 5-17: SEM images of FIB cross-section cuts of a NbN film deposited onto an electropolished Cu sample (a). Magnified image (b).

The effectiveness of this approach can be further seen in Figure 5-18. The same NbN thin film recipe as was used to deposit the sample imaged in Figure 5-4 has been used here, albeit onto a Cu sample prepared with the optimised surface preparation routine. The resultant surface of this sample stands in stark contrast to the original sample surface finish following nitric acid etching. This comparison shows the extent of the improvement made in the surface treatment process.

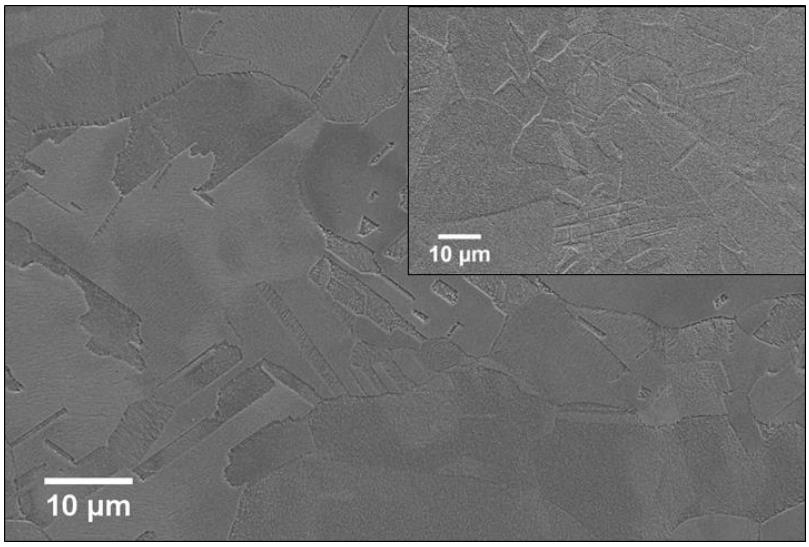

Figure 5-18: SEM images of (Main) Cu sample surface following preparation with the optimised surface preparation procedure and (Inset) NbN thin film deposited onto the optimally prepared Cu sample.

In order to better understand their crystal structure, the Cu substrates were further analysed with XRD and EBSD, with the results displayed in Figure 5-19. (a) Shows the XRD spectrum in log scale as obtained in Bragg-Brentano (BB) configuration. The spectrum exhibits a polycrystalline Cu structure with a preferred {200} orientation, as indicated by the changes to the relative peak intensities in comparison to the reference data [219]. This was further

investigated with pole figure measurements obtained for the Cu (111) (c) and Cu (200) (d) poles, corresponding to the positions 2θ = 43.3° and 2θ = 50.4°, obtained from the BB scan in (a). These results correlate with that shown in (a), indicating a {200} orientation for the Cu substrates. This is believed to be due to the rolling process used during manufacturing. EBSD analysis was also conducted on the same Cu substrate, with the results shown in (b). The surface of the Cu sample appears to be polycrystalline with no discernible preferred orientation. This result was replicated a number of times on multiple samples. These two results do not necessarily agree with one another, however, the information provided by the XRD measurements pertains to the entire substrate thickness, due to the penetration depth of the X-rays. On the other hand, due to the lower penetration depth (50 - 100 nm) [220] of EBSD scans, the results relate the conditions of the Cu substrate outer surface. As such, even though ~ 40 μm was removed from the Cu surface during EP, the observed surface structure is likely due to the effects of the mechanical processing steps, as detailed in Figure 5-1. The EBSD results further correlate the differential polishing rates observed for different Cu grain orientations following electropolishing, as shown in Figure 5-16 and Figure 5-18.

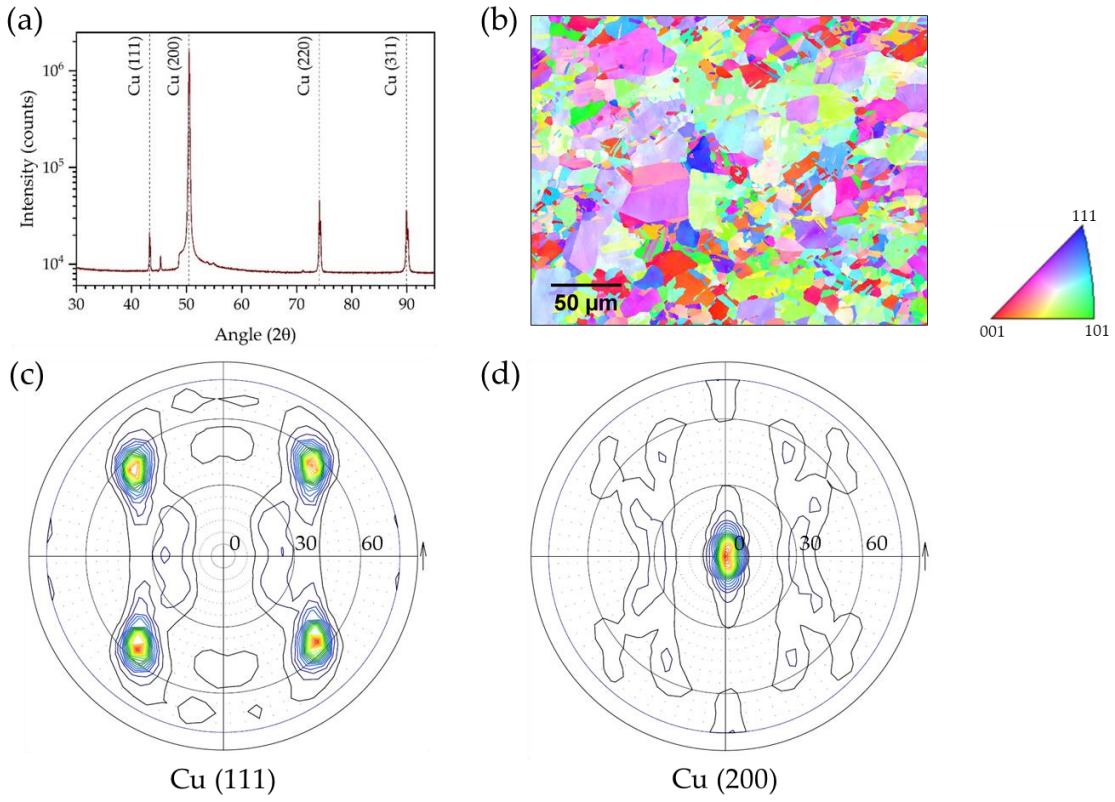

Figure 5-19: Collection of crystallographic characterisation method results for the Cu samples used in this work. (a) Indicative XRD spectrum. (b) EBSD surface investigation. (c) Cu (111) pole figure result. (d) Cu (200) pole figure result.

6. Experimental Methods

This chapter details the coating system used in this study as well as the characterisation equipment utilised to investigate the deposited samples. The settings and procedures for each of the characterisation tools is also detailed.

6.1 Coating Setup

A modified commercial, high-volume, fully automated, industrial coating machine (CC800, CemeCon AG GmbH, Germany) has been used to deposit all of the samples produced in this study. This system is presented in Figure 6-1. The deposition chamber contains a rotatable table, upon which a substrate holder is placed. The substrates are heated indirectly by an 8800 W radiant heating element positioned on the back wall of the deposition chamber. The table is rotated during heating to ensure a uniform temperature profile on the substrates. The substrate holder has been found to reach a maximum temperature of ≈ 300°C, corresponding to a maximum heater power of 8800 W.

Figure 6-1: CemeCon CC800 industrial coating machine. Two of the doors have been opened to better visualise the deposition chamber.

The rotatable table, and by extension the substrate holder, can be grounded or biased (DC and HiPIMS). The substrate holder can also be exchanged for other attachments that allow for the deposition of alternative geometries such as Quadrupole Resonator (QPR) samples. The deposition chamber contains three separate cathodes, typically fitted with Al, Nb and Ti targets. The Nb target is situated in the centre of the three and is 88 x 100 x 10 mm^3 in size

while the other two targets are 490 x 100 x 10 mm^3 in size. All cathodes are powered by ADL DC power supplies. The central cathode can also be used in HiPIMS operation, through the use of a capacitor storage system and programmable pulse settings. The targets can be individually concealed behind shutter doors, allowing for individual or multiple target deposition as well as target cleaning, without the risk of contamination.

During deposition of single layer films, the table is maintained in a stationary position, with the sample positioned directly opposite the target. In this position, a target to substrate distance of 55 mm is maintained. With the deposition of SIS films, the table was either rotated or rocked back and forth "pulsed" in front of the target in order to ensure a homogeneous coating thickness.

The deposition pressure inside the chamber is monitored and regulated by a combination of a Baratron pressure gauge and a series of mass flow controllers in a feedback-loop control system. The system is capable of utilising five separate gas species, however only three species, Ar, Kr and N_2, were used in this thesis study. When depositing in the reactive mode, the reactive gas (N_2) is set at a constant flow rate while the inert gas (Ar or Kr) is adjusted in order to regulate the deposition pressure. Thus, a specific N_2 flow rate has been found to correspond to specific N_2 % at different pressures.

As detailed in Chapter 5, the main substrates used during this study were OFHC Cu, cut into a square shape with dimensions of 25 x 25 mm^2, and a section of Si (100) wafer, which was used as a witness sample. The Si wafer also allowed for efficient cross-sectional analysis of the coatings. The Cu and Si samples were positioned such that they both lay opposite to the trench of the target, as can be seen in Figure 6-2.

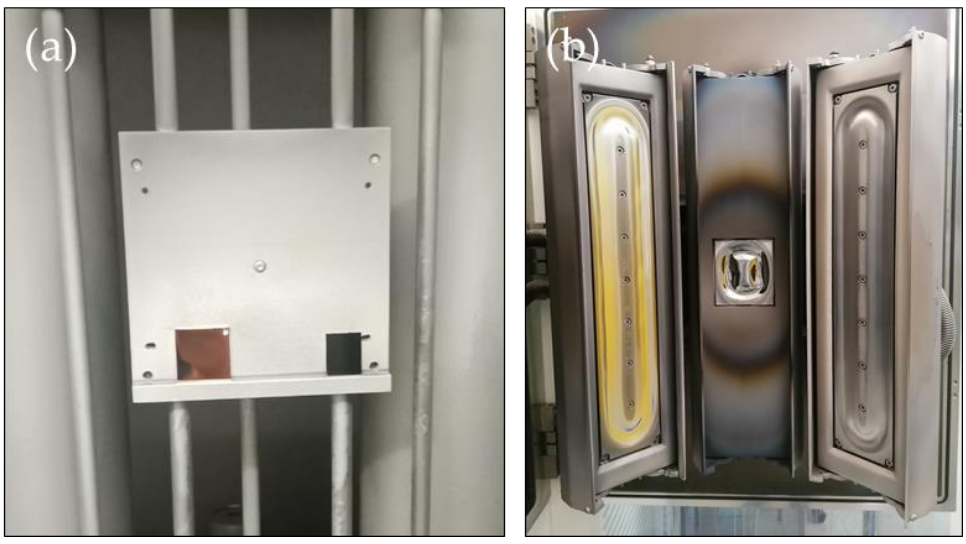

Figure 6-2: Image of substrate holder fitted with Cu sample and Si witness sample (a) and image displaying the target setup of the coating system (b). The Nb target is positioned in the centre.

6.2 Characterisation Equipment

Following the deposition of the respective thin films, the coated Cu and Si samples were analysed using various characterisation devices. The devices and their operating parameters are detailed below.

6.2.1 Scanning Electron Microscope (SEM)

In this work, a Zeiss Ultra 55 Field Emission Scanning Electron Microscope (FESEM) was utilised for microstructural analysis of the film surface on both the Cu and Si witness sample. The Si witness samples were also cleaved in order to determine the thickness of each film and to explore their cross-sectional structure. Two detectors, the In-Lens and SE (secondary electron), were utilised to gain different types of information about the surfaces. The In-Lens detector was utilised most often, due to its high lateral resolution at higher magnification levels whereas the SE detector provided valuable information concerning the topographical changes of the different samples. The system was typically operated with an accelerating voltage of 10 kV, due to the good conductivity of the samples, with a working distance of 6/7 mm.

An Energy Dispersive X-ray spectrometer (EDX) (Thermo Scientific) is integrated into the SEM, allowing qualitative assessment of the chemical composition of the samples, and identification of possible contaminants, such as C or O_2.

6.2.2 Atomic Force Microscope (AFM) and Confocal Laser Scanning Microscope (CLSM)

The surface roughness of the samples was determined with both an Olympus LEXT OLS 4000 Confocal Laser Scanning Microscope (CLSM), with a scan size of 257 x 257 μm, and a Halcyonics XE-100 Atomic Force Microscope (AFM) with a scan size of 5 x 5 μm and 20 x 20 μm. The AFM was operated in non-contact mode with commercial Si_3N_4 tips (PPP-NCHR-20, Schaefer Technologie GmbH). The tip radius was roughly 8 to 10 nm and the pixel resolution was set to 256 x 256. The use of both of these instruments provided a better understanding of the surface roughness at different length scales.

Due to the different scan sizes, the pixel density of the two methods differs considerably. The CLSM captures images with 15.9 pixels/μm² while the AFM achieves 10486 pixels/μm². Because of this, the AFM measurements are far more sensitive to any changes in the surface topography, especially at the nanometre scale.

6.2.3 X-ray Diffraction (XRD)

X-ray diffraction (XRD) studies were completed on all samples, using a Panalytical Empyrean diffractometer with a Cu kα source, producing x-rays with a wavelength of λ = 1.5406 Å. The XRD was mainly operated in Bragg-Brentano configuration at settings of 40 kV and 40 mA. The scans were typically between 2θ = 25° - 95°. A 0.04 radian soller slit, a 10 mm wide fixed mask and a 1° divergence slit were used to manage the resulting spot size of the beam and a nickel filter was installed to diminish the kβ radiation. The lattice parameters of all samples were determined using the Bragg equation and the result crystal plane spacing (d_{cryst}) obtained as follows:

$$n\lambda_x = 2d_{cryst}sin\theta \tag{6-1}$$

Where λ is the x-ray wavelength and θ is the diffraction angle that results in constructive x-ray interference with planes parallel to the sample surface. From this result, the lattice parameter was calculated based on the Miller indices of the lattice planes. Because the diffracting planes are parallel to the surface, the measured lattice parameter is perpendicular to the surface plane [221]. For a cubic crystal, this is completed as follows:

$$a = d_{cryst} * \sqrt{h^2+k^2+l^2} \tag{6-2}$$

Measurement of the lattice parameter allows for a first approximation of the state of stress in the deposited film. Typically, an increase in the lattice parameter above the unstressed powder measurements denotes an in-plane compressive film stress, while a decrease in the lattice parameter denotes a tensile film stress state [179]. The average crystallite sizes (L) of all samples were calculated using the Scherrer equation:

$$B(2\theta) = \frac{K\lambda}{L\,cos\theta} \tag{6-3}$$

Where B is the breadth of the diffraction peak, taken as the integral breadth of the peak in question in this thesis [222], K is the Scherrer constant, taken as 1 for (110) cubic crystallites and 1.16 for (111) crystallites [223] and λ and θ as above. In these calculations, the effects of instrumental broadening were accounted for by analysing and fitting a lanthanum hexaboride standard sample. The Scherrer equation is intended for measurements of powder samples. As such, the line broadening due to internal stresses affects the accuracy of the calculations.

A selection of samples was also subjected to pole figure measurements for texture studies. These scans were completed using the parallel beam XRD optics and a spot size of 4 x 4 mm^2 for all measurements. During the measurements, the stage was rotated through a φ = 0 - 360° in steps of 5°, with a time of 1.5 s per step. The stage was also tilted through a χ = 0 - 80° in 5° steps. A series of corrections were also made to the data. A background scan was collected

for all pole figure measurements to decrease the level of noise in the results. The defocusing of the x-ray beam at large tilt angles (> 60°) was accounted for based on the equation developed by Gale and Griffiths [224]. This results in an increased intensity towards the edge of the pole figure, which is more representative of the actual data. Finally, due to the finite thickness of the deposited films, the absorption of the x-rays was also accounted for by using the mass attenuation coefficient.

6.2.4 X-ray Photoelectron Spectroscopy (XPS)

X-ray Photoelectron Spectroscopy (XPS) measurements, using an Evans Analytical Group LLC XPS SSX-100, were completed with a selection of the NbN screening study samples. The XPS was used to probe the surface layer chemical composition (up to ~ 10 nm), as there is no ion milling possibility in the instrument. As a result, the oxide layer dominates the signal. These measurements were completed by Mrs Anna Schulte.

6.2.5 Rutherford Backscattering (RBS)

Due to the low penetration depth of the XPS system, Rutherford Backscattering (RBS) measurements of five initial samples were completed at the Centre for Nuclear Sciences and Technologies (C2TN) at the Technical University in Lisbon, Portugal. Measurements were performed using a hydrogen beam with 0° angle of incidence, 165° scattering angle and 25° exit angle. This provided a quantitative measurement of the elements present in the film.

6.2.6 Secondary Ion Mass Spectrometry (SIMS)

An IONTOF GmbH, TOF-SIMS 4 Secondary Ion Mass Spectrometry (SIMS) device was used to investigate the chemical composition of a number of samples, from the sample surface to a depth of ~ 1 μm. An area of 500 x 500 μm^2 was sputtered by Ar ions with an energy of 5 keV. An area of 300 x 300 μm^2 was then analysed in the positive mode. The measurements focused particularly on the SIS films, in order to observe the chemical changes stemming from the different material layers that were deposited. The detection of the NbO^+ signal specifically, detailed the presence of O within the films. These measurements were completed by Mrs Ulrike Koch.

6.2.7 Focused Ion Beam (FIB) and Electron Backscatter Diffraction (EBSD)

The FEI Helios NanoLab 600 DualBeam Focused Ion Beam (FIB) was used in conjunction with an SEM to investigate the cross-sectional microstructure of a selection of samples. A

1 μm protective Pt barrier was deposited using a gas injection system prior to the start of ion milling. A Gallium (Ga) ion source was used to etch (mill) selected material from the samples. The electron beam and the ion beam intersect at a coincident angle of 52°. Most notably, the FIB allowed for in-depth investigations of the thin film/Cu interface, particularly for Nb, in order to determine the improved level of interface voids. The FIB was also used by Dr. Yilmaz Sakali, from the Micro and Nanoanalytics Facility (MNaF) of the University of Siegen, to prepare a number of TEM samples.

The system is also fitted with an EDAX/TSL 3D Electron Backscatter Diffraction (EBSD) Pegasus - XM 4 detector for crystal structure investigations. The sample was maintained at a tilt angle of 70°, with respect to horizontal, during the analysis. An electron current of 11 nA and accelerating voltage of 20 kV were generally used for analysis purposes. Typical step sizes of 0.01 to 0.02 μm were used to allow for a detailed image across the grain boundaries. The EBSD detector was mainly used to investigate the potential epitaxial relationship between the deposited Nb films and the Cu substrate as well as to detail any changes through the film thickness.

6.2.8 Transmission Electron Microscope (TEM)

TEM studies were performed on a limited number of samples using a FEI Talos F200X (TEM/STEM). The crystal structure relationship between the different material layers was of particular interest. Therefore, HRTEM images were obtained of the interfaces between the different material layers. The Cu substrate/thin film interface was also of interest due to the known possibility of void formation. Further EDX mapping was also conducted in STEM mode. These investigations were conducted by multiple members of MNaF at the University of Siegen; namely, Ying Li, Dr. Julian Müller and Dr. Christian Wiktor.

6.2.9 Vibrating Sample Magnetometer (VSM)

Superconducting testing of small samples (2 x 2 mm^2) was completed by E. Seiler and R. Ries from the institute of Electrical Engineering at the Slovak Academy of Sciences (hereafter referred to as IEE), as part of the ARIES research program. Sections of the original coated samples were tested using a Quantum Design Physical Property Measurement System (PPMS) equipped with a Vibrating Sample Magnetometer (VSM) attachment. The measurements allowed the determination of the critical temperature (T_c) and the field of first magnetic flux entry (H_{en}). An AC Susceptometer attachment was utilised to determine the

transition temperatures of the different superconducting layers present in the multilayer Superconductor-Insulator-Superconductor (SIS) film coatings.

A VSM is used to measure the magnetic moment of superconducting samples in relation to changes in the applied magnetic field or test temperature. In this study, small samples of approximately 2 x 2 mm^2 were tested using a VSM option of the commercial Physical Property Measurement System (PPMS) system – Model 6000, from Quantum Design Inc. The following components comprise the main body of a VSM system [225] and can be visualised in Figure 6-3, with the exception that the electromagnet is replaced by a superconducting solenoid.

- A cryostat, which contains LHe, is used to reach the environment required for measurements of superconducting samples and keeps the superconducting solenoid magnet at the required operating temperatures.
- A superconducting solenoid magnet is placed inside the cryostat and provides the applied magnetic field for the measurements.
- A pick up coil set, which is used to measure the induced voltage from the sample, is placed within this solenoid and surrounds the sample to be tested.
- A sample holder connected to the linear motor allowing for the oscillatory motion of the sample.

The sample is positioned at the vertical centre of the pickup coils. The VSM is operated in a temperature range of 4 to 20 K with an oscillation amplitude of 2 mm and a frequency of 40 Hz [226].

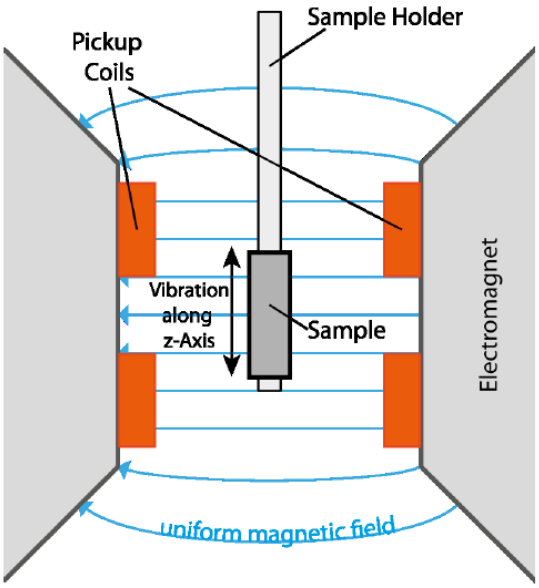

Figure 6-3: Illustration of the main components of a Vibrating Sample Magnetometer (VSM) [227].

As the name suggests, measurements involve the vibration (vertical oscillation) of a sample with respect to a magnetic field, which is applied either perpendicular or parallel to the sample. The vibration creates an oscillating (changing) field in the sample, which induces a voltage in a set of stationary pickup coils positioned near the vibrating sample. This induced voltage is governed by the following equations [228]:

$$V_{coil} = \frac{d\phi}{dt} = \left(\frac{d\phi}{dz}\right)\left(\frac{dz}{dt}\right) \tag{6-4}$$

Where ϕ is the magnetic flux enclosed by the pickup coil, z is the vertical position of the sample with respect to the coil and t is time.

In order to replicate the situation within a SRF cavity, a magnetic field applied parallel to the sample surface is preferred. The correct alignment and placement of a sample is critical to achieve accurate results with a large signal to noise ratio. If the sample is not aligned correctly, early onset of flux penetration will occur as well as possible transverse signal "cross talk" [128].

The VSM applies a DC magnetic field (H_a) and allows measurement of both the field of first magnetic flux entry, denoted shortly as the "entry field" (H_{en}) as well as the transition temperature (T_c) for each sample. These two values provide a good first indication of film performance and allow comparison among different samples. The DC magnetisation curves of the samples were measured at a constant temperature of 4.2 K, following cool-down below T_c in zero applied field. The magnetic moment (m) of the sample was then measured in relation to the monotonically increasing applied field H_a, oriented parallel to the flat sample face, recording the so-called virgin magnetisation curve. The entry field represents the applied field at which the magnetic flux starts entering into the superconductor. It was detected as the applied field at which the virgin magnetisation curve deviates significantly from the initial linear "Meissner trend" of the virgin curve. The entry field was determined using a 2 % relative difference criterion, i.e. the applied field at which the relative difference between the virgin magnetisation curve and the initial linear Meissner trend reaches 2 %. This is however, not H_{c1} and instead a value termed H_{en}.

In the VSM measurements, the field experienced at the sample surface is amplified with respect to the applied field (H_a) due to geometrical effects associated with the small samples. These effects, known colloquially as "edge effects", are related to the field enhancement near the sample edges as a result of immersing a sample of finite dimensions in an applied magnetic field. No correction for the geometrical effects was completed when evaluating the entry field. Therefore, the reported entry field values consider the applied field but are

smaller than the actual physical first magnetic flux entry field values experienced at the sample surface.

An analytical study completed by Chen *et al* [229], where an infinitely long rectangular bar in a transversely applied field, representing an idealised 2D approximation of the VSM sample geometry was considered, provides an estimate for the field enhancement factor. For our typical sample dimensions (aspect ratio ~ 0.002) these results show that the field on the top surface (sample face) is practically equal to H_a, while on the side surface of the sample (the edge perpendicular to H_a), the field reaches $2*H_a$ within a distance of approximately $0.025*t_{film}$ from the edge, increasing towards the sample edge. One could thus estimate the geometrical field enhancement factor to be approximately two for the samples considered in this study.

In the DC magnetisation studies, the critical temperatures have been determined from the temperature dependence of the magnetic moment in a constant magnetic field of 5 mT, applied parallel to the sample surface. The magnetic moment was measured while monotonically decreasing the temperature from 20 K to 5 K in 0.05 K steps. The superconducting transition (critical) temperature T_c was taken as the onset of the magnetic moment change [193]. In order to ensure measurement accuracy and to account for thermal contraction during cooldown, the sample holder is centred every 4 K by performing a "touchdown" process. Measurements are not performed during this process, which leads to small gaps in the data set.

VSM measurements result in the production of what are known as magnetisation or hysteresis loops. These loops contain three separate loops, denoted as the virgin, down and up curve. They present the magnetic moment response of a superconducting material to an applied magnetic field. A perfect superconductor, devoid of any defects, would display zero hysteresis effects and the virgin curve would react as shown in Figure 2-3 in Chapter 2.4. In reality, the presence of any type of defect, such as normal conducting inclusions, dislocations, rough surface topography etc. results in a change to the "ideal" magnetisation loop. An illustration of the typical discernible fields from a hysteresis loop are displayed in Figure 6-4. This enables one to determine valuable information about a superconductor's quality, such as the amount of trapped flux present in the sample (H_{tr}), the entry field value, denoted as H_{c1} in the figure and the full penetration field (H_p). H_{c2} is represented by the applied field at which the observed magnetic moment falls to zero.

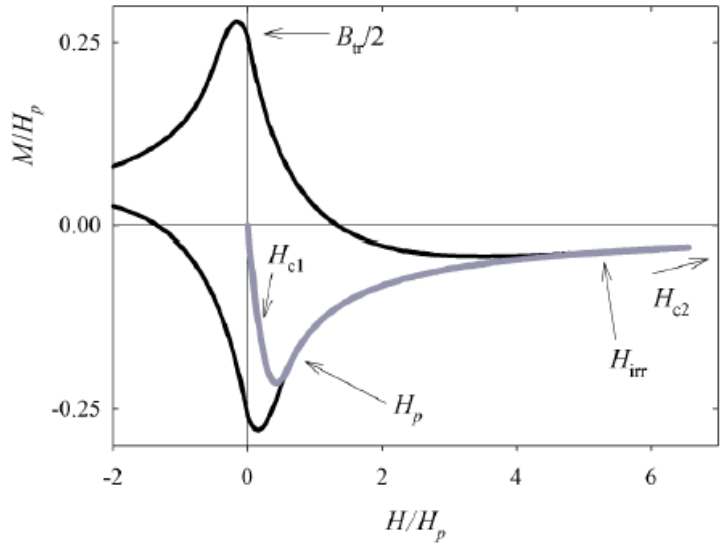

Figure 6-4: Characteristic fields of a superconductor discernible from a typical hysteresis loop [230].

In the case of the multilayer SIS samples, the applied 5 mT DC magnetic field was found to be too high to detect the superconducting transition of the thin NbN layer and only the transition of the much thicker Nb layer was clearly visible. In order to increase the sensitivity of the critical temperature measurement, the highest performing samples were also tested using the AC susceptometer option of the PPMS. In these measurements, an AC magnetic field with the amplitude of 0.02 mT and frequency of 42 Hz was applied perpendicular to the flat sample face. While decreasing the temperature from 20 K to 5 K in steps of 0.1 K, the real (m_{re}) and imaginary (m_{im}) parts of the first harmonic component of the sample's magnetic moment were measured. The T_c was determined as the onset of the m_{re} change with decreasing temperature.

6.2.10 Quadrupole Resonator (QPR)

The second superconducting test instrument used in this thesis was a Quadrupole Resonator (QPR), operated by an EASITrain colleague, D. Tikhonov, at HZB Berlin. The QPR utilises an RF field and as such, is a better predictor of film performance in an RF cavity as opposed to testing small samples in the VSM. Only a few QPR samples were produced and they required specialised surface treatment prior to coating. For this reason, only the final and optimised coatings were tested with the QPR system.

The Quadrupole Resonator (QPR) was developed by CERN in the late 90's in order to accurately measure the surface resistance, with nano-ohm resolution, of thin-film superconducting samples deposited on disk-shaped metallic substrates at RF frequencies used by the LHC (400 MHz) [231]. The QPR is made up by a pillbox-like Nb cavity with the

sample surface positioned in line with the bottom face of the cavity. The RF field is focused on the sample surface by using four resonator rods, which extend downwards from the top plate of the cavity, ending in two half-rings. These half rings illuminate the sample surface, which is positioned 1 mm below the half rings. One significant difference between the QPR and other similar devices is that the sample is simultaneously illuminated by both RF magnetic and electric fields, as is found in accelerating cavities [232]. The original design was later extended to operate at higher RF frequencies, namely 800 and 1200 MHz [233].

A modified design of the QPR was later developed by HZB, based on the CERN design, which shifted the design frequency to integers of 433 MHz to facilitate use of equipment optimised for 1300 MHz operation [216][217][234]. Further improvements have also been made which improve the resolution, decrease the peak electric field and increase the peak magnetic field to 120 mT. The layout of the QPR developed by HZB, and used in this thesis, is indicated in Figure 6-5 [235].

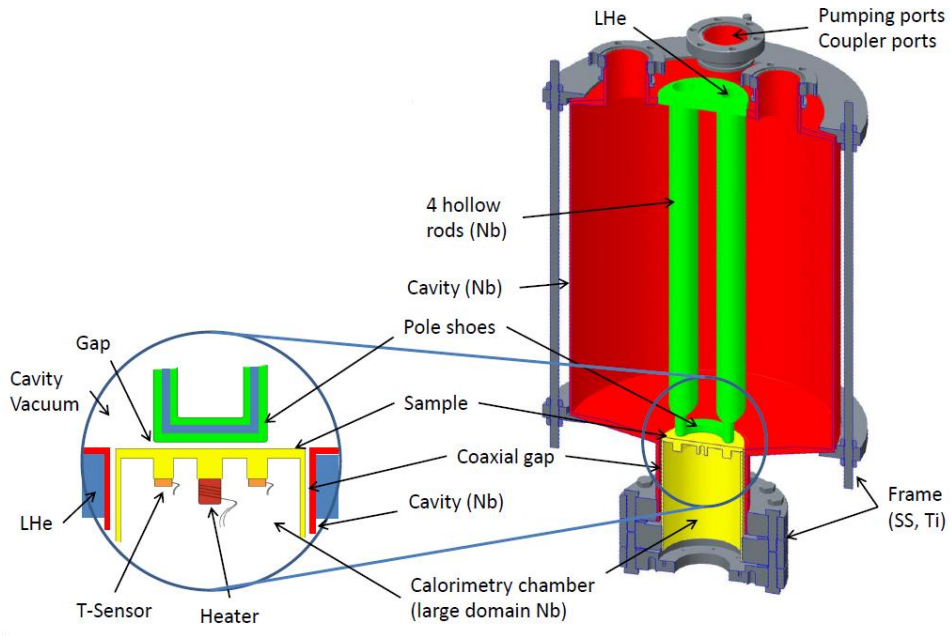

Figure 6-5: Illustration of the HZB Quadrupole Resonator (QPR) used for measurements of samples produced in this thesis as well as a close up view of the heater and thermocouple setup on the QPR sample [235].

The QPR sample comprises a 75 mm diameter Nb cylinder with a Cu plate electron beam welded to the top surface. A stainless steel flange is brazed to the base of the Nb cylinder to connect to the QPR. Below this, essentially inside the Nb cylinder, there is a calorimetry chamber, where a heater as well as a series of Cernox temperature sensors are located. This chamber is also kept under vacuum during testing. The sizing of the samples results in a 1 mm gap between the sample and the port of the QPR. This acts as a coaxial gap causing the

RF frequencies to decay exponentially when penetrating down towards the flange. This setup also thermally decouples the QPR sample from the QPR, which allows the sample temperature to be adjusted while maintaining the QPR at the temperature of the LHe bath. The magnetic fields focused onto the sample surface, created by the RF power coupled to the cavity, cause a dissipation of power from the sample which is measured by temperature probes located inside the calorimetry chamber. The measurement principle relies on an RF-DC compensation technique [236] whereby the heater power is adjusted to maintain the sample surface at a specific temperature in the range of 1.8 K to 15 K [237]. A simple overview of the testing methodology is described as follows [236]:

1. The temperature is set by adjusting the heater current at the backside of the sample surface. This results in an initial power $P_{DC,1}$.
2. The RF is switched on and the heater current is adjusted to maintain the sample surface temperature and total power dissipated at a constant value. This results in a new heater power $P_{DC,2}$.

The resulting power dissipated by RF is then the difference between these two heater values, with and without the applied RF field. The power dissipated by RF is directly related to the surface resistance of the sample R_s and the magnetic field present on the surface of the sample $\vec{B}$. Assuming R_s is constant over the entire sample surface; it can be determined as follows:

$$R_s = \frac{2\mu_0^2\left(P_{DC,1}\text{-}P_{DC,2}\right)}{\int\left|\vec{B}\right|^2 dS} \tag{6-5}$$

This allows the surface resistance of the samples to be measured for multiple temperatures, applied fields and frequencies, providing an informative overview of the performance of the deposited thin film. This measurement principle is visually depicted in Figure 6-6.

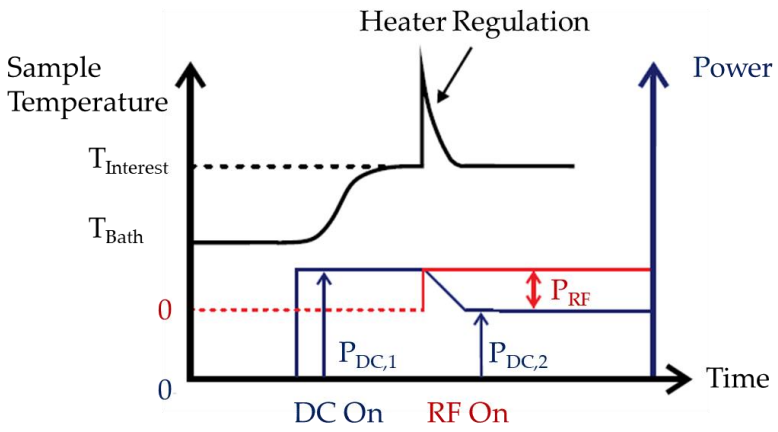

Figure 6-6: Graphic representation of the QPR testing procedure. Reproduced from [238].

7. Deposition of Niobium Nitride (NbN) Thin Films

This chapter will detail the experiments conducted in the pursuit of optimised NbN thin films deposited onto Cu substrates. The work investigating the poisoning of the target during reactive sputtering is detailed first, followed by the initial DC MS NbN deposition studies, which were split into four parts. Preliminary tests were completed to gain insight into the NbN system. A comprehensive screening study was undertaken to better understand the complexities of the NbN system and the broad effects of adjusting the deposition parameters. Following this, a refined parameter study was completed culminating in an optimisation study. Following the successful deposition of HiPIMS Nb films, detailed in Chapter 8, HiPIMS NbN films were also pursued. This was completed in an attempt to increase the density, and therefore the superconducting properties, of both the individual NbN films and the SIS films, shown in Chapter 9.

7.1 Target Poisoning

As discussed in Chapter 6.1, the coating system used in this study utilises reactive gas flow rate control to adjust the N_2 % in the chamber during coating. As such, the target is more likely to operate in the poisoned state than the metallic state. In order to discern the point at which the target transitions to the poisoned state, a series of investigations were made in both DC MS and HiPIMS modes. The DC MS investigation was completed for a single combination of deposition parameters.

The cathode voltage was measured at differing nitrogen flow rates for differing cathode power settings and deposition pressure values. A transition from the metallic state to the poisoned state is marked by a sudden increase in the cathode voltage. This is due to the increased energy required to sputter a compound than a metal. Figure 7-1 displays the target voltage as a function of the nitrogen flow rate for (a) DC MS operation at 8×10^{-3} mbar, (b) HiPIMS operation at 1.4×10^{-2} mbar, (c) HiPIMS operation at 1.8×10^{-2} mbar and (d) HiPIMS operation at 2.2×10^{-2} mbar.

The target transitions from the metallic state to the poisoned state at the same nitrogen flow rate value, regardless of the operating mode, deposition pressure or cathode power. This value consistently lies between 14 and 14.5 sccm nitrogen. As such, it is clear that all coatings completed in this study were done so with the target in the poisoned state. Therefore, it is understood that deposition conditions remained stable throughout the deposition processes.

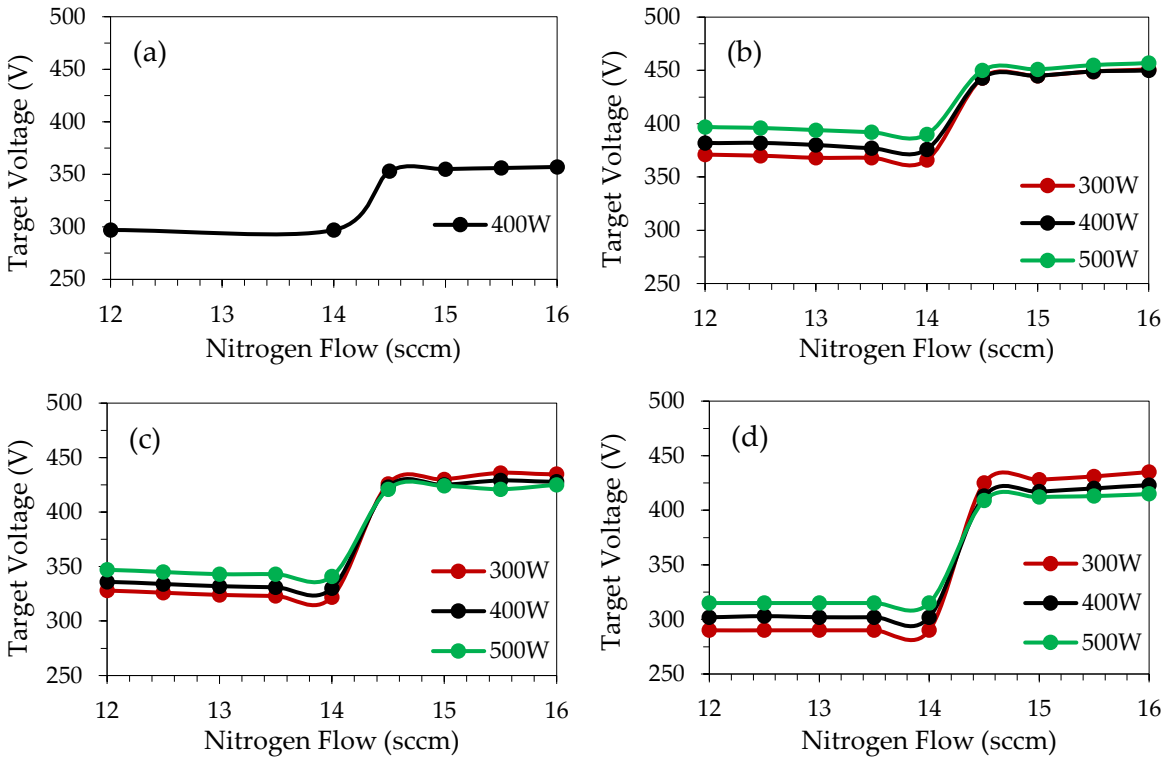

Figure 7-1: Graphical representation of the voltage versus nitrogen flow rate for (a) DC MS operation at 8 x 10^{-3} mbar, (b) HiPIMS operation at 1.4 x 10^{-2} mbar, (c) HiPIMS operation at 1.8 x 10^{-2} mbar and (d) HiPIMS operation at 2.2 x 10^{-2} mbar. The change in voltage is indicative of the transition from the metallic state to the poisoned state of the target.

7.2 Reactive DC Magnetron Sputtering (R-DC MS) NbN Thin Films on Copper

The deposition of NbN thin films was split into four separate coating series broken down as follows: An initial series of preparatory coatings were completed to gain an understanding of the NbN material system. Following this, a screening study was completed with the intent of providing a broad overview of deposition parameter effects on the NbN film properties. With these results in mind, a series of focused, individual parameter studies were completed, culminating in the deposition of a series of optimised DC MS NbN thin films.

In all of these coatings, an OFHC Cu substrate and a Si (100) witness sample were simultaneously coated via reactive DC magnetron sputtering (R-DC MS) using a Nb (RRR 300) target in the presence of a mixture of argon (99.999 Vol-%) or krypton (99.999 Vol-%) and nitrogen (99.999 Vol-%). The Ar or Kr to N_2 ratio was maintained via flow rate control of the two gases.

Prior to deposition, the system was passively baked at 290°C for 6 hrs, to assist in removing any built up adsorbents, and thereafter evacuated to a base pressure of ~ 5 x 10^{-7} mbar. The system was then backfilled to a pressure of 1.2 x 10^{-2} mbar for target plasma cleaning (10 min)

and etching of the Cu substrate in an Ar atmosphere (10 min). The etching process used will be expanded upon later.

7.2.1 Preparatory NbN films

The initial preparatory series of NbN thin films were deposited at a pressure of 1.5 x 10^{-2} mbar and a cathode power of 400 W in the presence of Ar and N_2 with the N_2% ranging from 0 to 100 %. These initial films were deposited with a thickness between 1 – 2 μm. The OFHC Cu substrates used in this study, 25 x 25 x 2 mm^3 in size, were prepared with mechanical polishing followed by a nitric acid etch, as detailed in Chapter 5.3.1. Analysis of the cleaved Si witness samples provided information regarding the deposition rate changes with changing N_2 gas percentage. As shown in Figure 7-2, the deposition rate of NbN decreases with increasing levels of nitrogen in the process gas. This is due to the lower mass of the N_2 ions compared to Ar ions, which leads to a lower sputter yield.

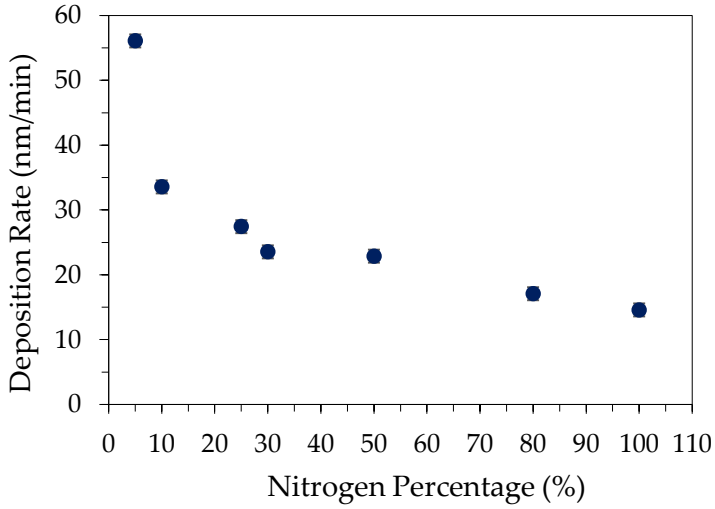

Figure 7-2: Graph detailing the NbN deposition rate vs. nitrogen percentage in the process gas for initial DC MS NbN films.

As detailed in Chapter 3.3.3, the superconducting properties of NbN are strongly dependent on the formation of the correct crystallographic phase. Therefore, in order to ensure the correct stoichiometry of the films, and the subsequent synthesis of the δ-NbN phase, five samples from the initial preparation studies were characterised with Rutherford Backscattering (RBS) analysis to obtain a quantitative chemical composition. These films were deposited with N_2 % ranging from 10 to 25 % (60 – 180 sccm N_2). An example of the fitting process for the 10 % sample is detailed in Figure 7-3. The yellow data points represent the raw data, the purple line details the fit to the data after the measurement and the grey lines

relate to the de-convoluted signal from the elemental composition. Initial fitting was attempted with just Nb and N; however, the addition of O was necessary to obtain a suitable result.

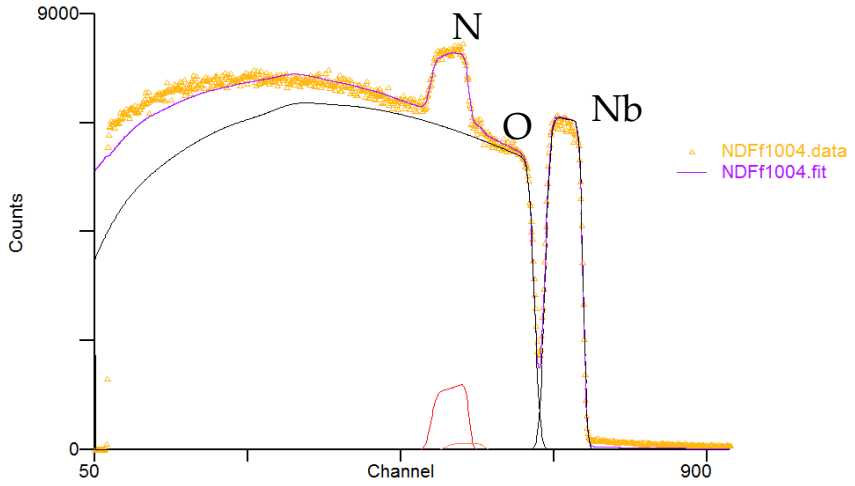

Figure 7-3: Rutherford backscattering spectroscopy data showing the elemental composition of the Nb nitride film deposited with 10% N_2. (Measurement performed by E. Alves and N.P. Barradas, Centro de Ciências e Tecnologias Nucleares, Portugal).

The results of the fits for all samples, detailed in Table 7-1, indicate a changing Nb:N ratio, where "x" defines the ratio of N:Nb. Films coated with ≤ 20 % N_2 are found to be under stoichiometric while those deposited with > 20 % are over stoichiometric. More importantly, all films fall within the range defined by Oya [103] for the δ-NbN phase.

Table 7-1: Elemental composition of NbN_x thin films deposited with different N_2 flow rates determined by RBS.

N_2 %	Nb (at.%)	N (at.%)	O (at.%)	x
10	48.8	46.2	5	0.95
15	48.75	45.17	6.07	0.93
20	48.30	45.75	6	0.95
25	45.71	51.37	2.90	1.12
30	48.70	50.86	0.43	1.04

The high percentage of nitrogen within the films indicates a lack of the β-NbN and γ-NbN phases, x = 0.4 to 0.8, for these deposition parameters. This is to be expected, due to the target operating in the poisoned state, as detailed in Chapter 7.1. The films also contain traces of O, although it is generally < 5 % and is found to decrease at higher N_2 %. This is understood to be due to a decreased ratio of O_2 to N_2 in the deposition chamber at higher N_2 %. The presence

of O in the films can be linked to the higher base pressure of the system and the ex-situ oxidation of the porous columnar NbN structure following removal from the deposition chamber. The formation of normal conducting oxides, oxynitrides and voids between NbN grains are issues known to affect the NbN film performance and are thought to lead to the high resistivity [110] and early flux penetration found in NbN films.

A selection of these samples were subjected to superconducting testing in the VSM detailed in Chapter 6.2.9. These initial samples were tested in a perpendicularly applied field. As detailed in Figure 7-4, the NbN samples display a maximum superconducting transition temperature of T_c = 14.9 K, which is obtained at 10 % N_2. A region of higher T_c values is found for films deposited with lower N_2 %, with an increase in the N_2 % leading to a decrease in the transition temperature. The NbN films also show a higher entry field value at lower values of N_2 %. The samples display an initial increase in entry field value with increasing N_2 % at low values, reaching a maximum at 20% N_2 where H_{en} = 5 mT. This value decreases at higher levels of N_2 %. This maximum value is still far below the theoretical maximum of 20 mT for NbN. Based on these results, the parameter set to be explored during the screening study was created.

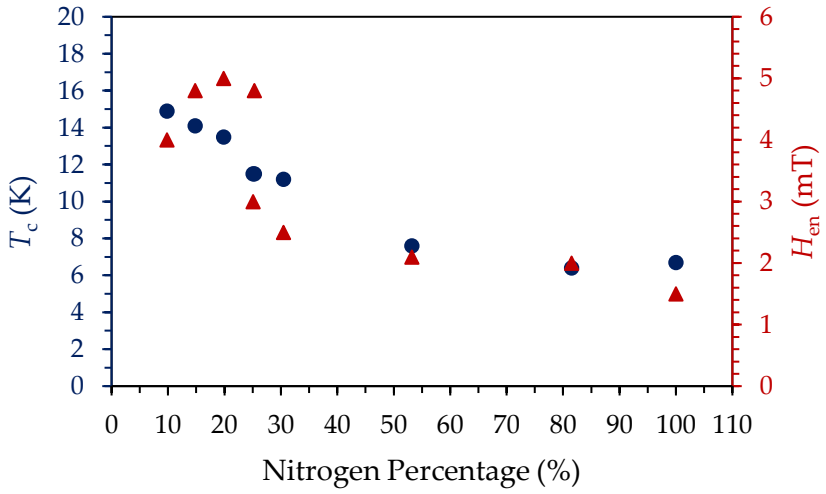

Figure 7-4: Transition temperature and entry field data for the initial preparatory NbN samples measured via VSM at IEE.

7.2.2 Screening Study

In order to gain a broader understanding of the effects of the deposition parameters on the resultant NbN thin films, further NbN thin films were deposited as part of a screening study. The NbN samples were synthesised in a randomised order developed using a Design of Experiments (DoE) approach, which utilised a high and low value for all parameters for both

Ar and Kr process gases. The values of the parameters are detailed in Table 7-2. The depositions were also randomised in order to reduce any effects from a linear deposition run. Overall, 36 samples were produced, listed fully in Appendix A.1. The Cu substrates in this study, 25 x 25 x 2 mm^3 in size, were again prepared with mechanical polishing followed by a nitric acid etching treatment, as described in Chapter 5.3.1.

Table 7-2: Deposition parameters used during the NbN screening study including set point values.

Parameter boundary	T_s (°C)	p_{dep} (mbar)	U_B (V)	N_2 %	Process Gas	P_{cath} (W)
high (+)	270	1.6×10^{-2}	-80	30	Ar	500
low (-)	120	8.0×10^{-3}	0	10	Kr	300

All results detailed here are based on investigations of the NbN films deposited onto Cu, except the SEM cross-section images, which required the use of cleaved Si samples. The cleaved Si samples provided an indication of the film thickness, with all films lying within the region of 1.2 ± 0.2 μm. The different deposition conditions resulted in deposition rates ranging from 11.4 to 49.5 nm/min, mostly affected by the Ar/N_2 ratio and the cathode power. Due to the parameters used in the sputter etching of the substrates, a thin interlayer (40 – 60 nm) of Nb was deposited on nearly all samples.

In the following paragraphs, for a convenient sample declaration, the parameter set is given as plusses "+" and minuses "-" in brackets for the respective high and low parameter boundary. The order of the parameters is the same as in Table 7-2. For example, sample 14 has a parameter set of (- - + + + +), meaning T_s = 120 °C, $p = 8 \times 10^{-2}$ mbar, U_B = -80 V, N_2 % = 30 %, process gas = Ar and P = 500 W.

The cross-sectional and surface morphology has been investigated for all samples. Figure 7-5 shows a selection of cross-sectional and plain-view micrographs of the NbN thin films on Si and Cu, respectively. NbN films are said to grow in a columnar fashion [239]. Based on the SEM investigations completed in this study, growth modes within NbN films are found to vary significantly depending on the deposition conditions. The identified trends in the results are detailed below.

The substitution of Ar with Kr as working gas does not change the growth modes significantly within this parameter window. The same holds true for the lower and upper boundary of the N_2 %. Due to parameter interdependency, no significant tendencies for the substrate temperature T_s were found. However, for a dense film, a high T_s is preferred but not mandatory, provided that a substrate bias and high cathode power is applied. This becomes

obvious in Sample 14 (- - + + + +), which is shown in Figure 7-5 (a) and (b). Here, a dense and compact film can be seen with no individual columns.

The deposition pressure *p* has the greatest impact on the growth mechanism. Figure 7-5 (c) to (f) show the samples 35 (+ - - + + +) and 36 (+ + - - + +), respectively. Sample 35, deposited at low pressure, shows a very dense and adherent structure with rounded peaks. This is related to the changes in the mean free path with changing deposition pressure leading to a higher/lower surface diffusion. Deposition at low-pressure results in adatoms arriving at the substrate with higher energy, thereby allowing higher rates of surface diffusion, leading to denser films. On the other hand, sample 36, deposited at high pressure, tends to grow with a very porous and highly columnar film structure, topped by faceted peaks. These columns grow from the substrate to the surface as individual grains, which are barely interconnected. This effect of high-pressure deposition can be suppressed by applying a substrate bias U_B. Sample 8 (+ + + + + +) and 32 (+ - + + - +) reveal this effect in the respective Figure 7-5 (g) to (j). Both cross-sections show a very dense and compactly grown film regardless of the deposition pressure.

Finally, in nearly all cases, a high cathode power *P* is needed for a dense film. An applied U_B can compensate for a lack of *P*, provided that there is a high enough mean-free-path (*p* is low), see sample 20 (- - + + - -) in Figure 7-5 (k) and (l).

Also apparent in some of these samples, figures (a), (e), (i) and (k), is the Nb interlayer, deposited as a result of the initial ion etching process used with these samples.

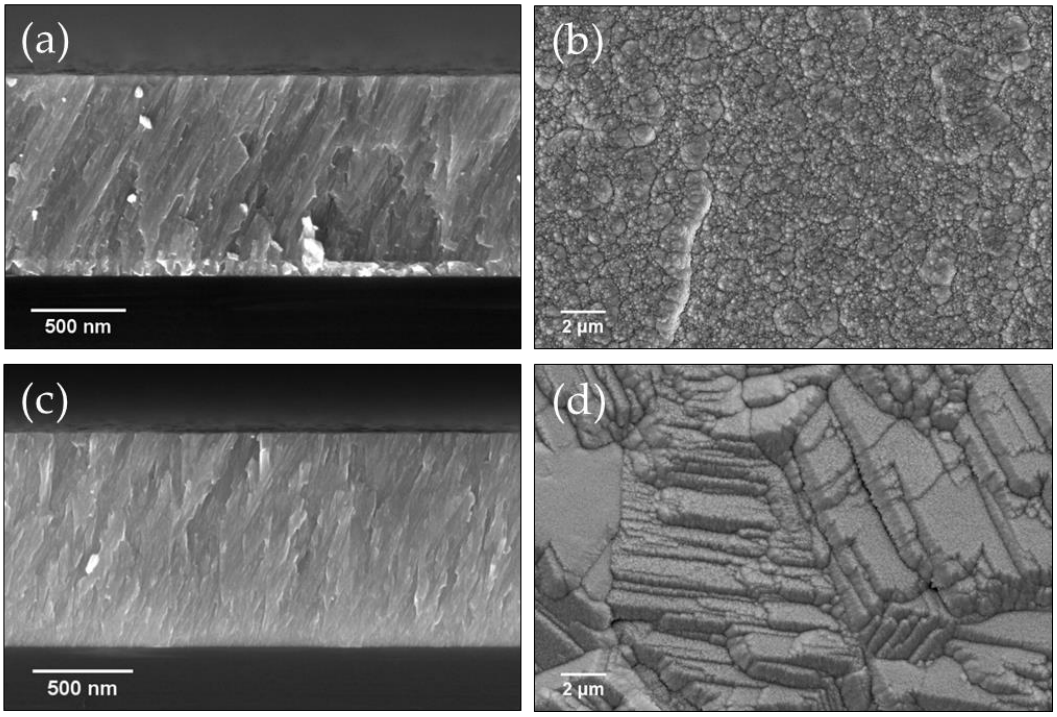

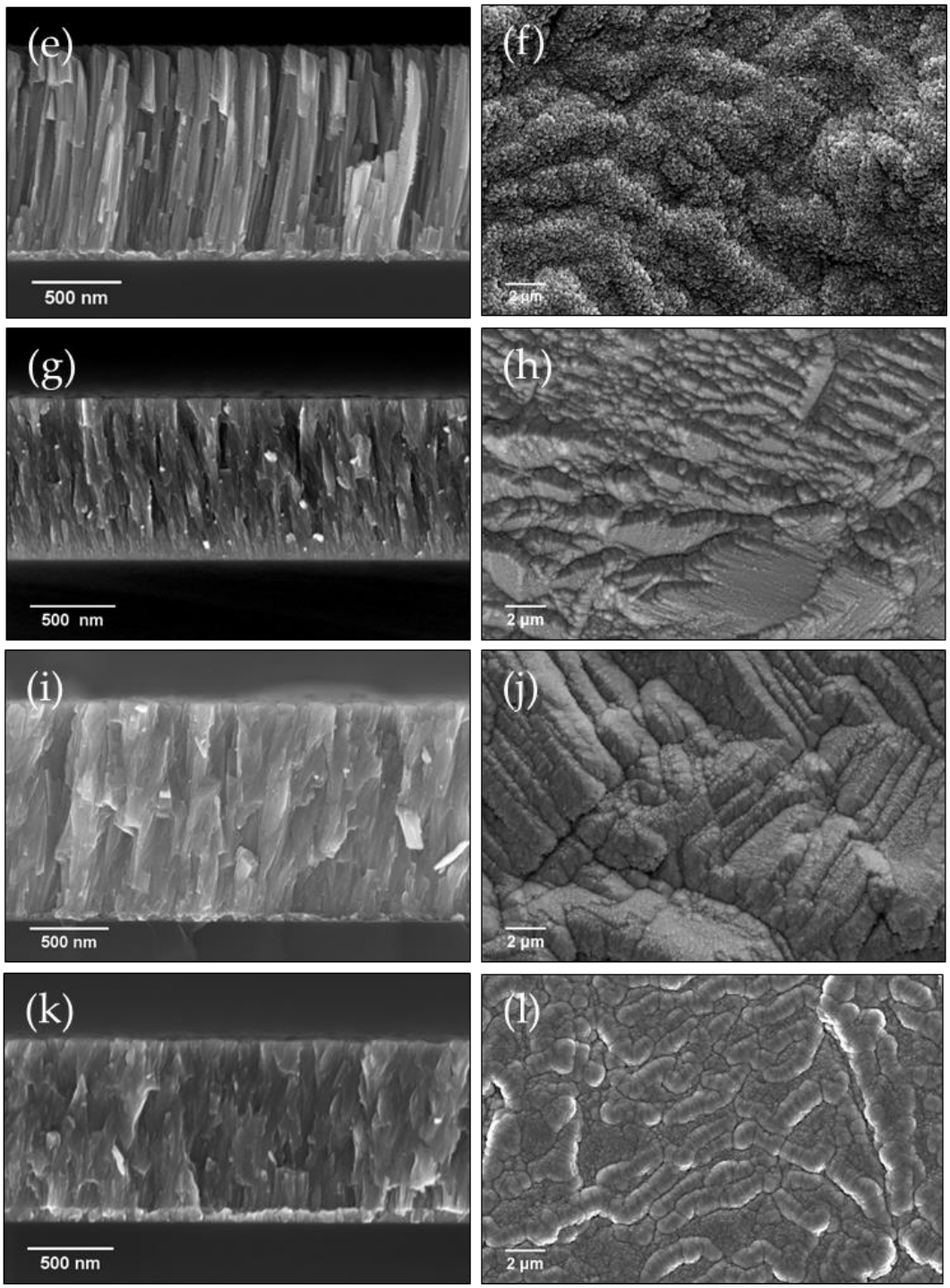

Figure 7-5: SEM micrographs of NbN thin films deposited on silicon (cross-section) and Cu (plain-view). (a) and (b) display Sample 14 (- - + + + +), (c) and (d) display Samples 35 (+ - - + + +), (e) and (f) display Sample 36 (+ + - - + +), (g) and (h) display Sample 8 (+ + + + + +), (i) and (j) display Sample 32 (+ - + + - +) and (k) and (l) display Sample 20 (- - + + - -).

Together with the SEM investigations above, all samples have been analysed by means of EDX spectroscopy. The measurements were performed on both the cross-section of the film on Si and the surface of the film deposited on Cu. Figure 7-6 shows two spectra of

representative samples. The analysis of sample 14 in (a) shows no signs of contamination, including no O. Sample 36 in (b) displays an O contribution.

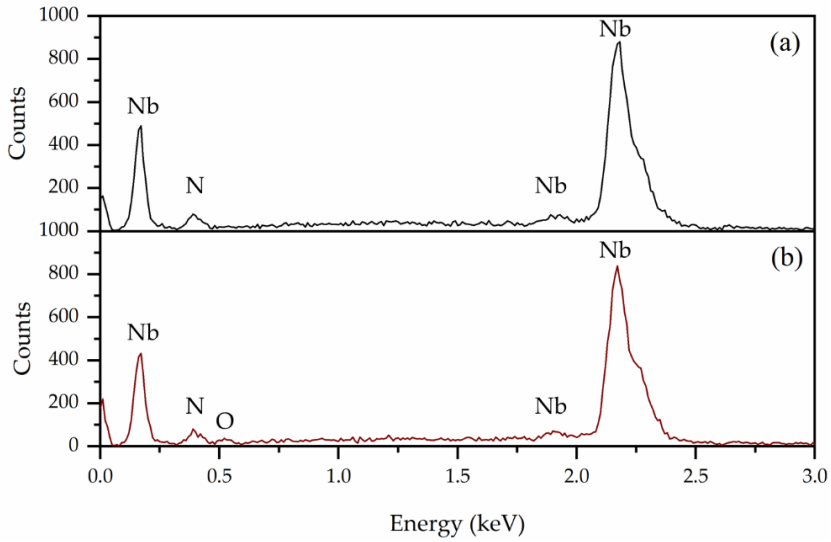

Figure 7-6: EDX spectra of NbN films on Cu in plain-view with (a) 30% and (b) 10% N_2 flow rate during the synthesis.

The most relevant deposition parameters for O contamination were found to be the process gas and the deposition pressure. Samples deposited using Kr were repeatedly found to contain more O than those deposited with Ar. This was confirmed through repetition coatings of samples of interest using both Ar and Kr gas. On the other hand, a lower deposition pressure leads to a decreased level of O within the films. These results are summarised in Table 7-3. The presence of O is found mainly in low N_2 % (10 %) films, which correlates with the RBS results presented in Table 7-1.

Table 7-3: EDX results for atomic percentage of O present in NbN films as a function of process gas and deposition pressure.

Process Gas	**Argon**		**Krypton**	
Pressure	**High**	**Low**	**High**	**Low**
Mean	2.84	1.18	10.48	2.46
St. Dev	4.66	0.98	4.96	2.38

Initial optical inspections of the samples showed a relatively dull surface finish, indicative of a rough surface. The films were also found to possess either a silver or gold film colour, where the gold colour is said to indicate the sought after cubic, δ-NbN film structure while the silver colour indicates a hexagonal structure (β, ε or δ' - NbN) [105]. However, this is not conclusive

evidence of good superconducting performance, as in some instances, films that are gold in colour, display low T_c values and films with a silver colour display high T_c values.

The purported increased surface roughness was confirmed by AFM, CLSM and SEM investigations, where the surface was found to closely conform to the underlying Cu surface as shown previously in Figure 5-4. The surface roughness measurements, conducted using both the AFM and CLSM, provided topographical information at two different length scales. The deposition parameter effects on the surface roughness are detailed in Table 7-4, with (+) indicating a resultant increase and (-) indicating a resultant decrease. Both the AFM and CLSM measurements detail similar trends, with all deposition parameters, except the substrate temperature, influencing the roughness of the resultant surface. The AFM measurements displayed greater variability in surface roughness between the high and low deposition parameters. This indicates a more noticeable influence at smaller length scales, representative of a large effect on film microstructure, such as grain morphology. The biggest influence is found to be due to the change from Ar to Kr gas. Which results in a 30 – 40% reduction in surface roughness.

Table 7-4: Deposition parameter effects on the surface roughness of screening study NbN films determined by AFM and CLSM measurements.

Parameter Boundary	T_s **(°C)**	p_{dep} **(mbar)**	U_B **(V)**	N_2 **%**	**Process Gas**	P_{cath} **(W)**
High	Equal	-	+	-	+	+
Low	Equal	+	-	+	-	-

The XPS setup used in this study is not fitted with an ion-milling device. As such, the recorded data provided information relating to the outermost ~ 10 nm of the film, which is largely constituted by the oxide layer. The XPS data of all measured samples were very similar, indicating no significant difference due to the deposition conditions. An example of the results from sample 8 (+ + + + + +) are displayed in Figure 7-7. The overall spectrum as well as the individual Nb3d, C1s, N1s and O1s spectrums and their deconvolution are presented.

The data illustrates the presence of a Nb_2O_5 oxide layer, indicated by the ~ 207 eV peak in the Nb3d spectrum and the 530 eV peak in the O1s spectrum [240]. A series of oxynitrides (NbO_xN_{1-x}), which are known to decrease the superconducting performance of NbN thin films, are indicated by the ~ 400 eV and ~401.4 eV peaks in the N1s spectrum [240] and the 532.3 eV peak in the O1s spectrum. NbN is detailed in both the N1s spectrum (~ 397 eV) and the Nb3d spectrum (~ 204 eV) [241]. Previous studies detail the disappearance of the

oxynitride peaks following the removal of surface oxide layer [241][242]. This was however not completed in this study. No unbound Nb, characterised by a peak at ~ 202.4 eV in the Nb3d spectrum, was found, providing further evidence for the lack of the β or γ-phase in the XRD scans. The presence of the C1s peak is believed to be due to the post deposition handling of the samples prior to the measurements. The peak at ~ 534 eV is attributed to the presence of OH^- [242], likely due to the low bake out temperature and high base pressure.

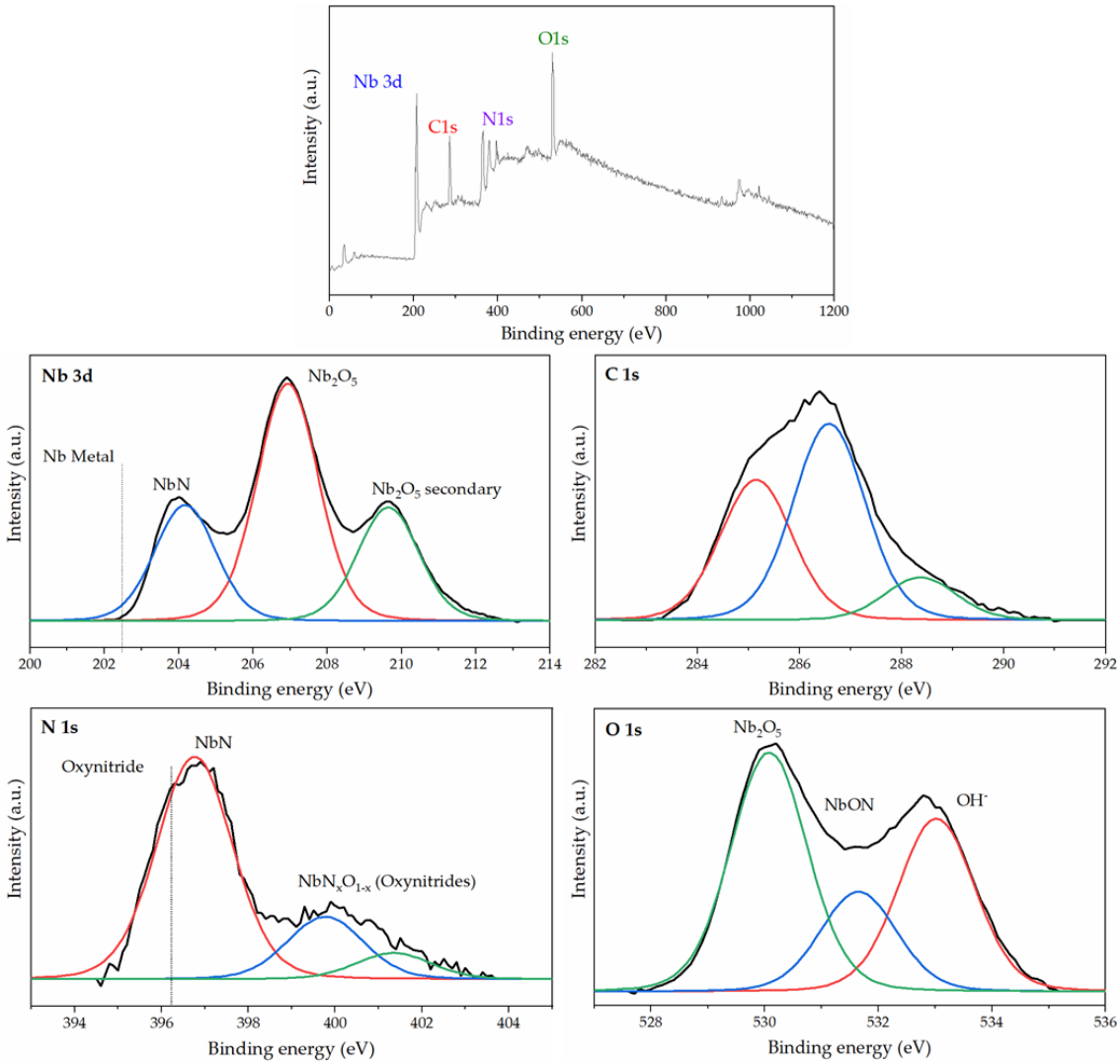

Figure 7-7: XPS spectra of sample 8 (+ + + + + +). Images of the overall spectrum, Nb3d, C1s, N1s and O1s spectrums are shown (measurement courtesy of A. Schulte, University of Siegen).

Bragg-Brentano XRD scans of each of the NbN/Cu samples were used to identify the phases present in the different films. Widely varying profiles were produced for the different deposition conditions, with a subset of representative scans presented in Figure 7-8. These scans pertain to films coated with a low (0 V) bias and a high (500 W) cathode power with the following variation in deposition parameters. Scans (a) to (d) detail films deposited at

high pressure (1.6 x 10^{-2} mbar), while (e) to (h) represent films deposited at low pressure (8 x 10^{-3} mbar). Scans (a), (c), (e) and (h) detail films deposited with high N_2 %, while (b), (d), (f) and (g) detail films deposited with a low N_2 %. Scans (a), (b), (e) and (f) were deposited at a low substrate temperature (115°C) while scans (c), (d), (g) and (h) were deposited at a high substrate temperature (270°C). Finally, scans (a), (d), (f) and (h) were deposited with Ar as the process gas while scans (b), (c), (e) and (g) were deposited with Kr.

Due to the nature of the overlapping NbN peaks, it is known to be challenging to characterise NbN phases from XRD data alone [243]. However, the RBS, SEM and XPS data assist in identifying all peaks at ~ 35.3° and ~ 41.05° as the cubic, δ-NbN (111) and δ-NbN (200) phase [244] while those at ~ 38.4° represent the Nb interlayer [245], aligned along a growth direction of (110), which was deposited due to the ion etching process with some samples. Examples of this interlayer are shown in Figure 7-5. The Cu substrate is also clearly visible and is identified by the peaks at ~ 43.3° (Cu (111)) and ~ 50.4° (Cu (200)) [219]. This is due to the penetration depth of the X-rays in Bragg-Brentano configuration and the low thickness of the NbN films (~ 1.2 μm).

From the scans, it is evident that NbN films deposited with a high pressure tend to grow with a preferred (111) orientation while those deposited at low pressure tend to grow with a (200) orientation. This correlates well with previous studies, which showed that a decrease in the deposition pressure leads to a change in orientation from NbN (111) to NbN (200) [115]. NbN films deposited with lower N_2 % showed an increase in the intensity of the (111) peak in comparison to those coated at higher N_2 %, with all other parameters kept equal. A significant peak broadening is also identified for samples deposited with higher N_2 %, indicating a decrease in the crystallite size of these NbN films. The use of Kr as the process gas also results in an enhanced NbN (111) growth relative to films coated with Ar, with all other parameters equal. Through comparing these results with the SEM cross-section investigations of these samples, not shown here, the following can be concluded: Samples with a higher relative NbN (111) orientation are characterised by columnar film growth topped by faceted peaks. On the other hand, those with a higher relative NbN (200) orientation possess a dense, non-columnar structure topped with rounded peaks.

The erosion of the Nb target, not accounted for in this study, has also been shown to lead to a more pronounced (111) texture of the NbN films regardless of nitrogen flow [115].

A selection of samples from this study were chosen for superconducting measurements in a VSM. These measurements were completed in a similar fashion as was described in Chapter 6.2.10, again with the samples subjected to a perpendicularly applied field. All of the

investigated samples were found to be superconducting, with T_c's ranging from 8.2 K to 14.8 K. Two general observations with respect to the deposition parameters can be made: Samples deposited with a lower N_2/Ar ratio proved to be superior. Samples deposited with Kr appear to perform better when deposited at low pressures, while those deposited with Ar appear to perform better when deposited at high pressures.

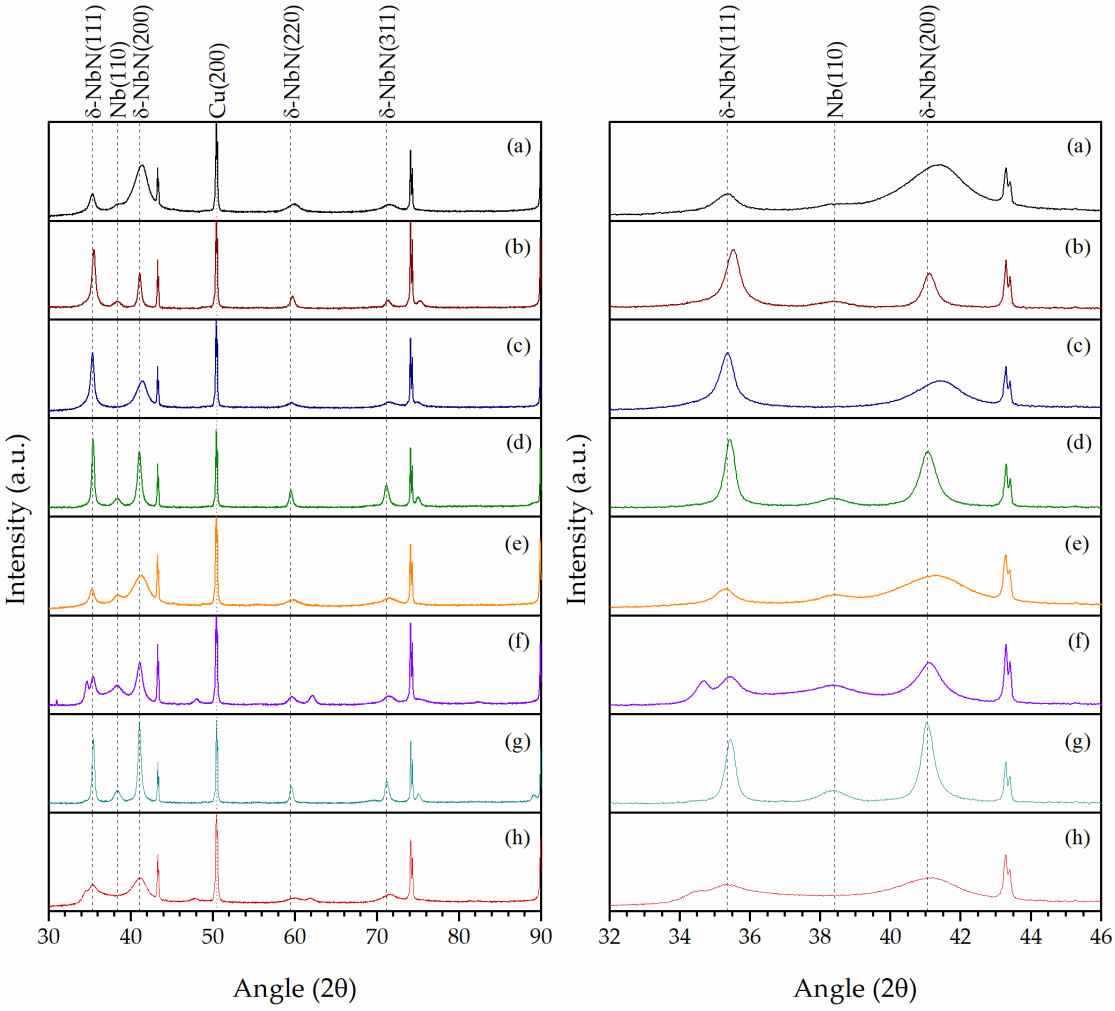

Figure 7-8: XRD data for eight representative NbN thin films deposited on Cu as part of the screening study. (Left) The full captured spectrum between 30 and 85°. (Right) The main area of interest for the two most significant peaks for identifying NbN between 32 and 46°. Data is plotted with a vertical log scale.

The highly columnar, faceted film growth mode, typically associated with (111) oriented films, is also found to be more prevalent in NbN films with high T_c. However, these films are characterised by lower entry field values. This is related to the film structure, which is very porous and disconnected, often with micrometre-sized pores (finite-size effect and shadowing). This allows the formation of oxynitrides in between the columns of NbN. This,

in turn, leads to high scattering of electrons, an increased number of pinning centres for magnetic field lines and flux concentration on the "sharp" faceted peaks.

This screening study showed that the synthesis of a superconducting NbN phase is possible on a polycrystalline Cu substrate with a wealth of different deposition parameters. In order to narrow these down, a first set of conclusions are given: In an attempt to avoid the possible formation of voids and/or oxynitride inclusions in between NbN grains, dense films with adherent columns should be pursued. Thus, a high substrate temperature or applied substrate bias and an optimised deposition pressure are required. A relatively high cathode power is also vital, keeping in mind the requirement for sufficient nitrogen to react with Nb. Furthermore, the use of lower nitrogen flows (~ 10 %) is critical for the formation of the δ - NbN phase. The use of Kr instead of Ar as a working gas leads to a lower surface roughness; however, there is a significant increase in O content. Therefore, future coatings utilise Ar exclusively. Finally, due to the deposition of the Nb interlayer, the use of the ion etching process was deemed unsatisfactory and should be replaced by an MF etching procedure, as provided by CemeCon AG GmbH.

7.2.3 Individual Parameter Studies

Based on the conclusions of the screening study, a series of individual parameter studies were completed in order to optimise the formation of high T_c δ - NbN thin films. Even though low deposition pressure leads to denser films, the formation of high T_c, δ - NbN at low deposition pressure is seen to be difficult. To further understand this, a first series of NbN films were deposited at a fixed deposition pressure of 8.0×10^{-3} mbar, with individual N_2 flow rates ranging from 6 to 30 % of the total Ar and N_2 flow rates. A second series of films were deposited with a constant 10 % N_2 flow rate and 8.0×10^{-3} deposition pressure, with individual substrate bias values ranging from 0 V to - 250 V. A final series of films were deposited with a constant 10 % N_2 flow rate, at individual deposition pressures ranging from 8.0×10^{-3} to 1.8×10^{-2} mbar. The films were deposited using a mixture of argon (99.999 Vol-%) and nitrogen (99.999 Vol-%) gases. The $N_2/Ar + N_2$ ratio was maintained via flow rate control of the two gases. The samples were deposited with a high cathode power (500 W).

The substrates used during these studies were 1 mm thick OFHC Cu samples with dimensions of 25 x 25 mm^2 and pieces of Si (100) wafer used as witness samples. The Cu substrates were prepared using the final optimised surface treatment methodology detailed in Chapter 5.7, using a combination of mechanical and electropolishing. Prior to deposition, the system, including the substrates, was passively baked at 280°C for 6 hrs. Following this,

the substrates were subjected to a medium frequency (MF) etching process for 10 min as a final surface treatment and the Nb target was sputter cleaned for 10 min to ensure all possible contaminants were removed. The system reached a base pressure of 6×10^{-7} mbar at the required substrate temperature. In total, 30 NbN samples were deposited with the deposition parameters summarised in Appendix B.

The Nb target used in the screening study, detailed in Chapter 7.2.2, was replaced with a new target before the start of these studies. The new target was again a RRR 300 Nb target that was cut from the same Nb ingot as the first target. Prior to starting the investigations, the target received a series of processing runs in order to obtain stable plasma conditions and repeatable coating conditions. This process required a total deposition time of ~ 10 hrs, distributed as shown in Appendix A.4

7.2.3.1 Nitrogen Percentage Study

The films in this study display a dense cross-sectional microstructure, regardless of the level of N_2 % in the process gas. There is also no evidence of voids between the film and the substrate, nor any evidence of film delamination. As detailed in Figure 7-9 (a), (b) and (c), films deposited with low N_2 % exhibit a dense, non-columnar structure with a smooth surface comprised of rounded grain peaks. This is supported by the BF TEM and SAED image inset in Figure 7-9 (c), which contains a set of homogeneously distributed ring patterns. The films become increasingly columnar with increasing N_2 %, as shown in Figure 7-9 (d), (e) and (f). The SAED pattern of the 12 % N_2 sample in the inset of Figure 7-9 (f) displays a set of discontinuous rings, indicating a preferred orientation in the film as well as in increase in the crystallite size, both of which were confirmed by XRD analysis. In spite of this, the surface structure remains smooth and is constituted by collections of rounded grain formations, albeit larger than those at low N_2 %, which gives the surface a smeared aubergine look. This smooth surface structure is similar for all films deposited in this series, regardless of N_2 %, and results in an average RMS surface roughness of $S_q = 8.19 \pm 3.68$ nm as measured by AFM.

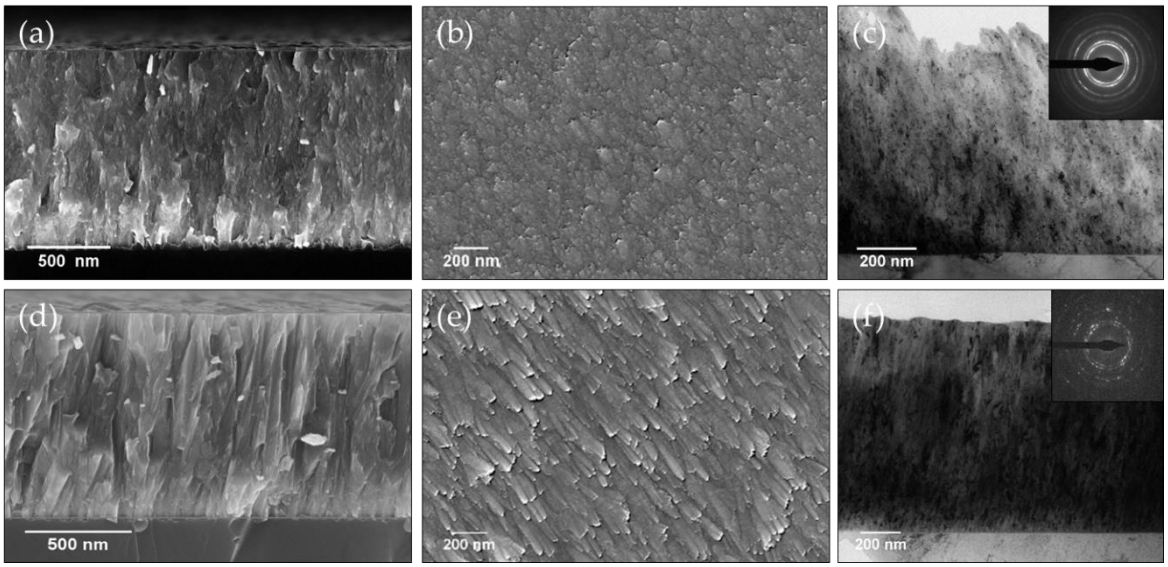

Figure 7-9: SEM and TEM images of samples deposited with low and high N_2 % at 500 W cathode power and a deposition pressure of 8 x 10^{-3} mbar. (a) The cross-section of the 8 % N_2 film deposited on Si. (b) Surface of the 8 % N_2 film deposited on Cu. (c) BF TEM cross-section image of the 8 % N_2 film as well as SAED image of the same film (inset). (d) The cross-section of the 18 % N_2 film deposited on Si. (e) Surface of the 18 % N_2 film deposited on Cu. (f) BF TEM cross-section image of the 12 % N_2 film as well as SAED image of the same film (inset).

The crystallographic relationship between the NbN film and the Cu substrate was also explored with HRTEM. Due to its superior entry field value, the film deposited at 8 % N_2, was chosen for analysis, with the results of the investigation displayed in Figure 7-10. From (a) it is evident that the Cu lattice planes are found to lie oblique to the surface. It is also evident that the NbN film initially grows epitaxially along the crystal orientation of the Cu substrate. Following the growth of a few nanometres, the crystal orientation is no longer influenced by the Cu substrate and the NbN grows in a separate crystal orientation. The lattice parameter of Cu is listed as a = 3.615 Å [219], while that of this NbN film was calculated to be a = 4.3829 Å. This results in a lattice parameter difference of 17.52 %. From (b) it is evident that the film is epitaxially grown for the initial few nanometres of the film. In these first few nanometres, the film is subjected to compressive strain. As the film thickness increases, this strain is released through the formation of dislocations, indicated by the red marks in (b). Based on the lattice mismatch, and the HRTEM image, one dislocation will form for every five Cu lattice planes. Even with this large lattice mismatch, no delamination of the films was observed.

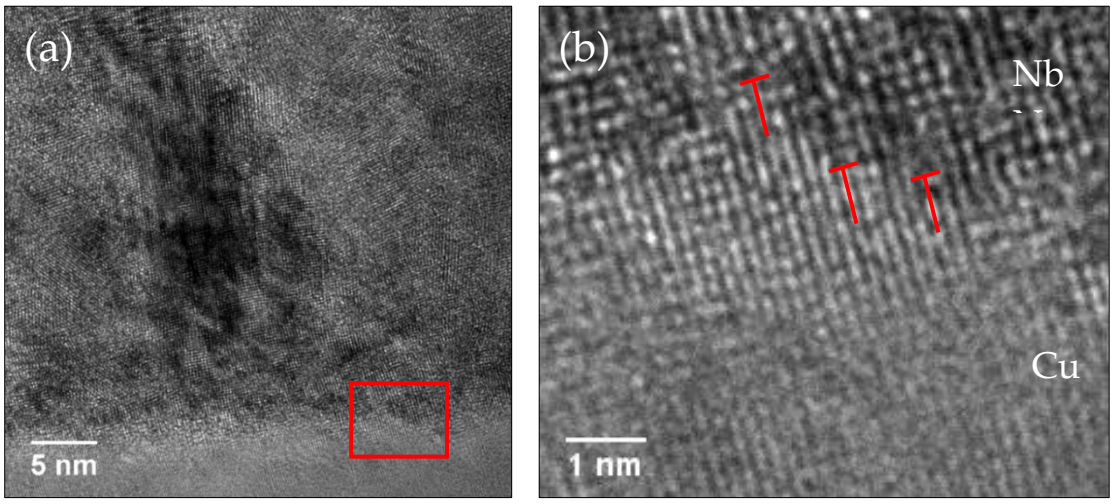

Figure 7-10: HRTEM image of (a) the interface between the NbN film grown with 8 % N_2 and the Cu substrate. (b) Magnified image of the area shown in red in (a) displaying the epitaxial relationship between Cu and NbN.

This structure was further found to be nanocrystalline, based on XRD data analysis, exhibited in Figure 7-11 and Figure 7-12 respectively. The δ-NbN phase is identified by the peaks at 35.35° and 41.05° [244]. The peaks are fairly broad, indicating a nano-crystalline structure, which correlates with the SEM results shown in Figure 7-9 (a). At lower N_2 %, samples display a δ-NbN (200) polycrystalline fibre texture, as confirmed by the (200) pole figure measurement displayed in Figure 7-11 (b). An increasing presence of the hexagonal, higher order nitride phase, Nb_5N_6, as evidenced by the peak at 34.5° [246], is seen with increasing N_2 %. The relative intensity of the higher order nitride peak exceeds that of the δ-NbN peak above 10 % N_2, where after the films are no longer preferentially δ-NbN (200) oriented, as shown by the (200) pole figure in Figure 7-11 (c). The increase in the hexagonal phase with increasing N_2 % was also observed by Havey *et al* [241], although they observed the δ'-NbN phase, and is likely due to increasing concentrations of N_2.

The lattice constant (a) of NbN films is often used as an indication of the stoichiometry and vacancy content of the films, with superior film properties found at lattice constants in the region of the bulk lattice parameter ($a = 4.3885 \pm 0.007$ Å) [48]. The changes in the lattice parameter and the average δ-NbN (111) crystallite size, as a function of the N_2 %, are detailed in Figure 7-12 (a). The entire plot range lies within the values defined for bulk δ-NbN.

The lattice parameter is found to increase with increasing N_2 % up to a maximum of 4.397 Å at 16 % N_2; thereafter it steadily decreases with further increase in N_2 %. This result is similar to that detailed by Brauer and Kirner [247]. They observed that the lattice parameter reaches a maximum at a ratio of Nb:N ~ 1. Higher or lower Nb:N ratios led to a decrease in the lattice

parameter due to crystallographic imperfections. This result also correlates well with the RBS analysis results presented in Chapter 7.2.1.

The average δ – NbN (111) crystallite size displays a similar trend to the lattice parameter, increasing to a maximum of 13 nm at 16 % N_2, where after it decreases. An increase in N_2 % results in a decreased adatom flux during film deposition, which results in an increased surface diffusion time leading to larger crystallites. This is responsible for the initial increase in δ-NbN (111) crystallite size up to ~ 16 % N_2. However, further increase in the N_2 % leads to an increase in the proportion of the hexagonal Nb_5N_6 phase. This in turn, results in a decrease in the δ-NbN (111) crystallite size at higher N_2 content.

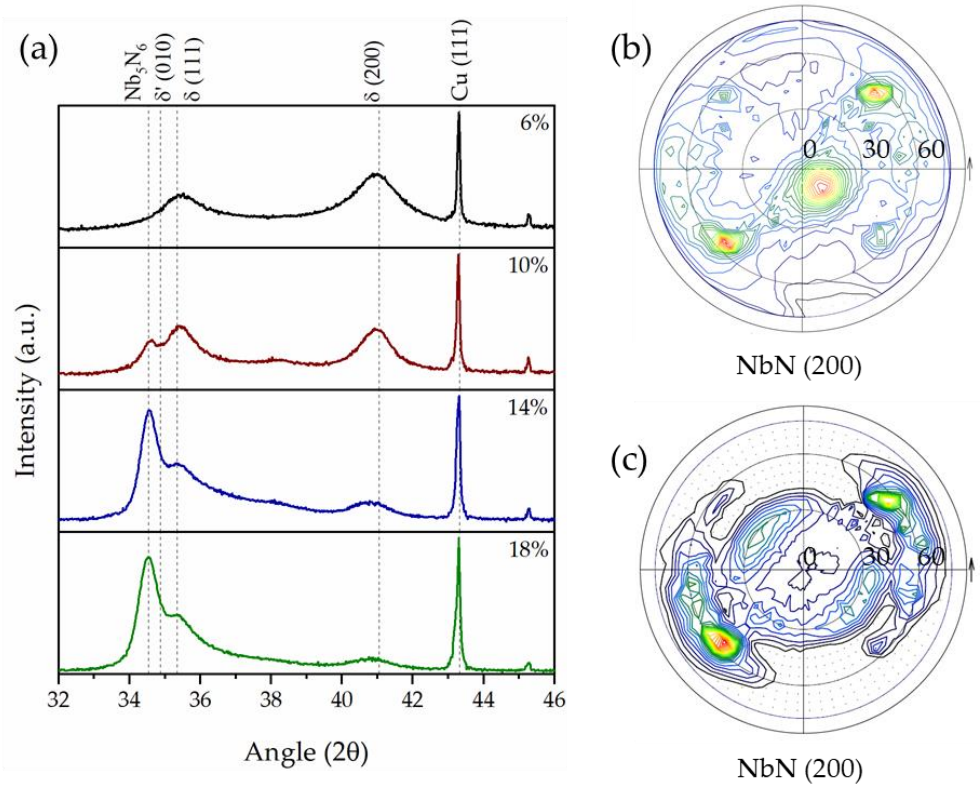

Figure 7-11: (a) XRD patterns of NbxNy on Cu samples deposited at different nitrogen to argon ratios, denoted as nitrogen percentages next to the respective scan. The spectra are plotted in log scale. (b) XRD pole figure of (200) NbN at 6% N_2. (c) XRD pole figure of (200) NbN at 18% N_2.

The results of VSM measurements are displayed in Figure 7-12 (b). It is evident that the critical temperatures of these films remain consistent at ~ 11 - 12 K, above 6 % N_2. The critical temperature of the 4 and 20 % samples could not be accurately discerned from the data at the 5 mT applied field and as such, they were excluded from this figure. The entry field is found to achieve a significant maximum of H_{en} = 13.0 mT at 8 % N_2, falling off at higher and lower values of N_2 %. This is related to the formation of non-superconducting hexagonal phases at higher N_2 %, as evidenced in the XRD scans, and incorrect stoichiometry at lower N_2 %.

The generally low entry fields of the NbN films, a few mT typically, were particularly difficult to determine, mainly due to the small number of data-points measured in the initial linear Meissner trend region. The $m(H_a)$ data-points were recorded at 0.2 mT steps for the virgin curves and as the measured magnetic moment values were correspondingly small in this low H_a region, the experimental noise of the magnetic moment measurement had a stronger impact on H_{en} determination compared to other types of samples. The overall precision of the H_{en} measurement is estimated to be ± 2 mT for the NbN samples. In the case of the NbN samples with H_{en} values close to 2 mT, the linear Meissner trend was always visible; however, the reported H_{en} value is only indicative.

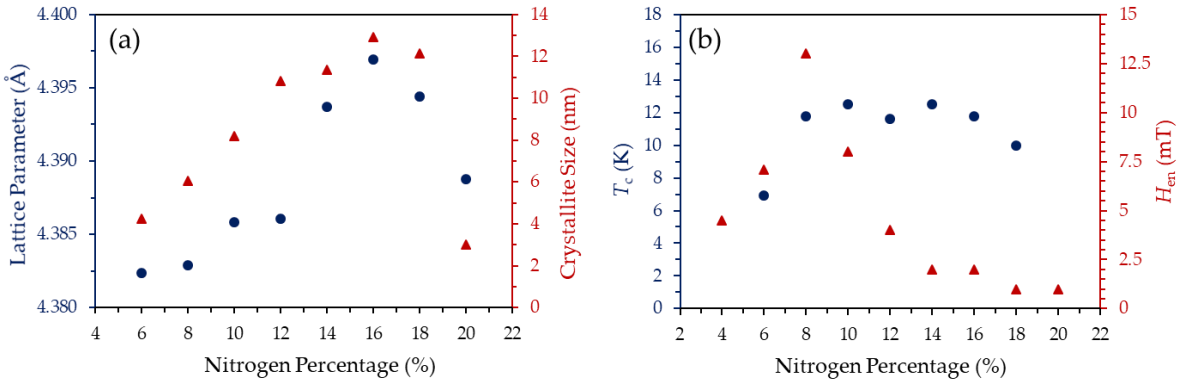

Figure 7-12: (a) Plot detailing the change in the lattice parameter and the average δ-NbN (111) crystallite size, with increasing N_2 %. (b) Plot detailing the change in critical temperature and entry field in parallel field, with increasing N_2 %.

7.2.3.2 Substrate Bias Study

The use of increasing substrate bias values did not significantly influence the NbN phase formation at this deposition pressure. The films displayed the presence of both a hexagonal phase and the sought after δ-NbN phase, similar to what was found with the 10 % N_2 sample above. The microstructure of the films also did not show a significant change other than to bring about a rounding to the grain peaks at higher substrate bias levels > 200 V. Because of this, an in-depth analysis is not included here.

7.2.3.3 Deposition Pressure Study

The most apparent change seen with the NbN films is brought about by increasing the deposition pressure. As shown in Figure 7-13, the colour of the film is observed to change from a silver to a more pronounced gold colour, which is synonymous with the superconducting δ-NbN phase [105]. This change becomes evident at deposition pressures ≥ 1.0 x 10^{-2} mbar.

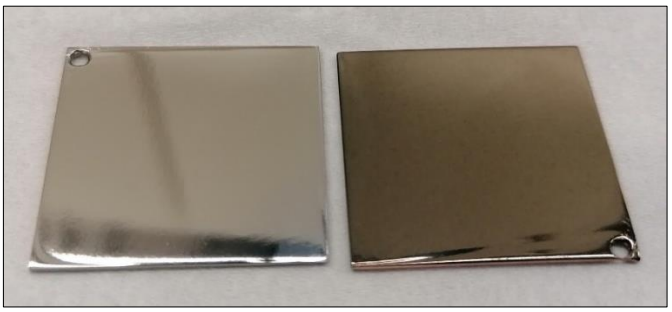

Figure 7-13: Image of NbN film deposited at low pressure (left) and high-pressure (right), displaying the change in colour experienced with an increase in deposition pressure.

As displayed in Figure 7-14 (a), (b) and (c), at low deposition pressure, the film displays a relatively dense cross-sectional structure while the surface consists of rounded, nano-crystalline grains. The dark spots in the TEM image in (c), which are grains in the Bragg condition, confirm this. This is similar to the structure shown in Figure 7-9 (a) and is synonymous with films deposited at low pressure. The SAED image in the inset in (c) also indicates a randomly oriented nano-crystalline structure. In comparison, films deposited at higher deposition pressures (> 1.2×10^{-2} mbar) display a pronounced columnar structure in conjunction with larger, faceted grains on the surface, typical of a Zone T film structure. This is showcased in Figure 7-14 (d), (e) and (f). The increased deposition pressure also leads to a spot like pattern in the SAED, shown in the inset in (f). This is a result of the increased crystallite size and the columnar growth structure. The presence of voids within the films, often in the form of disjointed columnar crystals, are also more apparent in those deposited at high pressures relative to those deposited at low pressures, while the only void discovered at the interface between all NbN films and Cu is seen at high pressure in (f). This change is related to a reduction in the mean free path of the sputtered atoms at higher pressures, leading to a lower surface diffusion rate of adatoms on the substrate.

The change in surface structure coincides with an increase in the surface roughness observed with increasing deposition pressure. The results of both AFM and CLSM measurements are detailed in the graph shown in Figure 7-15 (a). The AFM measurements produced a $S_q = 4.39 \pm 0.41$ nm at low deposition pressure and a $S_q = 21.86 \pm 2.22$ nm at high deposition pressure. Examples of these two measurements are shown in Figure 7-15 (b) and (c) respectively. The increase in surface roughness is more pronounced in the AFM results compared to the CLSM results, due to the different scan sizes employed in each method, detailed in Chapter 6.2.2.

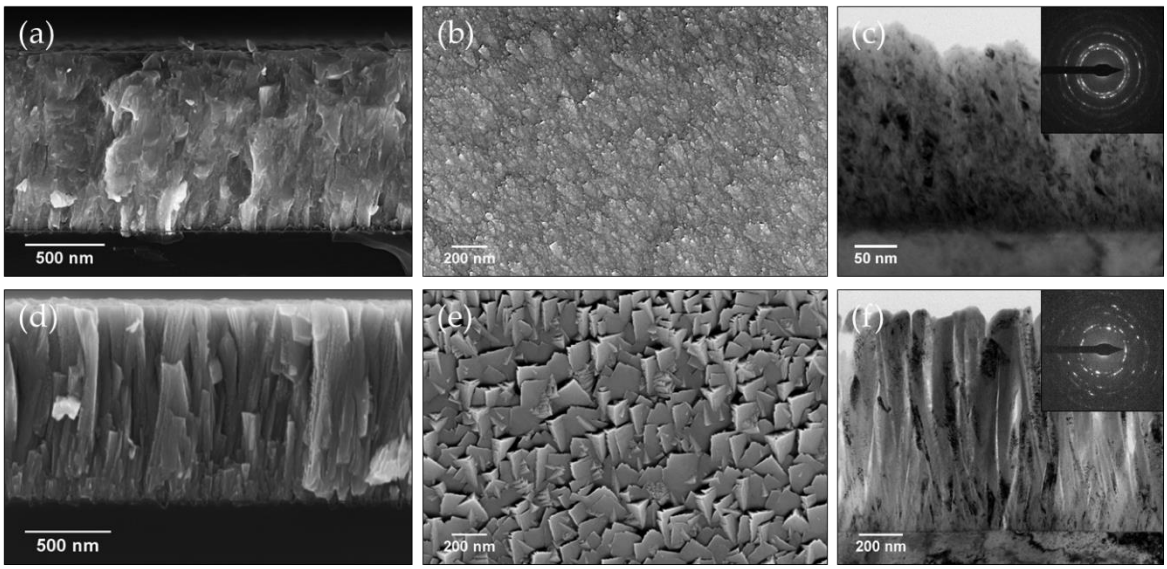

Figure 7-14: SEM and TEM images of samples deposited with low (8 x 10^{-3} mbar) and high (1.8 x 10^{-2} mbar) deposition pressure at 500 W cathode power and 10 % N_2. (a) The cross-section of the low-pressure film deposited on Si. (b) Surface of the low-pressure film deposited on Cu. (c) BF TEM cross-section image of the low-pressure film as well as SAED image of the same film (inset). (d) The cross-section of the high-pressure film deposited on Si. (e) Surface of the high-pressure film deposited on Cu. (f) BF TEM cross-section image of the high-pressure film as well as SAED image of the same film (inset).

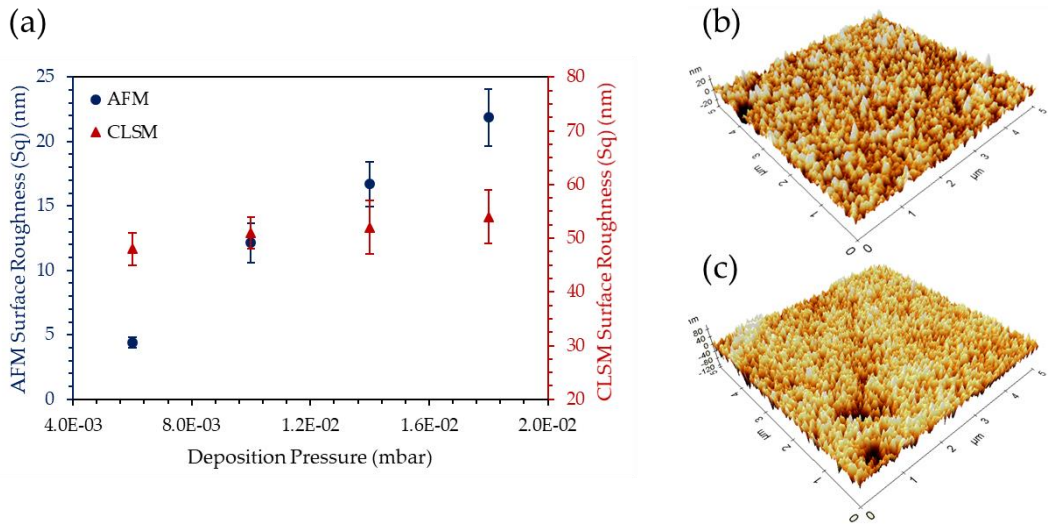

Figure 7-15: (a) Graph detailing the surface roughness as a function of deposition pressure measured by both an AFM and CLSM. (b) 3D AFM scan result at 6 x 10^{-3} mbar. (c) 3D AFM scan result at 1.8 x 10^{-2} mbar.

The XRD spectra, showcased in Figure 7-16 (a), also indicate a significant change with increasing deposition pressure. All films are identified as predominantly δ-NbN, however films transition from a (200) orientation at low pressures towards a pronounced (111) orientation at higher pressure. This is verified by the NbN (111) pole figure measurements which were obtained for the low and high-pressure samples, displayed in Figure 7-16 (b) and

(c) respectively. This is typical of face centred cubic materials, such as NbN [248]. The {111} pole figure in (b) displays four satellite spots around the 55° ring, although they are slightly offset in this instance, which indicates a (100) orientation of the film. These spots possess a modulated intensity in the azimuthal direction and as such, represent a slightly restricted fibre texture. On the other hand, the {111} pole figure in (c) presents a central spot of maximum intensity, with further spots, of modulated intensity, present on the 70° ring, also offset here. This indicates a (111) fibre textured film. The presence of the hexagonal δ' phase is also found at lower and intermediate pressures, indicated by the peak at 34.7° [249], but is not present at the highest pressure of 1.8 x 10^{-2} mbar.

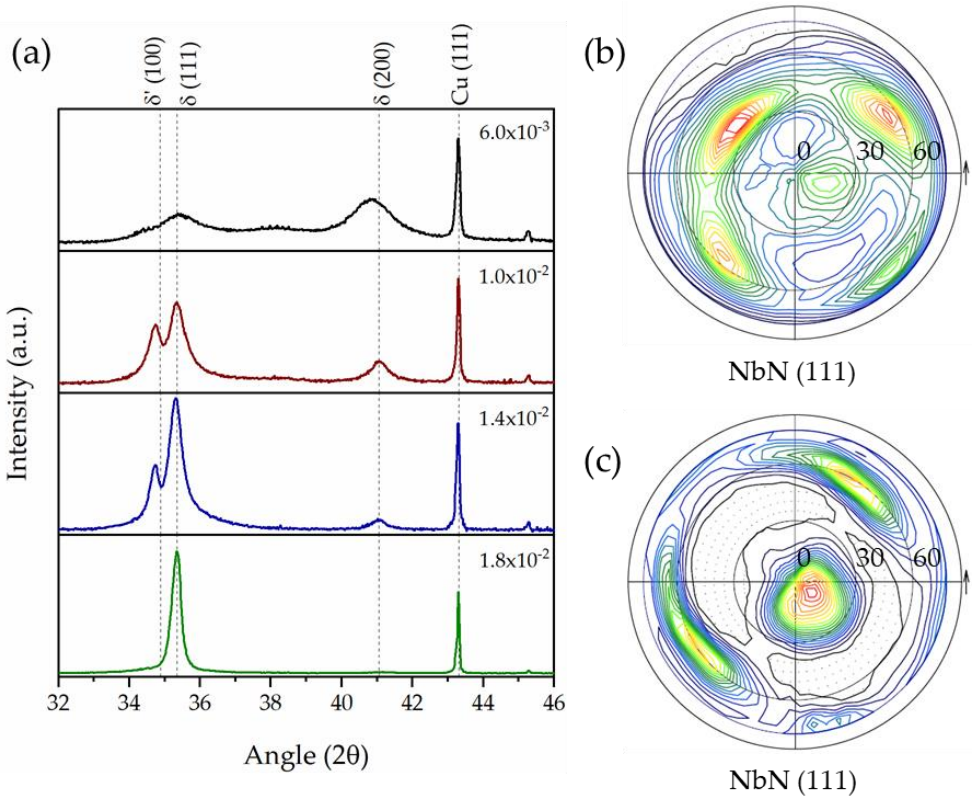

Figure 7-16: (a) XRD patterns of samples deposited at 10 % N_2 with different deposition pressures, displayed in mbar within the figure. The spectra are plotted in log scale. (b) XRD pole figure of (111) NbN at 6 x 10^{-3} mbar. (c) XRD pole figure of (111) NbN at 1.8 x 10^{-2} mbar.

The evolution of the lattice parameter and the δ-NbN (111) crystallite size, in relation to changing deposition pressure, is presented in Figure 7-17 (a). Again, the entire plot range lies within the values defined for bulk δ-NbN. The lattice parameter values display a further reliance on the deposition pressure, increasing up to a maximum of 4.398 Å at 1.4 x 10^{-2} mbar where after they decrease with further increase in pressure. The average crystallite sizes are

found to increase with increasing deposition pressure, from roughly 6 nm at 6.0 x 10^{-3} mbar to 24 nm at 1.8 x 10^{-2} mbar.

The results of the VSM measurements are presented in Figure 7-17 (b). The films show an increase in the critical temperature with increasing pressure up to a maximum of 15.3 K at 1.4 x 10^{-2} mbar, where after it decreases to 14 K at 1.8 x 10^{-2} mbar. This trend in T_c vs deposition pressure was shown previously by Bacon *et al* [118] and correlates well with the changes in the lattice parameter. Interestingly, the highest T_c film is constituted by multiple phases, while the single-phase δ-NbN film displays a reduced T_c. This is similar to the results obtained by Anderson *et al*, who found that the highest T_c NbN films always possessed a δ-NbN (111) texture with the presence of a small amount of δ'-NbN [116]. On the other hand, the entry field is seen to peak at 8.4 mT at a pressure of 1.0 x 10^{-2} mbar, where after it decreases with further increase in deposition pressure. This decrease in the entry field value is related to the faceted nature of the grain peaks above 1.0 x 10^{-2} mbar. These nano-scale faceted peaks lead to a local field enhancement and the suppression of the superheating field, resulting in early flux penetration [38][39].

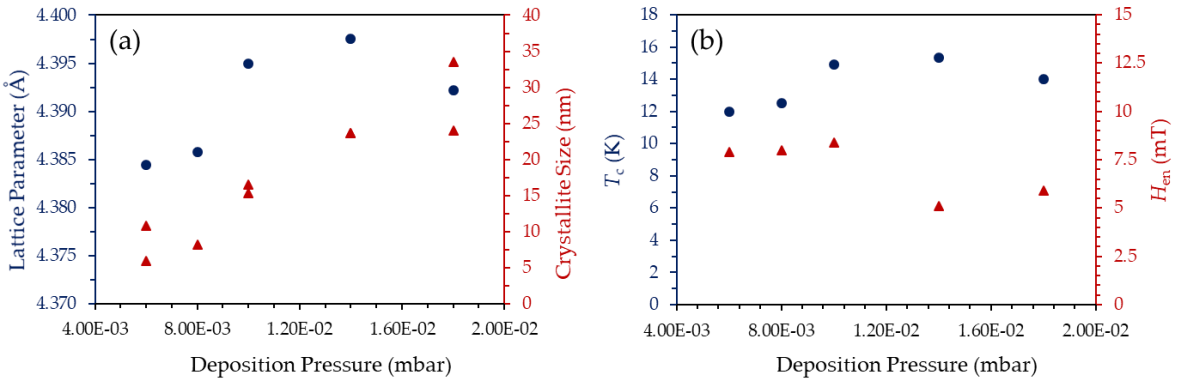

Figure 7-17: (a) Plot detailing the change in the lattice parameter and the average δ-NbN (111) crystallite size, with increasing deposition pressure. (b) Plot detailing the change in the critical temperature and the entry field in parallel field, with increasing deposition pressure.

7.2.4 Optimised NbN Thin Films

Following these initial investigations, a final series of eight optimised samples were deposited, taking into account the results of the previous samples. The aim with these samples was to maximise the superconducting transition temperature by combining a higher deposition pressure, lower N_2 % and the application of a low substrate bias to maintain a dense film in spite of the increased pressure. The list of samples is found in Appendix A.2. All of these samples possessed a gold film colour and achieved an average T_c = 15.0 ± 1.0 K.

Two samples in this series (889 and 891) were deposited with the same conditions as two samples from the N_2 % study (789 (6%) and 790 (8%)), except with a lower cathode power of 400 W instead of 500 W. This resulted in a transition to a more columnar growth mode of the film, as evidenced for sample 789 (a) and 889 (b) in Figure 7-18. The samples also display a larger, more faceted peak on the film surface. This change did not lead to a significant change in surface roughness however.

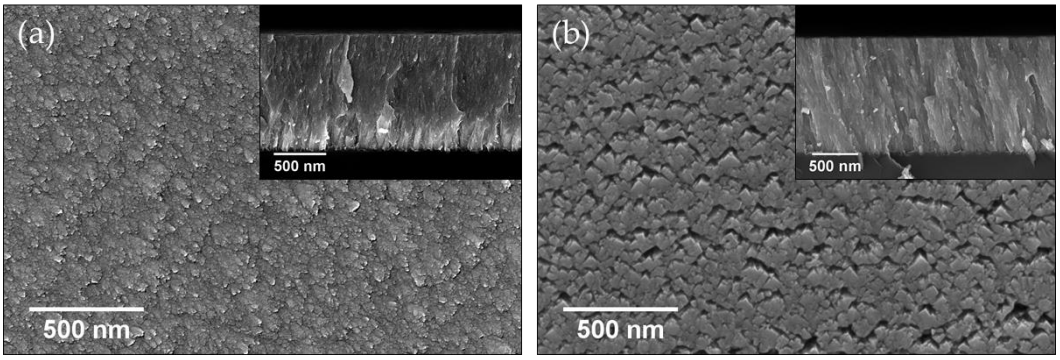

Figure 7-18: SEM images of sample 789 (a), deposited at high cathode power and sample 889(b), deposited at low cathode power. The main images display the surface of the films deposited on Cu and the insets display the cross-sections of the films deposited on the Si witness samples.

This reduction of cathode power also resulted in a noteworthy change in the XRD spectra, shown in Figure 7-19. With the decrease in the cathode power, the peak of highest intensity transitioned from the δ-NbN (200) phase, similar to that shown for the 6% sample in Figure 7-11, to the δ-NbN (111) phase. The FWHM of both peaks also reduced considerably, indicating an increase in crystallite size.

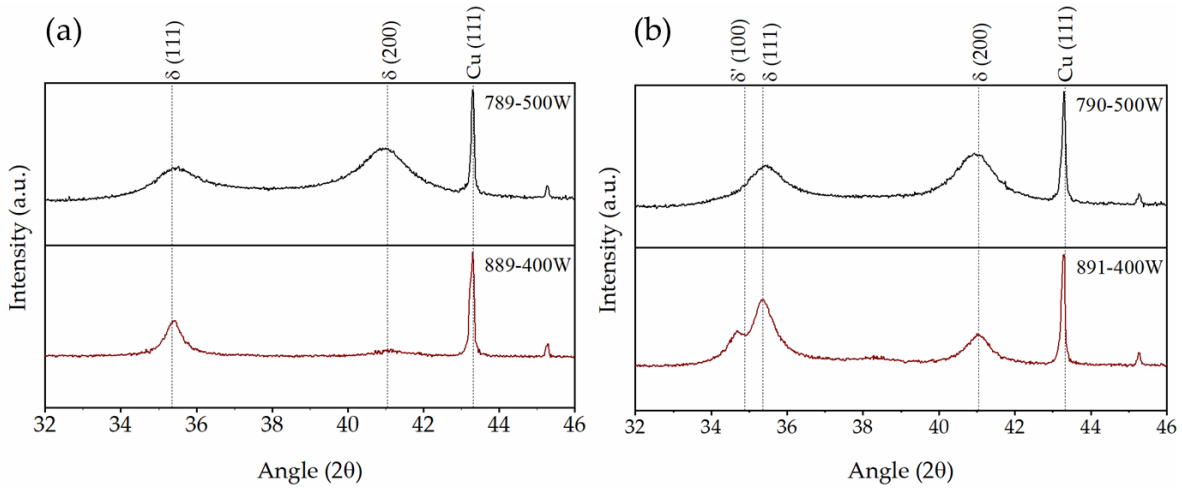

Figure 7-19: XRD patterns of (a) Samples 789 and 889 deposited with 6% N_2 at 500 and 400 W cathode power. (b) Samples 790 and 891 deposited with 8% N_2 at 500 and 400 W cathode power. The spectra are plotted in log scale and were normalised to Cu (111).

This points to an increased surface diffusion at lower cathode power, facilitating larger crystallite growth. Furthermore, the hexagonal δ'-NbN phase is now identified in sample 891, deposited with 8% N_2, which points to an interplay between cathode power, deposition pressure and N_2% in relation to NbN phase formation. This phase transition also resulted in an increase in the transition temperature of the samples deposited at lower cathode power, as shown in Table 7-5.

Table 7-5: Transition temperature change of optimised samples deposited at different cathode power levels.

N_2%	Transition Temperature (K)	
	High Cathode Power	**Low Cathode Power**
6	6.9	10
8	11.75	14

Of the final optimised samples, the three best performing samples: 897, 898 and 899, are now presented. Sample 897 was coated at a lower cathode power (400 W), an intermediate deposition pressure (1.2 x 10^{-2} mbar) and a 20°C higher substrate temperature of 290°C. This was in an attempt to produce the columnar film found at higher deposition pressures while increasing the film density by enhancing the mobility and surface diffusion of adatoms. A lower N_2 content of 8 % was also used to decrease the likelihood of the formation of any non-superconducting hexagonal phases. Similarly, samples 898 and 899 were both coated at 8 % N_2 and a substrate temperature of 290°C. A high cathode power (500 W) and a higher deposition pressure (1.4 x 10^{-2} mbar) were also used with these samples. Finally, sample 899 was deposited with a 75 V substrate bias to further increase surface diffusion and thereby film density. The deposition parameters of these samples, along with their superconducting test and surface roughness results are summarised in Table 7-6.

Table 7-6: Deposition parameters, superconducting test results and AFM surface roughness results for the three highest T_c, optimised NbN thin film samples.

Sample	T_s **(°C)**	p_{dep} **(mbar)**	N_2 **%**	U_B **(V)**	P_{cath} **(W)**	H_{en} **(mT)**	T_c **(K)**	S_q **(nm)**
897	290	1.2 x 10^{-2}	8	0	400	2.0	15.9	6.36 ± 0.42
898	290	1.4 x 10^{-2}	8	0	500	2.0	15.4	7.39 ± 2.34
899	290	1.4 x 10^{-2}	8	75	500	5.0	16.1	14.05 ± 2.32

The microstructure of 899, displayed in Figure 7-20, is similar to that shown for the high deposition pressure sample in Figure 7-14 and is representative of both 897, and 898 as well.

The general columnar nature of the structure has been maintained while the film density has been improved over the previous high-pressure sample. Even though sample 899 was deposited with an applied substrate bias, the lower portion of the grains still present a feather like structure, evident in (c), leading to voids between the columns in this region. The SAED image inset presents a far more spot-like pattern than previous samples. This structure also indicates a cubic orientation of the grains.

All samples possess a faceted grain peak, again similar to that seen in Figure 7-14 (d), homogeneously deposited across the sample surface. AFM analysis indicates a low RMS surface roughness for all samples, with values of 6.36 ± 0.42, 7.39 ± 2.34 and 14.05 ± 2.32 nm for samples 897, 898 and 899 respectively.

The EDX mapping of sample 899, displayed in (d), indicates no evidence of Ar or C contamination within the NbN film. The noise in the vacuum is a quantification artefact. There is slight evidence of O contamination within the film positioned between the columnar grains. The O and C at the vacuum-sample interface probably originates from some remaining sputtered epoxy.

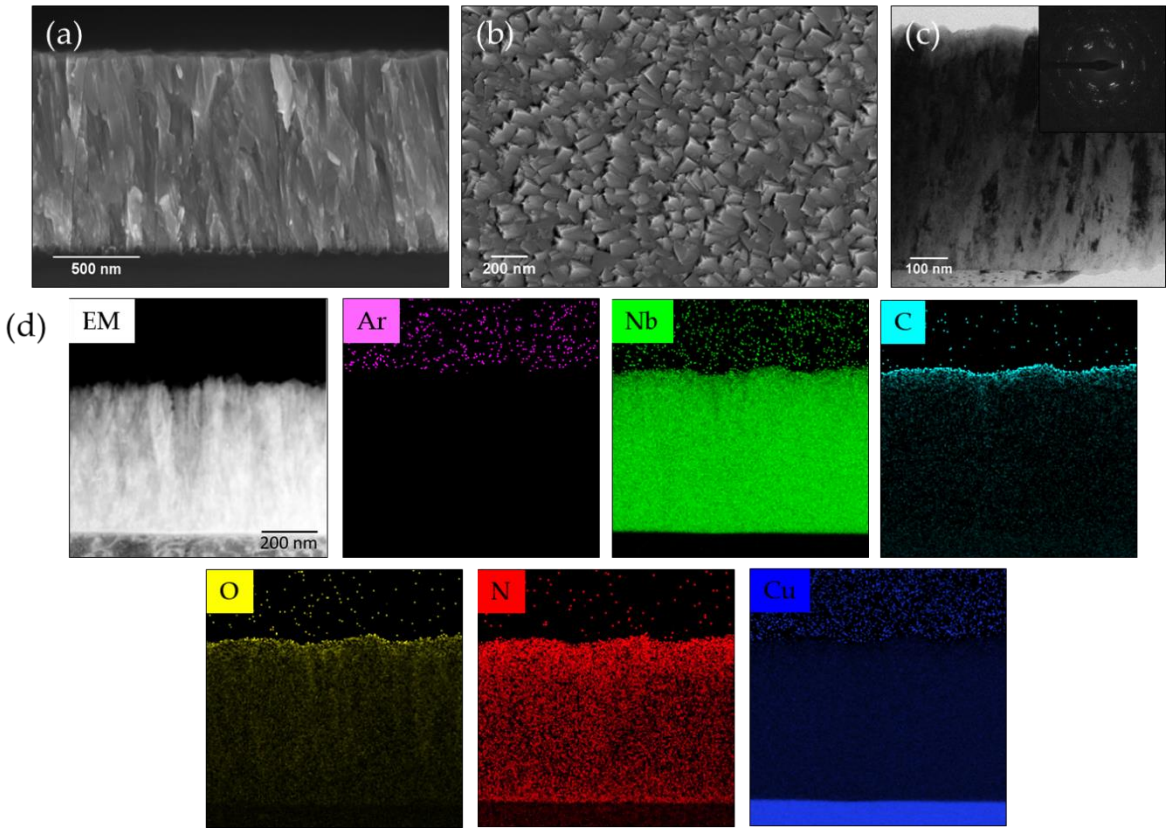

Figure 7-20: SEM, TEM and STEM images of the best performing sample, 899. (a) The cross-section of the film deposited on Si. (b) Surface of the film deposited on Cu. (c) BF TEM cross-section image of the film as well as SAED image of the same film (inset). (d) STEM-EDX mapping of sample 899.

The XRD scans of the optimised samples, presented in Figure 7-21, indicate a general δ-NbN (111) orientation for the samples. Samples 897 and 899 also display a very low presence of δ'-NbN. The lattice parameter of the samples remains around the value for bulk NbN (4.396, 4.397, 4.395 Å for 897,898 and 899 respectively) while the average crystallite size of the samples has further increased to 26.55, 32.15 and 26.46 nm for sample 897,898 and 899 respectively.

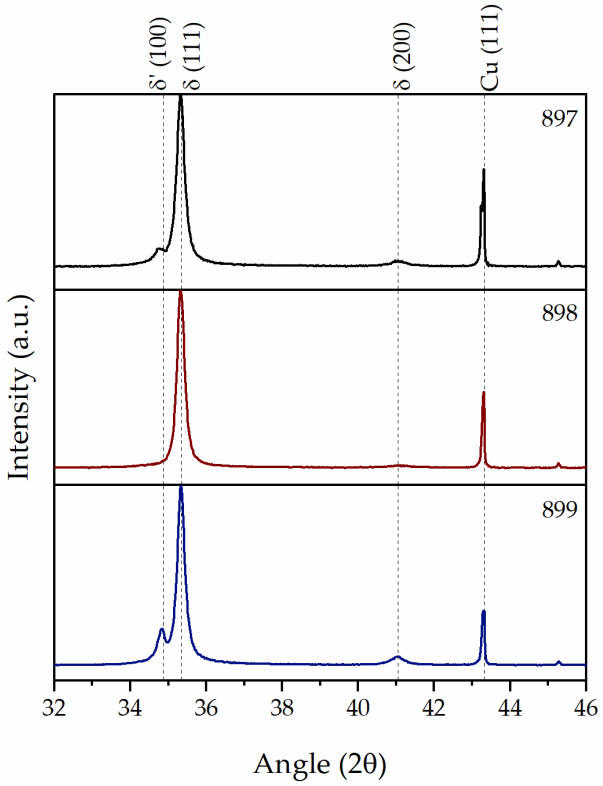

Figure 7-21: XRD spectra of the three optimised samples (normalised to δ-NbN). The spectra are plotted in log scale.

Based on initial VSM measurements, these three samples displayed the highest critical temperatures of all DC MS-deposited NbN samples. For a more accurate assessment, they were also measured in the AC susceptometer option of the PPMS. The measured m_{re} (T) curves, normalised to the m_{re} value at the low temperature plateau, are displayed in Figure 7-22. The changes in the deposition parameters for these three samples culminated in the highest critical temperature (T_c = 16.1 K) of all the DC MS NbN samples for sample 899 while sample 897 and 898 still displayed a T_c > 15 K. The presence of the secondary hexagonal δ'-NbN phase in the highest T_c films is similar to what was observed in the deposition pressure samples and previously by Anderson *et al* [116]. Sample 899 also displayed the highest H_{en} = 5.0 mT for the optimised samples, believed to be due to the increased density provided

by the use of substrate bias. The rest of the optimised samples displayed an average T_c ~ 14 – 15 K.

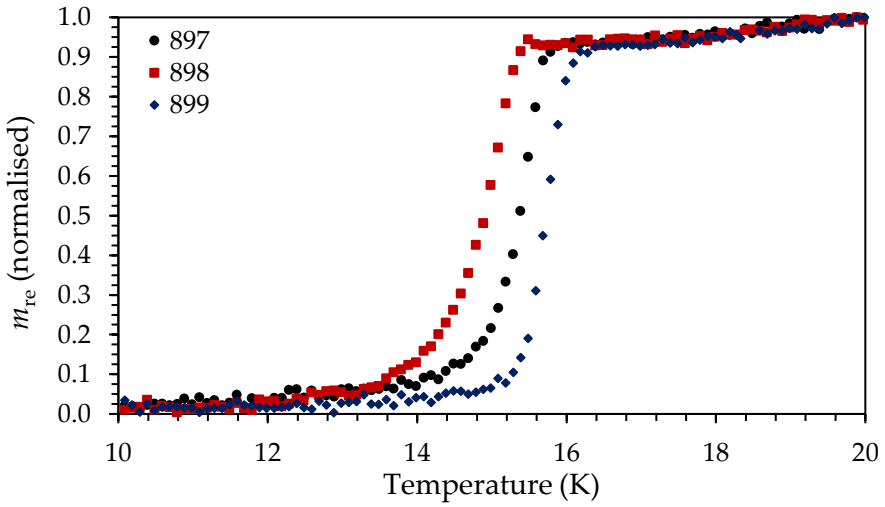

Figure 7-22: Normalised real portion of the AC susceptometry results indicating the critical temperature of the three optimised DC MS NbN samples.

7.3 Reactive High Power Impulse Magnetron Sputtering (R-HiPIMS) NbN Thin Films on Copper

Following the completion of the first series of SIS films, detailed in Chapters 9.2 and 9.3, it is evident that a shielding layer with a high entry field value is required for superior superconducting performance. Based on the results from Chapter 7.2, it is clear that this requires a dense film. The use of HiPIMS deposition is reported to lead to a densification of metallic and compound films [250]. Therefore, a series of NbN films were deposited using R-HiPIMS (simply HiPIMS hereafter) in order to improve the density of the film and thereby improve the entry field value of the NbN shielding layer for use in SIS films.

Similar to the tests completed for the HiPIMS Nb films, detailed in Chapter 8.2, the parameter range that allowed for stable plasma conditions, including the N_2 % of the process gas, was determined prior to the start of the HiPIMS NbN investigation. Based on the results of the HiPIMS Nb films, a pulse length of 120 μs and a frequency of 1000 Hz was maintained for all coatings. This results in a duty cycle of 12%, relatively high compared to normal applications. A higher duty cycle has been shown to lead to an increase in the number of metal ions in R-HiPIMS, due to the target surface cleaning and gas rarefaction [170], and therefore a higher deposition rate. The substrates used during these studies were 1 mm thick OFHC Cu samples with dimensions of 25 x 25 mm^2, as well as pieces of Si (100) wafer, which were used as witness samples. The preparation of the substrates and the coating chamber was as described in Chapters 5.7 and 6.1 respectively.

Following the results for the optimisation of NbN films with DC MS, four deposition parameters were focused on; cathode power, deposition pressure, nitrogen percentage and substrate bias. The parameter ranges explored in this study are detailed in Table 7-7 and the complete list of coatings is shown in Appendix A.3. Due to the changing deposition parameters, the film thicknesses in this study ranged from 0.68 to 1.91 μm, with deposition rates ranging from to 14.62 to 53.63 μm/min. As a result of the higher deposition pressure often used, the peak power values observed for many of these NbN films were similar to those observed for the pure Nb films, detailed in Chapter 8.2.

Table 7-7: Deposition Parameters used during the HiPIMS NbN study and the values thereof.

Parameter	Value
Cathode Power (Average)	300 to 600 W
Cathode Power (Peak)	4.26 to 8.86 kW
Substrate Temperature	180°C
Deposition Pressure	1.2×10^{-2} to 2.4×10^{-2} mbar
Nitrogen Percentage	5 to 22 %
Substrate Bias	0 to 100 V

Due to the interplay between the different deposition parameters, the studies were structured in a staggered formation. As such, the results will be presented in terms of the characterisation technique used instead of the deposition parameter changed.

7.3.1 Waveform Analysis

During the coating processes, the HiPIMS waveforms were monitored using an oscilloscope attached to the HiPIMS cathode. The variations in the waveforms with changing cathode power and deposition pressure are similar to those detailed for HiPIMS Nb films in Chapter 8.2, and are not presented here. Due to the variations in the cathode voltage because of the changing N_2 %, a significant change in the peak current was recorded. This is documented in Figure 7-23 for deposition at 400 W and 2.2×10^{-2} mbar. Evidently, the shape of the peaks is relatively consistent with changing N_2 % and is similar for further cathode power and deposition pressure values as well. Generally, the peak current decreases with increasing N_2 %, as was shown for DC MS NbN deposition. However, in this instance, it is clear that the 8 % N_2 peak is larger than that of 5 % and the 22 % peak is larger than the 18 % peak. This is attributed to the increased utilisation area of the Nb target due to the significant erosion observed between these coatings, as a result of target aging. A subsequent decrease in the measured cathode voltage is also found and has previously been shown for DC MS NbN

films, where the increased target surface area was said to be akin to an increase in the deposition pressure [125].

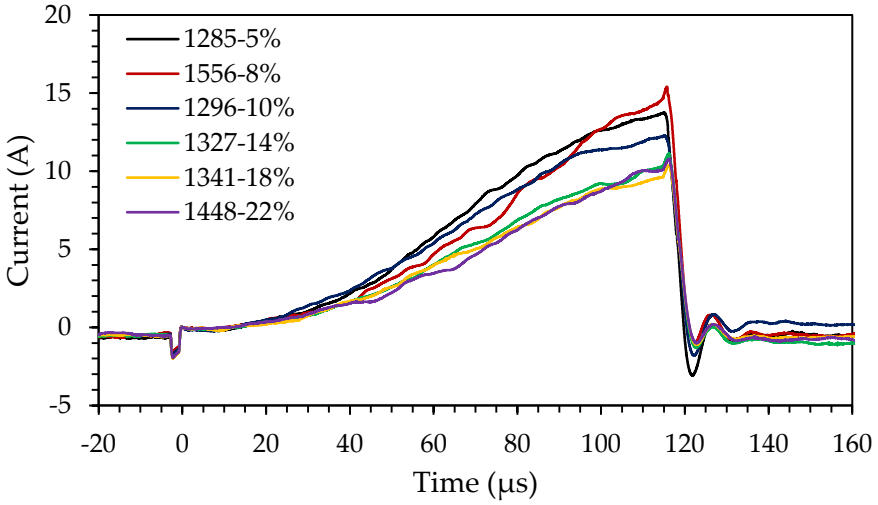

Figure 7-23: Cathode current waveform captured during HiPIMS NbN coatings with different cathode power values.

7.3.2 Microstructural Analysis

Immediately upon removal from the deposition chamber, the samples were imaged using an SEM. At low deposition pressure values, < 1.8 x 10^{-2} mbar, the films deposited onto the Si witness samples were found to buckle because of increased compressive stress. This was present across all cathode power and N_2 % values. Further buckling was also found at high substrate bias values (100 V), for all cathode power and N_2 % values, even though the deposition pressure was increased to 2.2 x 10^{-2} mbar. Importantly, this phenomenon was not found with the films deposited onto the Cu substrates however.

Figure 7-24 presents SEM images of films deposited at 400 W and 10 % N_2 at low and high deposition pressure values. The films deposited onto Cu substrates displayed a similar trend to what was observed for the previous DC MS films detailed in Chapter 7.2.3.3. A low deposition pressure results in a dense film microstructure, albeit significantly more columnar in nature, as shown in (a). The films are topped with a smooth grain peak, resembling either a spherical (b) or an elongated dome (c). This is found regardless of the cathode power or N_2 %. Interestingly, at low deposition pressures, films become increasingly nanocrystalline with increasing cathode power, likely due to the reduced diffusion time. An increase in the deposition pressure results in a slight reduction in the film density, though still largely superior to the high pressure DC MS NbN films, and an increase in the columnar nature of the films, presented in (d). The films also show growth of more faceted features on the film

surface, as evident in (e). Films which were deposited at a low cathode power value (300 W), showed a transition to a more columnar structure with sharper features at lower deposition pressure values while also showing a significantly more disjointed microstructure.

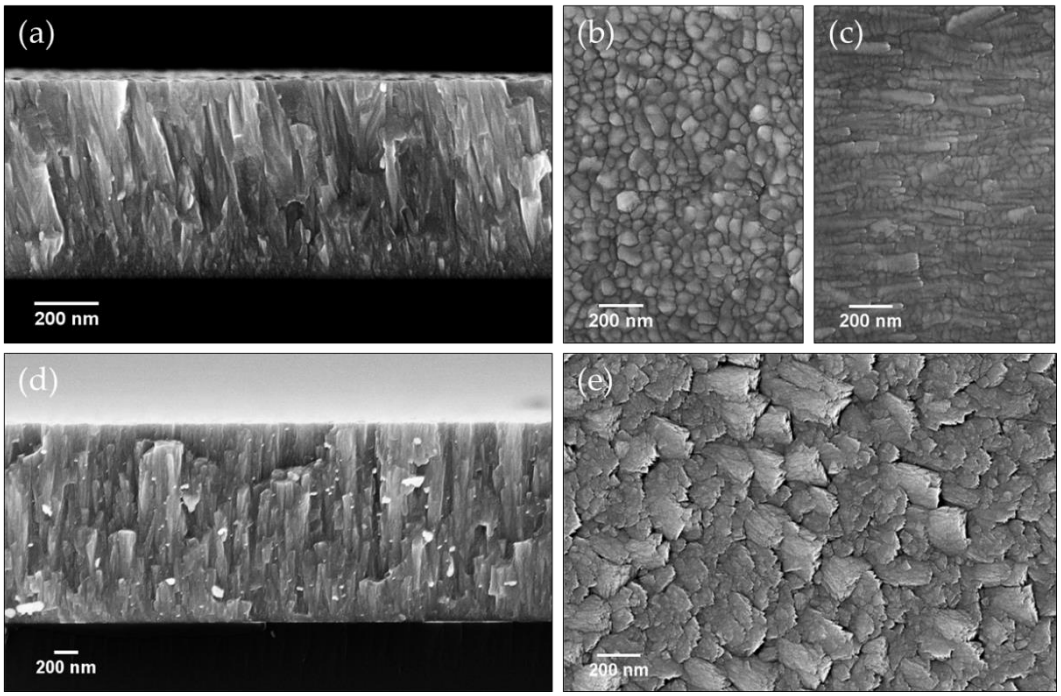

Figure 7-24: SEM images of samples deposited with low (1.4 x 10^{-2} mbar) and high (2.2 x 10^{-2} mbar) deposition pressure at 400 W cathode power and 10 % N_2. (a) The cross-section of the low-pressure film deposited on Si. (b) and (c) Surfaces of the low-pressure film deposited on Cu. (d) the cross-section of the high-pressure film deposited on Si. (e) Surface of the high-pressure film deposited on Cu.

Changes in the substrate bias and the N_2 % also led to further changes in the film microstructure, as presented for films deposited at 400 W and 2.2 x 10^{-2} mbar in Figure 7-25. At 0 V substrate bias (a), the films display a disjointed columnar structure, topped by faceted peaks, resembling either pyramids or stars. Increasing the substrate bias to 100 V (c) leads to an increased density of the deposited film, a shift to a more nanocrystalline growth as well as rounding of the grain peaks. A similar behaviour is observed with an increase in the N_2 %. The density of the deposited films is seen to increase with increasing N_2 %, coupled to a decrease in the lateral grain size. This is detailed for a change from 5 to 22% N_2 in figures (b) and (d) respectively. Note that (b) and (d) were deposited with 50 V substrate bias, with (b) indicating a typical intermediate substrate bias film. Furthermore, the surface features of the film transition from faceted peaks at low N_2 % to rounded features at higher N_2 %. The surface morphology is also less homogeneous at higher N_2 %. This transition is delayed at lower cathode power levels, which show faceted features to a higher N_2 %.

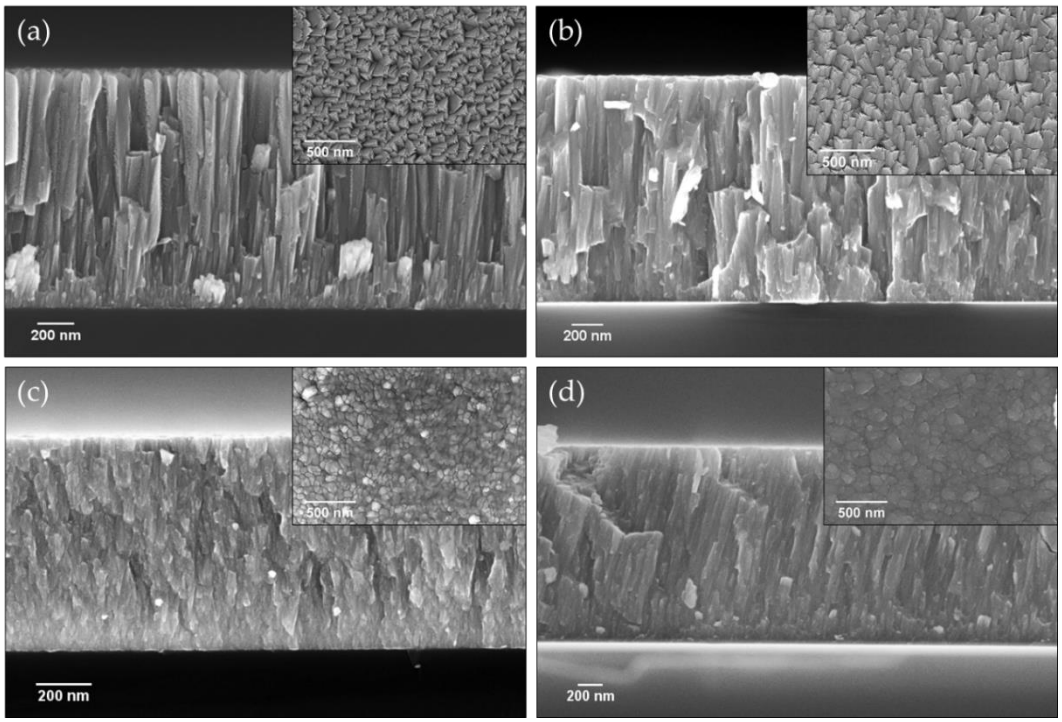

Figure 7-25: SEM images of samples deposited with 400 W cathode power and 2.2 x 10^{-2} mbar deposition pressure with different substrate bias and N_2 %. (a) and (c) denote the cross-section on Si and the surface on Cu of films deposited with 0 and 100 V substrate bias respectively. (b) and (d) denote the cross-section on Si and the surface on Cu of films deposited with N_2 % values of 5 and 22 % respectively.

These microstructural changes were also reflected in the surface topography, as detailed in Figure 7-26, which shows the results of AFM measurements conducted on the films deposited onto Cu substrates. The rounding of the grains with increasing N_2 % leads to a decrease in the surface roughness for both 300 and 400 W cathode power. This decrease is documented in (a), with the trend indicated by a linear fit to the data. This trend is in contrast to that shown by Ding *et al*, who reported an increase in surface roughness with increasing N_2 % [251]. However, in this study, the low target to substrate distance and the high deposition pressure already result in a smaller mean free path. Therefore, changes in the mean free path due to N_2 % changes, and the subsequent change in adatom energy do not play a significant role in surface topography in this study. Furthermore, the changing crystallographic phase associated with increasing N_2 %, presented in Chapter 7.3.3, is more likely to affect the surface microstructure than the mean free path.

It is also evident that samples deposited at lower cathode power values possess rougher surfaces. This is echoed in the results displayed in Figure 7-26 (b), which show an increase in the surface roughness with increasing deposition pressure. Again, films deposited at 300 W display higher surface roughness values. This trend is likely due to the increased crystallite

size observed with lower cathode power values as well as the improved formation of the faceted δ-NbN(111) phase, as determined from XRD measurements.

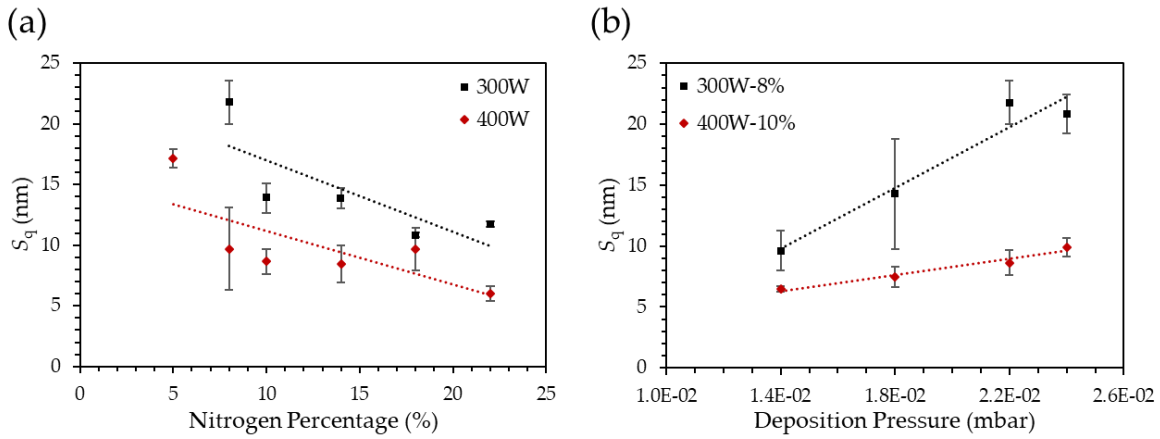

Figure 7-26: RMS surface roughness results as determined with three 5 x 5μm AFM measurements per sample. (a) The change in surface roughness as a function of N_2 %. (b) The change in surface roughness as a function of deposition pressure.

A further decrease in the surface roughness is also observed with increasing substrate bias > 50V. This is evident in the SEM images displayed in Figure 7-25 and is related to the increased energy of ion bombardment during film growth. However, the maximum substrate bias applied here was 100 V, below the value observed to cause film damage during the HiPIMS Nb studies detailed in Chapter 8.2.4. It should be noted that much of the microstructural and therefore topographical morphology changes are determined by the NbN phase formation and not necessarily simply the deposition parameters.

7.3.3 Crystal Structure Analysis

As detailed in Chapter 3.3.3 and reported in Chapter 7, the superconducting properties of NbN films are very dependent on the formation of the correct NbN phase. The results for the DC MS NbN films show that the highest T_c films were characterised by a combination of δ-NbN and δ'-NbN phases. As such, XRD analysis was performed on all samples to determine the effects of the different deposition parameters, so as to focus the study on δ-NbN forming settings.

Similar to the DC MS NbN films, the phase formation of the HiPIMS NbN films displays a significant reliance on the deposition pressure, as presented in Figure 7-27. Regardless of the cathode power or N_2 % used, an increase in the deposition pressure leads to a transition from a hexagonal Nb_5N_6 preferred film to a cubic δ-NbN preferred film. This is generally found at pressures > 2.0 x 10^{-2} mbar. When comparing the effects of the N_2 % and the cathode power,

both a slightly higher N_2 % (10 % used in (b) vs. 8% used in (a)) and a lower cathode power (300 W used in (c) vs 400 W used in (a)) result in transition to a cubic δ-NbN dominated film at lower deposition pressures. Furthermore, the transition to a cubic δ-NbN film also leads to a decrease of the FWHM of the peak of highest relative intensity, indicating an increase in the crystallite size with increasing deposition pressure. This correlates well with the results displayed in the SEM images in Figure 7-24.

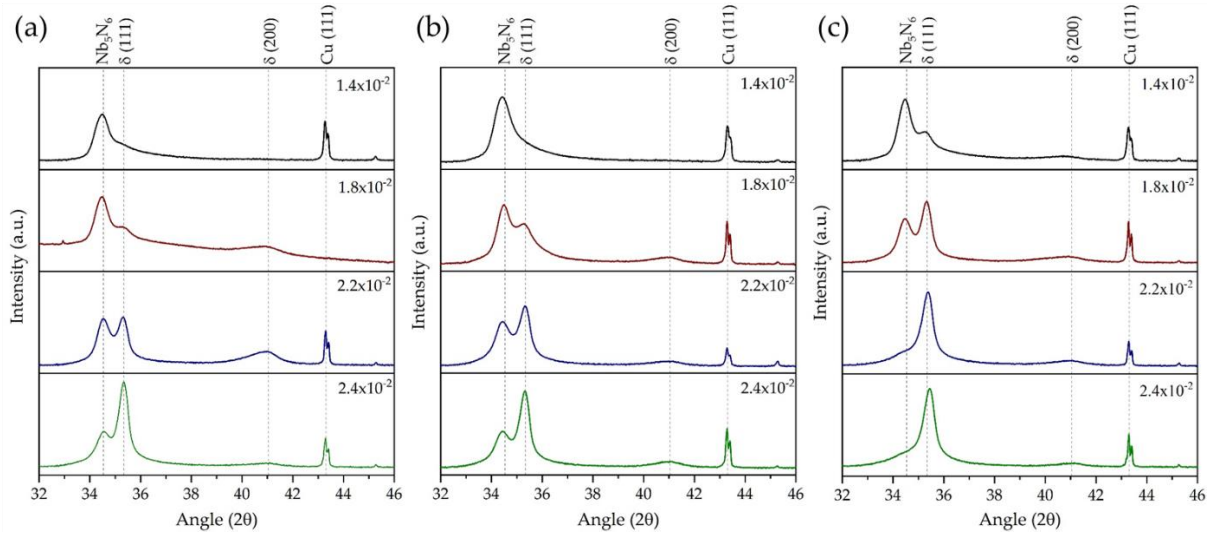

Figure 7-27: XRD patterns of samples deposited at different deposition pressure values, with separate cathode power and N_2 % values. (a) 400 W and 8 % N_2. (b) 400 W and 10 % N_2. (c) 300 W and 8 % N_2. The spectra are plotted in log scale.

The evolution of the lattice parameter and crystallite size for different cathode power and N_2 %, because of changing deposition pressure, is presented in Figure 7-28. The entire plot range lies within the lattice parameter values defined for bulk δ-NbN. For all values of N_2 % and cathode power, the lattice parameter decreases with increasing deposition pressure. On further inspection, films deposited at lower cathode power display smaller lattice parameters for all deposition pressures, likely due to the lower film stress levels because of their more disjointed microstructure, observed in the SEM results. An increase in the N_2 % also results in a slight decrease in the lattice parameter. From these results, a pronounced reliance on the proportion of δ-NbN within the film is also observed. Further to this, an increase in the average crystallite size is observed with increasing deposition pressure, a similar trend to that which was observed for the DC MS NbN films. A lower N_2 % also results in larger crystallite sizes.

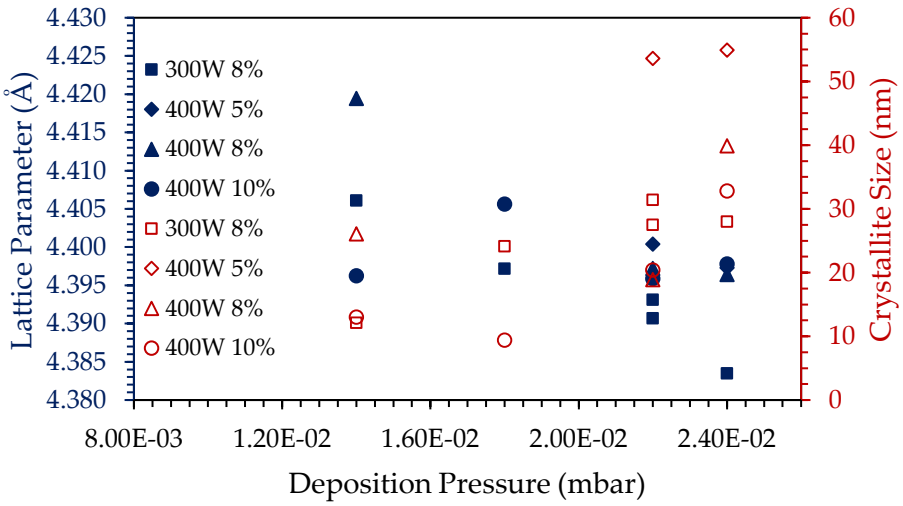

Figure 7-28: Plot detailing the change in the lattice parameter and the δ-NbN (111) crystallite size for HiPIMS NbN films with increasing deposition pressure, deposited with different cathode power and N_2 %.

Figure 7-29 displays the XRD patterns of samples deposited at 300 W cathode power, 8% N_2, 2.2 x 10^{-2} mbar and different substrate bias values. The emergence of a secondary peak at ~ 34.5°, representative of the hexagonal Nb_5N_6 phase, is first apparent as a shoulder at a substrate bias level of 50 V. With a further increase in the substrate bias, the hexagonal phase becomes the dominant NbN phase in the film, with the δ-NbN phase disappearing completely at 100 V. At substrate bias values ≥ 100V, films display a preferred Nb_5N_6 (030) orientation, represented by the peak at 61.84° [246], shown in (a). This phase is not apparent below bias levels of 75 V. The disappearance of the δ-NbN phase was apparent at higher substrate bias values regardless of changes to further deposition parameters.

As seen with the HiPIMS Nb films, increasing the substrate bias for HiPIMS NbN films leads to an ever-increasing lattice parameter value, indicative of an increasing stress state in the film. This reaches a maximum of 4.4229 Å at 75 V, a value greater than the reference values for bulk δ-NbN. Thus, as indicated by the XRD phase analysis, substrate values ≥ 75V result in a complete change in the preferred NbN phase. This is as a result of the increasing shot peening as well as incorporation of process gas species into the growing film. The increased substrate bias is also seen to affect the δ-NbN (111) crystallite size, which shows a marked decrease from ~ 63 nm at 60 V to ~ 11 nm at 75 V, similar to the results presented by Ding *et al* [251]. This was also found in the SEM investigations and is likely related to the impact of high-energy ions, which reduce the likelihood of significant island formation during film growth.

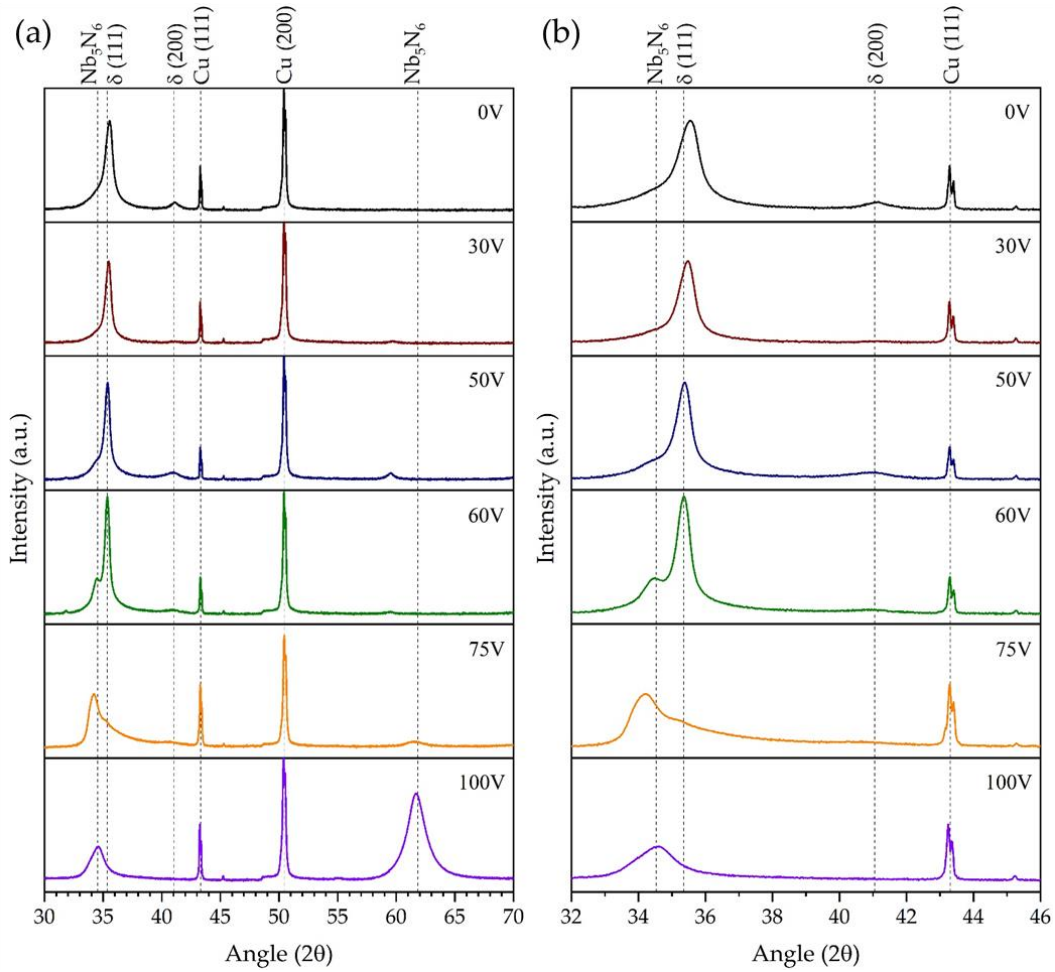

Figure 7-29: XRD patterns of samples deposited at 8 % N_2, 300 W cathode power, 2.2 x 10^{-2} mbar and different substrate bias values. (a) Shows the full measured spectrum while (b) displays the magnified area typically used for phase identification. The spectra are plotted in log scale.

The XRD spectra for samples deposited with increasing N_2 % at 2.2 x 10^{-2} mbar and 300 W as well as 400 W cathode power are displayed in Figure 7-30 (a) and (b) respectively. Both series of samples display a gradual transition from a preferred δ-NbN (111) orientation to a preferred δ-NbN (200) orientation with increasing N_2 %. As showcased in (b), this is more pronounced for the samples deposited at 400 W. This transition is opposite to that which was observed for the DC MS NbN films, which were deposited at a low deposition pressure, and points to an interplay between the sputter rate, deposition rate and mean free path changes as a result of the increased N_2 %. Samples deposited at 300 W, shown in (a), do not display evidence of the hexagonal phase above 10 % N_2, while this peak is still evident until 22 % N_2 for the 400 W samples. The increase in the proportion of cubic δ-NbN, at the expense of the hexagonal phase in the NbN films with increasing N_2 %, is similar to the results obtained for CrN films deposited with HiPIMS [252]. Furthermore, the increasing δ-NbN (200) orientation

preference with increasing N_2 % is in line with results obtained by Ding *et al*, who deposited their NbN films at > 28 % N_2, and displayed a δ-NbN (200) preferred orientation [251].

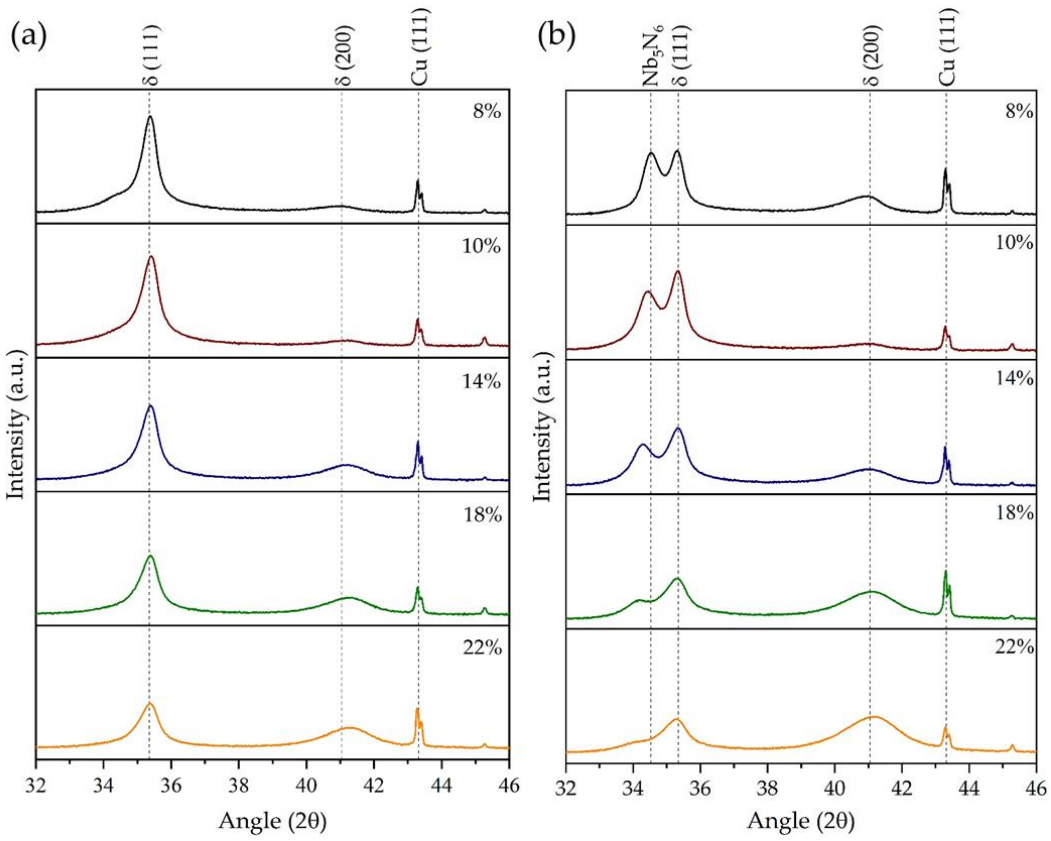

Figure 7-30: XRD patterns of samples deposited at different N_2 % values. The samples were deposited at a constant deposition pressure of 2.2 x 10^{-2} mbar and cathode powers of (a) 300 W and (b) 400 W. The spectra are plotted in log scale.

The lattice parameter and δ-NbN (111) crystallite size, for HiPIMS NbN films deposited at 300 W and 400 W cathode power, as a function of the N_2 % are displayed in Figure 7-31. From first impressions, it is clear that films coated at 300 W consistently display lattice parameters lower than those deposited at 400 W, though all are within the bounds described for δ-NbN. A specific minimum in the lattice parameter values is found in the region of 10 to 15 % N_2 depending on the cathode power. The slightly increased δ-NbN (111) crystallite sizes apparent at 300 W are likely due to the increased surface diffusion time and higher proportion of δ-NbN (111) relative to films deposited at 400 W. However, both series of films display a decreasing δ-NbN (111) crystallite size with increasing N_2 %, likely as a result of the increasing proportion of δ-NbN (200). This again is dissimilar to what was discovered for DC MS films, but is consistent with SEM observations displayed in Figure 7-25.

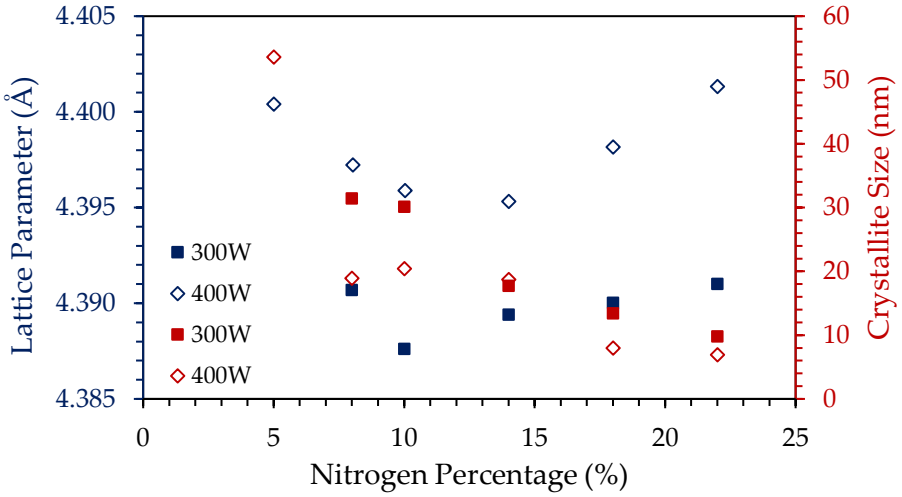

Figure 7-31: Plot detailing the change in the lattice parameter and the δ-NbN (111) crystallite size of HiPIMS NbN films deposited at 300 W and 400 W with increasing N_2 %. LP and CS represent the Lattice Parameter and Crystallite Size data respectively.

7.3.4 Superconducting Performance

The superconducting performance of NbN is very dependent on the formation of the correct stoichiometric phase, which is typically characterised by a specific lattice parameter value. For the sought after δ-NbN phase, this value lies between 4.38 – 4.42 Å, as shown in Table 3-2. The measured transition temperatures of a range of HiPIMS NbN samples, each with separately varied deposition parameters, are related to their respective out-of-plane lattice parameter values in Figure 7-32. A peak in the T_c of the films is visible for a lattice parameter of ~ 4.396 Å. This also correlates with the highest T_c DC MS NbN films. However, there is a definite spread in the results, likely due to the variable amounts of secondary phases brought on by the deposition parameter changes.

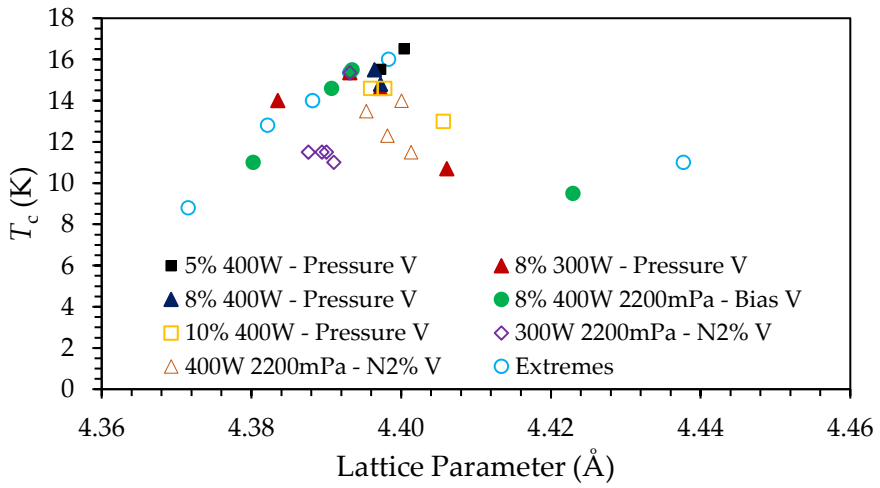

Figure 7-32: Plot detailing the HiPIMS NbN transition temperature as a function of the out-of-plane lattice parameter. The constant deposition parameters are indicated while the specific variable parameter is shown at the end and indicated by a "V".

The relationship between the deposition pressure and the T_c as well as the H_{en}, for a selection of NbN films deposited at 300 and 400 W with lower N_2 %, is detailed in Figure 7-33. Similar to the DC MS NbN films, the HiPIMS NbN films show an increase in the T_c and H_{en} values with increasing deposition pressure. This correlates well with the transition to a more δ-NbN dominated film, as shown in Figure 7-27. Significant maximums are observed at a deposition pressure of 2.2 x 10^{-3} mbar, where the highest T_c of all NbN films of 16.5 K and a relative maximum H_{en} = 28 mT are found. This high H_{en} is more than double that achieved by DC MS, with other samples showing results of similar values. Similar to the DC MS films, the highest T_c sample is also constituted by multiple phases. This takes the form of Nb_5N_6 in the HiPIMS films and displays a significantly higher relative proportion.

The samples deposited with 300 W cathode power show a higher T_c and H_{en} at lower deposition pressures, though the samples deposited at 400 W surpass them at higher deposition pressures. This is due to the improved δ-NbN formation observed at lower cathode powers. Interestingly, the trend in the T_c data is consistent with the trend in the crystallite size data, which is presented in Figure 7-28. In light of these results, a deposition pressure ≥ 2.2 x 10^{-3} mbar and a cathode power of 400 W were utilised for the deposition of further samples and the SIS film coating detailed in Chapter 9.4.

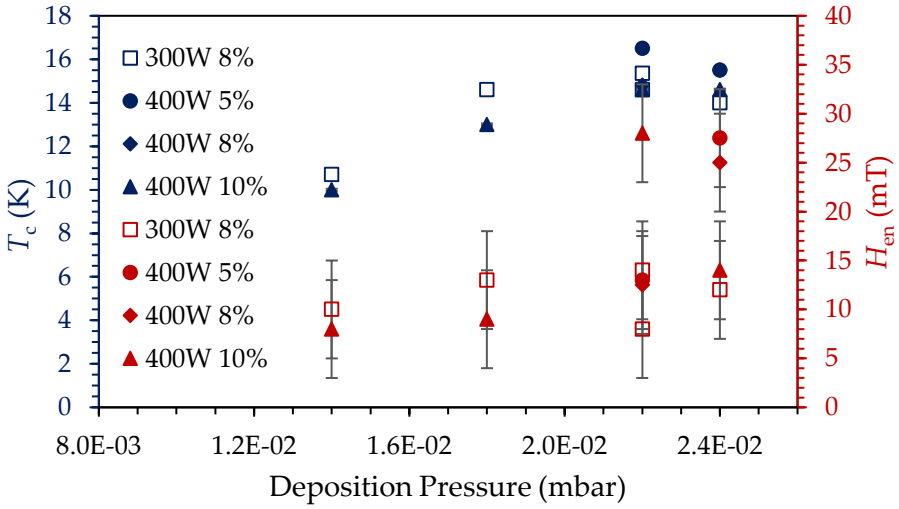

Figure 7-33: Plot detailing the change in the critical temperature and the entry field of HiPIMS NbN samples, in parallel field, with increasing deposition pressure.

As expected from the XRD results in Figure 7-29, samples deposited with a large substrate bias value (> 75 V), showed a significant reduction in superconducting performance. At 75 V, the T_c was below that of Nb (9.2 K), while at 100 V, no superconducting transition was observed down to 4.0 K. This was found even for samples deposited with 300 W cathode

power, which typically results in the preferential formation of the δ-NbN phase. As such, a substrate bias of 50 V was utilised for the remainder of the samples as well as the SIS film coating detailed in Chapter 9.4.

The relationship between the N_2 % and the T_c as well as the H_{en} of the HiPIMS NbN samples is shown in Figure 7-34. Samples deposited at 400 W show a continuous decrease in T_c with increasing N_2 %. This correlates well with the gradual change in preferred orientation of the films, from δ-NbN (111) to δ-NbN (200), observed in Figure 7-30 and is similar to what was observed for the DC MS films. On the other hand, samples deposited at 300 W show an initial decrease in T_c, where after it remains relatively constant to higher N_2 %. Similar to the deposition pressure samples, the T_c increased with increasing crystallite size, as shown in Figure 7-31.

The HiPIMS NbN films showed an initial increase in H_{en} with increasing N_2, a marked jump at 10 % N_2 and a maximum of 30 mT at 14% (400 W), where after it decreased. This is the highest H_{en} value achieved for all NbN films. However, a repeated deposition of this sample showed a significant reduction in H_{en} to 14.3 mT, which is still significantly higher than the values achieved for DC MS-deposited samples. Additionally, deposition at 400 W consistently resulted in better H_{en} values than 300 W. This is likely due to the observed reliance of H_{en} on the lattice parameter, with peak H_{en} values occurring for intermediate lattice parameters. Based on these results, 10% N_2 and 400 W cathode power were selected for use in the SIS film coatings detailed in Chapter 9.4.

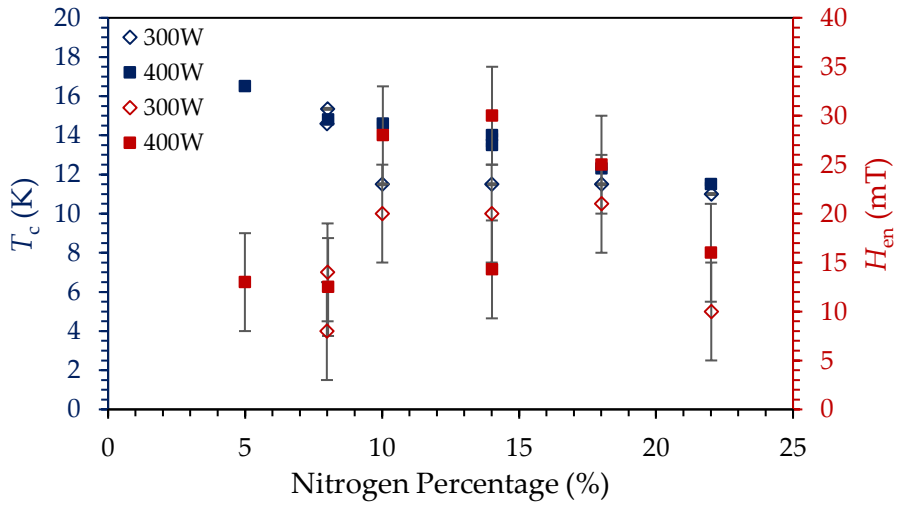

Figure 7-34: Plot detailing the change in the critical temperature and the entry field of HiPIMS NbN samples, in parallel field, with increasing nitrogen percentage.

7.4 Conclusions

DC MS NbN films have been successfully deposited onto Cu substrates, repeatedly achieving $T_c > 15.5$ K. The relationship between the achieved crystallographic phase and the resultant superconducting performances proved to be significant, with the δ-NbN (111) phase leading to higher transition temperature (T_c) values and the δ-NbN (200) phase leading to higher entry field (H_{en}) values. Based on the results, it is evident that a higher deposition pressure and lower cathode power lead to repeatable deposition of the correct NbN phase. The films display epitaxial growth onto Cu substrates with the lattice mismatch accounted for by interfacial dislocations. This resulted in a low level of film stress. Unfortunately, the entry field values achieved for these single layer DC MS NbN films do not lend themselves to use in SRF cavities, as this will result in early flux entry and large energy dissipation. This is largely due to the disjointed, columnar structure that prevails in the majority of DC MS-deposited NbN films. The optimised NbN films are however still applicable in multilayer SIS films. This was examined for both DC MS and HiPIMS Nb base layer samples, the results of which are presented in Chapters 9.2 and 9.3 respectively. The deposition parameters used for these DC MS NbN coatings are detailed in Table 7-8.

Table 7-8: DC MS NbN deposition parameters used for the shielding layer in DC MS Nb and DC MS NbN (Chapter 9.2) as well as HiPIMS Nb and DC MS NbN (Chapter 9.3) SIS films.

SIS Chapter	P_{cath} (Ave) (W)	p_{dep} (mbar)	U_B (V)	N_2 %	T_s (°C)
9.2	400	1.2×10^{-2}	0	8	290
9.3	500	1.4×10^{-2}	75	8	290
9.3	500	8.0×10^{-3}	0	8	270

In light of the results of the DC MS NbN and initial SIS film studies, the deposition of HiPIMS NbN was explored. The results of the study indicate the significant improvements offered by the use of HiPIMS for the deposition of NbN films. Most notably, the density of the films was significantly increased while also reducing their surface roughness. These improvements resulted in a significant increase in the entry field of these films, with most films achieving values more than the previous best obtained with DC MS and the best performing film nearly tripling this value. Many of the HiPIMS NbN films even achieved entry field values larger than the reported H_{c1} of bulk NbN, detailed in Table 3-1. Interestingly, the higher H_{en} values were achieved by films characterised by a δ-NbN (111) phase as opposed to the δ-NbN (200) phase shown in high H_{en} DC MS NbN films.

The increased density also leads to a decrease in impurities, especially O. Similar to the DC MS films, a higher deposition pressure and lower cathode power are more conducive to the formation of the correct δ-NbN phase. Furthermore, the use of a lower substrate bias (< 60 V) is essential, as higher substrate bias values lead to the formation of non-superconducting, hexagonal phases.

The highest measured T_c of NbN on Cu (16.5 K) was also achieved with HiPIMS deposition. However, a general decrease in T_c, compared to the DC MS films, was observed. The improved performance of these HiPIMS NbN films makes them especially applicable to SIS film coatings. As such, a series of SIS film samples were deposited using the best performing HiPIMS NbN film, with the results detailed in Chapter 9.4. The deposition parameters used for this HiPIMS NbN coating are detailed in Table 7-9.

Table 7-9: HiPIMS NbN deposition parameters used for the shielding layer in HiPIMS Nb and HiPIMS NbN SIS films.

P_{cath} (Ave) (W)	p_{dep} (mbar)	PL (μs)	f_{pulse} (Hz)	U_B (V)	N_2 %	T_s (°C)
400	2.2×10^{-2}	120	1000	50	10	180

8. Deposition of Niobium (Nb) Thin films

This chapter will detail the experiments which focused on the deposition of Nb thin films on Cu substrates. Initial experiments investigating the effects of different Cu surface treatments on the performance of Nb thin films were completed using purpose treated QPR samples. One of the QPR samples was further retreated and recoated at CERN with a HiPIMS Nb recipe developed at CERN. Due to the limitations of DC MS Nb thin films and the potential enhancement in Nb thin film performance offered by HiPIMS technology, a large investigation into the effects of individual deposition parameters for Nb thin films deposited by HiPIMS was completed resulting in an optimal deposition parameter set.

8.1 DC MS Nb QPR Samples

As detailed in Chapter 5.6, two Cu-fitted QPR samples (B-2 and B-3), were prepared with two separate Cu surface treatments at INFN Legnaro. These samples were then separately coated with a DC MS Nb thin film to determine their effects on the RF performance of the film. The QPR samples were coated in the same coating setup as detailed in Chapter 6.1. In order to reduce the likelihood of sample contamination, a flow cell was installed around the coating machine, which utilises a continuous laminar airflow across the coating machine entrance, as displayed in Figure 8-1 (a). The samples were positioned on a substrate holder that is situated directly opposite the Nb target, where it is kept stationary during coating, indicated in Figure 8-1 (b). The target-to-substrate distance for the QPR sample was similar to the small samples.

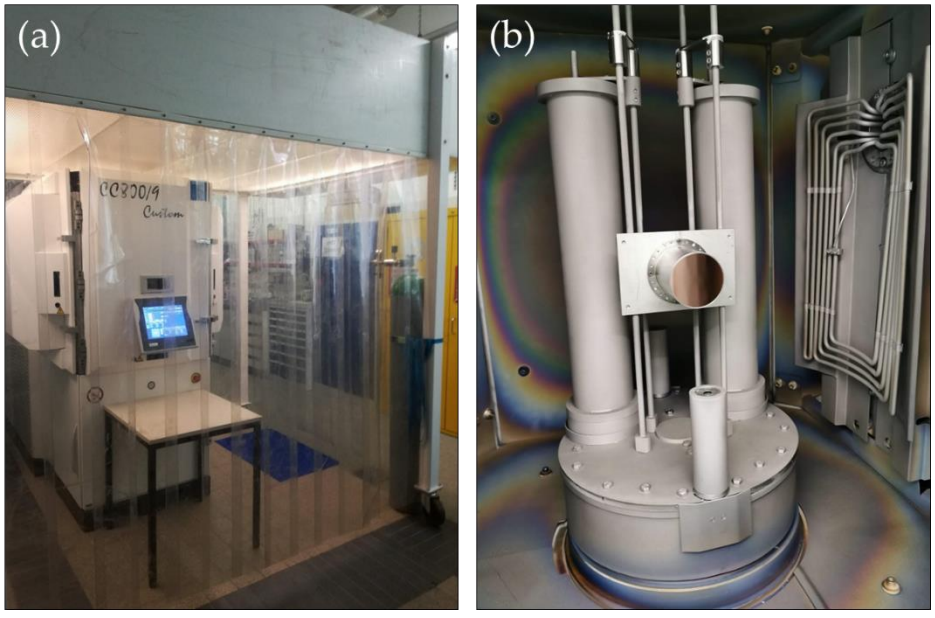

Figure 8-1: Images showing (a) the flow cell installed around the coating machine opening and (b) the QPR sample installed inside coating machine.

Prior to installation, the QPR sample was removed from it transport container and placed directly into the coating chamber, without the use of any gas blow process. The coating preparation procedure used here, consisting of bake-out, target cleaning and etching, was as described for the NbN samples in Chapter 7.2.

The QPR sample was coated with a DC MS Nb film using the parameters detailed in Table 8-1. This process produced a Nb film with a thickness of ~ 2.1 µm, as verified by XRF measurements conducted at CERN. The surface displayed a relatively homogeneous thickness with a maximum variation of 7 %, as shown in Figure 8-2 (a).

Table 8-1: Deposition parameters for the Nb coating of QPR sample B-2.

Parameter	T_s (°C)	p_{dep} (mbar)	P_{cath} (W)	**Process Gas**	U_B (V)
Value	265	8×10^{-3}	400	Argon	0

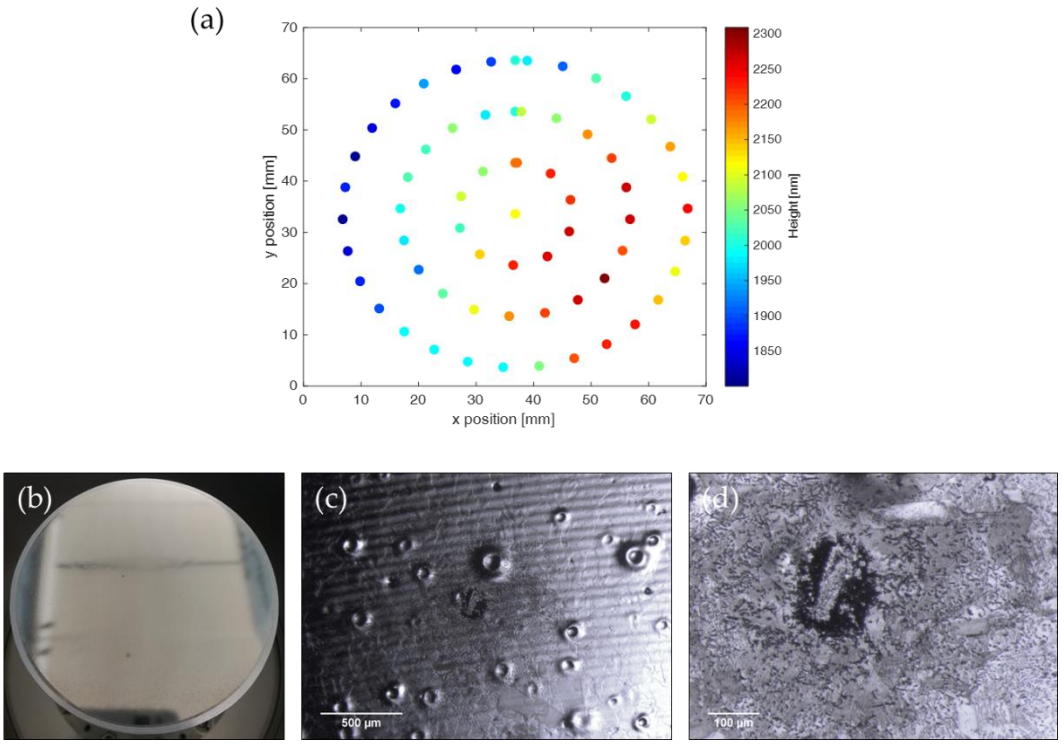

Figure 8-2: Results of analysis of sample B-2. (a) XRF film thickness results of sample. (b) Picture of the QPR sample surface. Some larger spots are visible. (c) Optical microscope image of the QPR surface indicating pitting and dust incorporation. (d)Magnified image of dust particle which has been processed and exploded on the surface.

Initial visual inspection of the surface of sample B-2 showed evidence of some dust incorporation into the film during coating in the form of "spots" on the surface, shown in Figure 8-2 (b). This was examined further with an optical microscope, which confirmed the presence of contamination within the film as well as surface pitting originating from the

SUBU5 preparation process. The magnified image, presented in Figure 8-2 (d), shows that an incorporated dust particle has most likely "exploded" during the RF testing phase as a result of processing. The incorporation of dust into the film is believed to have played a part in the poor superconducting results obtained from testing at HZB. The sample displayed a residual resistance of ~ 95 nΩ at 415 MHz, with further increase in the residual resistance with field. Further results and analyses are presented in [253], with an excerpt from the results displayed in Figure 5-14 in Chapter 5.6.

Following testing at HZB, the sample was sent to CERN for a second Nb coating using a HiPIMS process developed by CERN. The initial coating was stripped from the sample surface where after it was again treated with SUBU5, to mimic the initial SUBU5 treatment this sample received, thereby allowing comparison between the two coatings. The sample was then prepared with a High Pressure Rinse (HPR), blow dried with N_2 and loaded into the coating system in a clean room along with four, SUBU-treated Cu witness samples.

The coating system itself, shown in Figure 8-3, allows for simultaneous deposition of two separate sample holders positioned on opposite sides of a cylindrical Nb target. Prior to deposition, the chamber was baked out at 200°C for 48 hrs. A Residual Gas Analyser (RGA) was utilised to monitor the cleanliness of the vacuum. The sample was then coated for 6 hrs, resulting in a 7.3 μm thick film, as measured on the witness samples by XRF.

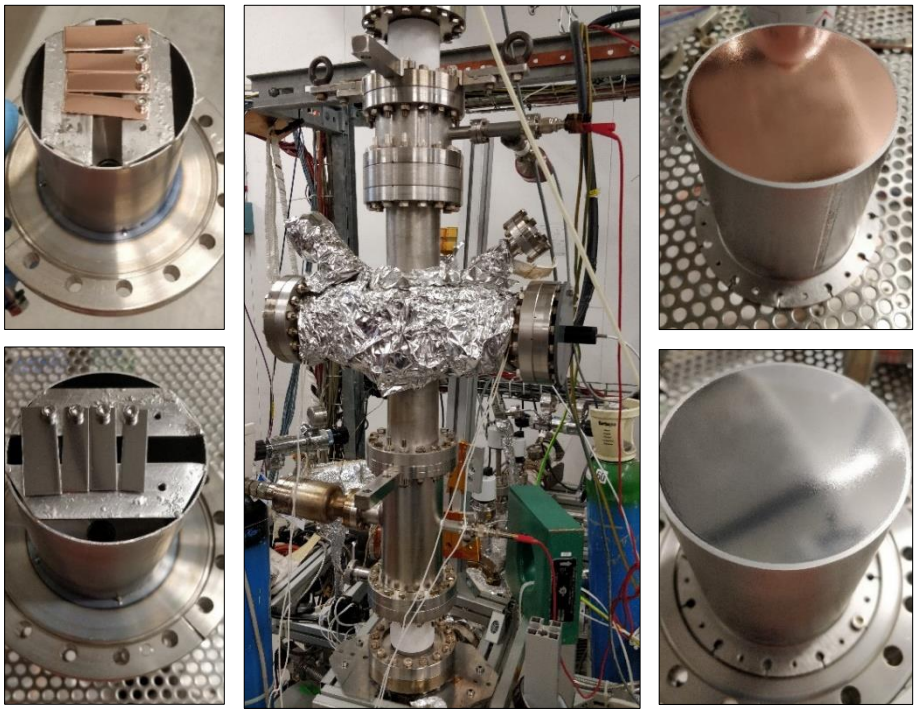

Figure 8-3: QPR deposition system used at CERN. Witness samples before (top) and after (bot) coating displayed on the left and the QPR sample before (top) and after (bot) coating displayed on the right.

A series of investigations on the witness samples were conducted to better understand the reasons for the RF performance. Three AFM scans, 20 x 20 μm² in size, were completed on one of the witness samples, resulting in an average RMS surface roughness of S_q = 50.05 ± 2.24 nm. A representative 3D AFM image of the sample surface is displayed in Figure 8-4 (a). This value is relatively high, likely due to the thickness of the film as well as the use of SUBU5 for the Cu preparation. The roughness is also seen to be a function of the specific scan location as the film surface presents multiple different grain structures, as indicated in the SEM image of Figure 8-4 (b).

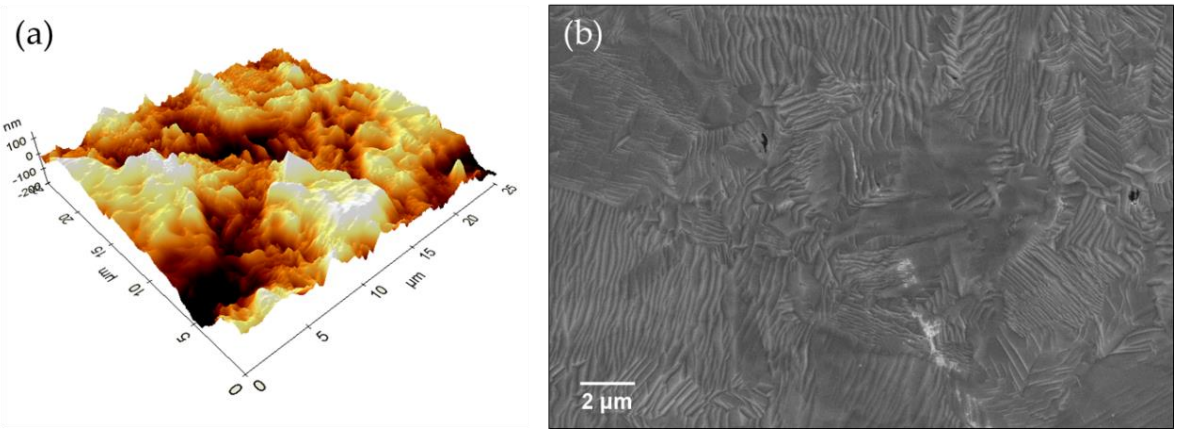

Figure 8-4: Surface analysis results for sample B-2 witness samples. (a) Representative 3D AFM scan result. (b) SEM image of the sample surface.

One of the witness samples was also tested in the VSM at IEE. Results show a T_c = 9.22 K, transition width of ΔT_c = 0.25 K and an entry field of H_{en} = 50.5 ± 2.53 mT, when measured in parallel field configuration. The crystal structure of the film was examined with XRD, the results of which are shown in Figure 8-5 (a). The Bragg-Brentano scan indicates a polycrystalline film with a Nb (110) preferred orientation for the film, as determined by the 38.49° peak, with an average crystallite size of 76 nm.

The texture of the film was also investigated using XRD pole figures in stereographic projection. The {110} Nb pole figure was recorded and the result is presented in Figure 8-5 (b). The result further indicates the (110) preferred orientation of the Nb film and is typical of Nb films deposited at low temperatures [67]. The sharp central spot and the spot-like pattern on the 60° ring indicates a restricted fibre in-plane texture of the film.

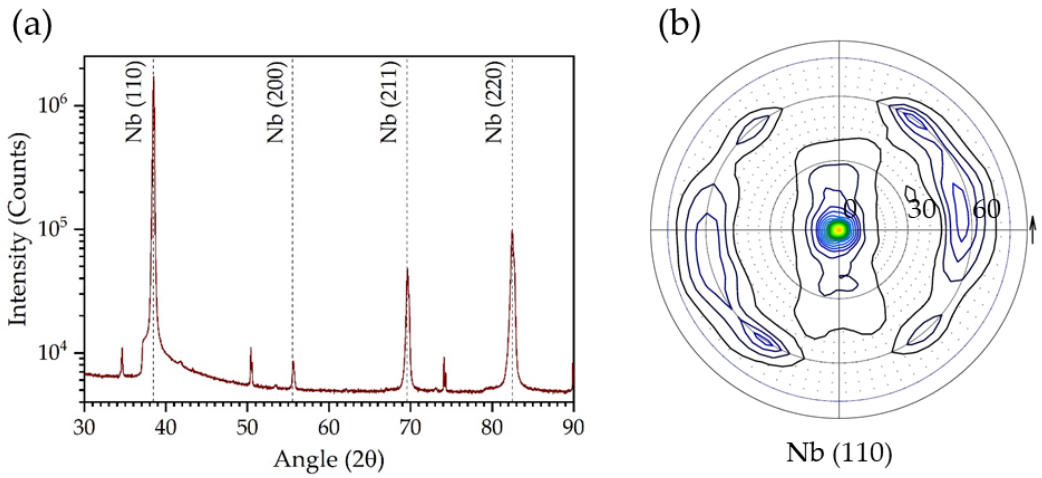

Figure 8-5: (a) Bragg-Brentano scan of a HiPIMS Nb witness sample coated during the recoating of QPR sample B-2 at CERN. (b) (110) Nb XRD pole figure of the same witness sample.

Following the results and lessons learned from the coating of sample B-2, the coating procedure for sample B-3 was adjusted slightly. Prior to installation into the coating machine, the sample surface was blown with ionised nitrogen gas, to ensure the removal of all dust particles. Based on analysis of further small samples coated in between the two QPR samples, it was discovered that the previous Nb ion etching process could result in the deposition of a Nb interlayer between the substrate and the final coating, serving as the seed layer for further growth of the film. In order to avoid this, the etching process was changed to an MF etching process, which proved successful in pre-trials. During the coating of preparatory samples, the presence of voids at the interface between the Cu substrate and the Nb film was found. Evidence of this is provided in Figure 8-6, which shows a FIB cut completed in a pre-trial coating of DC MS Nb film onto a Cu substrate. According to the thermal boundary resistance model, the presence of voids at the interface leads to localised heating and increased surface resistance [49].

In order to avoid this, a HiPIMS Nb interlayer was deliberately deposited with a thickness of ~ 200 nm, following successful pre-trials. The coating parameters used to deposit the film on the interlayer were identical to those of sample B-2, as displayed in Table 8-1. These changes led to a visual improvement in the deposited Nb film. Sample B-3 also showed improved superconducting performance compared to sample B-2, with a residual surface resistance value of 40 nΩ, less than half the value achieved previously. Further results and a detailed analysis are presented in [253], with an excerpt of the results displayed in Figure 5-14 in Chapter 5.6.

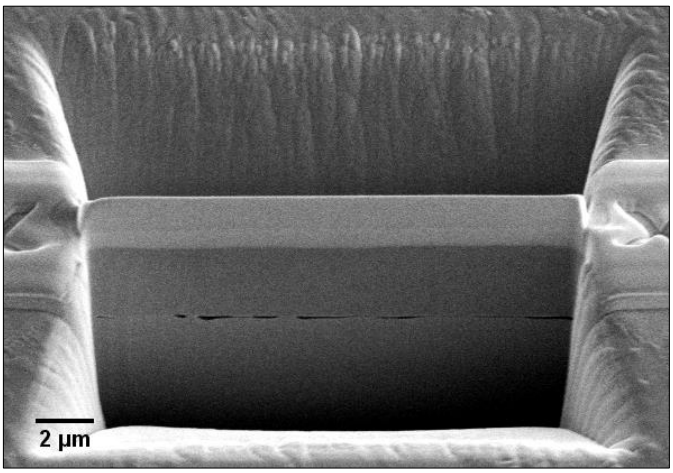

Figure 8-6: SEM images displaying a FIB cut used to investigate the interface between the DC MS Nb layer and Cu substrate during pre-testing for the deposition of QPR B-3.

8.2 HiPIMS Nb Thin Films

One of the main results originating from the DC MS coated SIS films, presented in Chapter 9.2, is that the underlying Nb film is of utmost importance in terms of the superconducting performance of SIS films deposited on Cu. The presence of voids at the Nb/Cu interface as well as the surface roughness of the Nb film have a significant impact on the superconducting performance of the SIS films. Therefore, given the improvements offered by using a HiPIMS coating process [81], a large study into the deposition of HiPIMS Nb thin films onto Cu substrates was completed.

The substrates used during these studies were 1 mm thick OFHC Cu samples with dimensions of 25 x 25 mm^2, as well as pieces of Si (100) wafer, which were used as witness samples. The Cu substrates were prepared using the final optimised surface treatment methodology detailed in Chapter 5.7, using a combination of mechanical polishing and electropolishing. Prior to deposition, the system, including the substrates, was passively baked at 290°C for 6 hrs, allowing the chamber to reach a base pressure of 6 x 10^{-7} mbar at the required substrate deposition temperature. Following this, the substrates were subjected to a medium frequency (MF) etching process for 10 min, as a final surface treatment, and the Nb target was sputter cleaned for 10 min to ensure all possible contaminants were removed.

Prior to the start of the HiPIMS Nb investigation, a series of tests were completed to determine the parameter range that allowed for stable plasma conditions. This was accomplished by monitoring the plasma through a sight glass, and by monitoring the cathode waveform output with an oscilloscope. The testing proceeded as follows: The cathode power and deposition pressure were set to a specific set point. Following plasma stabilisation, the pulse length was reduced in steps of 20 µs from the maximum of 200 µs, while maintaining

a set frequency, down to the pulse length where the plasma was no longer stable. This process was repeated for different frequency values, from the maximum (2000 Hz) down to the minimum frequency that still resulted in a stable plasma, in steps of 200 Hz. The same process was then repeated for a series of cathode power values (300 to 600 W) and deposition pressure values (6×10^{-3} to 1.2×10^{-2} mbar). Based on the initial results, any pressure value higher than this was deemed able to sustain a stable plasma. An example of the test results is displayed in Appendix A.5 for a cathode power of 300 W, a frequency of 1000 Hz and a series of different deposition pressure values. In this case, the minimum pulse length value resulting in a stable plasma, for all deposition pressures tested, was 80 μs. This minimum was found to change with the age of the target, decreasing as the target aged. Ar gas was used at all times as it resulted in a wider range of stable plasma conditions.

Typical HiPIMS deposition processes utilise a low duty cycle value, in the region of 1 – 10 % [4][84][87][254]. However, the system used here was unable to maintain a stable plasma across a series of different deposition parameters at a duty cycle lower than 8 %, other than for specific parameter combinations. For this reason, the bulk of the testing completed in this study was at a duty cycle of 10 %, but ranged between 2 – 20 %. The parameter ranges explored in this study are detailed in Table 8-2.

Table 8-2: Deposition parameters adjusted during the HiPIMS Nb study and the values thereof.

Parameter	Value
Cathode Power	300 to 600 W
Deposition Pressure	8×10^{-3} to 1.8×10^{-2} mbar
HiPIMS Pulse Length	80 to 200 μs
HiPIMS Pulse Frequency	800 to 2000 Hz
Duty Cycle (Calculated)	8 to 20 %
Substrate Bias (DC)	0 to 250 V
Substrate Temperature	115 to 290 °C
Film Thickness.	0.91 to 8.10 μm

For most of this work, only one parameter was adjusted per experimental series. This resulted in a specific "base" coating setting displayed in Table 8-3. Unless otherwise specified, film thicknesses were maintained > 2.5 μm, in order to allow for better comparability of superconducting testing results. A DC substrate bias was used for all coatings.

Table 8-3: Base HiPIMS Nb thin film deposition parameters.

P_{cath} (W)	p_{dep} (mbar)	PL (μs)	f_{pulse} (Hz)	U_B (V)	T_s (°C)
400	8×10^{-3}	100	1000	50	180

8.2.1 General Observations

Changing the deposition parameters was found to have a relatively insignificant impact on the Nb film grain morphology and texture. As such, a "typical" Nb film surface is presented and discussed here, while any significant changes due to specific deposition parameter changes will be detailed in the upcoming sections. It is evident from the SEM images in Figure 8-7 (a) and (b) that the Nb film grows with a multitude of different grain structures. Some of these have been identified previously and are present here, such as (b-3) which is reported to represent the Nb (110) grain growth [255]. However, the previous identification is not exhaustive as the research was completed on singly oriented Cu substrates and not polycrystalline substrates as in this study.

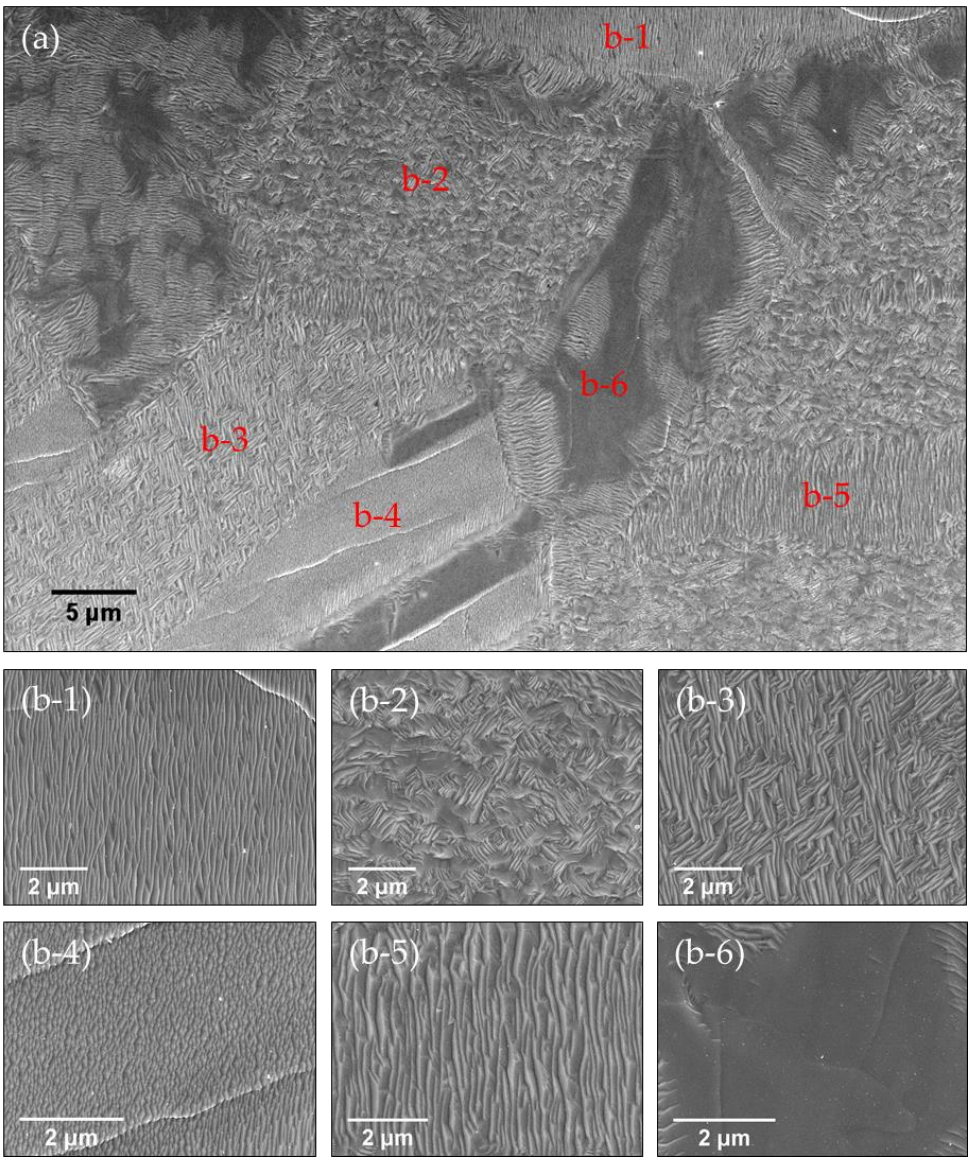

Figure 8-7: Indicative images of the general grain structure of a HiPIMS Nb film surface deposited on Cu. (a) SEM image of multi-grain region. (b) Magnified images of demarcated grain structures.

Due to the different grain structures present on the film surface, the Nb grain size is also dependent on the specific grain structure, varying from 10's to 100's of nm. Moreover, because of these different grain structures, the surface roughness of the Nb films is often an average of the different grain structures present in each measurement. Therefore, in order to capture as many grain structures as possible per scan, the size of the AFM surface measurements were increased to 20 x 20 μm^2. This is shown by the indicative 2D and 3D AFM scans in Figure 8-8 (a) and (b) respectively. An important note is the effect of the step height between different Cu grains, which becomes evident in the overgrown Nb film. This is best visualised in Figure 8-8 (b). These steps led to an increase in the measured surface roughness value. However, these features are present in all samples and were therefore not explicitly accounted for. Efforts were made to measure the roughness of the same individual grain structure on each separate sample, in order to obtain a better idea of the changes in surface roughness brought about by different deposition parameters while also considerably reducing the effects of the step-edge grain boundaries in the surface roughness measurements. When comparing films deposited at equal deposition pressure and similar average cathode power values, the use of HiPIMS resulted in a decrease in the RMS surface roughness of the Nb films compared to DC MS-deposited films, from 16.91 ± 0.93 (DC MS) to 11.19 ± 0.26 nm (HiPIMS). Further developments of the surface roughness due to deposition parameter changes will be detailed in the upcoming chapters.

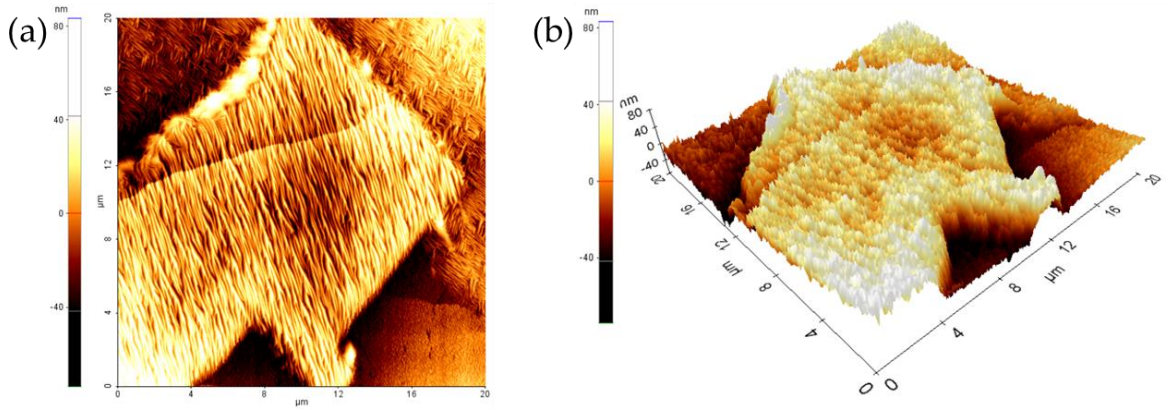

Figure 8-8: Indicative (a) 2D and (b) 3D AFM image of the same position indicating the different surface roughness of each grain structure and the influence of the step edge between different underlying Cu grains.

The purported improved interface between Nb and Cu due to HiPIMS deposition was also investigated. A series of samples were investigated using FIB cuts as well as Ar^+ ion cross-section polishing to compare the presence of voids at the interface to the previous DC MS Nb

coatings. Due to the time consuming nature of these sorts of measurements, around 15 samples have been analysed. From these results, a reduction in interfacial voids of ~ 85 % has been achieved using HiPIMS, based on the number of positions imaged that possess voids. This is indicated in Figure 8-9, which displays two representative images of the Nb/Cu interface, obtained with (a) a FIB cut and (b) Ar^+ ion cross-section polishing, for two separate Nb films deposited with HiPIMS. This is a significant improvement compared to the DC MS Nb film detailed in Figure 8-6, and should decrease the impact of the thermal contact resistance [49]. Also evident in Figure 8-9 is the change in the Nb grain structure across the Cu grain boundary, pointing to a significant influence of the Cu substrate.

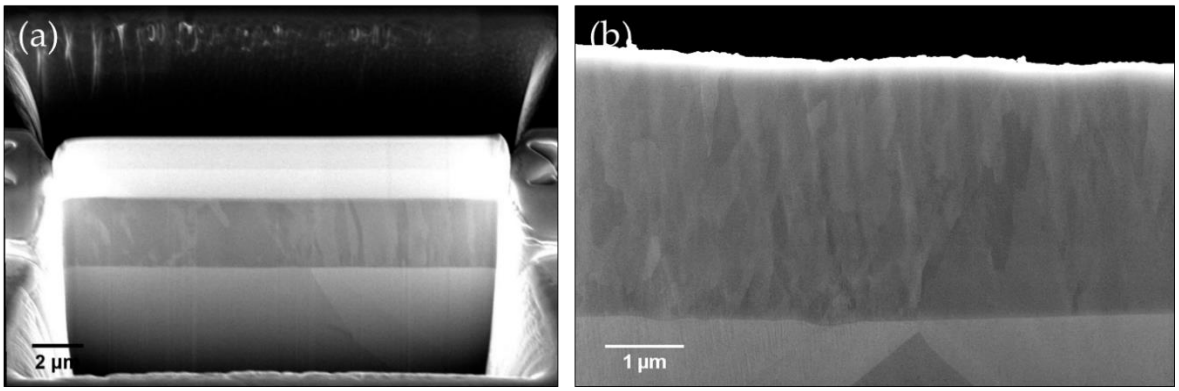

Figure 8-9: SEM images of the Nb/Cu interface obtained with (a) a FIB cut of the "base" HiPIMS Nb sample and (b) Ar^+ ion cross-section polishing of the best performing HiPIMS Nb sample.

The Bragg-Brentano (BB) XRD spectrum of the base Nb film, with intensity plotted in log scale, is displayed in Figure 8-10 as an example of all Nb samples. The XRD spectra of all Nb samples display a peak position shifted to lower angles compared to the unstressed bulk Nb reference positions [256]. This is indicative of a compressive in-plane stress state in all films, leading to an increase in the out-of-plane lattice parameter. In typical DC MS systems, or more specifically, systems which are used with a substrate at ground potential, this is as a result of the bombardment of the deposited film surface by energetic neutral atoms of the process gas [175]. In this study however, the compressive stress arises due to the bombardment of the film surface by energetic process gas and target ions, because of the applied substrate bias, as well as the difference between the thermal expansion coefficient of Cu (18.9×10^{-6}) and Nb (7.8×10^{-6}). Additionally, all Nb peaks, besides that pertaining to Nb (110) at $2\theta = 38.42°$, also displayed a marked decrease in their relative intensities with respect to the relevant reference data [256]. Based on this, the Nb films can be, qualitatively, said to be polycrystalline in nature, with a preferred (110) orientation. The shoulder evident in all scans is due to the *Kα2* radiation.

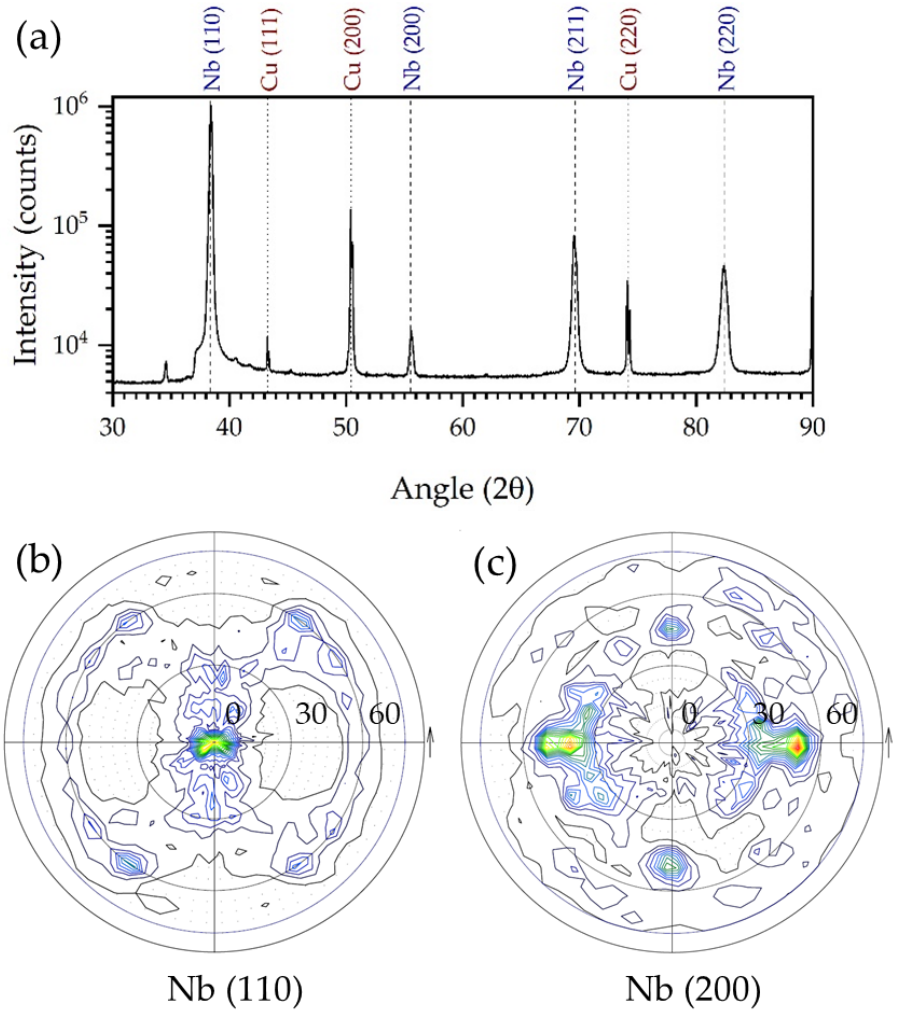

Figure 8-10: (a) XRD spectra of the "base" HiPIMS Nb film deposited on polycrystalline Cu displayed in log scale. Background corrected pole figures of the base HiPIMS Nb sample for (b) the (110) orientation and (c) the (200) orientation.

In light of the orientation preference displayed in the Bragg-Brentano scans, a series of pole figure (PF) and EBSD investigations were undertaken to better understand the texture of the Nb film as well as the orientation relationship between the Cu substrate and the Nb film. The pole figures of the Cu substrate, presented previously in Figure 5-19, are similar to those captured for all coated samples as well and are therefore not repeated here. The pole figures, presented in Figure 8-10, represent the (b) Nb {110} and (c) Nb {200} orientations, situated at diffraction angles of $2\theta = 38.42°$ and 55.58° respectively, obtained from the Bragg-Brentano scan shown in (a). Due to the penetration depth of x-rays in Nb [221], these results represent the crystal structure averaged across the entire sample thickness.

The {110} pole figure displays an intense central spot with further satellite spots around the 60° ring. These spots create a ring of modulated intensity in the azimuthal direction, pointing to a restricted fibre texture film, tending towards a monocrystalline film [257]. This is also

indicative of the presence of in-plane texture in the films. The 60° separation between the central spot and the satellite spots is due to the separation between the (110) and (101) planes in body-centred cubic (BCC) crystals. The {200} pole figure presents a further restricted spot pattern, with the spots situated at 45°, providing further evidence for a restricted fibre texture. This angle is due to the normal angle of 45° between the (110) and (200) planes. Here the {200} pole figure is used because the structure factor of the {100} diffraction is zero.

The obtained Nb (110)/Cu (100) orientation relationship is typical for both DC MS [221] and energetically deposited Nb films on Cu (100) substrates [67][258]. Moreover, this is the typical out-of-plane orientation for BCC materials [248]. However, the production of in-plane texture in the Nb films is believed to be due to the use of energetic deposition techniques, such as HiPIMS (this study), or ECR ([67][258]). The change has previously been shown for Ion-Beam-Assisted Deposition (IBAD) of Nb films [259]. In that study, the DC MS-deposited films displayed an azimuthally uniform intensity on the 60° ring, while those deposited with IBAD, showed four distinct intensity maxima on the 60° ring, similar to what has been shown here. Therefore, the use of such energetic deposition techniques allows for the preferential growth of specifically oriented Nb films. The above results were similar for all series of films, beside those deposited with higher levels of substrate bias, which will be detailed in Chapter 8.2.4.

In line with the pole figure texture investigations, a series of samples were investigated with EBSD. For complete understanding, both the cross-section and the surface of the films were analysed. As mentioned previously, EBSD analysis details the top 50 - 100 nm of a sample and is therefore far more sensitive to changes in orientation. The Orientation Index Maps (OIMs) and Inverse Pole Figure (IPFs) of two separate sample sets are presented in Figure 8-11. Image (a) and (b) pertain to the surfaces of the Cu substrate (before deposition) and the Nb film (after deposition) of sample 1, while (c) and (d) pertain to the same of sample 4. The Cu analysis recorded an average CI of 0.82 while the Nb achieved 0.79. As evident in (b) and (d), and consistent with the XRD results, there is no specific preferential growth direction in these films. Instead, the films are polycrystalline in nature with some positions showing a preferred (110) growth, such as (b). This is further indicated by the corresponding IPFs. This result is in line with work completed by other authors [260][261].

Spradlin *et al* previously showed that there is a specific epitaxial relationship between Nb and Cu when the Nb film is deposited onto Cu single crystals, specifically; Nb (110)/Cu (100), Nb (110)/Cu (111) and Nb (100)/Cu (110) [258]. In light of this, studies were completed to determine whether these same epitaxial relationships were present in Nb films when deposited onto polycrystalline Cu substrates. Four separate samples were prepared with

analyses performed on the surface of each sample before (plain Cu) and after deposition (Nb film). Based on Figure 8-11, there appears to be no overarching epitaxial relationship between the Cu substrate grain orientations and the resulting Nb film surface. Furthermore, the grain boundaries in the Nb films do not necessarily match with the underlying Cu, indicating expansion and overgrowth of the deposited Nb film. Therefore, due to the thickness of the films (> 2 μm), it is probable that the interfacial epitaxial relationship between Nb and Cu is not accurately represented at the film surface.

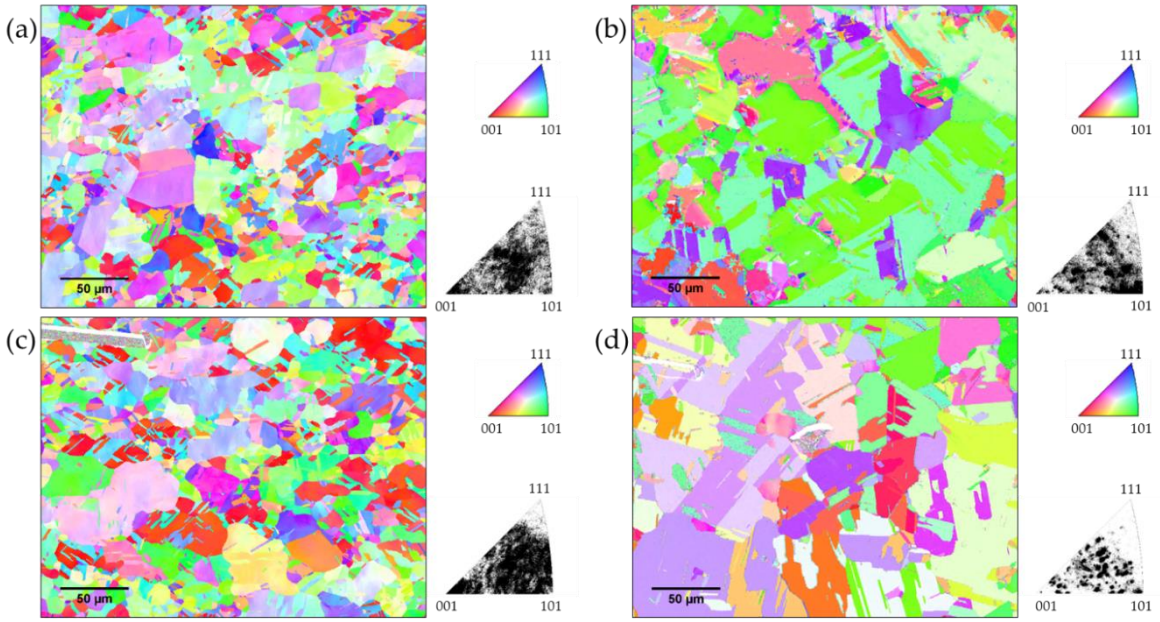

Figure 8-11: EBSD Orientation Index Maps (OIMs) and the corresponding Inverse Pole Figures (IPFs) of The Cu substrate surface prior to deposition. (b) and (d) the Nb film surface in the same position.

In order to better understand the growth of the Nb films, a series of sample cross-sections were imaged with EBSD. Two examples of the results obtained from the best performing sample (1077), which have not been post-processed, and one from the thickest grown film (1078) are presented in Figure 8-12. The different scales should be noted. The growth of this Nb film shows a marked reliance on the orientation of the underlying Cu substrate, as shown previously by Wilde [262]. In position (a), the film presents typical Zone T film growth, with the grain size increasing with increasing film thickness, resulting in the loss of the Cu substrate topography on the surface of the film, as detailed in Figure 8-11. This also follows the proposed selective growth model, whereby grains with different crystal orientations have different growth rates based on their thermodynamic potentials [263]. On the other hand, position (b) indicates the possibility for an individual grain to grow through the entire thickness of the film, resulting in grain sizes on the order of micrometres. Finally, position (c)

indicates the possibility to have two dissimilar growth modes on a singly oriented Cu grain, with large grain formation and competitive growth both apparent here, further decreasing the likelihood of the overgrown Nb film replicating the grain boundary layout of the underlying Cu substrate. Images (a) and (c) also indicate an apparent transition zone present in the Nb films, where the interfacial grains are significantly smaller than those at the film surface. This concept will be expanded upon in Chapter 8.2.7.

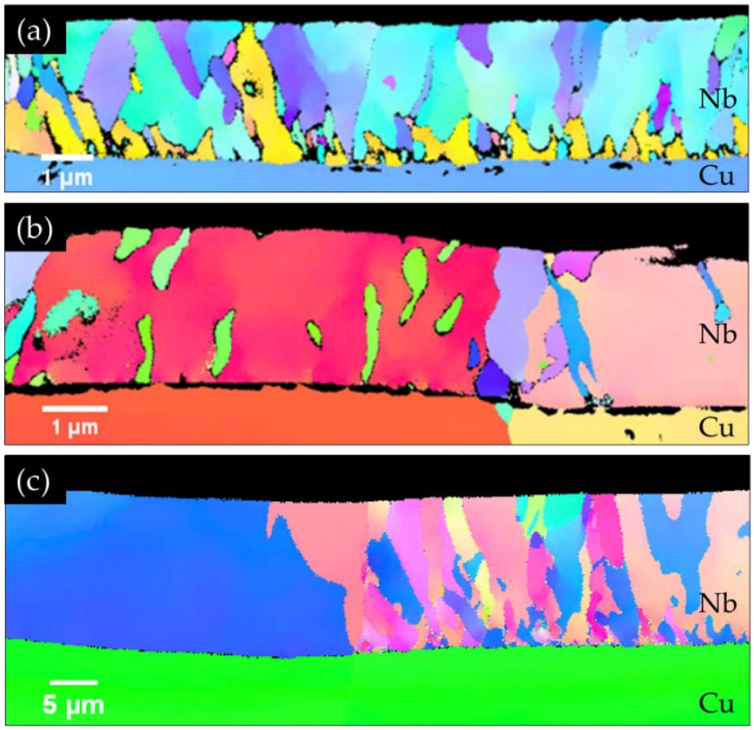

Figure 8-12: EBSD OIMs of the cross-section of the best performing HiPIMS Nb film displaying two separate positions which show (a) selective growth through the thickness and (b) Individual grain growth through the thickness. (c) Further EBSD OIM of the thickest Nb film sample displaying two separate grain growth phenomena on a single Cu grain.

Further to this, EBSD was used to try to identify the orientation of the different grain structures presented in Figure 8-7, whose nomenclature is repeated here. An SEM image of the investigated position is shown in Figure 8-13 (a). The OIM image in (b) displays the resulting orientations of the different grain structures. Grain structures b-1, b-4 and b-5 show instances of Nb (110) orientation; however, this varies and these same structures display other orientations as well. Therefore, it appears likely that each specific grain structure is not characterised by a single orientation and is instead dependent on the particular growth of that grain. This points to the effects of the underlying Cu grain, as detailed in Figure 8-12. This is further verified when investigating grains of type b-3. Previous authors have

identified this as Nb (110) [255], however in this investigation, the same grain structure is characterised by multiple orientations.

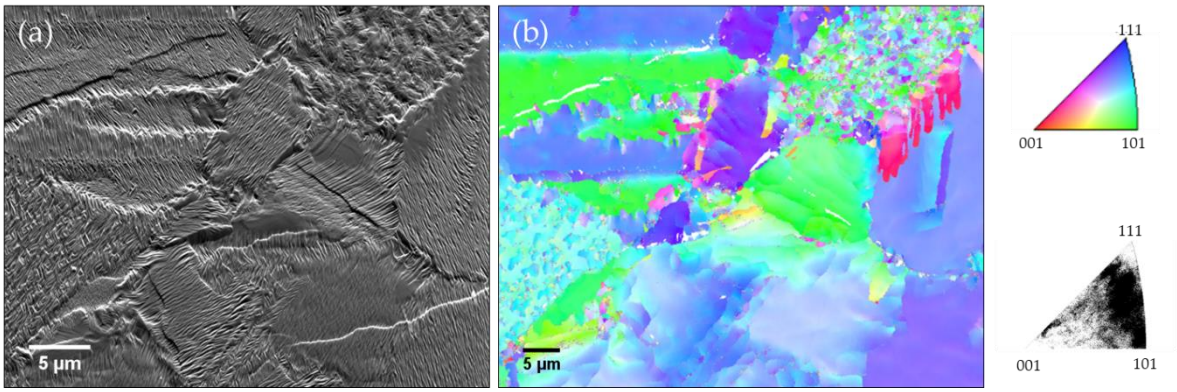

Figure 8-13: (a) SEM image of the magnified surface investigated for potential grain structure-orientation relationships. (b) OIM image of the same area.

The following sections will detail any specific changes found in the Nb films as a result of the individual deposition parameter in question. The changes are typically related to crystallographic or superconducting performance changes.

8.2.2 The Effects of Cathode Power

HiPIMS Nb films were deposited with the base setting detailed in Table 8-3, while the average cathode power was varied between 300 and 600 W, resulting in an average power density between 3.4 and 6.8 W/cm^2. The results of surface and crystallographic analysis techniques are summarised in Table 8-4.

Table 8-4: Selection of characterisation results for the HiPIMS Nb films deposited with different cathode power values.

P_{cath} (W)	C_{peak} (A)	P_{peak} (kW)	t_{film} (µm)	r_{dep} (nm/min)	a_0 (Å)	L (nm)	S_q (nm)
300	15.57	5.84	2.70	43.53	3.3110	105.1	8.71 ± 0.67
400	18.13	7.32	2.69	48.82	3.3117	116.6	11.19 ± 0.26
500	21.84	9.19	4.72	76.08	3.3116	107.2	17.07 ± 2.85
600	22.47	10.13	5.45	87.82	3.3093	129.7	17.61 ± 1.60

During the deposition process, the waveforms of the cathode power supply were captured using an oscilloscope, which allows for interpretation of the peak current, voltage and power of the HiPIMS pulses. The peak power position corresponds to the position of peak current during the pulse. The captured current waveform for this series is displayed in Figure 8-14. As expected, the peak current increases with an increase in the average power setting, from

15.57 to 22.47 A at 300 and 600 W respectively. This corresponds to a peak power of 5.84 and 10.13 kW respectively. Interestingly, the time delay (time from the start of the pulse to the peak current position) also decreases with an increase in the cathode power, and subsequent increase in the cathode voltage. This is attributed to the higher average energies of the impacting particles, leading to a change in the ionisation efficiency of the gas and target species at higher voltages [264]. The increase in the peak power also leads to an increase in the deposition rate from 43.53 to 87.82 nm/min at 300 and 600 W respectively.

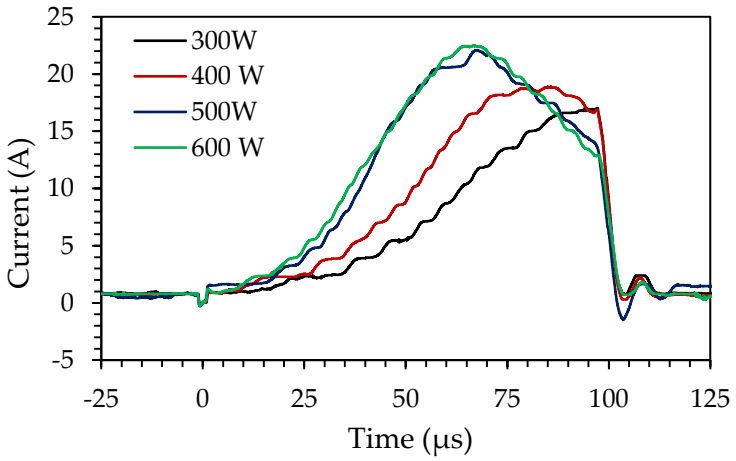

Figure 8-14: Cathode current waveform captured during HiPIMS Nb coatings with different cathode power values.

AFM analysis of these films indicated an increasing film roughness with increasing cathode power levels from 8.71 ± 0.67 at 300 W to 17.61 ± 1.60 nm at 600 W. The cause of this is believed to be two-fold. Firstly, the increased deposition rate at higher cathode power values decreases the time for surface diffusion of adatoms and secondly, an increased film thickness, as seen with the higher cathode power samples, typically results in a greater surface roughness due to the increased grain sizes of thicker films.

XRD analysis of these films showed a (110) preferred orientation for all films with a negative peak shift, as confirmed by the increase in the out-of-plane lattice parameter calculated for these films, shown in Figure 8-15 (a). This is because of a compressive in-plane stress within the films. The lattice parameters of these films were consistent, with a maximum difference of 0.048%, and the most bulk-like lattice parameter at 600 W. The FWHMs of the peaks in these scans, and therefore the average crystallite size of the films, are similar, ranging from 105.1 nm at 300 W to 129.7 nm at 600 W.

Sections of these samples were also measured with a VSM attachment to determine the transition temperature and to obtain the magnetisation loops for each sample. The results of

these measurements are detailed in Table 8-5. The transition temperatures of these samples, measured during cooldown of the VSM attachment and taken as the onset of the change in the magnetic moment, are similar for all cathode power levels. Because of the compressive stress state of the films, the transition temperature, T_c = 9.29 K, is slightly higher than that of bulk Nb, T_c = 9.2 K. The Δ T_c, taken as 80 % of the difference between the onset of change in the magnetic moment and the start of the Meissner state, is also relatively consistent for all cathode power values, presented in Table 8-5.

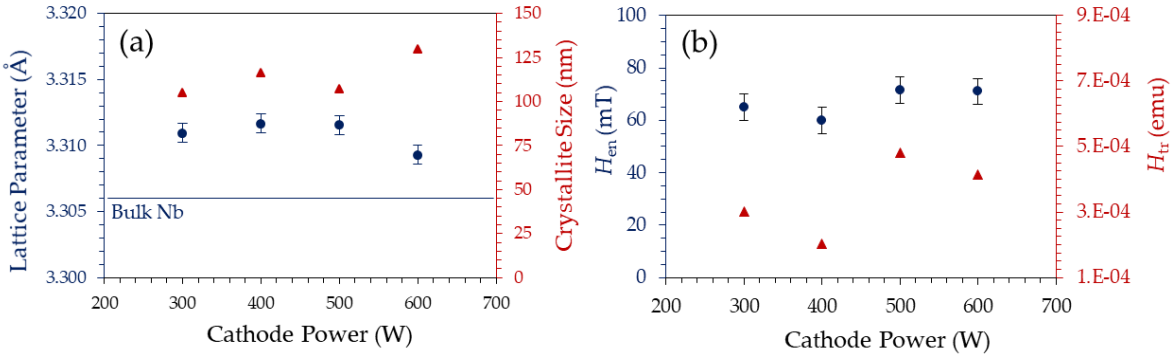

Figure 8-15: (a) Plot detailing the change in the lattice parameter and the average Nb (110) crystallite size of HiPIMS Nb samples deposited with increasing cathode power. (b) Plot detailing the change in the entry field and the trapped flux in parallel field, of HiPIMS Nb samples deposited with increasing cathode power.

Table 8-5: Superconducting characterisation results for HiPIMS Nb samples deposited with different average cathode power values.

P_{cath} (W)	T_c (K)	ΔT_c (K)	H_{en} (mT)	H_{tr} (emu)	H_{Max} (mT)
300	9.25	0.160	65.0 ± 3.25	0.000303	147.8 ± 7.39
400	9.29	0.198	60.0 ± 3.00	0.000203	150.1 ± 7.51
500	9.25	0.161	71.5 ± 3.58	0.00048	156.7 ± 7.84
600	9.25	0.161	71.0 ± 3.55	0.000414	157.7 ± 7.89

The normalised magnetisation loops, presented in Figure 8-16 (a), display stable flux pinning conditions for all samples as well as the presence of the signature Bean-Livingston (BL) surface barrier. This is shown by the nearly field invariant moment in the high field region of the reverse loop [265]. The stable flux pinning is indicative of a clean film with good thermal conductivity [254]. The dip in the moment on the reverse loop in the low field region is also purported to be indicative of a surface barrier/pinning phenomenon. This barrier is largest for the higher cathode power samples due to the larger film thickness.

The amount of trapped flux present in the sample, given by the y-intercept of the reverse magnetisation loop, is lowest for the 400 W sample, as shown in Figure 8-15 (b). The entry

field value, provided by the deviation from the Meissner state in the virgin curve, displayed as the Meissner ratio in Figure 8-16 (b), is largest for the high cathode power samples. However, this result is attributed to their increased film thickness, as will be covered in Chapter 8.2.7. The highest H_{en} value obtained of 71.5 mT is larger than all previous DC MS Nb films and the CERN-deposited HiPIMS Nb film but still well below the H_{c1} = 160 mT of small Nb samples [265]. This is largely due to the edge effects present with testing of small samples in a VSM, which were detailed in Chapter 6.2.9 [229]. Even though the films present different entry fields, the M/M_i ratio remains consistent for fields > 100 mT, displaying a very similar behaviour for films deposited at different cathode power values.

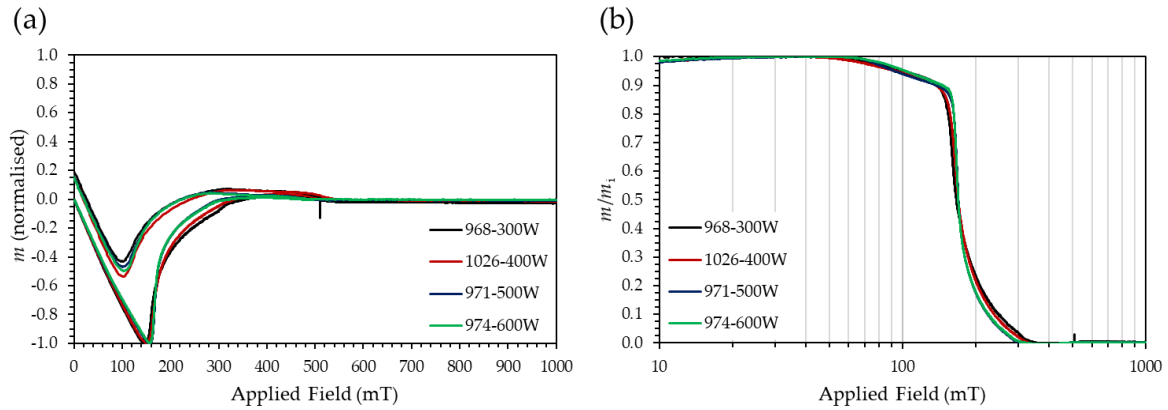

Figure 8-16: (a) Sections of the normalised magnetisation loops for HiPIMS Nb samples deposited with different cathode power values. This includes the virgin magnetisation loop and the positive portion of the reverse loop. (b) The normalised dc hysteresis curves of the same samples.

8.2.3 The Effects of Deposition Pressure

HiPIMS Nb films were deposited with the base setting detailed in Table 8-3, while the deposition pressure was varied between 8.0 x 10^{-3} and 1.8 x 10^{-2} mbar, resulting in a mean free path ranging from 1.26 cm at 8 x 10^{-3} mbar to 0.56 cm at 1.8 x 10^{-2} mbar. The results of waveform, surface and crystallographic analysis techniques are summarised in Table 8-6.

Table 8-6: Selection of characterisation results for the HiPIMS Nb films deposited with different deposition pressure values.

p_{dep} (mbar)	C_{peak} (A)	P_{peak} (kW)	t_{film} (μm)	r_{dep} (nm/min)	a_0 (Å)	L (nm)	S_q (nm)
8.0 x 10^{-3}	18.13	7.32	2.69	48.82	3.3117	116.6	11.19 ± 0.26
1.0 x 10^{-2}	20.9	7.78	3.23	52.06	3.3093	132.2	8.99 ± 0.10
1.4 x 10^{-2}	24.35	8.53	3.17	51.08	3.3080	171.1	11.56 ± 2.42
1.8 x 10^{-2}	26.24	8.78	3.51	56.63	3.3098	182.1	7.87 ± 0.50

The captured current waveforms are displayed in Figure 8-17. The peak current increases with an increase in the deposition pressure, from 18.13 to 26.22 A at 8.0×10^{-3} and 1.8×10^{-2} mbar, which corresponds to a peak power of 7.32 and 8.78 kW respectively. This increase is related to the increased amount of gas atoms within the chamber. The increase in the peak power results in an increase in the deposition rate from 48.82 to 56.63 nm/min at 8.0×10^{-3} and 1.8×10^{-2} mbar respectively. Because of the increased current and constant average power, the cathode voltage decreased from 436.2 to 365.9 V, leading to a decrease in the impact energy at the target. This indicates an interplay between the deposition pressure, and therefore gas particles, in the chamber and the cathode voltage with regards to the deposition rate. The increase in the deposition pressure overcomes the decreased sputtering yield due to the lower cathode voltage to result in a nett increase in the deposition rate.

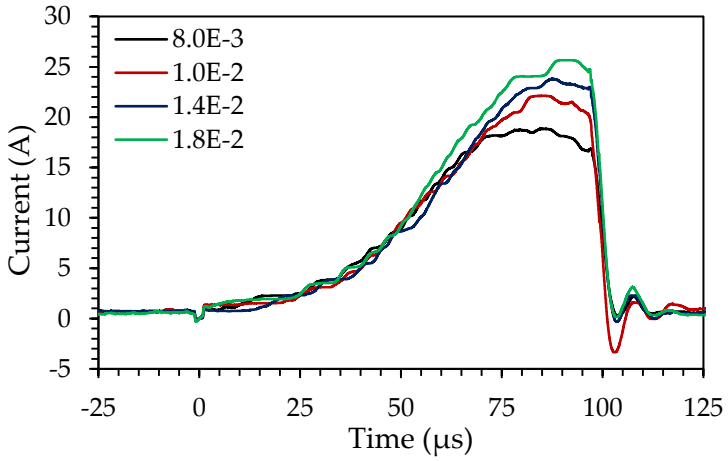

Figure 8-17: Cathode current waveforms captured during HiPIMS Nb coatings with different deposition pressures.

Increasing the deposition pressure resulted in a decrease in the surface roughness of the Nb films, as shown by AFM analysis, from 11.19 ± 0.26 at 8.0×10^{-3} mbar to 7.87 ± 0.50 nm at 1.8×10^{-2} mbar. Due to the similar film thicknesses, this is purely due to the deposition pressure. This decrease was also found for the single grain structure measured across all samples. This indicates an interplay between the energy enhancement due to the substrate bias, the energy reduction due to collisions between the target and the substrate and the increased presence of impinging gas ions due to the increased number of gas particles, resulting in the optimum energy level for surface diffusion and lower defect creation.

As with the previous series, XRD analysis of these films showed a (110) orientation for all films, confirmed with pole figure measurements, not displayed here. The calculated lattice parameters, detailed in Figure 8-18 (a), again indicate a compressive stress state in the films,

regardless of deposition pressure. Nevertheless, an increase in the deposition pressure results in a decrease in the lattice parameter, indicating a decrease in the compressive stress state of the film. The lattice parameter reaches a minimum of 3.3080 Å at 1.4 x 10^{-2} mbar, the most bulk-like lattice parameter of all HiPIMS Nb films. This trend has previously been shown for DC MS Nb films and is related to the decreasing mean free path associated with increasing deposition pressure and the subsequent decrease in the incident energy of the impinging adatom and ionised species at the substrate surface [179]. However, the use of a substrate bias and the increased presence of ionised particles in a HiPIMS process compared to DC MS results in a continuous compressive stress state. Further to this, a significant increase in the crystallite size, displayed in Figure 8-18 (a), has been found with an increase in the deposition pressure. This is again related to the interplay mentioned above for the surface roughness.

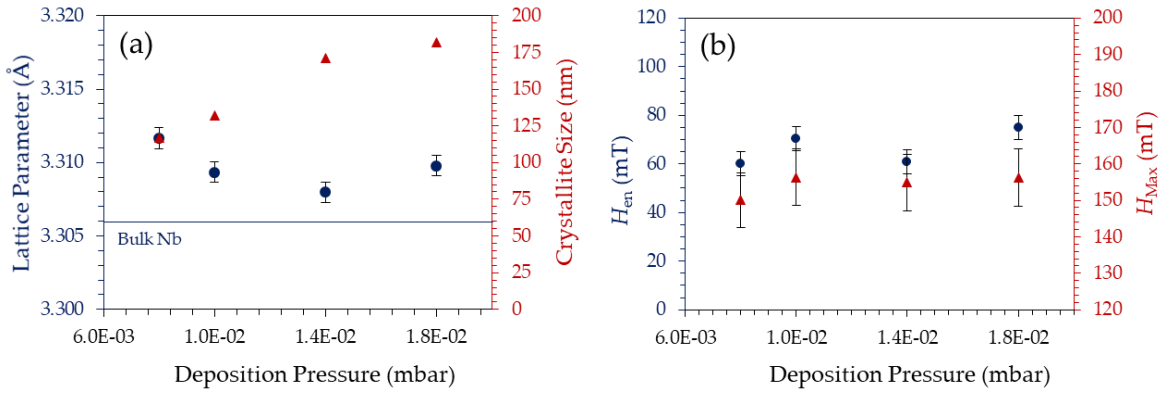

Figure 8-18: (a) Plot detailing the change in the lattice parameter and the average Nb (110) crystallite size of HiPIMS Nb samples deposited with increasing deposition pressure. (b) Plot detailing the change in the entry field and the maximum field, in parallel field, of HiPIMS Nb samples deposited with increasing deposition pressure.

Based on the VSM results, depicted in Figure 8-18 (b) and Table 8-7, there is no specific trend in the entry field values related to the changes in deposition pressure. The lower pressure samples do present a stronger dip in the reverse loop, not shown here, though it is not significant. The trapped flux value is also greater for samples deposited at higher pressures, though the trend is non-linear. Similar to the previous samples, the maximum flux values, which indicate the field at which the sample is fully penetrated, are found to increase with increasing film thickness. The T_c values of these films are slightly above bulk Nb and show a variability of ~ 0.05 K. Interestingly, the film with the most bulk-like lattice parameter did not possess the most bulk-like T_c.

Table 8-7: Superconducting characterisation results for HiPIMS Nb samples deposited with different deposition pressures.

p_{dep} (mbar)	T_c (K)	ΔT_c (K)	H_{en} (mT)	H_{tr} (emu)	H_{Max} (mT)
8.0 x 10^{-3}	9.29	0.198	70.5 ± 3.53	0.000203	150.1 ± 7.51
1.0 x 10^{-2}	9.25	0.118	60.0 ± 3.00	0.000416	156.4 ± 7.82
1.4 x 10^{-2}	9.29	0.200	61.0 ± 3.05	0.000567	154.9 ± 7.75
1.8 x 10^{-2}	9.30	0.160	75.0 ± 3.75	0.000485	156.3 ± 7.82

8.2.4 The Effects of Substrate Bias

HiPIMS Nb films were deposited with the base setting detailed in Table 8-3, while the substrate bias was varied between 0 and -250 V, thereby increasing the impact energy of impinging ions of the gas and target material. The waveforms were similar for all samples and are not presented here.

Of all the different deposition settings, the change in the substrate bias had the most significant impact on the surface and crystallographic structure of HiPIMS Nb films. This can initially be seen by the changes in the film thickness, in spite of the constant deposition time for all coatings. The initial decrease in the film thickness is due to the increased density of the films, resulting from the bombardment of accelerated ionised particles. However, the significant decrease in film thickness, at substrate levels ≥ 150 V, is due to the onset of resputtering of the deposited Nb film as the impact energy of the impinging ions increases above the surface binding energy of the Nb film [266]. Thus, the quoted deposition rate includes the effects of resputtering of the substrate surface. The results are stated in Table 8-8.

Table 8-8: Selection of characterisation results for the HiPIMS Nb films deposited with different substrate bias values.

U_B (V)	C_{peak} (A)	P_{peak} (kW)	t_{film} (μm)	r_{dep} (nm/min)	a_0 (Å)	L (nm)	S_q (nm)
0	17.75	7.04	2.96	47.68	3.3169	99	16.38 ± 0.98
50	18.13	7.32	2.69	44.9	3.3117	116.6	11.19 ± 0.26
100	18.08	7.01	2.68	43.19	3.3150	89.6	20.24 ± 4.13
150	18.7	7.28	2.25	36.25	3.3271	54	27.15 ± 3.68
200	19.29	7.53	2.14	34.56	3.3398	38.8	25.49 ± 0.47
250	19.24	7.54	1.97	31.70	3.3419	44.9	26.15 ± 5.97

The reported resputtering of the deposited Nb film and the high energy of impinging ions results in significant damage to the film surface. A comparison between the 50 V sample and the 250 V sample surface is displayed in Figure 8-19 (a) and (b) respectively. The high bias sample shows substantial evidence of surface pitting and breakdown of the grain structures which are seen in the lower bias films.

The RMS surfaces roughness values, measured by AFM, are detailed in Table 8-8. The sample coated at 0 V bias has a surface roughness similar to the DC MS coated Nb films (16.38 ± 0.98 nm). The initial increase in substrate bias to 50 V results in a decrease to the lowest surface roughness of this series (11.19 ± 0.26 nm), as a result of defect annihilation and coating densification. With further increase in the substrate bias ≥ 100 V, the surface damage caused by the impinging ions leads to a marked increase in the surface roughness, effectively doubling in value. This is similar to the results observed by Burton *et al* [261].

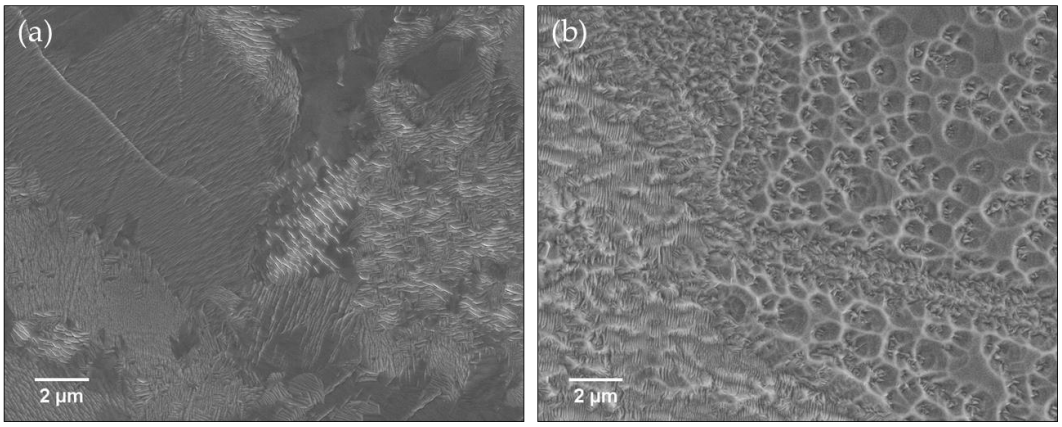

Figure 8-19: SEM images of (a) HiPIMS Nb film surface coated with 0 V substrate bias and (b) HiPIMS Nb film surface coated with 250 V substrate bias.

The magnified spectra of the Nb (110) peaks are displayed in Figure 8-20 (a). As with the previous series, XRD analysis of these films showed a (110) orientation for all films, confirmed with pole figure measurements, displayed in Figure 8-20 (b) (100 V) and (c) (250 V) respectively. The Nb (110) peaks display a continuously increasing shift to lower diffraction angles with increasing substrate bias. This indicates a significant compressive stress component present in the films deposited at high substrate bias.

This is confirmed through calculation of the lattice parameters, the results of which are displayed in Figure 8-21 (a). There are two mechanisms which led to the observed increase in compressive stress; an increasing intensity of the atom peening mechanism [178], and the likely increased incorporation of the process gas species. The pole figures further indicate a loss of in–plane texture with increasing substrate bias, changing from a restricted fibre growth at low substrate bias to fibre growth at high substrate bias levels. This is indicated by the azimuthal ring pattern visible at 60° in Figure 8-20 (c) as opposed to the spot pattern displayed in Figure 8-20 (b).

The peaks themselves also display a significant broadening with increasing substrate bias. This can be accounted for by a decreasing crystallite size and increasing micro strain with

increasing substrate bias. During initial film growth stages, the high-energy ions impacting the surface reduce the likelihood of significant island formation, thereby restricting the crystallite size of the film, as shown in Figure 8-21 (a).

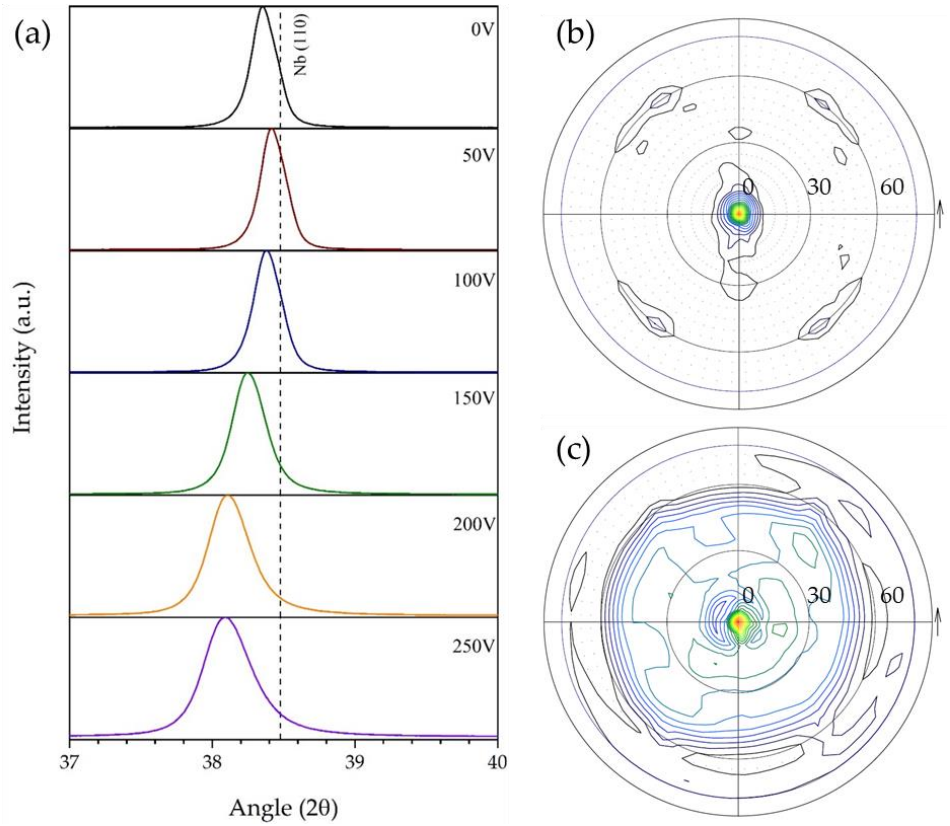

Figure 8-20: (a) Magnified XRD patterns focused on the Nb (110) peak of HiPIMS Nb samples deposited with different substrate bias values. (b) XRD pole figure of (110) Nb at 100 V bias. (c) XRD pole figure of (110) Nb at 250 V bias.

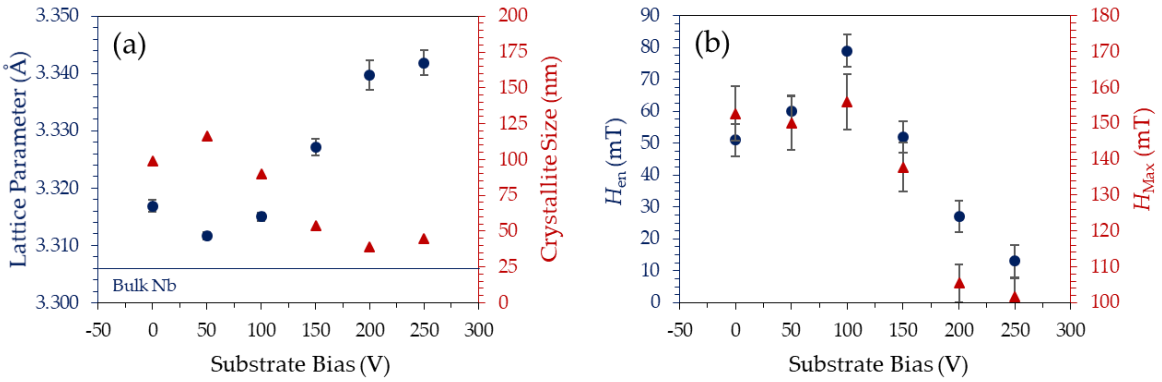

Figure 8-21: (a) Plot detailing the change in the lattice parameter and the average Nb (110) crystallite size, for HiPIMS Nb films deposited with increasing substrate bias. (b) Plot detailing the change in the entry field and the maximum flux in parallel field, for HiPIMS Nb films deposited with increasing substrate bias.

It is well known that films under compressive stress display transition temperature values greater than bulk Nb. This is evident in Figure 8-22, which depicts the transition of these Nb samples from the normal conducting to superconducting state. This is determined from the normalised magnetic moment measured in the samples during cooldown of the VSM.

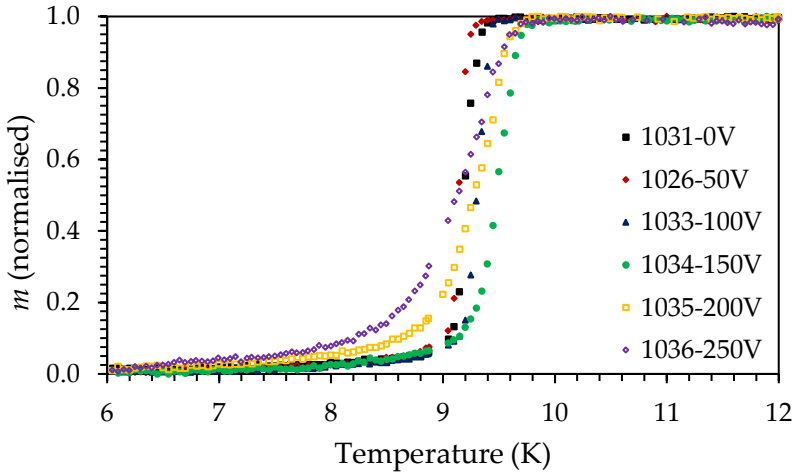

Figure 8-22: Graph depicting the normalised magnetic moment vs. the temperature for HiPIMS Nb samples deposited with different substrate bias values during cooldown in the VSM. This graph is used to determine the transition temperature and the transition width.

The transition temperatures and the transition widths of these samples, determined from this data, are presented in Table 8-9. As expected, the films with increased lattice parameters, those deposited at higher substrate bias, display the highest T_c values. The transition width, which is an indicator of the extent of defects within the film, is also found to increase considerably with increasing substrate bias, which correlates with the damaged surface shown in Figure 8-19.

Table 8-9: Superconducting characterisation results for HiPIMS Nb samples deposited with different substrate bias values.

U_B (V)	T_c (K)	ΔT_c (K)	H_{en} (mT)	H_{tr} (emu)	H_{Max} (mT)
0	9.35	0.300	51.0 ± 2.55	0.00129	152.7 ± 7.63
50	9.29	0.198	60.0 ± 3.00	0.000416	156.4 ± 7.82
100	9.40	0.200	79.0 ± 3.95	0.00492	155.9 ± 7.80
150	9.70	0.360	52.0 ± 2.60	0.00426	137.8 ± 6.89
200	9.70	0.560	27.0 ± 1.35	0.00323	105.4 ± 5.27
250	9.65	0.680	13.0 ± 0.65	0.00560	101.7 ± 5.08

Figure 8-23 (a) presents the magnetisation loops of these films. The characteristic dip in the reverse loop of the magnetisation loop disappears at substrate bias values > 100 V, likely due

to the surface damage. The trapped flux in the films also increases significantly at this point, indicating the pinning effects of film defects. Furthermore, the Bean-Livingstone barrier signature is nearly non-existent at bias levels ≥ 200 V, indicating significant degradation of the film surface. The use of a substrate bias initially reduces defect densities within the Nb films. This is shown by the increase in the entry field value to H_{en} = 79 mT at 100 V bias, as determined from the deviation of M/M_i from Figure 8-23 (b). Further increase of the substrate bias produces more defects than are being annihilated, leading to a significant decrease in both the entry field and the maximum flux values, shown in Figure 8-21 (b).

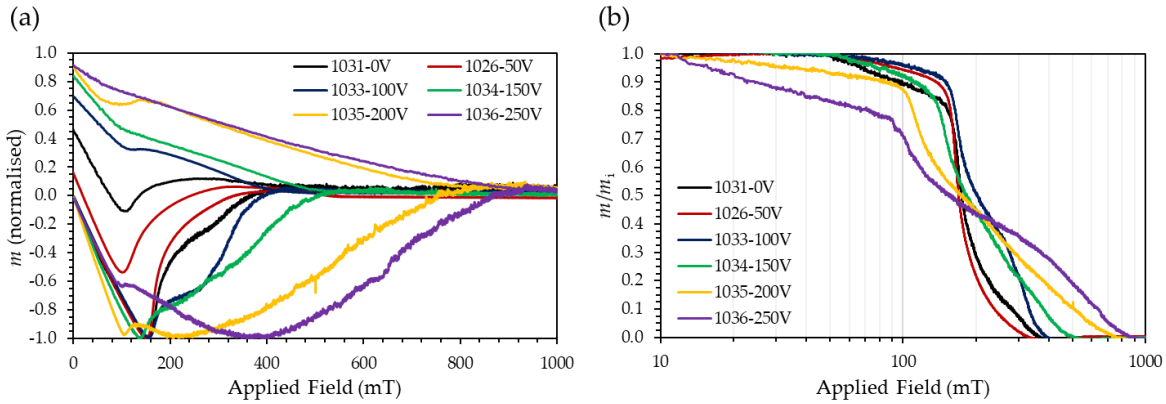

Figure 8-23: (a) Sections of the normalised magnetisation loops for HiPIMS Nb samples deposited with different substrate bias. This includes the virgin magnetisation loop and the positive portion of the reverse loop. (b) The normalised dc hysteresis curves of the same samples.

8.2.5 The Effects of Substrate Temperature

HiPIMS Nb films were deposited with the base setting detailed in Table 8-3, while the substrate temperature was varied between 115 and 290°C. The waveforms were similar for all samples and are not presented here. However, as shown in Table 8-10, it is evident that there is a decreased peak current value at the highest temperature setting, which is likely due to the lower gas density at high temperatures.

The use of an increased substrate temperature was expected to lead to an increase in the grain size. However, this is not apparent in either the SEM or AFM images, not shown here. This is attributed to the high melting temperature of Nb (2468°C) and the subsequently small changes to the homologous temperature with increasing substrate temperature in this study, from T_h = 0.142 at 115°C to T_h = 0.206 at 290°C. This is further evident in the relatively similar surface roughness values detailed in Table 8-10. In light of this, it appears as if the annihilation of defects is more reliant on the applied substrate bias than the substrate temperature, similar to results obtained by Wilde [254].

Table 8-10: Selection of characterisation results for HiPIMS Nb films deposited with different substrate temperatures.

T_s (°C)	C_{peak} (A)	P_{peak} (kW)	t_{film} (μm)	r_{dep} (nm/min)	a_0 (Å)	L (nm)	S_q (nm)
115	18.7	7.2	2.74	44.25	3.3109	128.3	11.45 ± 2.15
180	18.13	7.32	2.69	48.82	3.3117	116.6	11.19 ± 0.26
265	18.35	7.3	2.83	45.65	3.3196	154.8	12.57 ± 1.01
290	17.13	7.01	2.94	47.36	3.3222	207	11.72 ± 1.72

As detailed in Chapter 4.5, a large difference in the thermal expansion coefficients of the substrate and the deposited thin film results in significant thermal stresses within the deposited film. This is exacerbated by the use of a high substrate temperature. Evidence of this increased stress state with higher deposition temperatures is shown in the XRD spectra presented in Figure 8-24. The increasing negative shift of the Nb (110) peak, and the subsequent increase in the out-of-plane lattice parameter, shown in Figure 8-25 (a), point to the increase of compressive in-plane film stress with increasing substrate temperature. Typically, peak broadening is indicative of a decrease in the film crystallite size. However, in this case, the evident broadening of the XRD peaks is because of the significant increase in the micro strain within the films. Therefore, a noteworthy increase in crystallite size was still calculated with increasing substrate temperature, as indicated in Figure 8-25 (a).

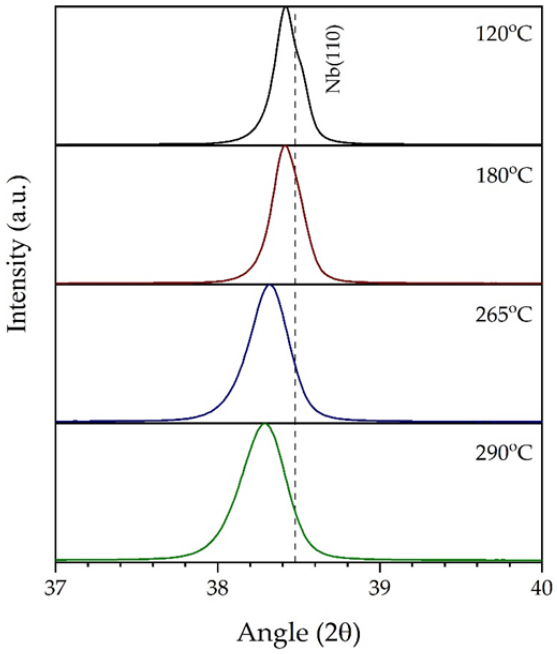

Figure 8-24: Magnified XRD patterns focused on the Nb (110) peak of HiPIMS Nb samples deposited with different substrate temperature values.

As displayed in Figure 8-25 (b), there is no specific trend in the entry field values with increasing substrate temperature. However, the sample deposited at 265°C displays an anomalously low entry field value. As a result, a new section of this sample was retested, with the same result. A decrease in the maximum field is found for increasing substrate temperature. This is ascribed to the increase in compressive stress of the films and is a similar result to the films deposited at high substrate bias. The increased compressive film stress in the high temperature samples also results in an increase in T_c at higher substrate temperatures, again, similar to the high substrate bias films, as shown in Table 8-11. An absence of the dip in the reverse loop of the magnetisation loops, not shown here, is also noted for high temperature samples. This is in line with the results of the substrate bias samples. These samples also possess the highest amount of trapped flux.

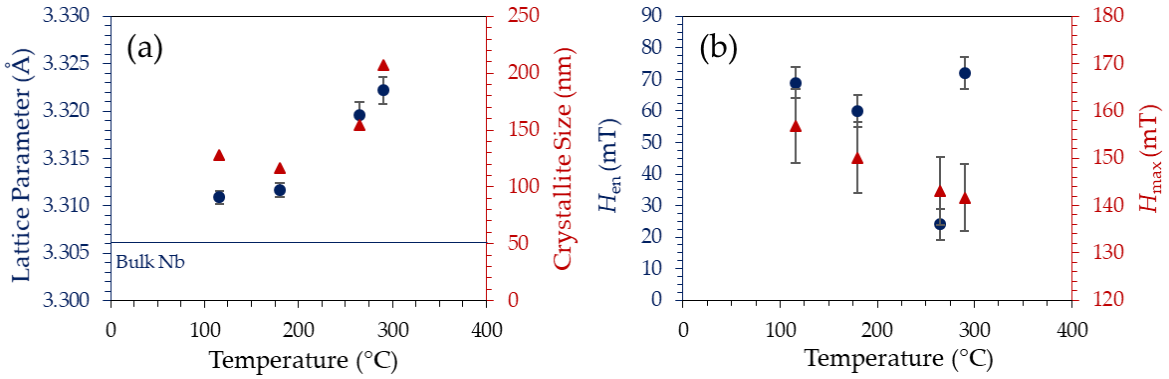

Figure 8-25: (a) Plot detailing the change in the lattice parameter and the average Nb (110) crystallite size, of HiPIMS Nb samples deposited with increasing substrate temperature. (b) Plot detailing the change in the entry field and the maximum flux in parallel field, of HiPIMS Nb samples deposited with increasing substrate temperature.

Table 8-11: Superconducting characterisation results for samples deposited with different substrate temperatures.

T_s (°C)	T_c (K)	ΔT_c (K)	H_{en} (mT)	H_{tr} (emu)	H_{Max} (mT)
115	9.30	0.160	69.0 ± 3.45	0.00176	156.7 ± 7.84
180	9.29	0.198	70.5 ± 3.53	0.000203	150.1 ± 7.51
265	9.50	0.357	24.0 ± 1.20	0.00328	143.1 ± 7.15
290	9.60	0.399	72.0 ± 3.60	0.00291	141.7 ± 7.08

8.2.6 The Effects of HiPIMS Duty cycle

The HiPIMS duty cycle is controlled by both the pulse length and the frequency of the pulses. As such, two separate series of samples were deposited with equal duty cycle values, but by individually adjusting either the pulse length or frequency.

The peak current, the peak voltage and subsequently, the peak power all decrease considerably with an increasing duty cycle; due to the resultant decreased charging time of the capacitors. This is visually displayed in Figure 8-26 (a) and (b), which depict the current waveforms as a function of increasing pulse length and frequency respectively. In spite of the decreasing peak current, the deposition rate is still found to increase with increasing duty cycle. The deposition rate reaches a maximum for 140 µs and 1800 Hz respectively, as detailed in Table 8-12, where after it decreases. The changes in the deposition rate with changing HiPIMS parameters are rather complex, with a couple relevant issues included here; the increased densification of films due to ion deposition, decreased sputter yield due to self-sputtering and a decrease in the gas rarefaction at higher duty cycles [147]. This was summarised well by Anders [160].

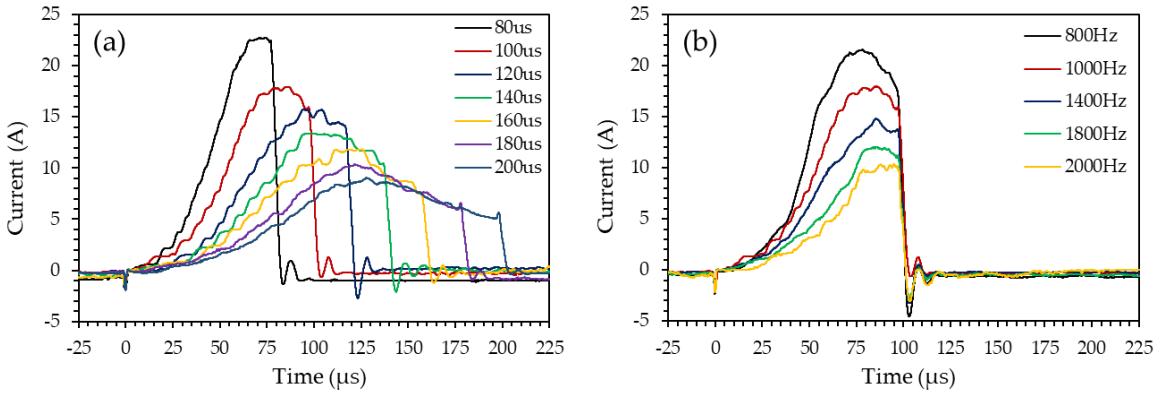

Figure 8-26: (a) Current waveforms as a function of the HiPIMS pulse length. (b) Current waveforms as a function of the HiPIMS frequency.

Similar to the previous studies, the change in the duty cycle did not result in any significant changes to the film surface topography. This is indicated by the similar surface roughness values across all samples in this series, presented in Table 8-12.

Details of the crystallographic properties of the films are shown in Figure 8-27 (a) and (b). A general increase in the crystallite size is shown for an increase in the duty cycle, because of individually adjusting either the pulse length or the frequency. Furthermore, a common minimum in the lattice parameter, denoting the film with the least compressive stress and that with the most bulk-like properties, is found for films coated with a duty cycle of 12/14%, though the variability is low.

The results of the VSM tests conducted on these samples are detailed in Figure 8-27 (c) and (d) for changes in the pulse length and frequency respectively. It is evident that the films with the most bulk-like lattice parameters, those deposited at 12/14 % duty cycle, display the

highest entry fields for changes in both the pulse length and the frequency. On the other hand, the maximum field value shows no significant dependence on the duty cycle.

Table 8-12: Selection of characterisation results for HiPIMS Nb films deposited with different duty cycles, determined by adjusting the pulse length and frequency.

Value (μs/Hz)	C_{peak} (A)	P_{peak} (kW)	Duty Cycle (%)	t_{film} (μm)	r_{dep} (nm/min)	a_0 (Å)	L (nm)	S_q (nm)
Pulse Length								
80	24.36	10.44	8	4.04	56.08	3.3092	122.9	11.74 ± 2.60
100	18.13	7.32	10	2.69	48.82	3.3117	116.6	11.19 ± 0.26
120	16.03	6.24	12	4.44	71.68	3.3092	136	10.02 ± 2.89
140	13.13	4.88	14	4.77	76.97	3.3087	140.3	9.94 ± 0.59
160	12.55	4.51	16	3.59	57.94	3.3110	127.3	13.31 ± 0.28
180	10.66	3.79	18	3.04	69.14	3.3098	131.9	12.48 ± 0.29
200	9.04	3.10	20	2.48	62.03	3.3119	139	9.31 ± 2.69
Frequency								
800	20.85	8.57	8	2.48	40.07	3.3143	94.9	10.39 ± 1.78
1000	18.13	7.32	10	2.69	48.82	3.3117	116.6	11.19 ± 0.26
1400	14.367	5.51	14	3.9	48.70	3.3105	123.5	13.30 ± 1.04
1800	12.05	4.47	18	2.98	59.52	3.3120	122.6	13.00 ± 1.45
2000	11.66	4.25	20	2.97	54.05	3.3121	143.3	8.55 ± 0.27

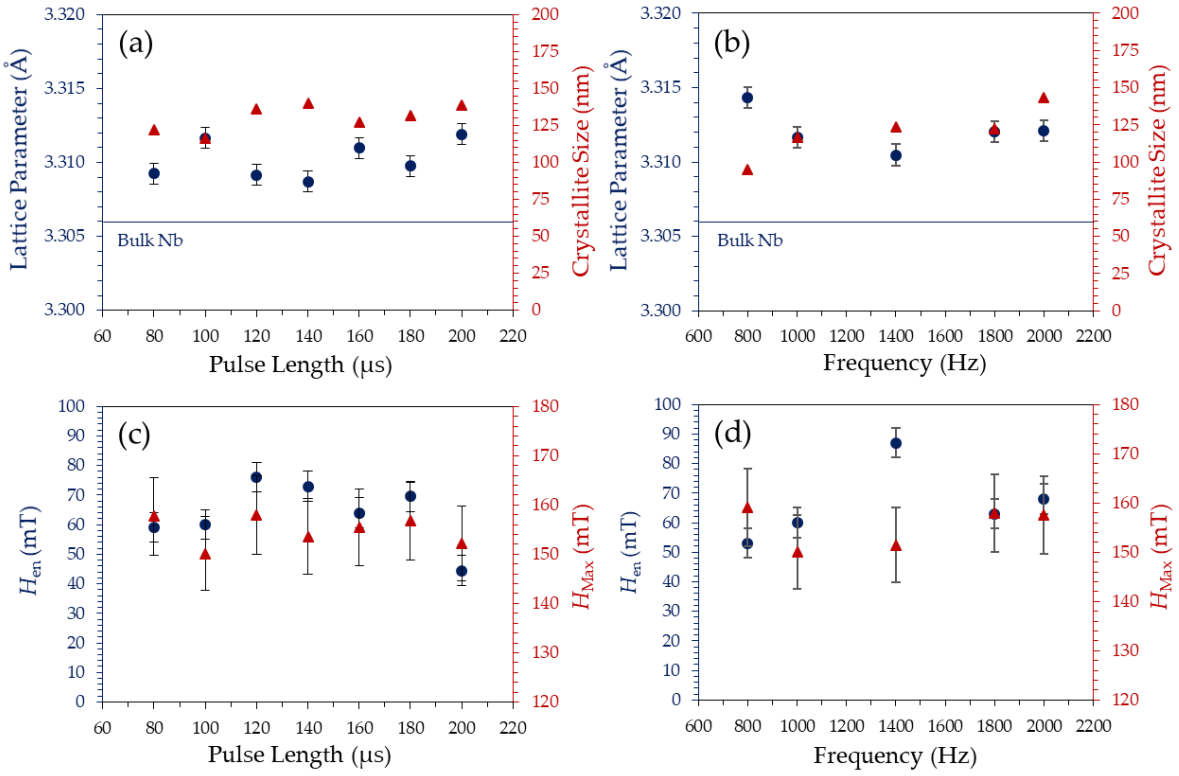

Figure 8-27: Plot detailing the change in the lattice parameter and the average Nb (110) crystallite size, of HiPIMS Nb samples deposited with increasing pulse length (a) and frequency (b). Plot detailing the change in the entry field and the maximum flux in parallel field, of HiPIMS Nb samples deposited with increasing pulse length (c) and frequency (d).

The resultant magnetisation loops are displayed in Figure 8-28 (a) and (b). The loops pertaining to the changes in pulse length do not display significant variability. It should be noted, the loops that are larger in size, 180 and 200 μs, are associated with the thinnest films. Interestingly, a significant increase in the size of the loops is found when varying the frequency, besides the sample coated at 1000 Hz. There is no indication as to why this has transpired, based on any previous characterisation results. A series of anomalous features are also present in all the loops besides the 1000 Hz sample. This is likely due to unstable flux pinning within the sample resulting in rearrangement of vortices [254]. It should be noted again, that the sample with the largest loop (800 Hz) is the thinnest film. Due to the larger loops, there is also a significant increase in the amount of trapped flux in this series of films. Nevertheless, the film coated at 1400 Hz displays the largest entry field of any sample up until this point, H_{en} = 87.0 ± 4.35 mT.

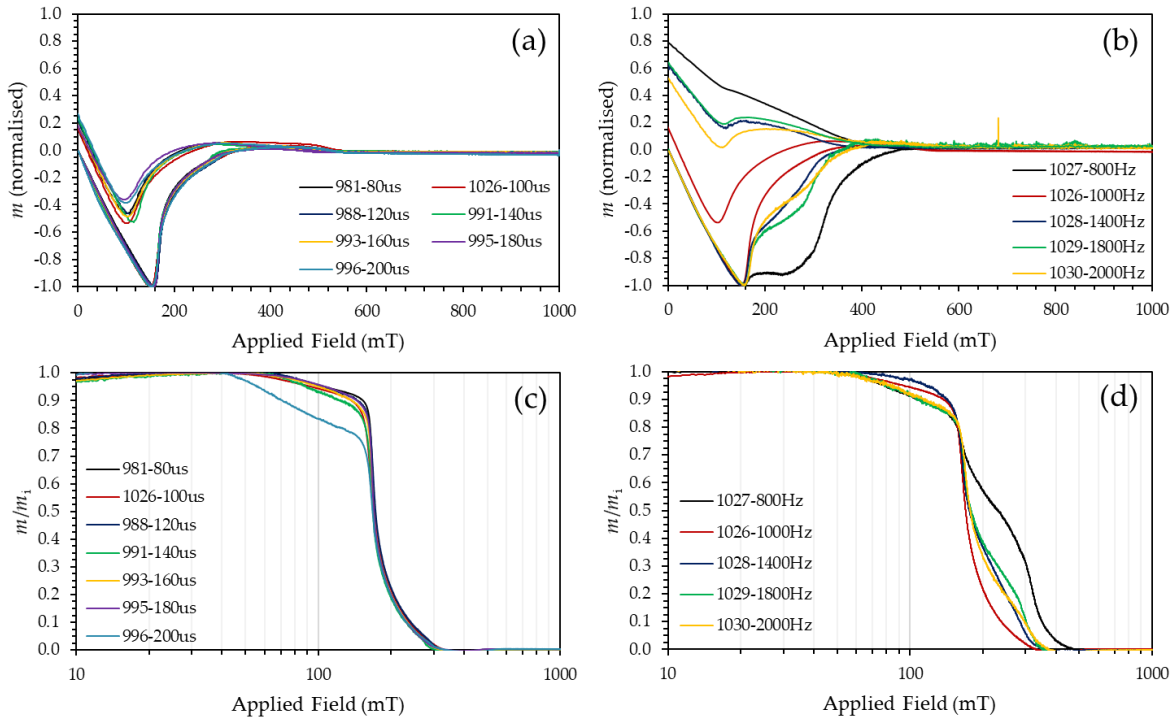

Figure 8-28: Plots detailing the virgin magnetisation loop and the positive portion of the reverse loop for HiPIMS Nb samples deposited with different pulse length (a) and frequency (b). The normalised dc hysteresis curves of the samples deposited with different pulse length (c) and frequency (d).

The superconducting test results are summarised in Table 8-13. The low variability in the lattice parameters and their close proximity to that of bulk Nb are represented in the low variability of T_c. It is however apparent that the films are under the effects of some stress due to the increased value of T_c ~ 9.30 K over that of bulk Nb (9.20 K).

Table 8-13: Superconducting characterisation results for HiPIMS Nb samples deposited at different duty cycles, determined by adjusting the pulse length and frequency.

Value (μs/Hz)	T_c (K)	ΔT_c (K)	H_{en} (mT)	H_{tr} (emu)	H_{Max} (mT)
Pulse Length					
80	9.30	0.200	59.0 ± 2.95	0.000323	157.7 ± 7.88
100	9.29	0.198	60.0 ± 3.00	0.000203	156.3 ± 7.82
120	9.30	0.199	76.0 ± 3.80	0.000574	158.0 ± 7.90
140	9.25	0.159	73.0 ± 3.65	0.000475	153.6 ± 7.68
160	9.30	0.200	64.0 ± 3.20	0.000395	155.4 ± 7.77
180	9.30	0.200	69.5 ± 3.48	0.000328	156.7 ± 7.84
200	9.35	0.239	44.5 ± 2.23	0.000381	152.2 ± 7.61
Frequency					
800	9.35	0.239	53.0 ± 2.65	0.00605	159.1 ± 7.95
1000	9.29	0.198	60.0 ± 3.00	0.000203	156.3 ± 7.82
1400	9.30	0.200	87.0 ± 4.35	0.00432	151.5 ± 7.57
1800	9.34	0.237	63.0 ± 3.15	0.00294	157.9 ± 7.89
2000	9.34	0.236	68.0 ± 3.40	0.00177	157.5 ± 7.88

A series of films were also deposited to explore the low duty cycle regime. In order to achieve stable plasma conditions with the lower duty cycle settings, the deposition pressure was increased to 1.0 x 10^{-2} mbar and the cathode power decreased to 300 W average power. The results with these films present similar results with the previous sample series, displaying a marked reliance on the film thickness, in terms of the entry field and the lattice parameter. However, the appearance of a second peak in the current waveform at low duty cycles, as shown in Figure 8-29 (a), indicated the initiation of self-sputtering. This is short lived though, as the current drops shortly afterwards due to rarefaction [267]. The appearance of the second peak at low duty cycles is found to be dependent on the pulse settings, as shown in Figure 8-29 (b). In spite of the equal 4 % duty cycle, there is no evidence of a second peak for the sample deposited at a pulse length of 200 μs, although the maximum current remained similar to those that did.

The trends in the superconducting entry field data of the above samples are dominated by the effects of the film thickness. Therefore, it appears as if changes to the duty cycle for HiPIMS deposition of Nb films do not have a significant influence on the resulting thin films and more emphasis should be placed on the other deposition parameters. However, the use of an increased pulse frequency does allow for the use of a lower deposition pressure [84], which would lead to lower incorporation of the process gas in the growing film as well as decreased deposition time, based on this work. The influence of incorporated gas atoms is not as apparent in the DC superconductivity testing completed in this work and the move to RF testing would provide further information.

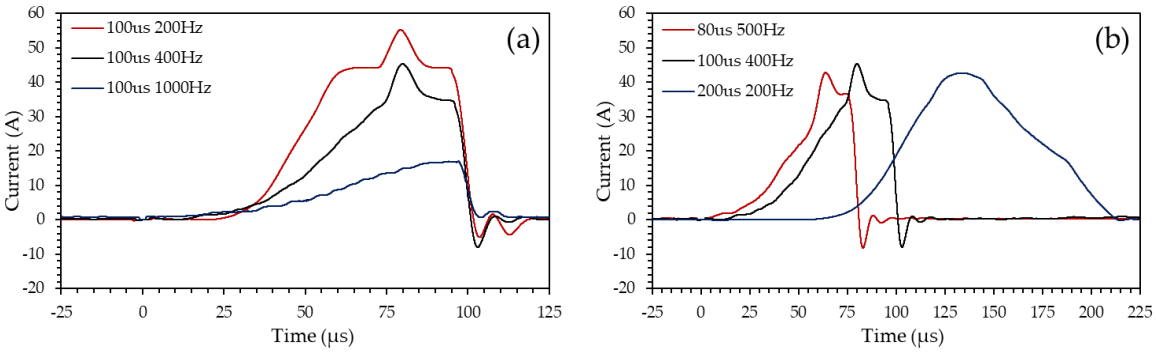

Figure 8-29: Cathode current waveforms captured during low duty cycle coatings. (a) Depositions completed with 300 W and 4% duty cycle with different pulse length and frequency settings. (b) Depositions completed at 100 µs pulse length and different frequencies.

8.2.7 The Effects of Film Thickness

Based on the overwhelming indication that the film thickness is the most significant parameter in terms of the entry field, a series of HiPIMS Nb films, with thicknesses varying from 0.91 to 8.10 µm, were deposited. These samples were deposited with the base setting detailed in Table 8-3, except the pulse length was increased to 120 µs, as this was the best performing sample in terms of H_{en} at the time of coating.

Investigation of the captured SEM and AFM images shows no significant changes to the grain structure of the films with increasing thickness. The increase in the surface roughness, documented in Table 8-14, is primarily due to the increased role of the step edge grain boundaries imaged for these samples. When imaging the individual grains themselves, the surface roughness still increases, albeit to a lesser extent.

Table 8-14: Selection of characterisation results for HiPIMS Nb films deposited with different film thicknesses.

t_{film} (µm)	r_{dep} (nm/min)	a_0 (Å)	L (nm)	S_q (nm)
0.91	60.81	3.3157	103.2	9.40 ± 1.09
1.76	58.83	3.3100	145.9	9.65 ± 4.79
3.68	59.42	3.3092	130.5	9.50 ± 3.07
5.09	57.85	3.3083	125	10.09 ± 0.26
6.45	59.90	3.3092	138	14.47 ± 0.38
8.10	57.10	3.3082	121.8	18.29 ± 0.91

In addition to the thermal stresses, the intrinsic stresses due to the lattice mismatch between the substrate and the deposited film have a significant effect on the deposited films, especially in thinner films. In this instance, the mismatch between the Nb film and the Cu substrate is ~ 9 %. Due to the significant thickness differences between the film and the substrate, this

mismatch is typically accommodated for by the deposited film, in the form of dislocations. This is evident in Figure 8-30 (a), where the lattice parameters of the thinner films are noticeably larger, indicating an increased compressive stress. The decrease in the lattice parameter with increasing thickness is opposite to what was shown by Peck for DC MS Nb films [221]. However, Peck states that the results could be due to "an enhanced bombardment of the growing film with gas atoms caused by the asymmetry of the discharge". The decrease in the film stress observed in this study, as indicated by the decreasing lattice parameter with increasing film thickness, is most likely due stress relief by yielding of the film.

The crystallite sizes of these films are found to be relatively consistent above 2 µm film thickness, indicating an apparent transition zone during the initial growth phase of the Nb films, most likely as a result of the selective growth model [263]. This was shown previously in Figure 8-12 in the EBSD analysis of the Nb film cross-section detailed in Chapter 8.2.1.

The decrease in the film stress with increasing film thickness also manifests itself in a decrease in the T_c of the films with increasing thickness, as shown in Table 8-15. Evidence for the existence of a transition zone is also found in the H_{en} results of these films, detailed in Figure 8-30 (b). A sharp increase in the entry field exists with increasing film thickness up to 3.68 µm, where after the entry field remains relatively consistent. Sample 1077, with a film thickness of 3.68 µm, was the sample with the highest entry field value during these individual parameter studies. Although this value is still significantly lower than the purported H_{c1} = 160 mT for small Nb samples [265], it is more than double that achieved with previous DC MS coatings. As detailed earlier, this is most likely due to the geometrical edge effects associated with fully immersing samples in the magnetic field during testing.

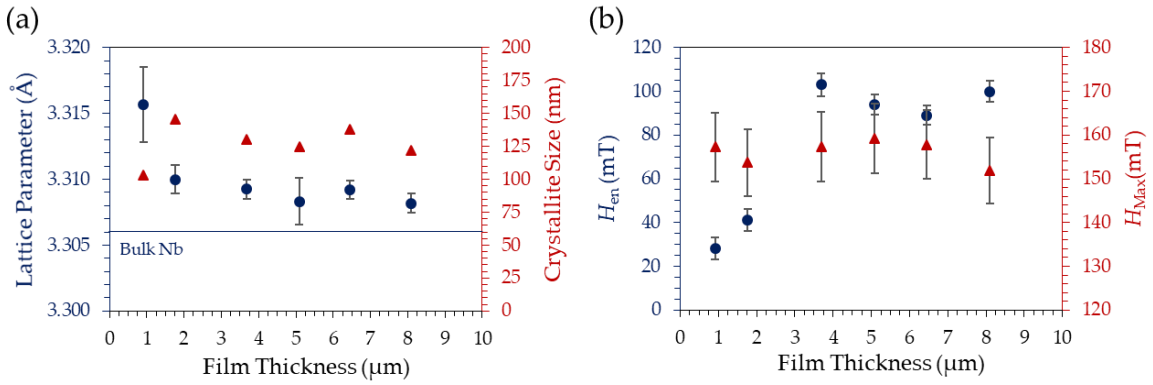

Figure 8-30: (a) Plot detailing the change in the lattice parameter and the average Nb (110) crystallite size, of HiPIMS Nb films deposited with increasing film thickness. (b) Plot detailing the change in the entry field and the maximum flux in parallel field, of HiPIMS Nb films deposited with increasing film thickness.

The normalised magnetisation loops, detailed in Figure 8-31 (a), show a similar trend to the entry field results. A significant relative decrease in the size of the loop and a subsequent decrease in the trapped flux is visible with increasing film thickness, except for the thickest film, which shows an anomalously high trapped flux value. This decrease is most likely due to a reduction of defects in the penetration depth of the film, linked to the transition zone. Increasing the film thickness also leads to the appearance of the dip in the reverse loop, visible at thickness ≥ 1.76 μm. The M/M_i ratio, shown in Figure 8-31 (b), is the last piece of evidence for the transition zone theory. For film thicknesses ≥ 3.68 μm, the ratio remains relatively equal regardless of the film thickness. The superconducting results for these films are summarised in Table 8-15.

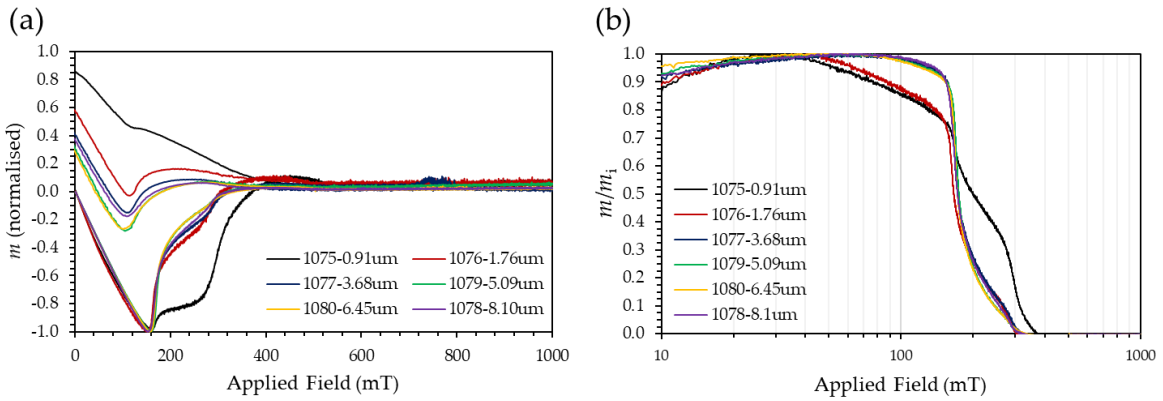

Figure 8-31: (a) Sections of the normalised magnetisation loops for HiPIMS Nb samples deposited with different film thicknesses. This includes the virgin magnetisation loop and the positive portion of the reverse loop. (b) The normalised dc hysteresis curves of the same samples.

Table 8-15: Superconducting characterisation results for HiPIMS Nb samples deposited with different film thicknesses.

T_{film} (μm)	T_c (K)	ΔT_c (K)	H_{en} (mT)	H_{tr} (emu)	H_{Max} (mT)
0.91	9.35	0.197	28.0 ± 1.40	0.00241	157.3 ± 7.87
1.76	9.35	0.201	41.0 ± 2.05	0.00105	153.7 ± 7.69
3.68	9.30	0.199	103.0 ± 5.15	0.00148	157.3 ± 7.87
5.09	9.30	0.159	94.0 ± 4.70	0.00140	159.1 ± 7.96
6.45	9.30	0.200	89.0 ± 4.45	0.00129	157.8 ± 7.89
8.10	9.25	0.117	100.0 ± 5.00	0.00264	151.8 ± 7.59

8.3 Conclusions

The results of the above experiments indicate the significant influence of three specific deposition parameters: the substrate temperature, substrate bias and the Nb film thickness. The observed changes in the superconducting performance are specifically related to changes

in the crystallographic structure of the Nb films as well as their state of stress. This relationship is presented for the films deposited in this study in Figure 8-32. In spite of the spread in the results, there is an overwhelming trend which indicates that depositing Nb thin films with a crystal structure which approaches that of unstressed, bulk Nb leads to superconducting performance improvements for these thin films. In light of this, Nb thin films used for SRF cavities, in either single or multilayer structures, should be deposited with thicknesses between 3 - 5 μm, at an intermediate temperature with a relatively low substrate bias. Coupled to this, a lower average cathode power is recommended in order to decrease the resultant surface roughness by allowing sufficient time for surface diffusion.

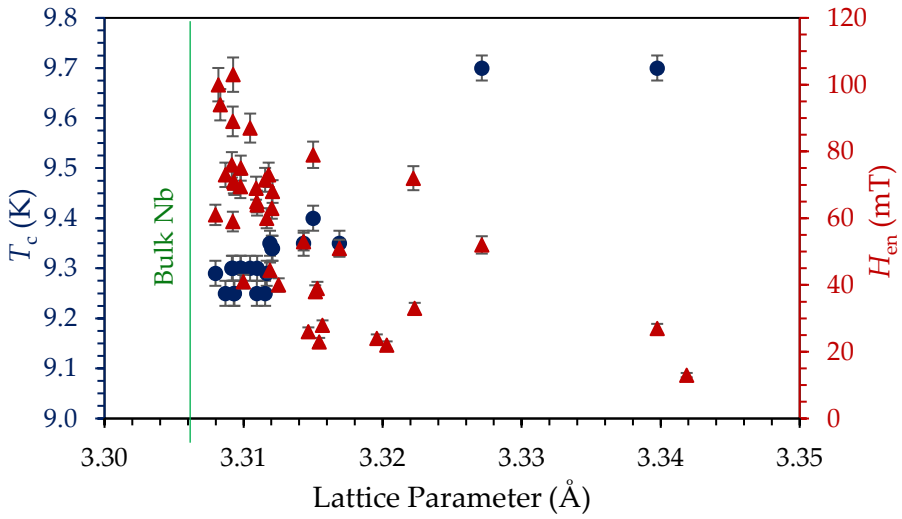

Figure 8-32: Plot detailing the relationship between the transition temperature and the entry field of HiPIMS Nb thin films and their respective lattice parameters.

Changes to the duty cycle did not result in any significant changes to the crystallographic structure of the films, although specific maximums were obtained during superconducting tests. Therefore, given the increased deposition rate at higher duty cycle values, it is possible to deposit films of higher quality than with DC MS systems in a comparable time scale. The increase in duty cycle also allows for operation at lower deposition pressures, which results in lower gas entrapment in the deposited films, not explored here. It must be noted that the superconducting performance of these films was measured in a DC system. Therefore, the energy dissipation, which would arise due to oscillatory motion of trapped vortices in an oscillating field, was not documented. However, it was considered in the choice of the optimum coating parameters by comparing the entry field and trapped flux values as well as the magnetisation loop size. Following these recommendations, a single HiPIMS Nb recipe, with deposition parameters detailed in Table 8-16, was used for the remainder of the

multilayer films in this thesis, also allowing for better comparability. These are presented in Chapters 9.3, 9.4 and 9.5.

Table 8-16: HiPIMS Nb deposition parameters used for SIS film coatings.

P_{cath} (W)	p_{dep} (mbar)	PL (µs)	f_{pulse} (Hz)	U_B (V)	T_s (°C)
400	8.0×10^{-3}	120	1000	50	180

9. Deposition of Superconductor-Insulator-Superconductor (SIS) Thin Film Coatings

This chapter will present the experiments that focused on the deposition of multilayer SIS films onto Cu substrates. In this study, only a single multilayer structure (Nb/AlN/NbN) was pursued. Prior to the start of SIS film coatings, a study into the deposition of a suitable AlN layer with DC MS was completed. Initial SIS films were deposited using DC MS for all three layers. This highlighted the limitations of DC MS Nb as a base layer. The second series of SIS films were deposited following completion of the HiPIMS Nb study and utilised a HiPIMS Nb film as the base layer, with the remaining AlN and NbN layers coated with DC MS. This highlighted the difference in performance of SIS films due to the Nb base layer as well as the effects of different NbN recipes. The final series of SIS films were coated following the completion of the HiPIMS NbN study and utilised a HiPIMS Nb base layer, DC MS AlN layer and an outer HiPIMS NbN layer. This final series of SIS films highlighted the increased performance offered by HiPIMS-deposited films as well as the efficacy of depositing SIS films onto Cu as a whole.

9.1 AlN Insulating Layer Investigation

In order to facilitate the deposition of multilayer SIS film samples, a recipe to deposit an insulating layer needed to be developed. AlN was chosen for two reasons: to avoid possible detrimental exposure of the already deposited Nb layer and the Nb target itself to O, in the event of depositing Al_2O_3 or MgO as the insulating layer, as well as the low lattice mismatch between AlN (002) and NbN (111) [268], which facilitates its growth in the subsequent superconducting layer. Normally, RF sputtering is used to deposit insulating coatings such as AlN. However, the setup used in this study did not contain an RF power supply, therefore requiring deposition by DC MS to avoid removal of the sample from the deposition chamber in between coatings.

A review of previous research, completed by Iqbal and Mohd-Yasin [269], as well as a comprehensive analysis of the effects of deposition parameters by Chiu *et al* [270], provided valuable information regarding favourable deposition conditions for the growth of AlN (002) with DC MS. A low deposition pressure leads to favourable conditions for its growth, while too high a pressure leads to a phase switch to the (100) orientation. A higher power density also favours the growth of AlN (002) while also resulting in a lower surface roughness. An intermediate substrate temperature leads to increased adatom diffusion and subsequent AlN (002) favoured growth. Further authors detailed the use of a higher N_2 % in the process

gas, up to 100 % N_2, to achieve the required AlN (002) phase during reactive sputtering [271][272].

Based on this, a series of experiments were completed, varying the cathode power, deposition pressure and N_2 % in the process gas, to investigate the formation of AlN (002). The films were deposited onto Si (100) wafers, which facilitated ease of analysis. The films were coated in the same system described in Chapter 6.1. Prior to each deposition process, the Al target, which is 490 x 100 x 10 mm^3 in size, was sputter-cleaned for 10 min behind closed shutters. All of the samples were analysed by SEM and XRD, in order to determine the deposition rate, film microstructure and AlN phase of each sample.

Initial experiments showed an improved microstructure of the AlN film at higher N_2 % values. However, the use of too high a cathode power (> 12 W/cm^2) resulted in damage to the Al target and the growth of large 3D island structures. Therefore, a lower power, cathode power study, detailed in Table 9-1, was completed, by increasing the power density from 4 to 8 W/cm^2. The films in this study were deposited with an 80/20 mixture of N_2/Ar in the process gas, due to the improved microstructure observed in pre-testing, and at a substrate temperature of 165°C.

Table 9-1: Deposition parameters of AlN films deposited with different cathode power values.

Sample	**T_s (°C)**	**p_{dep} (mbar)**	**N_2 %**	**ρ_{Power} (W/cm^2)**	**Time (min)**
859	165	8 x 10^{-3}	80	8	10
860	165	8 x 10^{-3}	80	7	10
861	165	8 x 10^{-3}	80	6	10
862	165	8 x 10^{-3}	80	5	10
863	165	8 x 10^{-3}	80	4	10

Samples 859 and 862, deposited at a high and low power density respectively, are displayed in Figure 9-1. The SEM investigation of the film cross-section, presented in (a) and (c), shows similarly dense, columnar films regardless of cathode power used. On the other hand, the film surface shows a slight change with changing cathode power. The presence of 3D islands is found at higher power levels, as shown in (b). These 3D island structures disappear at power levels below 6 W/cm^2, with the surface populated by rounded grain peaks, as presented in (d). However, the frequency of these 3D islands is significantly reduced compared to the initial samples deposited at > 12 W/cm^2. With decreasing DC power, the deposition rate also decreased dramatically from 52.76 nm/min at 8 W/cm^2 to 22.33 nm/min at 4 W/cm^2.

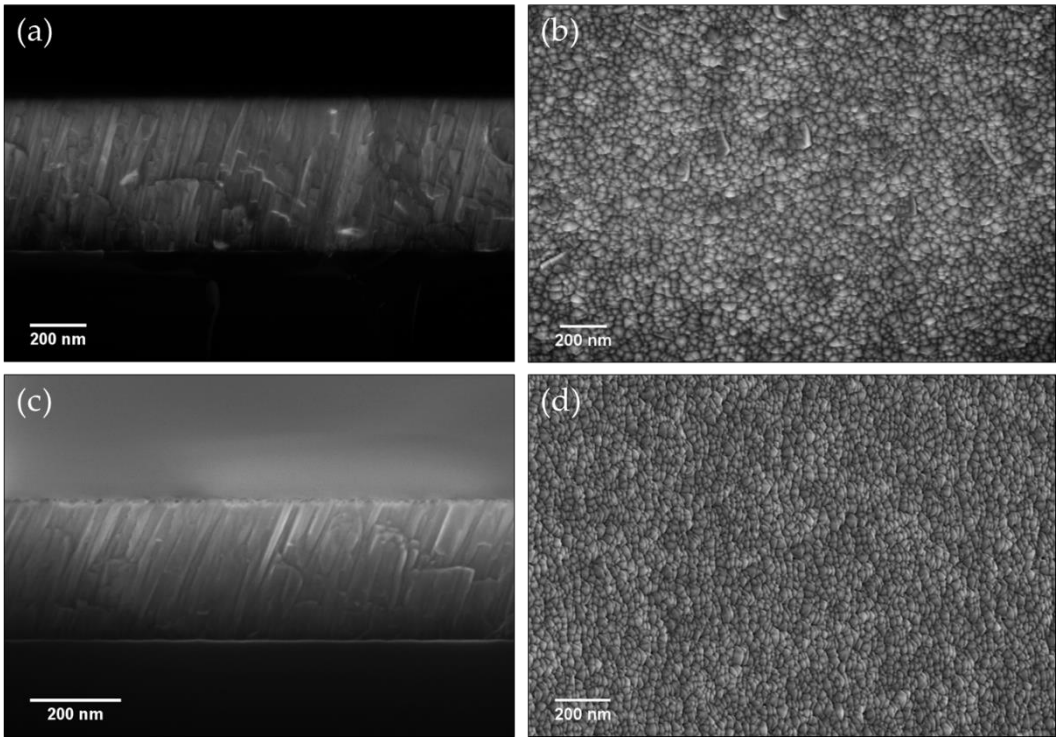

Figure 9-1: SEM images of the cross-section and surface microstructure of AlN films deposited at, (a) and (b) high cathode power and (c) and (d) low cathode power.

Further samples were coated at the higher cathode power level (8 W/cm^2) with different deposition pressure values and N_2 % in the process gas, as documented in Table 9-2. The microstructure of both the cross-sections and the surfaces of these samples were very similar to that displayed in Figure 9-1 (a) and (b) for the high power sample. The deposition rate of these samples was consistent regardless of N_2 %, varying by a maximum of 7 nm/min.

Table 9-2: Deposition parameters of AlN films deposited with different pressure and N_2 % in the process gas.

Sample ID	T_s (°C)	p_{dep} (mbar)	N_2 %	ρ_{Power} (W/cm^2)	Time (min)
864	165	6 x 10^{-3}	80	8	10
865	165	4 x 10^{-3}	80	8	10
866	165	6 x 10^{-3}	90	8	10
867	165	6 x 10^{-3}	100	8	10
868	165	6 x 10^{-3}	70	8	10

All of the AlN samples were analysed by XRD in order to determine the effects of the deposition parameters on the crystalline phase. The resulting spectra are plotted in log scale in Figure 9-2. The peak at 36.033° was identified as the AlN (002) phase [273]. All of the deposited samples display a pronounced (002) orientation, with no evidence of any further phases. The peak located at ~ 68° is related to the Si (100) substrate. The magnified spectra

displayed in the right image of Figure 9-2 were used for comparison of the different AlN films. Both samples 859 and 863 were coated with 80% N_2 flow rate, but the former was coated at a higher cathode power. A slight increase in intensity is seen for the higher cathode power sample, due to increased film thickness. Samples 864 and 865 were both coated at 80 % N_2 flow rate and higher cathode power, however at decreased pressures of 6×10^{-3} and 4×10^{-3} mbar respectively. This resulted in a decrease of the FWHM of the AlN (002) peak, indicating AlN crystallite growth, and an increase in the absolute peak intensity. Finally, sample 867 was coated at 6×10^{-3} mbar and high cathode power; however, the N_2 % was increased to 100 %. This resulted in a further decrease in the (002) peak FWHM coupled with a further increase in the absolute intensity, reaching a maximum for all AlN samples. The crystallite size of sample 867 also displays the maximum value of all samples, at 81.4 nm. This indicates a significant influence of both the pressure and the N_2 % on the formation of AlN (002). Based on these results, the recipe for sample 867 was selected for use in the multilayer SIS films.

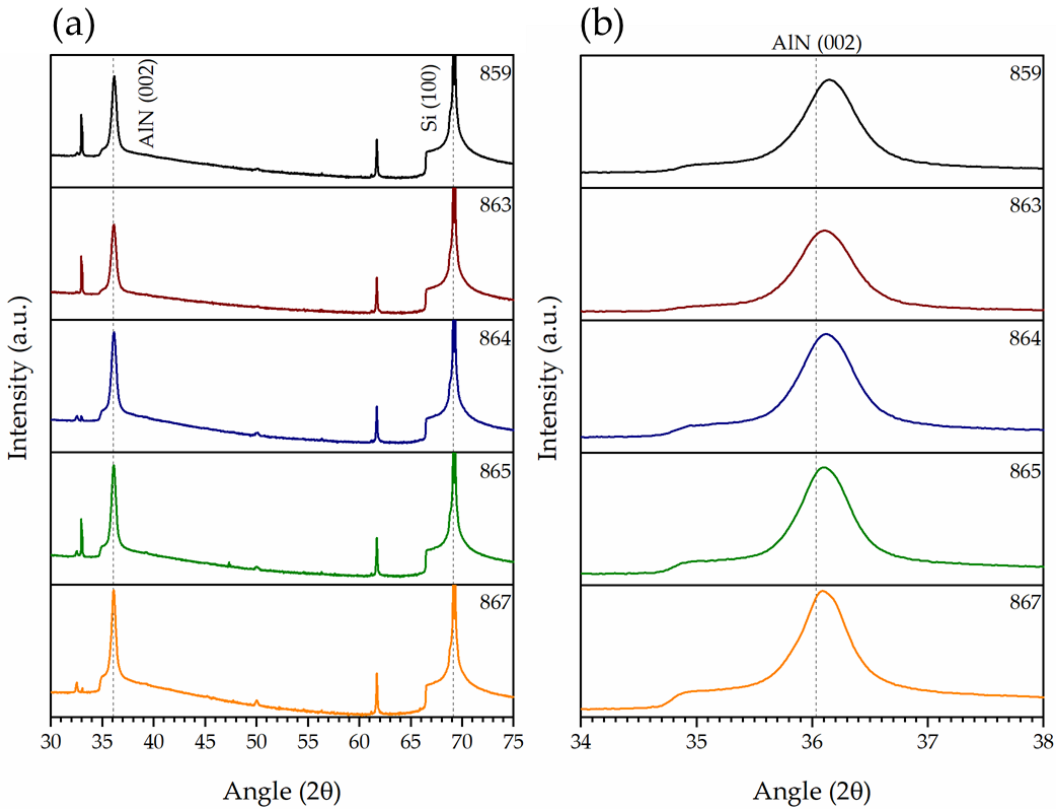

Figure 9-2: XRD spectra of selected AlN samples. (a) Full scanning range. (b) Range of interest for (002) AlN. Scans completed in Bragg-Brentano configuration with Cu (kα) radiation.

9.2 DC MS Nb and NbN SIS Films

Much of the research up until this point concerning SIS film coatings has been focused on their deposition onto bulk Nb cavities. Therefore, a series of SIS films were deposited onto Cu samples in order to determine the applicability of the proposed SIS film structure to Cu cavities. Following the successful development of the DC MS NbN and AlN films, SIS films with a Nb/AlN/NbN structure, shown in Figure 9-3 (a), were deposited onto electropolished Cu substrates, prepared as detailed in Chapter 5.7. Four SIS film samples were deposited with varying NbN film thickness, based on the work by Kubo [31]. The deposited NbN layer thicknesses were 80, 120 and 150 nm, while the Nb and AlN thicknesses were maintained at 4.5 μm and 30 nm respectively. The NbN recipe from sample 897, detailed in Table 7-6, was chosen for use in the deposition of the SIS films. The DC MS Nb recipe was as detailed in Table 8-1, and the AlN recipe stems from sample 867, presented in Table 9-2.

These films were deposited in a single coating run, without removal from the deposition chamber. It is imperative to deposit homogeneously thick outer insulating and superconducting layers in SIS film coatings in order to ensure optimum superconducting performance. As such, the substrate holder was set to rotate during the deposition of the AlN and NbN films, in order to avoid a thickness gradient in the film. Between the deposition of each layer, a period of two hours was used to allow for temperature stabilisation, due to the different substrate temperature set points. For consistency, the substrates were also pre-treated with an MF etching process for 10 min and the targets were sputter cleaned for 10 min as well. A single DC MS Nb layer was also deposited on a similar Cu substrate using the same conditions as the base layer of the SIS film for the purpose of superconducting performance comparison. The characterisation results for these films are summarised in Table 9-3.

Table 9-3: Topographic, crystallographic and superconducting properties of the DC MS SIS films, pure DC MS Nb film, DC MS Nb/AlN film and pure DC MS NbN film.

Sample (t_{NbN}) (nm)	**S_q (nm)**	**a_0 (Å)**	**d (nm)**	**H_{en} (mT)**	**H_{Max} (mT)**	**H_{tr} (x 10^{-3} emu)**	**T_c (Nb) (K)**	**T_c (NbN) (K)**
927 (120)	12.79 ± 2.49	4.3912	35.0	64.5	144.7	0.504	9.4	14.7
931 (118)	13.16 ± 1.61	4.3856	17.2	14.5	93.0	0.162	9.2	14.5
935 (78)	15.74 ± 1.22	4.3861	11.2	24.0	80.0	0.236	9.2	14.0
937 (147)	13.00 ± 2.15	4.3914	39.8	26.5	109.5	1.090	9.4	14.9
Nb	19.38 ± 4.33			52.0	130.5	0.497	9.4	
Nb/AlN	15.79 ± 1.70							
NbN (897)	6.36 ± 0.42	4.3964	26.6	2.0				15.9

An initial SIS film trial, albeit with a thin Nb layer, was deposited on a Si (100) sample to better understand the growth of the SIS layers and to fine-tune the process. An SEM image of this film, including layer thicknesses, is displayed in Figure 9-3 (b). It is clear that the NbN layer structure is similar to what was achieved for the single layer NbN sample (897) that this recipe is derived from, while the thicknesses of the AlN and NbN layers are homogeneous across the sample surface. The different films also present a well-connected interface with no visible voided regions.

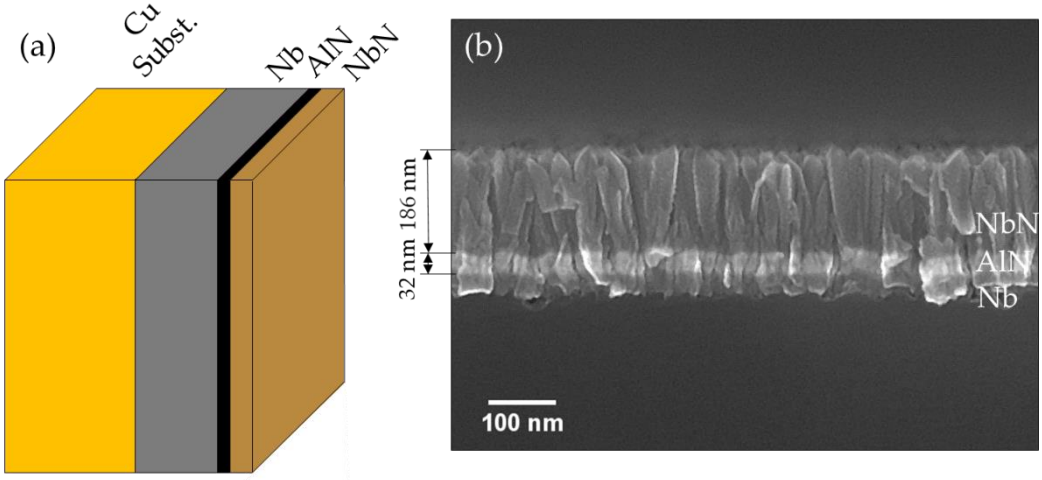

Figure 9-3: (a) Illustration of a multilayer SIS structure to be deposited onto electropolished Cu (b) SEM image of the pre-trial SIS film deposited on Si with a minimal thickness Nb (30 m) base layer.

Due to the difficulty of cleaving SIS films on Si, a Focused Ion Beam (FIB) was used to remove a section of the film on selected Cu SIS samples to understand their structure better. The result for sample 927, the best performing SIS sample in this series, is presented in Figure 9-4 (a). It is evident that the interface between the Cu substrate and the Nb film is plagued by voids. Further investigations of the other samples provided evidence of similar interfacial voids as well as partial film delamination, significantly undermining the use of SIS films. A section of sample 927 was also investigated with TEM. A magnified image of the near-surface multilayer (ML) structure is shown in Figure 9-4 (b). The AlN and NbN layers display a conformal, homogeneous thickness, of ~ 30 and ~ 150 nm respectively, across the entire surface. The interface between the different material layers is also free of voids. It is also apparent that the Nb film surface is considerably rougher than the underlying Cu surface, as shown by the surface roughness results in Table 9-3.

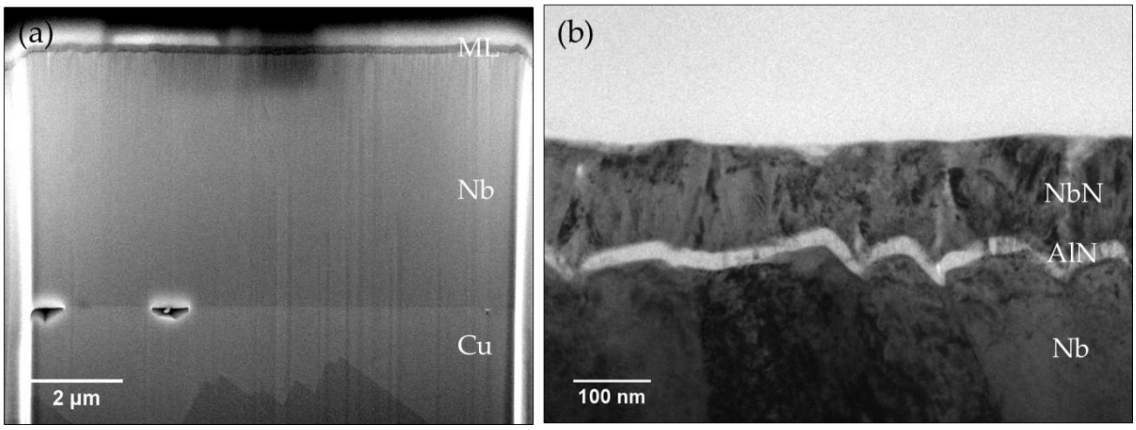

Figure 9-4: (a) SEM image showing a FIB cut through full thickness of sample 927 and (b) Magnified TEM image of the multilayer (ML) SIS structure of sample 927.

The proposed lattice matching between the multilayer interfaces was investigated via HRTEM. Multiple different positions were examined in order to determine whether the relationship was consistent across the film. The HRTEMs, as well as magnified sections of the Nb, AlN and NbN layers and the FFT of the selected areas, are presented in Figure 9-5.

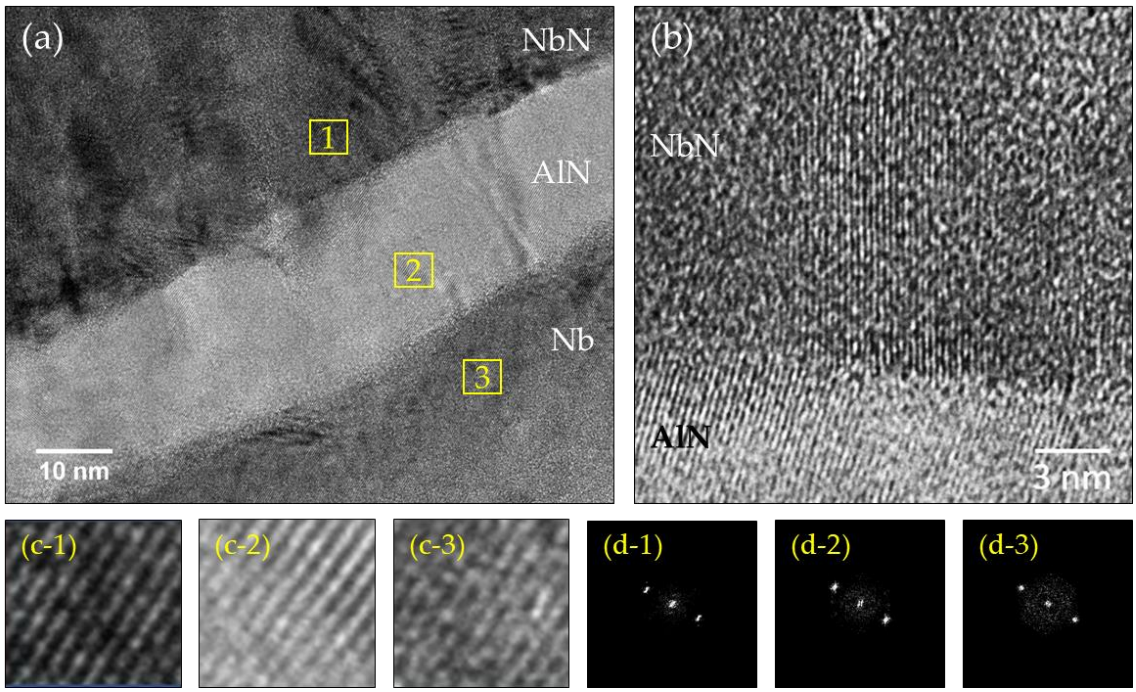

Figure 9-5: HRTEM of the interface between the Nb, AlN and NbN layers of 927. (a) Overview of the proposed NbN (111)/AlN (111) coherent interface. (b) Magnified view of the proposed coherent NbN (111)/AlN (002) lattice plane position. (c) Magnified sections of (a). (d) Corresponding FFT images of (a).

Figures (a), (c) and (d) display a similar orientation and interplanar distance, for both NbN grown on AlN and AlN grown on Nb. This indicates the high quality epitaxial coherency of these layers and is attributed to a NbN (111)/AlN (111) relationship. No evidence of AlN (111)

was found during initial trials; however, this may be due to the influence of the Nb base layer as opposed to the Si (100) wafer used during testing. The lack of the AlN (111) peak in the XRD spectra of the SIS films is also likely due to the overlap of this peak with that of the NbN (111) peak. This arrangement is found to vary along the length of the sample however, with some positions displaying differing NbN and AlN orientation relationships. The interface imaged in (b) shows the sought after NbN (111)/AlN (002) relationship and presents a further coherent, epitaxial relationship between these two layers. Both of these interfacial structures have previously been reported by Wen *et al*, who indicated a change in the relationship according to the thickness of the AlN layer [274].

The deposited NbN layer is found to grow in a somewhat disjointed columnar fashion. Given that Nb is a good getter of O_2 and readily forms the oxide Nb_2O_5, this type of growth is known to result in the formation of both oxides and oxynitrides. This subsequently leads to a decrease in the superconducting performance of the film. The increased presence of O within the NbN film was investigated with STEM EDX, the results of which are shown in Figure 9-6. The O map clearly indicates its penetration into the thickness of the NbN film. There is a complete lack of O within the AlN layer while a small percentage can be found in the Nb layer as well. The results also indicate no inter-diffusion of the different sputtered species. The blurring of the layers in some regions is due to the overlapping features through the thickness of the STEM sample while the C contamination is due to handling of the sample following deposition.

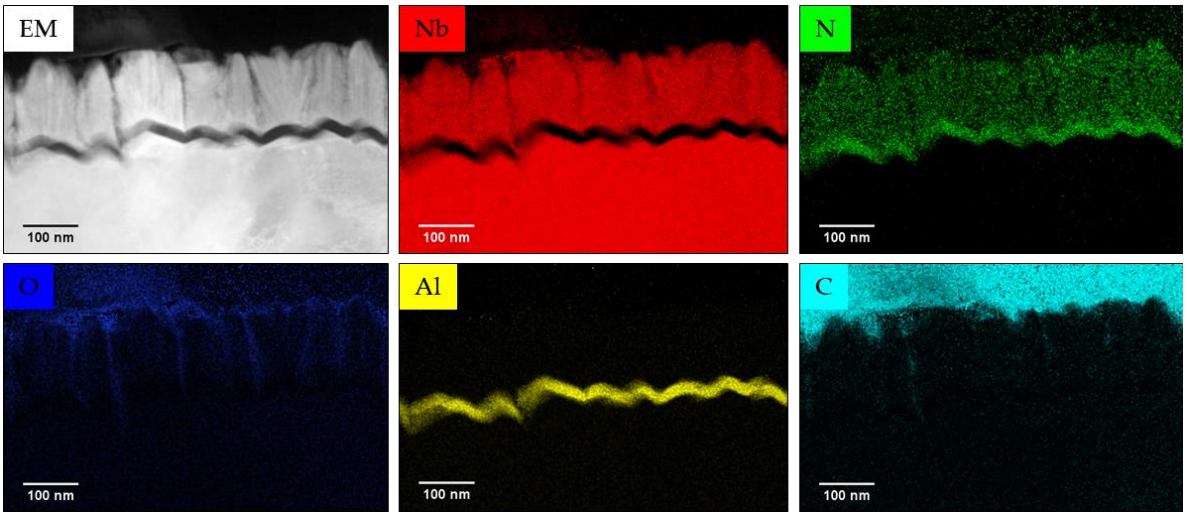

Figure 9-6: STEM EDX mapping results from DC MS SIS sample 927, displayed in atom percent.

The presence of the O in the NbN layer is also reflected in the SIMS depth profile measurements, shown in Figure 9-7, which were obtained from the best performing SIS

sample, 927. The initially large signal is due to surface contamination. These contaminants, such as K^+, Ca^+ and Na^+ were measured at the surface and decreased to insignificant levels within a short period and have therefore been excluded here. In this instance, the NbO^+ signal is used to identify the presence of O within the sample, as the sample was probed in the positive detection mode, due to the increased number of available signals. This confirms the formation of oxynitrides in the NbN layer, with the O level decreasing substantially in the AlN and Nb layers. Importantly, a relatively insignificant signal from all other species is observed in the Nb film, indicative of its clean state. A sizeable increase in the Nb^{2+} and Nb^{3+} signal is observed when transitioning from the NbN layer to the Nb layer and indicates their involvement in the formation of the NbN film.

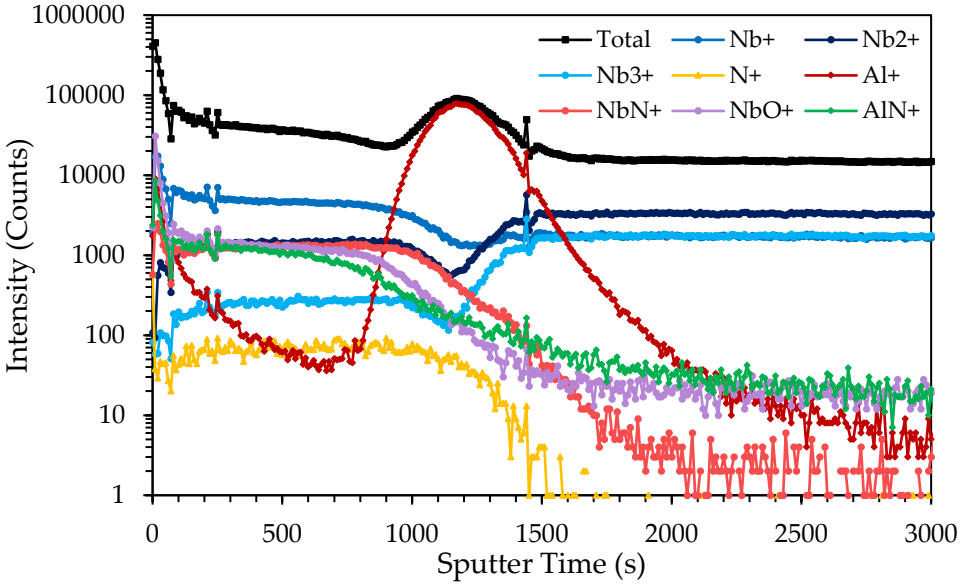

Figure 9-7: SIMS depth profile measurement of DC MS Nb base layer SIS film sample 927, measured in positive mode.

The surface roughness values, measured by AFM, for the SIS film samples, the pure Nb film, the Nb + AlN film and the single NbN layer film (897) are shown in Table 9-3. Of the SIS films, sample 927 has the lowest surface roughness; however, the variance between the samples is small. The results indicate a significantly rougher surface for the SIS films compared to that of the individual NbN layer that they are based on (897). The single Nb layer sample possesses the highest roughness of all samples, while the Nb/AlN bi-layer possesses a roughness value in between that of the Nb layer and the SIS film. The results point to the noteworthy influence of the Nb layer on the resultant SIS film surface roughness. The influence of the Nb layer is further visible when comparing the surface structure of the single layer NbN film with the single layer Nb and SIS film surfaces. The surfaces of the single

layer NbN films, presented in Chapter 7.2, consisted of homogeneous grain structures whereas the surfaces of the SIS films display features similar to those of the Nb films shown in Chapter 8.2, consisting of a multitude of different grain structures. However, from Figure 9-8 it is evident that the nanoscale NbN grains themselves are still homogeneously grown on the surface of the Nb/AlN layers.

Further inspections of the SIS film surfaces, presented in Figure 9-8, indicate a distinct difference between sample 927 and the rest of the samples. Sample 927, Figure 9-8 (a), displays a dense, coherent film surface while the rest of the DC MS SIS samples, which have a similar surface to Figure 9-8 (b), possess evidence of gaps between the different grain structures. This can lead to inhomogeneous shielding of the underlying Nb layer and is accredited to the heightened roughness of the underlying Nb layer.

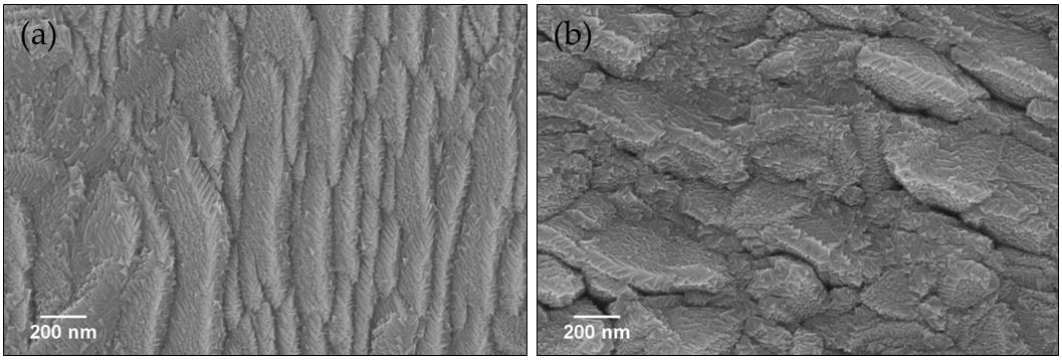

Figure 9-8: Representative SEM images of the SIS film surface. (a) Displays sample 927 while (b) displays sample 935. These images indicate the difference in density and quality of the two surfaces.

The XRD spectra for the NbN film that the SIS samples utilise, and the best performing SIS film, 927, are shown in Figure 9-9. The results for the NbN layer used in the SIS film are consistent with what was measured with the single NbN layer film of sample 897. Once more, the film is characterised by a high intensity δ-NbN (111) peak at 35.4° as well as the presence of a secondary δ'-NbN peak at 34.6°. The AlN peak is indiscernible from the XRD patterns, due to its low relative thickness. The main peak present in the scan of sample 927 is that of the Nb layer, identified by the peak at 38.45° [245].

The FWHM of the NbN peak is found to decrease with increasing NbN film thickness. Consequently, the crystallite size increases with increasing NbN layer thickness, from 10 nm for NbN thickness of 78 nm to 39.6 nm for NbN thickness of 147 nm. This is larger than that achieved by the single layer film (26.55 nm). The out-of-plane lattice parameter of these films is slightly reduced compared to those of the individual layer, displaying a change in the stress

state of the film, likely due to the AlN interlayer, which provides a lattice matched interface. These values are presented in Table 9-3.

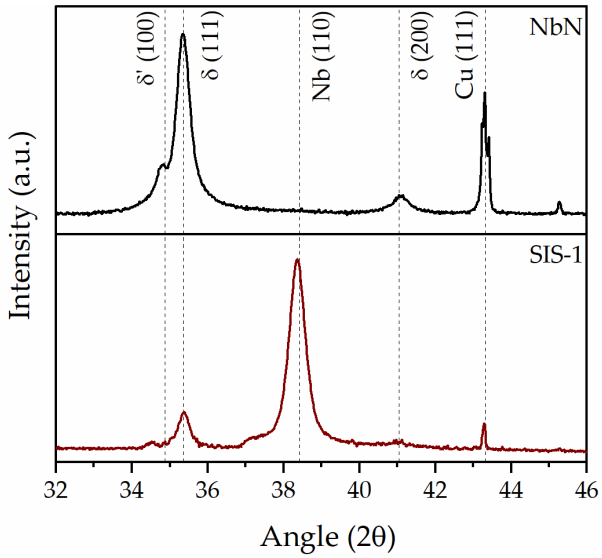

Figure 9-9: XRD Spectra of the NbN sample whose recipe was used to deposit the SIS film (top) and the resultant SIS film (bottom).

The critical temperature of the SIS films was measured using an AC susceptometer, which is able to detect the superconducting transition of both the underlying Nb layer as well as the outer NbN layer. The results for the four SIS films are illustrated in Figure 9-10. The critical temperature of the outer superconducting layer in the SIS films is noticeably lower than the single NbN layer, achieving a T_c = 14.7 K in sample 927, compared to T_c = 15.9 K for the single NbN layer (897). This T_c reduction is believed to be due to a combination of reduced film thickness in SIS structures and the increased roughness of the underlying Nb and AlN layers. Besides the observed T_c reduction, the transition temperature of the NbN layer is found to increase with increasing film thickness, though there is a more pronounced relationship between the crystallite size and the transition temperature. This was previously shown for ultrathin single layer NbN films [113]. Further results of the superconducting measurements are also displayed in Table 9-3.

The entry field (H_{en}) measurements of the SIS films were also conducted using the VSM. As described above, the sample is immersed in the applied magnetic field H_a. Here, both the Cu substrate-to-Nb film interface and the NbN ("top") surface of the sample are exposed to the applied field. In this configuration, it seems likely that the signal of the Meissner effect comes mainly from the Nb film, which is approximately 20 times thicker than the NbN top-layer. However, the quality of the Nb surface at the substrate side, predominately in terms of the surface roughness, is higher than that at the Nb-to-AlN interface and much higher than that

of the NbN surface at the NbN-to-vacuum interface. Therefore, the field penetration is believed to start at the NbN-to-vacuum interface, where after the field propagates towards the Nb layer at much smaller applied fields than those required for penetration from the substrate side of the Nb layer. Support for this is found in the considerably different H_{en} values determined for all four SIS samples despite the same Cu substrate and Nb deposition procedure being used for all four samples. Nevertheless, the magnetic moment measured with the VSM originates, predominantly, from the Nb layer. Subtle changes in the measured moment that would indicate field penetration into the NbN layer cannot be realistically detected. The entry field values determined for the SIS samples therefore mark the start of field penetration into the SIS system as a whole.

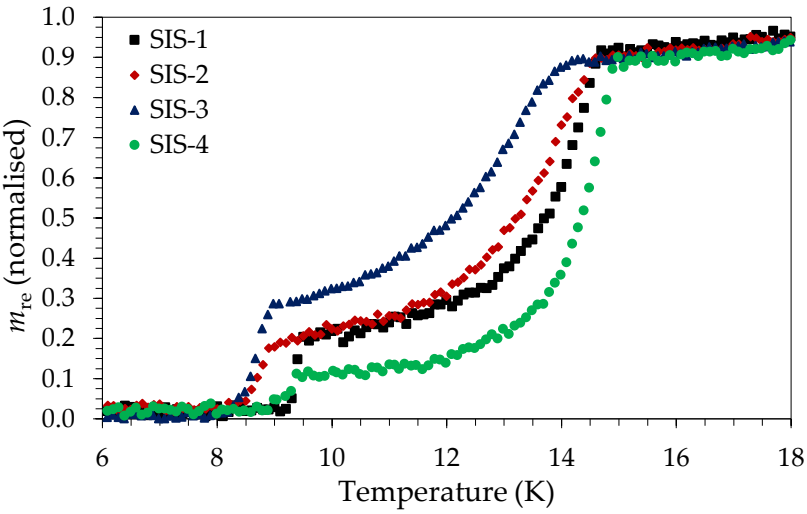

Figure 9-10: Normalised real component of the AC susceptibility measurements detailing the transition temperature of the Nb and NbN layers of the DC MS Nb base layer SIS films.

As presented in Table 9-3, samples 931, 935 and 937 display H_{en} values significantly lower than the individual Nb layer sample. On the other hand, sample 927 displays H_{en} = 64.5 mT, surpassing the value obtained with the pure Nb sample, H_{en} = 52.0 mT. This result indicates the possibility of delaying the field penetration into the Nb layer, as predicted for SIS film coatings.

The poorer entry field results for some samples are believed to be due to the lower surface quality of these films, as presented in Figure 9-8. However, damage created at the thin film edges in the cutting process could also play some role, although the same procedure was followed and the same cut-off machine was used in preparation of all the investigated samples. In any case, the homogeneity and density of the surface layer is of utmost importance in order to provide the sought after shielding effect from SIS films.

Figure 9-11 presents the DC magnetisation curves as a function of the applied field (H_a), measured at 4.2 K for the two superconducting component films of the SIS film coatings: the single DC MS Nb layer and the single NbN layer used in the SIS films (897). The best performing SIS film (927) is also included for comparison. Figure 9-11 (a) displays sections of the full magnetisation loops measured on the three samples. These loops indicate the presence of the surface barrier to the magnetic flux penetration for both the SIS and Nb films, more pronounced for the SIS film, even though there is no visible barrier in the single NbN film itself. The NbN layer instead presents a smooth curve, indicative of a stable flux pinning state. The Nb and SIS films also display similar levels of trapped flux while the maximum flux value of the SIS film has increased above that of the Nb film. In (b) the virgin magnetisation curves are presented, in a plot where the measured sample magnetic moment $m(H_a)$ is divided by a linear field dependence of the magnetic moment followed in the Meissner shielding state $m_{lin} = c\,H_a$ (c – constant, different value for each sample). The deviation from the Meissner state, marked by the decline in m/m_{lin}, appears significantly earlier for the single NbN layer than the Nb and SIS films. The SIS film displays very similar curves to the Nb film although it possesses a delayed deviation from the Meissner state, indicating a greater entry field.

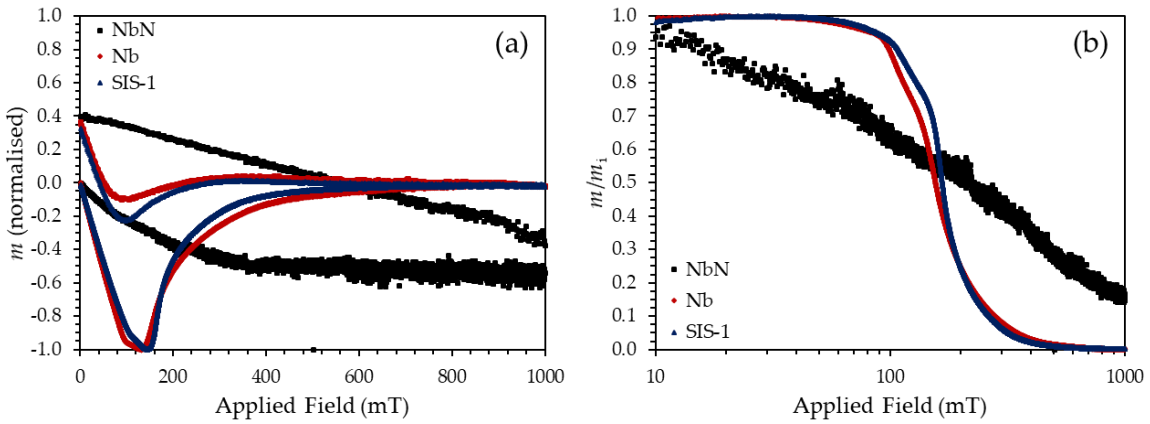

Figure 9-11: (a) Sections of the normalised magnetisation loops for the single Nb layer (black), single NbN film (897) (red) and the SIS film (927) (blue) are plotted. This includes the virgin magnetisation loop and the positive portion of the reverse loop full magnetisation loops as a function of magnetic field, at 4.2 K. (b) The normalised dc hysteresis curves of the same samples.

The above results provide an indication of the possible enhancement of the entry field value associated with SIS films when compared to single layer Nb films, therefore displaying the shielding effect proposed by Gurevich [5]. However, the performance of the SIS films is dependent on the homogeneity of the film surface and as such, is greatly affected by the quality and surface roughness of the Nb base layer. Because of this, efforts were made to

investigate the deposition of HiPIMS Nb films in order to determine the relative improvement of the SIS films. This is documented in Chapter 8.2. Because of the inconsistency in the quality of the SIS layer surface and the subsequent variability in the entry field values, no specific shielding layer thicknesses can be chosen to best protect the Nb film at this time. Due to the different superconducting properties of the separate NbN films, it is also important to determine whether the moderate T_c, high entry field (δ-NbN (200)) or the high T_c, low entry field (δ-NbN (111)) films provide superior shielding for the base Nb layer in SIS film coatings. The effects of the different NbN films as shielding layers is documented next, in Chapter 9.3.

9.3 HiPIMS Nb and DC MS NbN SIS Films

As detailed in Chapter 8.2, the use of the HiPIMS deposition technique resulted in significant performance improvements to the deposited Nb thin films. As such, all further multilayer SIS films were deposited using the HiPIMS Nb recipe shown in Table 8-16 as the base layer. The AlN layer recipe stems from sample 867, presented in Table 9-2. The different superconducting properties of the separate NbN films, detailed in Chapter 7.2, indicate a potential performance difference when used in SIS film coatings. In order to determine which superconducting parameter is most important when choosing a shielding layer, four samples, with outer layer thicknesses of 100, 150, 200 and 250 nm, were deposited with the NbN recipe from sample 899 (High T_c) and three samples, with outer layer thicknesses of 150, 200 and 250 nm, were deposited using the NbN recipe from sample 790 (High H_{en}). These are indicated in Table 9-4. The Nb layer thickness was maintained at ~ 3.5 μm while the AlN layer thickness was kept at 30 nm.

Table 9-4: Topographic, crystallographic and superconducting properties of HiPIMS Nb-based SIS films, HiPIMS Nb/AlN film and the individual HiPIMS Nb film.

Sample (nm)	**t_{NbN} (nm)**	**S_q (nm)**	**a_0 (Å)**	**d (nm)**	**H_{en} (mT)**	**H_{Max} (mT)**	**H_{tr} (x 10^{-3} emu)**	**T_c (Nb) (K)**	**T_c (NbN) (K)**
1165 (899)	207	12.05 ± 0.62	4.3949	25.3	39.0	158.41	1.887	9.3	15.3
1166 (899)	155	12.80 ± 0.87	4.3955	35.3	38.0	156.49	1.654	9.3	15.8
1167 (899)	99	13.21 ± 1.86	4.3964	24.0	34.0	155.58	1.090	9.3	15.5
1169 (899)	254	11.47 ± 0.27	4.3954	39.8	33.0	158.11	1.758	9.3	16.1
1170 (790)	181	12.29 ± 3.85	4.3958	26.9	61.0	153.31	2.025	9.3	15.2
1171 (790)	144	10.62 ± 3.53	4.3972	38.3	61.5	157.75	5.782	9.4	15.0
1172 (790)	246	13.13 ± 0.48	4.3973	31.8	59.0	157.76	2.641	9.3	15.3
1176 (AlN)		9.71 ± 1.31							
1077 (Nb)		9.50 ± 3.07			103.0	157.33	1.483	9.35	

All samples were prepared as per the optimised surface treatment procedure detailed in Chapter 5.7. Again, in order to maintain the film thickness homogeneity, the sample holder was set to rotate continuously during the coating. Because of this, the microstructure of the NbN films changed considerably. This is visible for both sets of SIS samples in Figure 9-12, which shows a comparison between the single layer growth structure, (a) and (c), and the multilayer structures, (b) and (d), both imaged on Si (100) witness samples for ease of investigation. Figures (a) and (b) pertain to the SIS films deposited with the NbN recipe from sample 790 and figures (c) and (d) pertain to the SIS films deposited with the NbN recipe of sample 899. In both sets, the films change from a dense microstructure in the individual NbN films to a pronounced zone T-like, columnar structure with significant gaps between the individual columns and a feather-like growth. This is attributed to the large variation in the arrival angle of the adatoms on substrate surface.

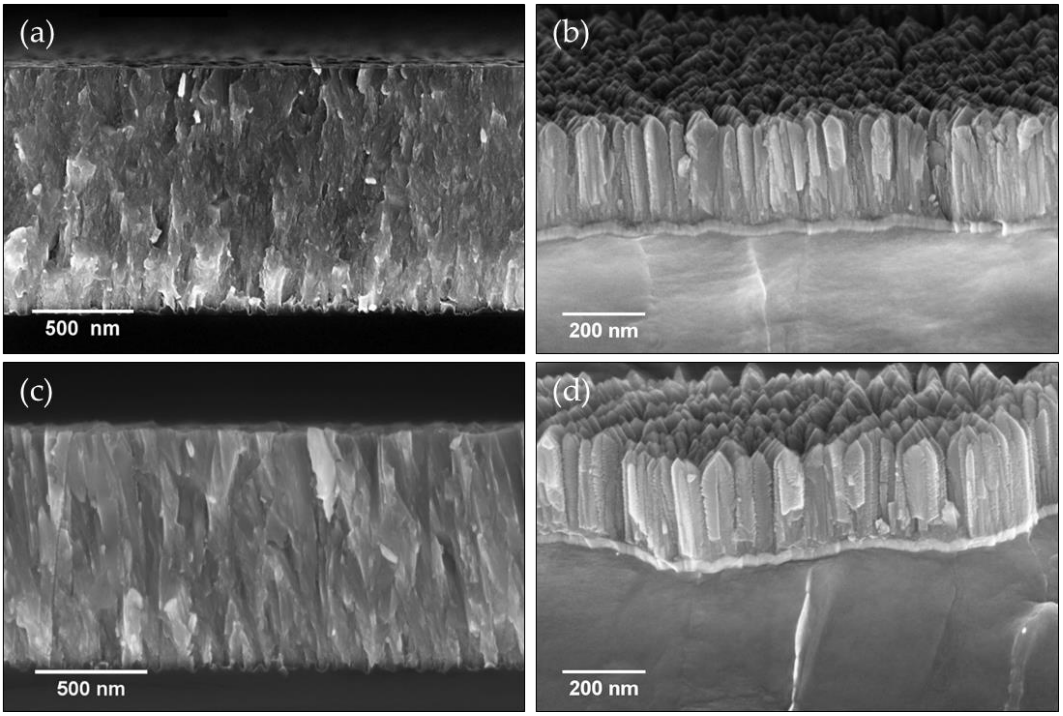

Figure 9-12: SEM images of the cross-sections of the single-layer NbN film deposited on Si and the same film except deposited on Si in a multilayer with sample holder rotation. (a) displays sample 790, (b) shows sample 1169, which uses the recipe of sample 790. (c) Displays sample 899, (d) shows sample 1172, which uses the recipe of sample 899.

The results from a TEM investigation of sample 1171, displayed in Figure 9-13, indicate the significant influence of the Nb film on the AlN and NbN layers. Due to careful sample preparation, the overview image in (a) and the magnified image in (b) capture the interface for two pieces of the same sample. The upper piece possesses a smooth Nb grain and a

subsequent smooth NbN surface. The upper piece also shows a relatively dense, columnar microstructure, similar to that shown in Figure 9-12 (a) and (c). Conversely, the lower piece possesses a rougher Nb grain structure, which leads to zone T-like growth of the NbN film and a rougher resultant surface. This piece is similar to that shown in Figure 9-12 (b) and (d). Nevertheless, these films display an improved interface and surface compared to the DC MS Nb SIS films, allowing for improved shielding conditions. The HRTEM investigation of this position, not shown here, also indicated a coherent epitaxial growth of these layers, similar to that shown for the DC MS films in Figure 9-5.

In light of the similar NbN film microstructure, the surface roughness of these films, visible in Table 9-4, is consistent, regardless of the NbN recipe. Encouragingly, these films display surface roughness values less than those measured for the DC MS Nb SIS films, due to the use of a HiPIMS Nb base layer. This was previously shown in Chapter 8.2, where a decrease in the surface roughness of the individual HiPIMS Nb film relative to the DC MS Nb film was found.

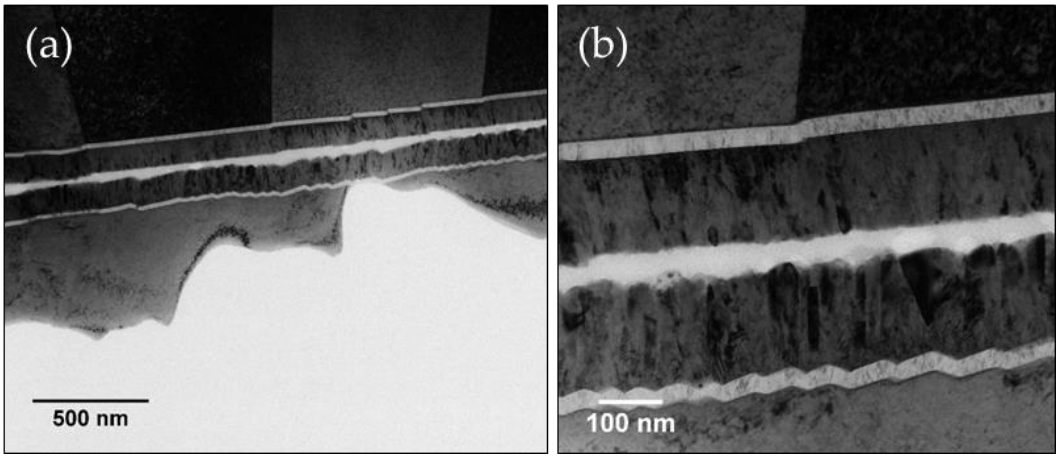

Figure 9-13: TEM and HRTEM images of the interface between the Nb, AlN and NbN layers of 1171. (a) Overview of the investigated position. (b) Magnified view of the investigated position.

The results of the positive SIMS depth profile measurements on the HiPIMS Nb SIS films and STEM EDX analysis, not shown here, are similar to those presented for the DC MS SIS films, displayed in Figure 9-7. The presence of O in the NbN layer of these films, as was seen in the DC MS SIS films, is largely due to the disjointed columnar structure of the NbN film, resulting in the formation of oxynitrides. Importantly, the O signal is once again insignificantly small in the underlying HiPIMS Nb layer.

The microstructural changes in the NbN layers were also apparent in the crystallographic analysis results. The XRD spectra of the original NbN films (790 and 899) as well as the best

and worst performing SIS films based on each recipe are displayed in log scale in Figure 9-14. The films based on sample 899 continue to display a similar NbN phase composition in the SIS films as was identified for the individual NbN film, albeit with an absence of the δ-NbN (200) phase. On the other hand, the SIS films based on sample 790 show a phase transition of the NbN film due to the use of table rotation during the SIS film coating. This was later confirmed by depositing a series of samples, with and without table rotation, and analysing the resultant film structure and XRD spectra. With the addition of table rotation, films change from a relative δ-NbN (200) oriented film to a δ-NbN (111) oriented film. This phase formation is then similar to the results achieved for the SIS films based on sample 899. The nanocrystalline nature of the films also changed, as is visible in Figure 9-12 (a) and (b), increasing from a crystallite size of ~ 6 nm in the original film to ~ 25 nm in the SIS films. The lattice parameters of the δ-NbN (111) peak for all films is ~ 4.396 Å, regardless of the recipe used, and is in the region of that measured for the original sample 899 (4.3956 Å).

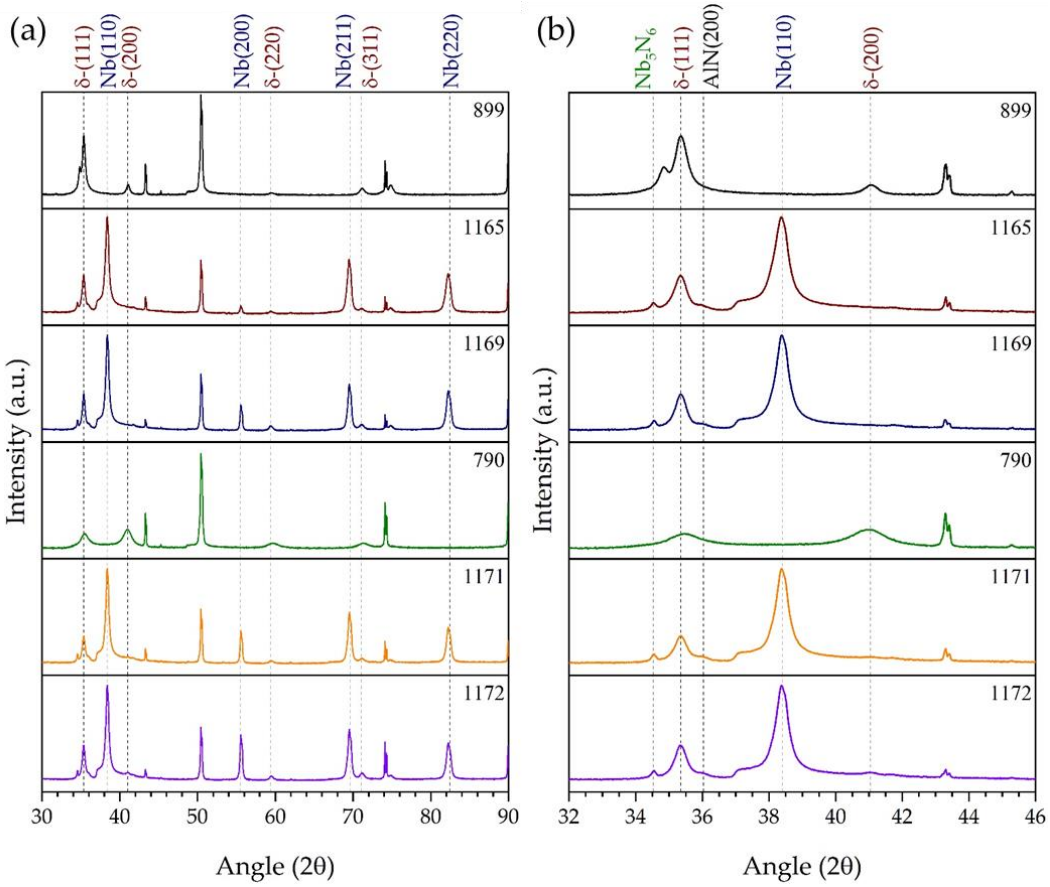

Figure 9-14: XRD spectra, displayed in log scale, of the original NbN films (790 and 899) and the best and worst performing SIS films which utilised each of these NbN recipes. (a) Complete scan range. The unidentified peaks pertain to the Cu substrate. (b) Region of interest used to identify the NbN phases.

In order to accurately determine the transition temperature of the NbN layers in the SIS films, each sample was measured using an AC susceptometer attachment. Despite the similar results for the microstructure and crystallographic properties of these two sets of SIS films, the superconducting results displayed a clear division between the two NbN recipes. The normalised results of the T_c measurements are displayed in Figure 9-15. Upon initial inspection, the samples based on sample 899 display consistently higher NbN T_c values compared to those based on sample 790, in line with the results for the original NbN films. The NbN films based on sample 790, which were deposited in these SIS films, display an increased T_c compared to the original films though. This is attributed to the change in the crystallographic properties, and NbN phase, of the films brought on by the use of table rotation. Both sets of SIS films display a general increase in the NbN T_c with increasing NbN film thickness, similar to what was observed with the DC MS SIS films. One important note, the highest T_c = 16.1 K for sample 1169 is the same value as that achieved for the individual NbN layer. This is attributed to the superior surface afforded to the growth of the AlN and NbN layer due to the use of the HiPIMS Nb base layer. The T_c of the HiPIMS Nb base layer, measured during cooldown of the VSM, is found to be consistent for all of the SIS film samples, T_c = 9.3 K, equal to that of the individual HiPIMS Nb layer.

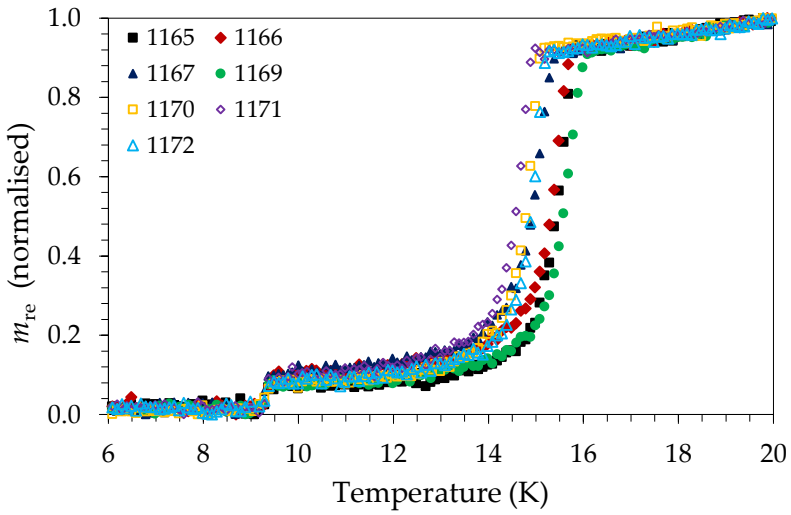

Figure 9-15: Normalised real component of the AC susceptibility measurements detailing the transition temperatures of the Nb and NbN layers of the HiPIMS Nb base layer SIS films. Solid symbols denote NbN recipe 899 while the empty symbols denote recipe 790.

Based on the VSM results displayed in Figure 9-16, all of the samples based on sample 790 displayed higher entry field values than those based on sample 899. This is most evident when comparing (c) and (d), where the deviation of the Meissner state is noticeably earlier for the SIS films based on sample 899 (c). For reference, the maximum value for the SIS films

based on sample 899 was H_{en} = 39.0 ± 1.95 mT, while those based on sample 790 achieved a minimum of H_{en} = 59.0 ± 2.95 mT. However, the maximum value of these SIS films (61.5 ± 3.01 mT) was lower than the maximum value achieved for both the individual HiPIMS Nb film and the best entry field achieved for the DC MS Nb SIS films. This indicates the need for optimisation of the deposition process. Encouragingly though, the values of H_{en} for the HiPIMS Nb based SIS films are consistently high, further indicating the superiority of the HiPIMS Nb base layer. Interestingly, the trapped flux for the samples based on sample 790 was higher than those based on sample 899, shown by the increased magnetisation loop size in (b) compared to (a). The presence of a surface barrier is also more evident for the samples based on sample 899.

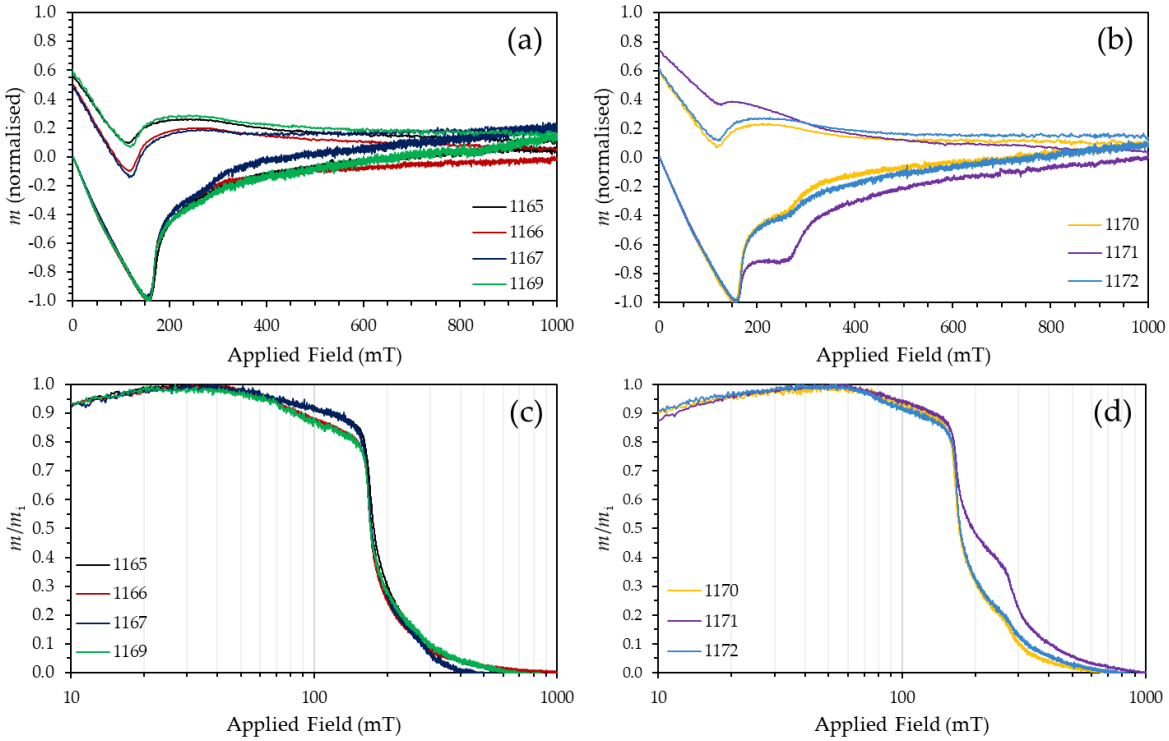

Figure 9-16: Superconducting results for the two sets of HiPIMS Nb based SIS films. (a) and (b) display sections of the normalised magnetisation loops of the samples based on sample 899 and 790 respectively. (c) and (d) display the Meissner state ratio of the samples based on sample 899 and 790 respectively.

The effects of the different recipes and the NbN film thicknesses on the superconducting transition temperature and entry field are detailed in Figure 9-17. Here the increase in T_c with increasing NbN film thickness is clearly visible for both sets of samples as well as the higher T_c of films deposited with the recipe from sample 899. In terms of the entry field, specific maximums are visible for the film thicknesses of the different NbN layers. In this instance, a maximum at ~ 150 nm for the samples deposited with 790 and between ~ 150 and 200 nm for

sample 899 is found. This is reported to indicate a change in the "cleanliness" of the NbN films [31]. As the films become cleaner, the NbN layer thickness required for maximum shielding increases.

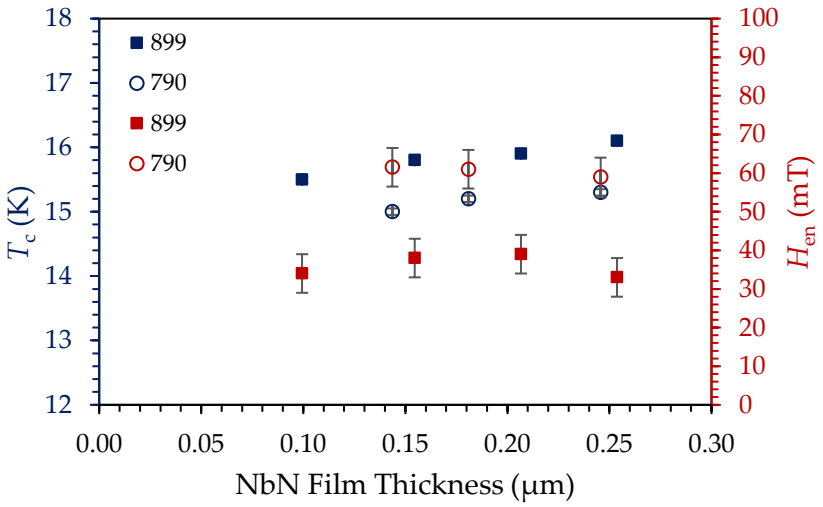

Figure 9-17: Superconducting transition temperature and entry field values as a function of NbN film thickness for SIS film samples deposited with HiPIMS Nb base layers and two separate DC MS NbN film recipes. Sample ID detailed in plot.

Based on the above results, it can be said that the use of HiPIMS Nb as a base layer provides a better surface on which to deposit subsequent layers, which leads to increased T_c values for the outer shielding layer and more consistent SIS film performance. The use of NbN films, which display higher H_{en} values in individual layer format, is found to result in SIS films that also display higher H_{en} values. Therefore, NbN films with higher H_{en} values should be pursued for use in SIS film coatings. In conjunction with this, the use of substrate rotation leads to an unwanted change of the NbN phase as well as the film microstructure, with the decreased density observed in these SIS films believed to be the reason for the lower H_{en} values compared to the individual HiPIMS Nb sample. Thus, methods to overcome this should be implemented. Based on the penetration of O into the NbN layer, as detailed in Figure 9-6, it is also necessary to improve the density of the NbN shielding layer. As such, the use of HiPIMS to deposit the NbN layer was also explored and is detailed in Chapter 9.4.

9.4 HiPIMS Nb and NbN SIS Films

The successful implementation of the HiPIMS Nb base layer in the SIS film coatings in Chapter 9.3 was overshadowed by the observed microstructural and phase changes resulting from the use of continuous substrate rotation, and the subsequent less than ideal

superconducting properties of these films. In order to overcome these issues, instead of completely rotating the substrates, a small "pulse" of the substrate, back and forth in front of the target to minimise the change in the incidence angle during the deposition of the AlN and NbN films, was implemented. Coupled to this, the use of HIPIMS for the deposition of the NbN film also reduces the spread in incidence angle due to the ionisation of the sputtered material, while facilitating an increase in the density of the NbN film and a subsequent reduction in O contamination, as found in Chapter 7.3.

Similar to the previous SIS samples, these samples were deposited in a single coating run, without removal from the deposition chamber. The substrates were also pre-treated with an MF etching process for 10 min followed by 10 min of target sputter cleaning. All of the samples were deposited with a Nb base layer thickness of ~ 3.5 μm using the HiPIMS Nb recipe shown in Table 8-16, while the AlN recipe from sample 867, presented in Table 9-2, and was maintained for these samples. Following discussions with A. Gurevich as part of the ARIES research program, two separate values for the AlN layer thickness were investigated; ~ 10 and ~ 30 nm, to verify the effects thereof. Based on the results of Chapter 9.3, the HiPIMS NbN film with the highest measured H_{en} at the time of coating was chosen, with thicknesses ranging from 75 to 232 nm. The recipe for this sample is detailed in Table 7-9.

Importantly, due to the unstable operation of the turbopump during the initial series of SIS film samples (1496 – 1573), a second series of samples was deposited at a later time (1594 – 1600), allowing for AlN thickness variation. A summary of the samples and their characterisation results are displayed in Table 9-5, with the split between the two series indicated. The data for the base HiPIMS Nb layer and the individual HiPIMS NbN layer are also included.

In preparation for SIS film deposition, a series of Si (100) samples were coated with different substrate-holder pulse angles to determine which value resulted in the film microstructure and crystal structure most similar to the original, individual HiPIMS NbN film selected for use in the SIS films (1296). Pulse angles were successively reduced from 30° (either side of the target) to 10°, during both the AlN and HiPIMS NbN coatings. The results of the pulse tests, and a comparison to the original film, are displayed in Figure 9-18. The film microstructure of the original HiPIMS NbN film, shown in (a), is dense and columnar with a smooth surface. With the addition of pulsing, the density and connectivity of the films decreases for both the 30° and 15° pulse sizes, shown in (b) and (c) respectively. The surface roughness of the 30° sample is also found to be significantly higher. The use of a 10° pulse angle results in a return of the film microstructure to a dense columnar structure, shown in (d).

Table 9-5: Topographic, crystallographic and superconducting properties of HiPIMS Nb/AlN/HiPIMS NbN SIS films, the individual HiPIMS Nb film and the individual HiPIMS NbN film.

Sample (t_{NbN}-t_{AlN}) (nm)	**S_q (nm)**	**a_0 (NbN) (Å)**	**d (NbN) (nm)**	**H_{en} (mT)**	**H_{tr} (x 10^{-3} emu)**	**T_c (Nb) (K)**	**T_c (NbN) (K)**
1496 (204-10)	12.48 ± 0.36	4.4596		88.0	2.2234	9.3	12.58
1497 (157-7)	14.11 ± 3.24	4.4576		57.0	2.4497	9.3	11.68
1498 (232-9)	12.01 ± 2.03	4.4410	43.8	80.0	3.5930	9.3	12.88
1572 (102-8)	10.35 ± 0.19	4.4163	8.7	52.0	4.6660	9.35	12.78
1573 (75-9)	10.18 ± 1.47	4.4200	12.2	63.0	3.6450	9.35	11.98
1594 (100-9)	11.07 ± 1.17	4.4130	13.3	62.0	0.1634	9.3	12.68
1595 (143-9)	8.93 ± 2.52	4.4102	14.4	30.0	0.2507	9.3	13.68
1596 (173-9)	7.90 ± 0.90	4.4094	11.9	36.0	0.2187	9.3	13.98
1597 (207-10)	9.64 ± 1.51	4.4101	15.3	31.0	0.2542	9.3	14.08
1598 (179-29)	11.16 ± 0.07	4.4080	16.4	68.0	0.3197	9.25	14.38
1599 (209-30)	11.20 ± 4.50	4.4079	20.0	40.0	0.6528	9.3	14.48
1600 (147-32)	9.97 ± 2.11	4.4106	19.1	56.0	0.5453	9.3	14.28
1077 (Nb)	9.50 ± 3.07	-	-	103.0	1.483	9.35	-
1296 (NbN)	8.64 ± 1.03	4.3959	20.40	28	-	-	14.6

The XRD patterns of the preparatory films, not shown here, display a similar change of the NbN film from a mixture of NbN (111) and Nb_5N_6 to a single NbN (111) orientation for pulse angles > 10°, similar to what was shown for the full rotation of the substrates in Chapter 9.3. With the reduced pulse angles, the XRD spectra indicate a return to the same crystal structure combination as the stationary coated, individual film. The AlN films all display the sought after AlN (002) orientation for all pulse angles. Following this, all further SIS films were coated with a 10° substrate pulse in front of the target for both the AlN and NbN coatings.

The results of this are illustrated for two separate HiPIMS SIS samples, both coated with ~ 200 nm NbN and AlN thicknesses of (e) 10 nm (sample 1597) and (f) 30 nm (sample 1599). Both of these films display a similar microstructure. Therefore, the apparent changes between the film observed in (d) and these are due to the HiPIMS Nb base layer. The film still presents a denser microstructure with a significantly smoother surface compared to previous SIS film samples. It is evident that the deposition of the Nb base layer has resulted in a shift to more zone T film growth, where the grains increase in size with increasing film thickness. These widening NbN columns typically occur where a surface "mound" is present on the Nb surface. Thus, the microstructure and surface morphology of the NbN film is largely dependent on the underlying Nb film.

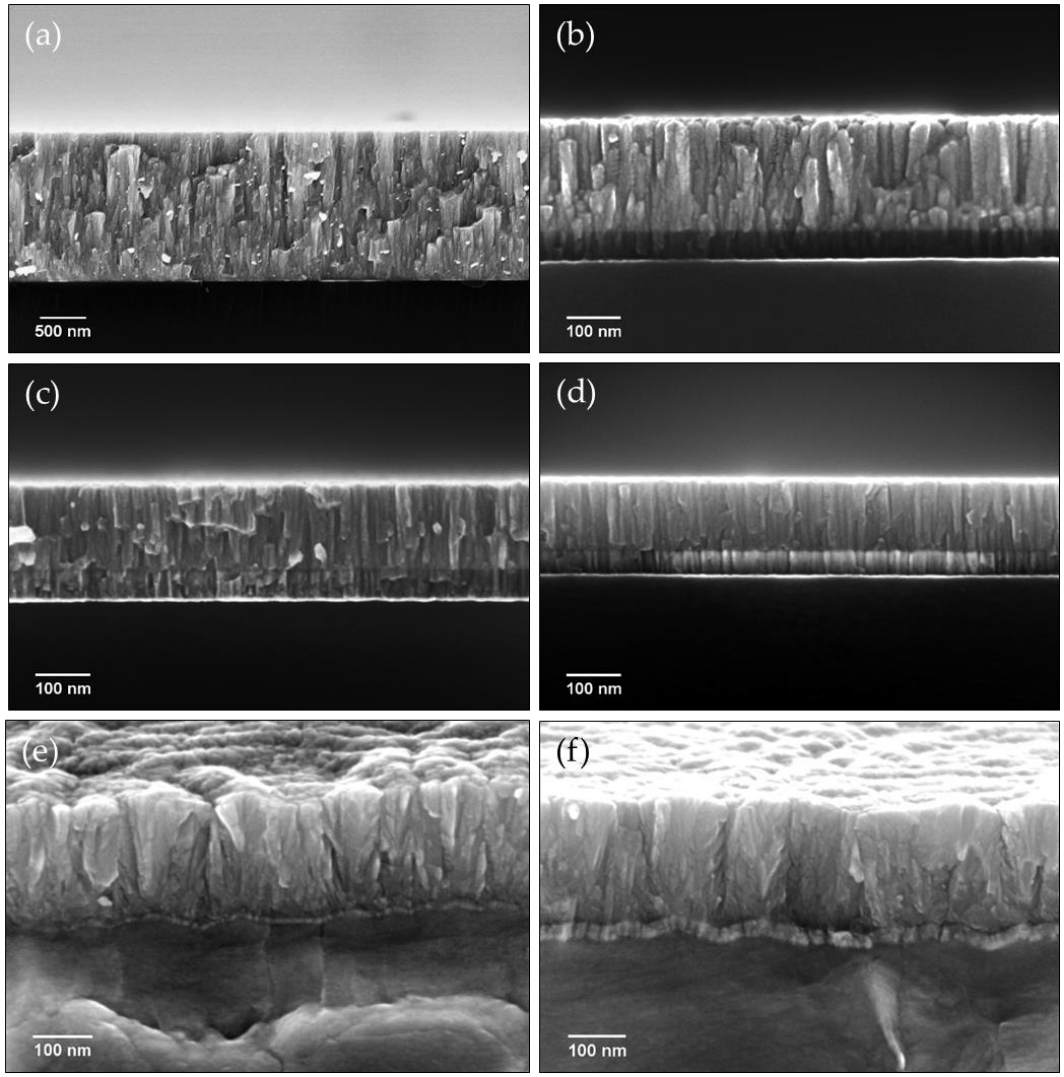

Figure 9-18: SEM images of the cross-sections of SIS film preparatory coatings. (a) The individual HiPIMS NbN film to be used for SIS film coatings. (b) 30° pulsed HiPIMS NbN film. (c) 15° pulsed HiPIMS NbN film. (d) 10° pulsed HiPIMS NbN film. (e) SIS film sample 1597 deposited with 10 nm AlN and 10° pulses. (e) SIS film sample 1599 deposited with 30 nm AlN and 10° pulses.

In line with the results of the individual HiPIMS NbN film, these HiPIMS based SIS films display the lowest surface roughness values of all the SIS films coated so far, as detailed in Table 9-5. The surface is also constituted by nanocrystalline rounded grain peaks, as opposed to the sharp features present in the previous SIS films, shown in Figure 9-12. This reduces the likelihood of flux enhancement and subsequent penetration. Also similar to the previous SIS films, the surfaces of these SIS films are characterised by a multitude of different grain structures. However, this does not necessarily affect the structure of the NbN grains, which appear as if they are superimposed on top of the Nb film structure. This is visualised in Figure 9-19. Image (a) displays an overview of the imaged area while the individual areas (b-x) display the magnified view of the surface of different apparent grain structures. It is clear that the underlying Nb film affects the overall surface topography, but the NbN grains

themselves appear to have a similar nanocrystalline microstructure, regardless of the underlying Nb grain morphology. This surface topography is similar for all SIS films deposited in this series.

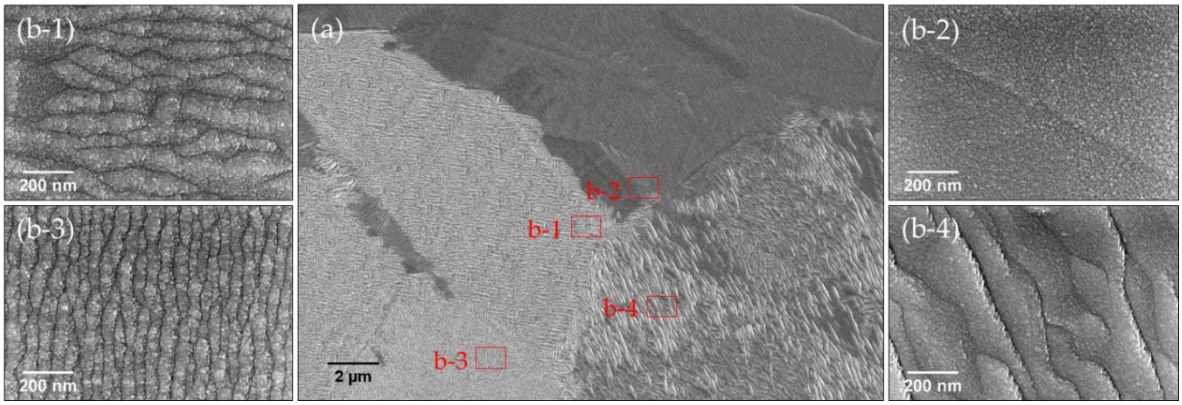

Figure 9-19: SEM images of the typical surface microstructure of HiPIMS based SIS films. (a) Overview image showing multiple grain structures. (b) Magnified images showing NbN microstructure grown on different Nb grain structures.

The effects of the different Nb grain morphologies are further evident in the cross-section images of these films, displayed in Figure 9-20. Figure (a) shows the overview and magnified image of sample 1596, deposited with a 9 nm AlN interlayer, while (b) displays the same for sample 1598, deposited with a 29 nm AlN interlayer. It must be noted, the observed top layer in the magnified images is re-deposition following Ar^+ ion polishing. The NbN film grown on the undulating Nb surface is characterised by a Zone T microstructure, while those grown on relatively flat Nb grain surfaces show dense columnar structures, indicating the significant influence of the underlying Nb film. This is apparent regardless of the AlN layer thickness. Nevertheless, the films display an increased density compared to those deposited with DC MS and an improved surface topography.

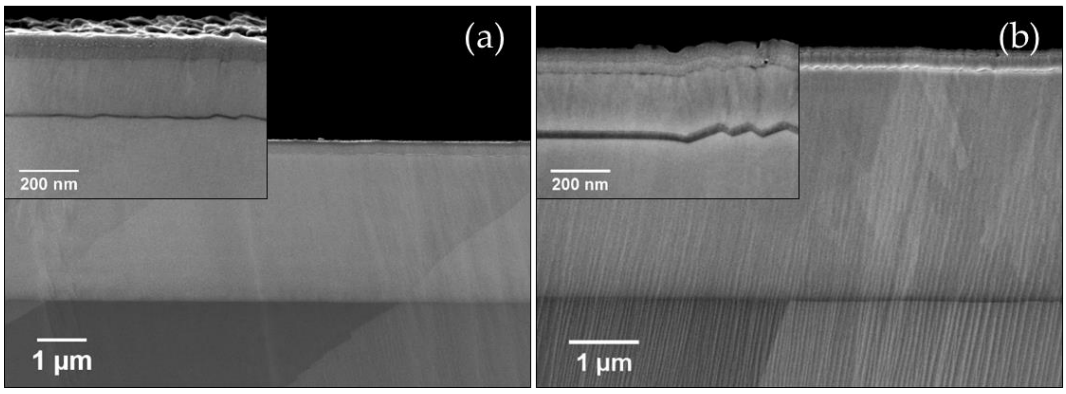

Figure 9-20: SEM images of the cross-section of two SIS films deposited on Cu. (a) Overview and magnified portion of sample 1596. (b) Overview and magnified portion of sample 1598.

The effect of the increased film density due to the use of HiPIMS to deposit NbN was immediately apparent in the EDX measurements completed on the individual layers and the STEM EDX completed on the SIS films themselves, presented in Figure 9-21. As opposed to the results detailed in Figure 9-6 for DC MS SIS films, there is no presence of O within the outer HiPIMS NbN film as a result of the significantly improved film density.

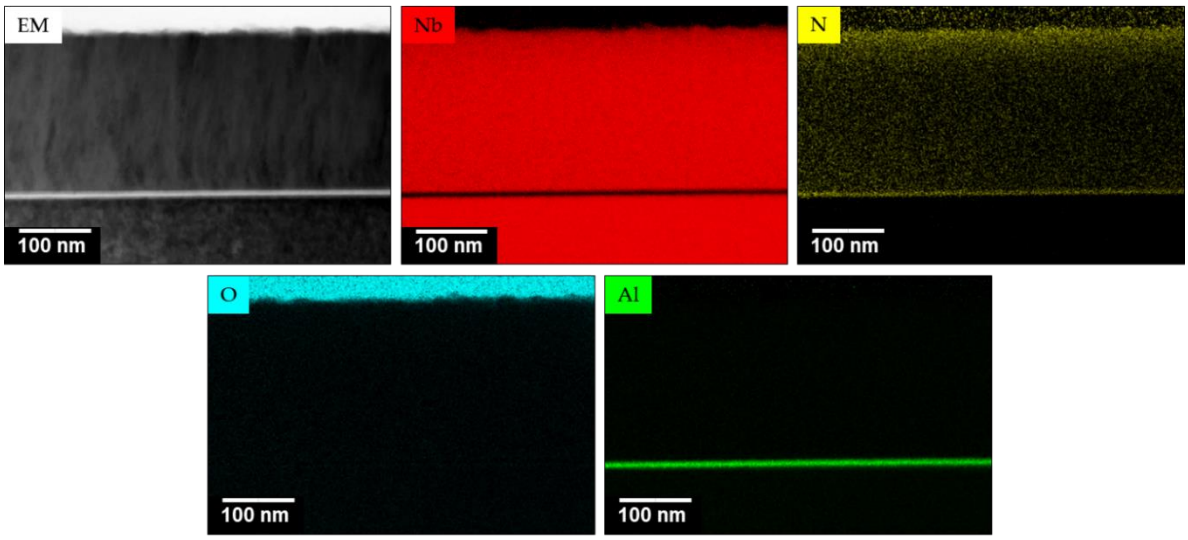

Figure 9-21: STEM EDX mapping results from HiPIMS SIS sample 1597, displayed in atom percent.

The decreased O content is also visible in the results of the SIMS measurements, displayed in Figure 9-22, which show a substantial decrease of the NbO^+ signal, compared to Figure 9-7, which represents the DC MS NbN films utilised in the previous two SIS films series. This NbO^+ signal is taken as representative of the state of oxidation of the NbN film. The reduced AlN thickness is also visible through the decreased sputter time of the Al^+ signal while the delayed time to reach the AlN layer compared to the previous SIS films is due to the increased NbN layer thickness of the investigated film.

The full XRD spectrum (a) and magnified XRD spectrum (b) of the individual layer HiPIMS NbN sample (1296), unstable turbopump SIS sample 1496 with 10 nm AlN and 200 nm NbN, SIS sample 1597 with 10 nm AlN and 200 nm NbN, and SIS sample 1599 with 30 nm and 200 nm NbN are presented in Figure 9-23. Because of the initial deposition pressure instabilities, the XRD spectra for the initial HiPIMS SIS films, represented here by sample 1496, showed a change in the NbN phase formation compared to the original single layer HiPIMS NbN sample. The film shows a short, sharp Nb_5N_6 peak phase with a broad δ-NbN (111) peak. This can only be attributed to the effects of deposition pressure fluctuations during coating as this effect disappeared with resolution of the instabilities. Further SIS

samples, such as 1597 and 1599, show NbN peaks in line with the results of the individual layer HiPIMS NbN sample used to deposit the SIS samples, regardless of the AlN layer thickness. These NbN films, individual and SIS, display a δ-NbN (111) preferred orientation with a small presence of the hexagonal Nb_5N_6 phase.

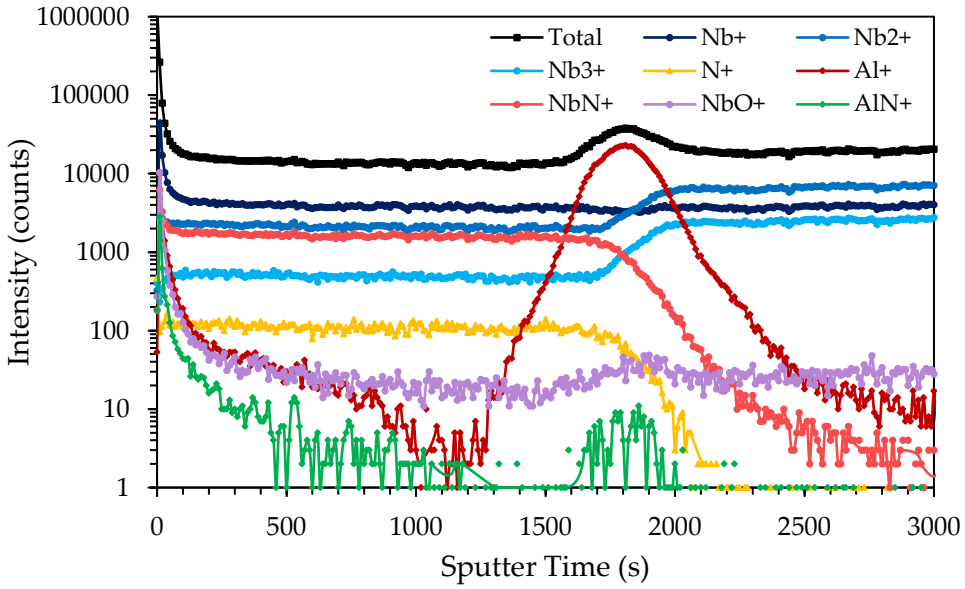

Figure 9-22: SIMS depth profile measurement of HiPIMS Nb base layer, HiPIMS NbN outer layer, SIS film sample 1496, measured in positive mode.

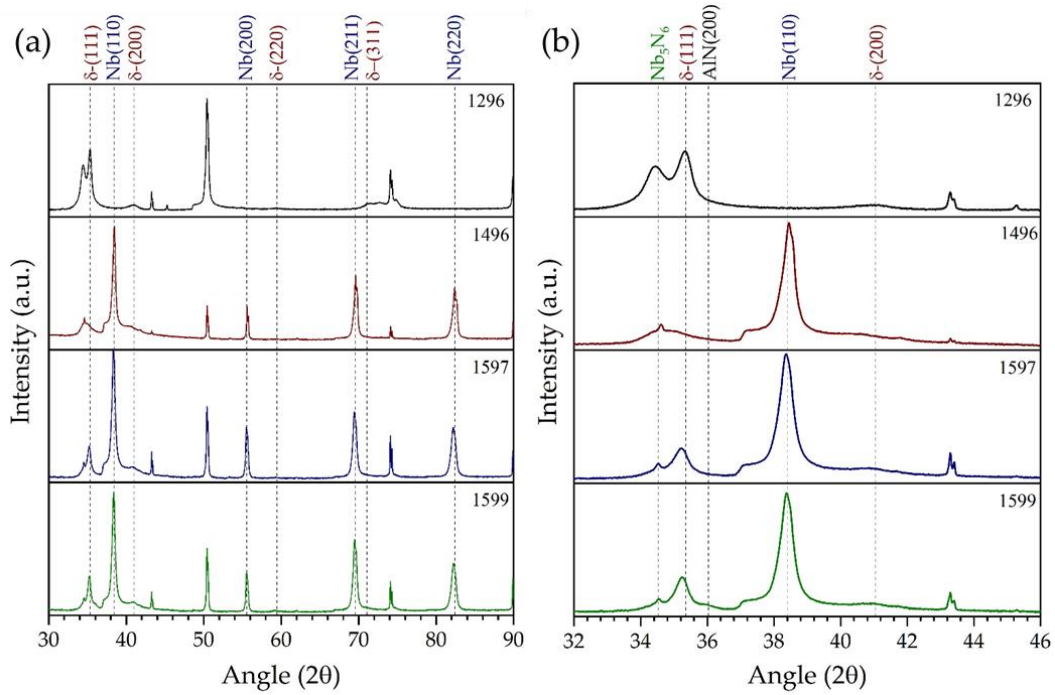

Figure 9-23: XRD spectra of the original HiPIMS NbN film (1296), the unstable SIS film with 10 nm AlN interlayer (1496) and the stable SIS films with 8 nm (1597) and 30 nm (1599) AlN interlayers. SIS films with 200 nm NbN layer. (a) Complete scan range. (b) Region of interest used to identify the NbN phases. Spectra displayed in log scale with unidentified peaks pertaining to the Cu substrate.

All of the NbN films in these SIS samples display a negative shift of the δ-NbN (111) peak position. This is more pronounced for the first series of films, which display a preferred Nb_5N_6 phase formation. As a result of this, these films possess slightly elevated δ-NbN (111) lattice parameter values compared to the previous DC MS NbN SIS films and the single HiPIMS NbN film, with an average of 4.4527 Å for the first series and 4.4117 Å for the second series. This places the first series out of the range for δ-NbN and the second series within the range of δ-NbN, detailed in Table 3-2. This is indicative of a significantly increased stress state in the first series of films as well as a smaller increase in the film stress for the second series of films. This is likely due to the reduced thickness of these films compared to the individual layers and the improved NbN film density, allowing for stress transfer between the columnar grains. The DC MS NbN films deposited in previous SIS films possessed disjointed columnar structures, which allowed for significant stress relaxation. Further to this, the deposition pressure instabilities led to a lower deposition pressure and increased N_2 %, resulting in an increased film stress.

The underlying Nb films are characterised by the Nb (110) peak, seen at $2\theta = 38.42°$, whose relative intensity indicates a Nb (110) preferred orientation, similar to the base Nb film detailed in Chapter 8.2. Furthermore, the Nb (110) peak is shifted to lower angles, indicating an increased lattice parameter, with an average of 3.3159 Å, symbolic of a compressive in-plane stress. This is in line with the previous SIS films as well as the individual HiPIMS Nb films. The AlN interlayer is again characterised by its AlN (200) peak at ~ 36°, indicating formation of the sought after phase, and as expected, is more apparent in the SIS films with a thicker AlN layer.

Due to the age of the target, the peak current during the HiPIMS pulses for the NbN films was noticeably larger for the SIS film deposition compared to the individual layer study. This increased target current likely results in an increased adatom and ion current at the substrate, resulting in an increased atom peening effect. This is a possible explanation for the increased state of stress observed in the NbN films in the SIS film coatings compared to the original single layer NbN films.

Similar to the previous SIS samples, the HiPIMS based SIS samples were also tested in an AC susceptometer, in order to determine the T_c of the NbN shielding layer. The normalised results of these measurements, for the two separate SIS film series, are displayed in Figure 9-24. The results for the first series of HiPIMS SIS films, which suffered deposition pressure instabilities, are presented in (a). These films show a decreased NbN T_c compared to both the individual NbN layer as well as the second series of HiPIMS SIS films. This decrease is related

to the change of preferential phase of the NbN films as well as the significant increase in their lattice parameter values. The T_c of the HiPIMS NbN layers showed a significant lattice parameter dependence, as detailed in Figure 7-32. The second series of HiPIMS SIS films, displayed in (b) showed a comparatively decreased lattice parameter, towards the associated peak T_c values. As such, all of these films showed a higher T_c than the first series. Nevertheless, the highest T_c of these SIS films, T_c = 14.48 K for sample 1599, is still slightly less than that achieved for the individual layer (14.6 K). This is again related to the increased lattice parameters of the HiPIMS NbN layers in these SIS films. Interestingly, the second series of films shows a further split in results between the two different AlN layer thicknesses. The NbN films deposited onto the 30 nm thick AlN interlayer showed higher T_c values, for equal or similar NbN layer thicknesses, than those deposited onto the 10 nm thick AlN interlayer. Regardless of the effects of the turbopump or the AlN layer thickness, the NbN T_c displayed a strict thickness dependence, in line with previous SIS film samples.

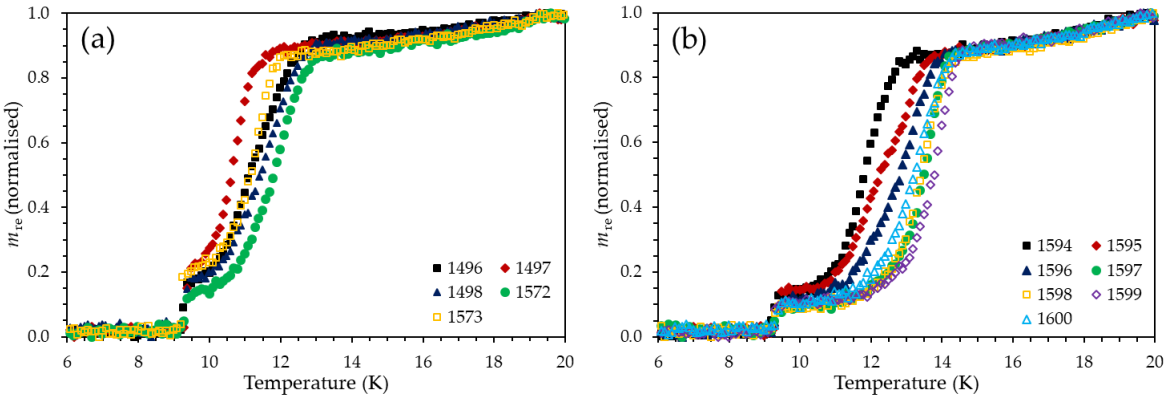

Figure 9-24: Normalised real component of the AC susceptibility measurements detailing the transition temperatures of the Nb and NbN layers of the HiPIMS SIS films. (a) displays the first series of films, with AlN layer thickness of 10 nm while (b) displays the second series of films, where the solid symbols pertain to films with a 10 nm thick AlN layer while the empty symbols pertain to films with a 30 nm thick AlN layer.

The results of the VSM testing for these HiPIMS SIS films are presented in Figure 9-25. The effects of the deposition pressure instabilities during deposition are particularly evident when comparing the sections of the normalised magnetisation loops of series one and two, shown in (a) and (b) respectively. In (a), the virgin curve shows evidence of magnetic moment instabilities, which is worse for the thinnest NbN layers. In (b) however, the virgin curve maintains a smooth shape throughout. Further to this, the samples deposited in series two possess far smaller magnetisation loops compared to series one, indicative of a lower amount of trapped flux. Both series of films present a dip in the reverse loop, but this is significantly more pronounced in series two, indicating an improved surface barrier condition.

Additionally, the amount of trapped flux increased with both the increase in the AlN layer thickness and the increase in NbN thickness. Finally, but most importantly, the SIS film samples in series two possess the smallest magnetisation loops and lowest amount of trapped flux of all SIS films, indicating the improvements offered by the use of HiPIMS NbN as the shielding layer and the necessity for process optimisation.

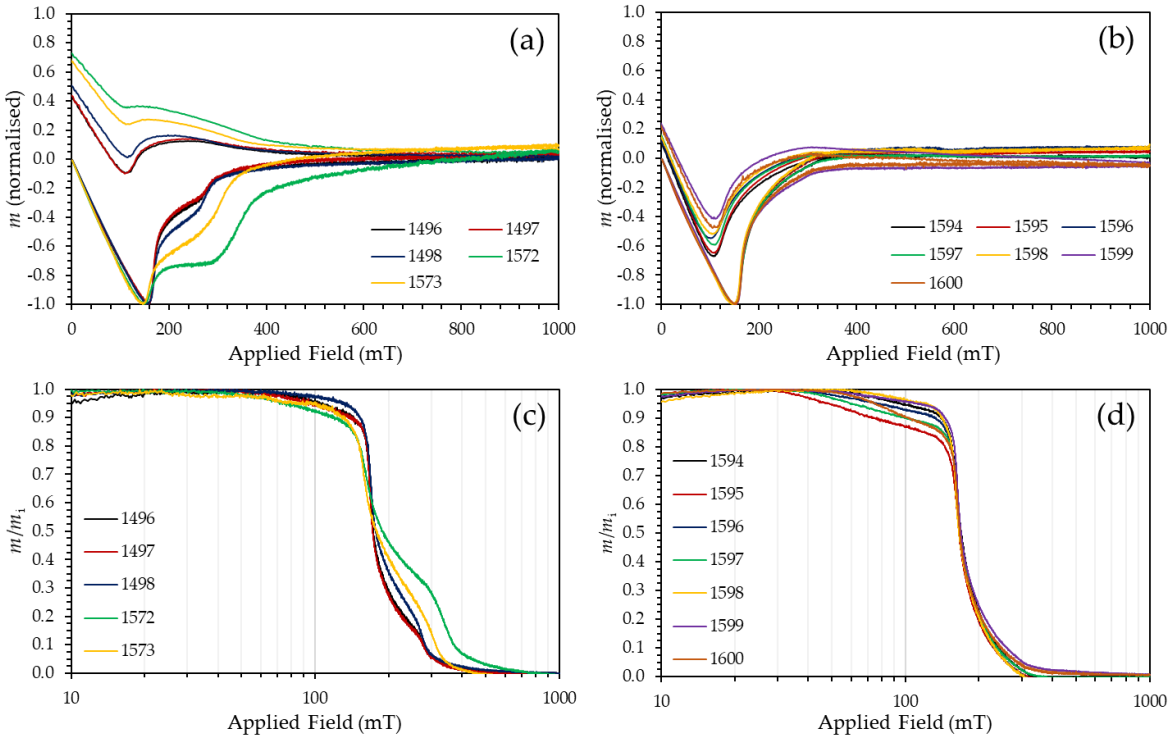

Figure 9-25: Superconducting results for the two sets of HiPIMS SIS films. (a) and (b) display sections of the normalised magnetisation loops of the first and second series of samples respectively. (c) and (d) display the Meissner state ratio of the first and second series of samples respectively.

The two series of HiPIMS SIS films also show a noticeable divide when comparing their entry field data, indicated by the Meissner ratios presented in (c) and (d). The films deposited in the first series show a consistently higher H_{en}, even at low NbN film thickness, with lower variability. The highest H_{en} = 88.0 ± 4.4 mT of all SIS samples was recorded for sample 1496, deposited in this series, while the maximum achieved for the second series of samples was H_{en} = 62.0 ± 3.1 mT (10 nm AlN) and H_{en} = 68.0 ± 3.4 mT (30 nm AlN). Based on the results of other characterisation methods, this is likely linked to the NbN phase formation; though more information is required to accurately assess this. Regardless, the maximum H_{en} value achieved for these HiPIMS SIS films is still lower than that achieved by the base HiPIMS Nb film, allowing for further process optimisation. Interestingly, the second series of films hints at a further split between the films based on the AlN thickness, with the three films coated with a 30 nm AlN interlayer showing consistently higher H_{en} values compared to those

deposited with a 10 nm interlayer, though more results and further test methods are required to confirm this.

The reported effects of the NbN layer thickness as well as the AlN interlayer thickness are graphically represented in Figure 9-26. All of these HiPIMS SIS films display an increasing NbN T_c with increasing layer thickness. A further effect of the AlN layer thickness is evident in (b), where the thicker AlN samples possess a higher NbN T_c. similar to the previous SIS film samples, specific maximums in the entry field are observed for specific NbN layer thicknesses. An increase in the NbN layer thickness responsible for the highest entry field, compared to previous SIS samples is observed in (a). This is indicative of the cleaner NbN films as evidenced by the SIMS results presented in Figure 9-22. However, this is not necessarily the case for the second series of films, where the 10 nm AlN layer samples show a maximum entry field at a NbN thickness of ~ 100 nm, while the 30 nm AlN samples show a maximum entry field at a NbN thickness of ~ 180 nm. These inconsistencies indicate the necessity for further superconducting testing methods, such as third harmonic testing, to accurately assess the entry field of SIS films samples.

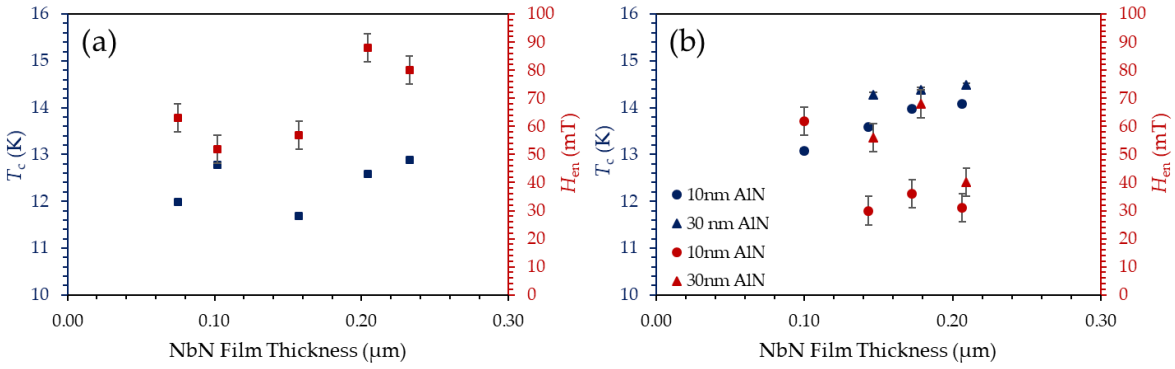

Figure 9-26: Superconducting transition temperature and entry field values as a function of NbN film thickness for the two series of HiPIMS SIS films. (a) Pertains to series one and (b) pertains to series two, with the different AlN layer thicknesses indicated as well.

As a final remark, even though the films from the first HiPIMS SIS series displayed higher H_{en} values, the smaller size of the magnetisation loops, and the associated lower amount of trapped flux in the second series of films, will likely result in better SRF performance, due to the oscillatory nature of the applied field in SRF cavity operation.

9.5 Multilayer QPR Samples

In order to gain further insight into the efficacy of SIS films on Cu for SRF applications, three QPR samples were coated with three different SIS films. All of the QPR samples were

prepared at INFN Legnaro using electropolishing [215]. This was often completed following stripping of a previous film.

The typical QPR deposition process, shown in Figure 9-27, proceeded in the same manner as with the small samples, with three separate, successive coatings before the sample was removed. Images (a) and (b) show the QPR sample before and after coating while (c), (d) and (e) display the QPR sample during the coating of the respective Nb, AlN and NbN films.

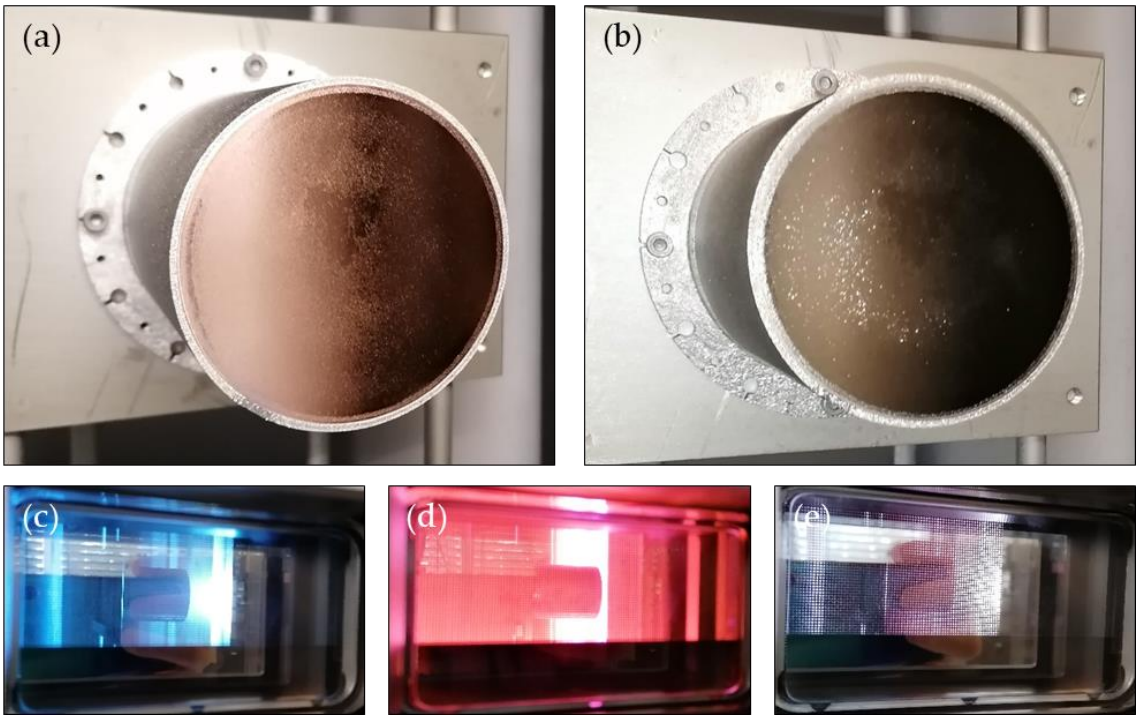

Figure 9-27: Images of the HiPIMS SIS film coating on the QPR sample. (a) and (b) show the QPR sample before and after SIS film coating. (c), (d) and (e) show the coating process during Nb, ALN and NbN deposition respectively.

The first QPR sample was coated in two separate stages. The initial stage focused on the coating of the individual Nb base layer, as detailed in Chapter 8.1. The coating was comprised of a HiPIMS interlayer (~ 200 nm) and a DC MS Nb film (~ 3 µm). Following testing of this sample in the QPR system at HZB [216][217], the sample was further coated with a ~ 30 nm AlN layer and a ~ 200 nm DC MS NbN layer based on sample 899, similar to samples in Chapter 9.3. This sample was then sent back to HZB and retested. The testing of the QPR samples was again completed by D. Tikhonov at HZB Berlin. The performance of the original Nb layer was detailed in Chapter 5.6, as part of the Cu treatment studies. The results from the QPR tests after the second coating, i.e. of the SIS film coating (B-3.7), are detailed in Figure 9-28. Overall, the results indicate a decrease in performance of the sample compared to the pure Nb coating, likely due to contamination as a result of the two-stage coating process.

With the successful development and deposition of HiPIMS SIS films on small samples, two HiPIMS SIS films were deposited onto two further Cu QPR samples. The samples were coated using the same SIS recipe as samples 1596 and 1598, with the same recipes for the base HiPIMS Nb layer (~ 3.5 µm thick) and the outer HiPIMS NbN layer (~ 180 nm,) but different AlN layer thicknesses of ~ 8 nm (B-4.9) and ~ 24 nm (B-4.18) respectively. These two separate AlN thicknesses were utilised in order to determine the influence of the AlN thickness on the surface resistance results of these coatings. The thicknesses were based on discussions within the ARIES research program as well as the HiPIMS Nb SIS film results from Chapter 9.3. The results from the testing of the SIS film QPR samples, at 2.5 and 4.5 K, are displayed in Figure 9-28 (a) and (b) respectively.

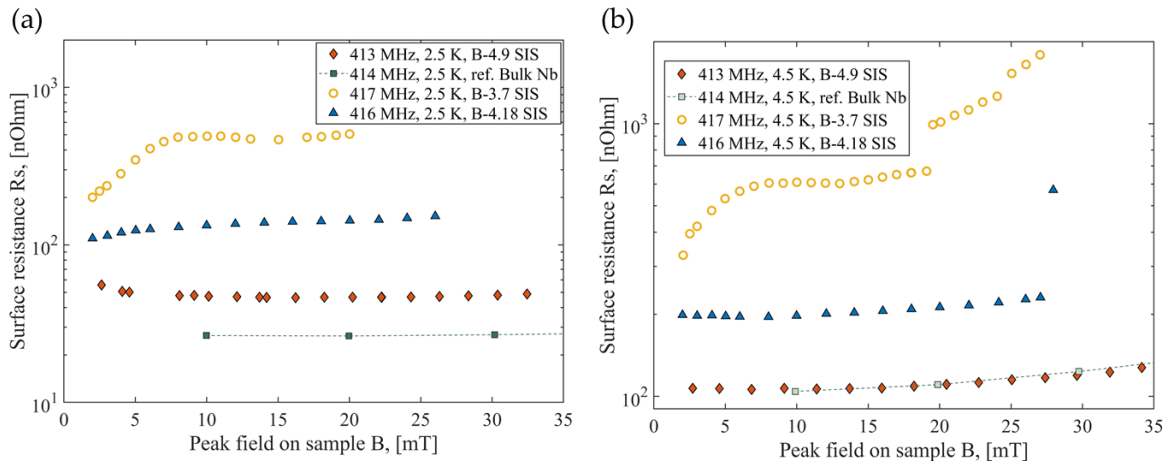

Figure 9-28: Surface resistance vs. Peak field for the different SIS film QPR samples, tested at (a) 2.5 K and (b) 4.5 K. The samples are compared to a reference bulk Nb sample also tested in the QPR. QPR testing and data analysis courtesy of D. Tikhonov (HZB Berlin) [218].

The first HiPIMS SIS film QPR sample (B-4.9), with an 8 nm AlN interlayer, displayed a significant improvement in the surface resistance, compared to the two-stage coated sample, B-3.7. This is likely due to the change to a HiPIMS-based coating for the Nb base layer and the NbN shielding layer, coupled to the improved single stage coating process. At lower testing temperatures of 2.5 K, the surface resistance shows no noticeable increase with increasing field, while at higher testing temperatures of 4.5 K, the surface resistance is comparable to a reference bulk Nb sample, indicated in (b).

With an increase in the AlN layer thickness from 8 to 24 nm in sample B-4.18, the surface resistance of the SIS film QPR sample increases considerably, at both 2.5 and 4.5 K, as detailed in Figure 9-28 (a) and (b) respectively. Nevertheless, the surface resistance behaviour of both of these samples shows a relatively monotonic relationship with an increase in the field,

indicating the improved adhesion and performance by these films. Most significantly, sample B-4.9 maintains a similar surface resistance vs. peak field relationship to the reference bulk Nb sample until high fields, at 4.5 K. This is a good indication of the impressive performance of these samples and the successful optimisation of the deposition parameters in the separate coatings. Further in-depth analyses of the RF performance of SIS films and the role of the AlN layer are detailed by D. Tikhonov [218].

9.6 Conclusions

Multiple separate series of SIS films were successfully deposited onto Cu substrates, utilising the step-wise advances made in the deposition of each individual layer. The films deposited with DC MS-only displayed the potential for delayed flux entry, while also indicating the potential drawbacks of a rough base layer and a low-density shielding layer. The microstructure of the films was constituted by coherent, epitaxially grown layers with no evidence of interlayer-voids. However, further evidence of the drawbacks of DC MS Nb were found with the presence of voids between the base Nb film and the Cu substrate.

The use of the HiPIMS Nb base layer resulted in a significant improvement in the surface roughness of the base layer as well as the SIS films themselves while also nearly eradicating the presence of voids between the Nb and Cu. The quality of the Nb base layer was seen through the high T_c values achieved for the NbN shielding layers, which equalled those of the individual NbN layers in some instances. The benefits of a high H_{en} shielding layer were shown by the superior performance of SIS films coated with a higher H_{en} NbN recipe. The use of table rotation during the coating process led to a complete change of the microstructure and crystallographic phase of the NbN film. In order to combat this, "pulsing" of the table, and thus the substrate, in front of the target was instituted.

By adopting the HiPIMS NbN layer for the shielding layer recipe, further improvements to the surface roughness of the films were achieved while the "pulsing" of the table during coating allowed for retention of film microstructure and crystallographic phase found in the individual NbN layers. The presence of impurities in the films, mainly O, also showed a noteworthy decrease. As a result of all of these improvements, the full HiPIMS SIS films displayed the highest H_{en} values of all SIS films, achieving values near to those of the base Nb layer in some instances. A marked reliance on the shielding layer thickness was also observed, confirming theoretical predictions. However, the large variability in the H_{en} results of the HiPIMS SIS films compared to the relatively consistent performance of the individual HiPIMS Nb films calls into question the accuracy of measuring SIS films only with a VSM.

The AlN layer thickness also displayed a marked effect on the transition temperature, trapped flux and entry field of the SIS films, though this requires more investigation for accurate assessment. An important note is that the use of a lower turbopump speed led to instabilities in the deposition pressure and a subsequent change to the crystallographic phase of the NbN shielding layer. As a result, a significant difference was observed between films coated at a low turbopump speed and a higher, more stable turbopump speed. This was accounted for in the data analysis.

Finally, three multilayer QPR samples were successfully coated and provided valuable insight into the efficacy of SIS film coatings on Cu substrates.

10. Summary and Future Developments

10.1 Summary

The main aim of this thesis has been to improve the performance of thin film-coated Cu accelerating cavities. The use of improved deposition techniques, namely HiPIMS, alternative materials, specifically NbN, and alternative methodologies, such as SIS film coatings, have been studied. This is the first such project focused on the deposition of superconducting thin films in our institute and as such, much of the work already completed in other institutes was newly started during this study, in order to produce a "body of knowledge" in our own institute.

The key issue with thin film coated, typically Nb, Cu cavities is the so-called Q-slope, whose origin has been linked to multiple issues, such as poor interfacial adhesion, an increased number of pinning sites and poor surface topography. In order to improve the superconducting performance, it is necessary to focus on specific problem areas. To this end, the studies undertaken were focused on decreasing the surface roughness of both the Cu substrate and the deposited thin films, improving the interfacial adhesion between Nb and Cu, depositing dense, bulk-like Nb and NbN thin films and determining the efficacy of SIS film coatings for Cu cavities.

Typical Cu cavity preparation techniques were explored in order to optimise the Cu sample preparation process. Studies utilising mechanical polishing, chemical polishing, namely the chemical mixture SUBU5, electropolishing (EP) as well as combinations of all of these were completed. Results indicated a smoother and more homogeneous surface finish as well as improved superconducting performance of films deposited onto samples prepared with a combination of mechanical polishing and electropolishing.

Initial Cu samples were coated with thin films of NbN by DC magnetron sputtering (DC MS), in order to determine the effects of the different deposition parameters on the resulting morphological, crystallographic and superconducting properties. The relationship between the achieved crystallographic phase and the resultant superconducting performance proved to be significant, with the δ-NbN (111) phase leading to higher transition temperature (T_c) values and the δ-NbN (200) phase leading to higher entry field (H_{en}) values. Based on the results, it is evident that a higher deposition pressure and lower cathode power lead to repeatable deposition of the sought after δ-NbN (111) phase, with a $T_c > 15.5$ K routinely achieved. Unfortunately, the entry field values achieved for these single layer NbN films do not lend themselves to use in SRF cavities, as this will result in early flux entry and consequently, increased energy dissipation. The low entry field values observed for these

samples are typical of NbN films but are often exacerbated by the observed disjointed columnar microstructure, leading to higher levels of impurities, and a faceted surface topography, leading to flux concentration. In light of this, and following the significant improvements noted with the deposition of Nb films with HiPIMS, a HiPIMS NbN study was completed in order to increase the density of the NbN films, in an attempt to improve their entry field values.

The results of the study showed a significant improvement in the density of the NbN films while also reducing their surface roughness. These improvements resulted in a significant increase in the entry field of these films compared to the previous DC MS NbN films. A maximum of 30 mT was achieved, higher than the reported H_{C1} for bulk NbN of 20 mT [48]. Moreover, the average entry field value of the HiPIMS NbN films (16 mT) exceeded the maximum achieved with DC MS (13 mT). The increased density also led to a decrease in impurities, specifically O. Similar to the DC MS films, a higher deposition pressure and lower cathode power are more conducive to the formation of the δ-NbN (111) phase. Furthermore, the use of a lower substrate bias (< 60 V) is essential, as higher substrate bias values resulted in the formation of non-superconducting, hexagonal phases. The highest measured T_c of NbN on Cu (16.5 K) was also achieved with HiPIMS deposition. However, a general decrease in T_c, compared to the DC MS films, was observed. Nevertheless, the improved entry field performance of these HiPIMS NbN films makes them particularly applicable to SIS film coatings.

In order to improve the base layer in the SIS film coatings, a series of Nb films were successfully deposited onto Cu substrates using HiPIMS. Due to the nature of the coating system, higher duty cycles than previous investigations, in the region of 8 – 20 %, were required. The results point to three specific deposition parameters as the most significant: the substrate temperature, substrate bias and film thickness. The observed changes in the superconducting performance are related to changes in the crystallographic structure of the Nb film, its state of stress and the resultant grain morphology in the penetration depth of the RF field. It is evident that films whose crystal structure approaches that of unstressed, bulk Nb have superior superconducting properties. Coupled to this, films deposited at an intermediate temperature and lower substrate bias value possessed lower stress states than others. Crystallographic investigations detailed the presence of an apparent transition zone during the initial few micrometres of film growth. In this region, higher stress levels and competitive growth of different Nb orientations are observed. Films thicker than ~ 3.5 μm presented more coherent grain structures and a decreased film stress, resulting in better

superconducting performance. The use of HiPIMS was further found to result in the formation of in-plane texture in the resultant films, which were characterised by a Nb (110) orientation.

Changes to the duty cycle did not result in any significant changes to the crystallographic structure of the films. An increase in the duty cycle did however allow for operation at lower deposition pressures, resulting in lower gas entrapment in the deposited films, not fully investigated here. This needs to be balanced against the beneficial reduction of compressive stresses at higher deposition pressures. Most notably, the use of HiPIMS resulted in an 85 % reduction in the number of interfacial voids, significantly improving the adhesion and heat transfer between the Nb film and Cu substrate.

A series of separate studies focused on the deposition of SIS films, as first proposed by Gurevich [5], were completed. These SIS films were constituted by a Nb/AlN/NbN structure and were deposited onto Cu substrates. The SIS film coatings were concluded in a staggered fashion, based on the step-wise improvements made to both the Nb and NbN coatings.

As part of the SIS film coatings, an initial investigation into the deposition of AlN films with DC MS was completed. Following their successful development, initial SIS films were deposited onto Cu using DC MS only. The films were deposited with a constant 30 nm thick AlN layer and NbN thicknesses from 80 to 150 nm, using the optimised DC MS NbN recipe. In order to ensure film thickness homogeneity, the initial SIS films were coated with a continuously rotating substrate holder. The films displayed a coherent epitaxial structure with no presence of voids between the layers. The superconducting results displayed a slightly lower T_c for the SIS film NbN layer, compared to the individual films. Encouragingly, the potential for delayed field entry was observed, but the relatively rough DC MS Nb film resulted in some inconsistencies in the outer layers of some samples, thereby hindering interpretation of the results. Furthermore, the low energy deposition associated with DC MS Nb coatings led to interfacial voids between the Nb base layer and the Cu substrate. This led to the investigation of HiPIMS Nb thin films.

Following the completion of the HiPIMS Nb study, two sets of SIS samples were deposited, both using a HiPIMS Nb base layer and DC MS NbN shielding layers. Two different NbN "recipes" were used for the outer shielding layer, one with a high T_c and one with a high H_{en}, while also investigating the role of the shielding layer thickness. The AlN layer was again maintained at 30 nm with the NbN layer varying between 100 and 250 nm, again utilising complete rotation of the substrate holder during deposition. The superconducting results indicated a definite split between the two series with those deposited with the high H_{en} NbN

film proving to be superior. The results also exhibited specific maximums in the entry field for each NbN "recipe" series, related to the shielding layer thickness. This correlates with optimum thickness predictions [31] and previous results [131] from other authors. The T_c values of the NbN layers showed an increase with increasing thickness, and were similar to those of the original, single layer films. These results highlighted the importance of using high H_{en} films for the shielding layer but did not improve upon the entry field values obtained with the pure HiPIMS Nb film.

Given the significant improvements to the entry field values of the NbN films deposited with HiPIMS, a final series of HiPIMS SIS samples were produced using the same HiPIMS Nb base layer and the HiPIMS NbN recipe with the highest H_{en}. The effects of the AlN and NbN film thicknesses were also investigated. The AlN films were deposited with a thickness of either 8 or 30 nm, with NbN layer thicknesses between 75 and 250 nm, deposited on each AlN layer thickness. Instabilities in the deposition pressure, due to lower turbopump speeds, resulted in changes to the crystallographic phase of the NbN shielding layer in the initial series of HiPIMS SIS films, necessitating the deposition of a second set of HiPIMS SIS films. In spite of this, all HiPIMS SIS films displayed a vast improvement in the microstructure, topography and impurity concentration of the films compared to the previous SIS films. The entry field values of the majority of these HiPIMS SIS films were higher than those of the previous SIS film series; equalling that of the HiPIMS Nb base film in some instances. Again, a specific maximum in the entry field was found for a specific NbN film thickness in the first series of films, further pointing to its role in effectively shielding the underlying Nb film. However, the variability and change in the NbN film thickness resulting in the maximum entry field with these two HiPIMS SIS film series points to the need for further superconducting testing of SIS film samples.

The second series of HiPIMS SIS films resulted in the smallest magnetisation loops of all samples and subsequently, the lowest amount of trapped flux of all coatings deposited during the entire study, including the single-layer HiPIMS Nb coatings. The use of different AlN layer thicknesses was also observed to affect the superconducting properties of the SIS films, most notably the transition temperature of the NbN shielding layer. Further investigation of these effects are required prior to a definitive conclusion. Lastly, three multilayer QPR samples were successfully coated with separate SIS films, based on the improvements detailed above. The testing, completed by D. Tikhonov at HZB Berlin, provided valuable insight into the performance of SIS film coatings, with similar performance to a bulk Nb QPR sample observed at 4.5 K.

It must be noted that the superconducting performance of all films was measured in a DC VSM system. As such, the results are susceptible to edge effects as well as sample misalignment. Due to the DC field, the energy dissipation that would arise due to the oscillatory motion of trapped vortices in an oscillating field was not applicable to these measurements. Because of the nature of the measurements, a full understanding of the SIS film results, more specifically the position of flux entry, is therefore not clear.

In closing, the results of this thesis further indicate the significant improvements available to coated cavities with the use of energetically deposited thin films while also indicating the specific parameters to be focused on. Furthermore, the efficacy of SIS film coatings for Cu cavities have been clearly demonstrated, with further advances possible through additional deposition parameter optimisation and the use of alternative shielding layer materials, such as NbTiN and Nb_3Sn.

10.2 Future Developments

This work set out to demonstrate the efficacy of SIS film coatings deposited onto Cu substrates. Now that this has been shown, a number of further lines of research are deserving of more effort in the future. As such, several suggestions are proposed in order to facilitate the improvement of future SIS film coatings.

Due to the observed step-edge at the grain boundaries on the surfaces of the Cu substrates following electropolishing, the use of a shorter electropolishing time, 20 - 30 min, is recommended. Further to this, the use of alternative surface treatments, such as Plasma Electrolytic Polishing (PEP), is advised.

In light of the significant improvements observed with the use of HiPIMS, its continued usage is recommended for the deposition of both Nb and NbN films. A significant amount of optimisation is still available, specifically at lower duty cycle values.

The changing crystallographic structure of the HiPIMS NbN films when deposited in SIS film coatings, and the resultant changes to its superconducting properties, requires further investigation. The observed increase in the lattice parameter likely resulted in the decreased T_c of the NbN layer. This can be combatted by using a lower cathode power, as observed during this study. However, this requires further optimisation of the remaining deposition parameters.

The vast majority of superconducting tests performed in this study relied upon the use of a VSM system. As such, due to the immersion of the entire sample in the applied field, the exact entry point of the flux into the sample is unknown. Therefore, further superconducting

testing methods, such as those based on third harmonics, are recommended for use. These results will complement the VSM results, by localising the applied field on the surface of the SIS film coating, thereby enhancing the understanding of SIS film coating performance.

11. References

[1] H. Padamsee, "50 years of success for SRF accelerators — a review," *Supercond. Sci. Technol.*, vol. 30, 2017, doi: 10.1088/1361-6668/aa6376.

[2] C. Benvenuti, S. Calatroni, P. Darriulat, M. A. Peck, A.-M. Valente, and C. A. V. Hof, "Study of the residual surface resistance of niobium films at 1.5 GHz," *Phys. C Supercond. its Appl.*, vol. 351, no. 4, pp. 421–428, 2001, doi: 10.1016/S0921-4534(00)01645-2.

[3] D. Boussard and T. Linnecar, "The LHC superconducting RF system," *Proc. Jt. Cryog. Eng. Conf. Int. Cryog. Mater. Conf.*, 1999.

[4] A.-M. Valente-Feliciano, "HiPIMS : A New Generation of Film Deposition Techniques for SRF Applications," in *Proceedings of 16th International Conference on RF Superconductivity (SRF 2013)*, 2013, pp. 754–760.

[5] A. Gurevich, "Enhancement of rf breakdown field of superconductors by multilayer coating," *Appl. Phys. Lett.*, vol. 88, no. 1, p. 012511, 2006, doi: 10.1063/1.2162264.

[6] C. Z. Antoine, J.-C. Villegier, and G. Martinet, "Study of nanometric superconducting multilayers for RF field screening applications," *Appl. Phys. Lett.*, vol. 102, no. 10, Mar. 2013, doi: 10.1063/1.4794938.

[7] A.-M. Valente-Feliciano, "Development of SRF monolayer / multilayer thin film materials to increase the performance of SRF accelerating structures beyond bulk Nb," Ph.D. Thesis, Université Paris Sud, 2015.

[8] H. Padamsee, *RF Superconductivity: Science, Technology and Applications*. Wiley-VCH, 2009.

[9] H. Kamerlingh Onnes, "Further experiments with liquid helium," *KNAW, Proc.*, vol. 13 II, no. September, pp. 1274–1276, 1910.

[10] W. Meissner and R. Ochsenfeld, "Ein neuer Effekt bei Eintritt der Supraleitfähigkeit," *Naturwissenschaften*, vol. 21, no. 44, pp. 787–788, Nov. 1933, doi: 10.1007/BF01504252.

[11] "Diamagnetism." https://commons.wikimedia.org/wiki/File:EXPULSION.png (accessed Apr. 17, 2019).

[12] M. Martinello, "The Path To High Q-Factors in Superconducting Accelerating Cavities: Flux Expulsion and Surface Resistance Optimization," Ph.D. Thesis, Illionois Institute of Technology, 2016.

[13] B. S. Deaver and W. M. Fairbank, "Experimental Evidence for Quantized Flux in Superconducting Cylinders," *Phys. Rev. Lett.*, vol. 7, no. 2, pp. 43–46, Jul. 1961, doi: 10.1103/PhysRevLett.7.43.

[14] F. London and H. London, "The Electromagnetic Equations of the Supraconductor," *Proc. R. Soc. Lond. Ser. Math. Phys. Sci.*, vol. 149, no. 866, pp. 71–88, 1935.

[15] C. . Gorter and H. Casimir, "On supraconductivity I," *Physica*, vol. 1, no. 1–6, pp. 306–320, Jan. 1934, doi: 10.1016/S0031-8914(34)90037-9.

[16] H. Padamsee, J. Knobloch, and T. Hays, *RF Supercondcutivity for Accelerators*, Second Edi. Wiley-VCH, 2008.

[17] A. B. Pippard and P. R. S. L. A, "An experimental and theoretical study of the relation between magnetic field and current in a superconductor," *Proc. R. Soc. London. Ser. A. Math. Phys. Sci.*, vol. 216, no. 1127, pp. 547–568, Feb. 1953, doi: 10.1098/rspa.1953.0040.

[18] R. R. Hake, "Paramagnetic Superconductivity in Extreme Type-II Superconductors," *Phys. Rev.*, vol. 158, no. 2, pp. 356–376, Jun. 1967, doi: 10.1103/PhysRev.158.356.

[19] V. L. Ginzburg and L. D. Landau, "On the Theory of superconductivity (In Russian)," *Zh.Eksp.Teor.Fiz*, vol. 20, pp. 1064–1082, 1950.

[20] J. Bardeen, L. N. Cooper, and J. R. Schrieffer, "Microscopic theory of superconductivity," *Phys. Rev.*, vol. 106, no. 1, p. 162, Nov. 1957, doi: 10.1080/00107516808220097.

[21] C. Pira, "Nb thick films in 6 GHz superconducting resonant cavities," Ph.D. Thesis, Università degli Studi di Padova, 2018.

[22] A. E. Dane, "Reactive DC Magnetron Sputtering of Ultrathin Superconducting Niobium Nitride Films," Master Thesis, Massachusetts Institute of Technology, 2015.

[23] J. Pearl, "Current distribution in superconducting films carrying quantized fluxoids," *Appl. Phys. Lett.*, vol. 5, no. 4, pp. 65–66, Aug. 1964, doi: 10.1063/1.1754056.

[24] E. H. Brandt, "Theory of type-II superconductors with finite London penetration depth," *Phys. Rev. B*, vol. 64, no. 2, p. 024505, Jun. 2001, doi: 10.1103/PhysRevB.64.024505.

[25] S. Posen, M. Liepe, G. Catelani, J. P. Sethna, and M. K. Transtrum, "Theoretical field limits for multi-layer superconductors," in *Proceedings of 16th International Conference on RF Superconductivity (SRF 2013)*, 2013, pp. 794–799.

[26] I. Santoso, "k-space Microscopy of Bi2Sr2CaCu2O8+δ :Fermiology and Many-body Effects," Ph.D. Thesis, Universiteit van Amsterdam, 2008.

[27] W. Buckel and R. Kleiner, *Superconductivity: Fundamentals and Applications*, Second Edi. Wiley-VCH, 2004.

[28] C. Z. Antoine *et al.*, "Magnetic screening of NbN multilayers samples," in *Proceedings of 15th International Conference on RF superconductivity (SRF 2011)*, 2011, pp. 281–286.

[29] G. Catelani and J. P. Sethna, "Temperature dependence of the superheating field for superconductors in the high-κ London limit," *Phys. Rev. B*, vol. 78, no. 22, p. 224509, Dec. 2008, doi: 10.1103/PhysRevB.78.224509.

[30] A. Gurevich, "Superconducting Radio-Frequency Fundamentals for Particle Accelerators," *Rev. Accel. Sci. Technol.*, vol. 05, pp. 119–146, Jan. 2012, doi: 10.1142/S1793626812300058.

[31] T. Kubo, "Multilayer coating for higher accelerating fields in superconducting radio-frequency cavities: a review of theoretical aspects," *Supercond. Sci. Technol.*, vol. 30, no. 2, p. 023001, Feb. 2017, doi: 10.1088/1361-6668/30/2/023001.

[32] F. P.-J. Lin and A. Gurevich, "Effect of impurities on the superheating field of type-II superconductors," *Phys. Rev. B*, vol. 85, no. 5, pp. 1–11, Feb. 2012, doi: 10.1103/PhysRevB.85.054513.

[33] V. Galaĭko, "Stability Limits of the Superconducting State in a Magnetic Field for Superconductors of the Second Kind," *Sov. J. Exp. Theor. Phys.*, vol. 23, no. 3, p. 475, 1966.

[34] M. K. Transtrum, G. Catelani, and J. P. Sethna, "Superheating field of superconductors within Ginzburg-Landau theory," *Phys. Rev. B - Condens. Matter Mater. Phys.*, vol. 83, no. 9, pp. 1–8, 2011, doi: 10.1103/PhysRevB.83.094505.

[35] D. B. Liarte, S. Posen, M. K. Transtrum, G. Catelani, M. Liepe, and J. P. Sethna, "Theoretical estimates of maximum fields in superconducting resonant radio frequency cavities: stability theory, disorder, and laminates," *Supercond. Sci. Technol.*, vol. 30, no. 3, p. 033002, Mar. 2017, doi: 10.1088/1361-6668/30/3/033002.

[36] K. Saito, "Surface smoothness for high gradient Niobium sc rf cavities," in *Proceedings of 11th Workshop on RF Superconductivity (SRF 2003)*, 2003, no. 2, pp. 637–640.

[37] C. Xu, H. Tian, C. E. Reece, and M. J. Kelley, "Enhanced characterization of niobium surface topography," *Phys. Rev. Spec. Top. - Accel. Beams*, vol. 14, no. 12, p. 123501, Dec. 2011, doi: 10.1103/PhysRevSTAB.14.123501.

[38] T. Kubo, "Field limit and nano-scale surface topography of superconducting radio-frequency cavity made of extreme type II superconductor," *Prog. Theor. Exp. Phys.*, vol. 2015, no. 6, pp. 63G01-0, Jun. 2015, doi: 10.1093/ptep/ptv082.

[39] C. Z. Antoine, "How to Achieve the Best SRF Performance: (Practical) Limitations and Possible Solutions," *arXiv*, vol. XII, Jan. 2013, doi: 10.5170/CERN-2014-005.209.

[40] C. Benvenuti *et al.*, "Study of the surface resistance of superconducting niobium films at 1.5 GHz," *Phys. C Supercond. its Appl.*, vol. 316, no. 3–4, pp. 153–188, May 1999, doi: 10.1016/S0921-4534(99)00207-5.

[41] A. Gurevich and G. Ciovati, "Effect of vortex hotspots on the radio-frequency surface resistance of superconductors," *Phys. Rev. B - Condens. Matter Mater. Phys.*, vol. 87, no. 5, 2013, doi: 10.1103/PhysRevB.87.054502.

[42] J. T. Maniscalco, D. Gonnella, and M. Liepe, "The importance of the electron mean free path for superconducting radio-frequency cavities," *J. Appl. Phys.*, vol. 121, no. 4, p. 043910, Jan. 2017, doi: 10.1063/1.4974909.

[43] A. Gurevich, "Theory of RF superconductivity for resonant cavities," *Supercond. Sci. Technol.*, vol. 30, no. 3, p. 034004, Mar. 2017, doi: 10.1088/1361-6668/30/3/034004.

[44] A. Grassellino *et al.*, "Nitrogen and argon doping of niobium for superconducting radio frequency cavities: a pathway to highly efficient accelerating structures," *Supercond. Sci. Technol.*, vol. 26, no. 10, p. 102001, Oct. 2013, doi: 10.1088/0953-2048/26/10/102001.

[45] C. Pira, "Nb Thin Films," *EASISchool 3 Lectures - Superconductivity and its applications*. 2020.

[46] C. Benvenuti *et al.*, "Properties of copper cavities coated with niobium using different discharge gases," in *Proceedings of 8th Workshop on RF Superconductivity (SRF 1997)*, 1997, pp. 6–10.

[47] J. Knobloch and H. Padamsee, "Reduction of the surface resistance in superconducting cavities due to gas discharge," in *Proceedings of 8th Workshop on RF Superconductivity (SRF 1997)*, 1997, pp. 345–351.

[48] A.-M. Valente-Feliciano, "Superconducting RF materials other than bulk niobium: a review," *Supercond. Sci. Technol.*, vol. 29, no. 11, p. 113002, Nov. 2016, doi: 10.1088/0953-2048/29/11/113002.

[49] V. Palmieri and R. Vaglio, "Thermal contact resistance at the Nb/Cu interface as a limiting factor for sputtered thin film RF superconducting cavities," *Superconductor Science and Technology*, vol. 29, no. 1. 2015, doi: 10.1088/0953-2048/29/1/015004.

[50] A. Miyazaki and W. V. Delsolaro, "Two different origins of the Q -slope problem in superconducting niobium film cavities for a heavy ion accelerator at CERN," *Phys. Rev. Accel. Beams*, vol. 22, no. 7, p. 073101, Jul. 2019, doi: 10.1103/PhysRevAccelBeams.22.073101.

[51] D. Gonnella, J. Kaufman, and M. Liepe, "Impact of nitrogen doping of niobium superconducting cavities on the sensitivity of surface resistance to trapped magnetic flux," *Journal of Applied Physics*, vol. 119, no. 7. 2016, doi: 10.1063/1.4941944.

[52] S. Calatroni and R. Vaglio, "Surface Resistance of Superconductors in the Presence of a DC Magnetic Field: Frequency and Field Intensity Limits," *IEEE Trans. Appl. Supercond.*, vol. 27, no. 5, pp. 1–6, Aug. 2017, doi: 10.1109/TASC.2017.2691604.

[53] V. Arbet-Engels *et al.*, "Superconducting niobium cavities, a case for the film technology," *Nucl. Instruments Methods Phys. Res. Sect. A Accel. Spectrometers, Detect. Assoc. Equip.*, vol. 463, no. 1–2, pp. 1–8, 2001, doi: 10.1016/S0168-9002(01)00165-6.

[54] G. Arnolds-Meyer and W. Weingarten, "Comparative measurements on niobium

sheet and sputter coated cavities," *IEEE Trans. Magn.*, vol. 23, no. 2, pp. 1620–1623, 1987.

[55] B. Aune *et al.*, "Superconducting TESLA cavities," *Phys. Rev. Spec. Top. - Accel. Beams*, vol. 3, no. 9, p. 092001, Sep. 2000, doi: 10.1103/PhysRevSTAB.3.092001.

[56] C. Antoine, "Materials and surface aspects in the development of SRF Niobium cavities," no. EuCARD Series, Vol. 12. Publishing Office of Warsaw University of Technology, Warsaw, Poland, 2012, [Online]. Available: http://cds.cern.ch/record/1472363/files/EuCARD-BOO-2012-001.pdf?version=1.

[57] O. Kugeler, W. Anders, A. Neumann, and J. Knobloch, "Improving the intrinsic quality factor of srf cavities by thermal cycling," in *Proceedings of 15th International Conference on RF superconductivity (SRF 2011)*, 2011, pp. 724–727.

[58] A. Romanenko, A. Grassellino, O. Melnychuk, and D. A. Sergatskov, "Dependence of the residual surface resistance of superconducting radio frequency cavities on the cooling dynamics around Tc," *J. Appl. Phys.*, vol. 115, no. 18, p. 184903, May 2014, doi: 10.1063/1.4875655.

[59] T. Junginger, "Field dependent surface resistance of niobium on copper cavities," *Phys. Rev. Spec. Top. - Accel. Beams*, vol. 18, no. 7, p. 072001, Jul. 2015, doi: 10.1103/PhysRevSTAB.18.072001.

[60] J.-M. Vogt, O. Kugeler, and J. Knobloch, "Impact of cool-down conditions at Tc on the superconducting rf cavity quality factor," *Phys. Rev. Spec. Top. - Accel. Beams*, vol. 16, no. 10, p. 102002, Oct. 2013, doi: 10.1103/PhysRevSTAB.16.102002.

[61] O. Kugeler *et al.*, "Investigation of trapped magnetic flux in superconducting niobium samples with polarised neutron radiography," in *Proceedings of 8th International Particle Accelerator Conference*, 2017, pp. 964–967.

[62] M. Kelly, "Superconducting Radio-Frequency Cavities for Low-Beta Particle Accelerators," *Rev. Accel. Sci. Technol.*, vol. 05, pp. 185–203, Jan. 2012, doi: 10.1142/S1793626812300071.

[63] J. Knobloch, "Advanced Thermometry Studies of Superconducting Radio-Frequency Cavities," Ph.D. Thesis, Cornell University, 1997.

[64] H. Padamsee, "Designing superconducting cavities for accelerators," *Accel. Phys. Technol. Appl.*, pp. 336–362.

[65] S. Posen, "Understanding And Overcoming Limitation Mechanisms In Nb3Sn Superconducting RF Cavities," Ph.D. Thesis, Cornell University, 2015.

[66] E. Bemporad, F. Carassiti, M. Sebastiani, G. Lanza, V. Palmieri, and H. Padamsee, "Superconducting and microstructural studies on sputtered niobium thin films for accelerating cavity applications," *Supercond. Sci. Technol.*, vol. 21, no. 12, p. 125026, Dec. 2008, doi: 10.1088/0953-2048/21/12/125026.

[67] M. Krishnan *et al.*, "Energetic condensation growth of Nb thin films," *Phys. Rev. Spec. Top. - Accel. Beams*, vol. 15, no. 3, p. 032001, Mar. 2012, doi: 10.1103/PhysRevSTAB.15.032001.

[68] V. Palmieri, "New materials for superconducting radiofrequency cavities," in *Proceedings of 10th Workshop on RF Superconductivity (SRF 2001)*, 2001, pp. 162–169.

[69] X. Xi, "Prospects for Higher Tc Superconductors for SRF Application," *Proceedings of 13th International Workshop on RF Superconductivity (SRF 2007)*, 2007.

[70] H. Padamsee, "Future Prospects of Superconducting RF for Accelerator Applications," *Rev. Accel. Sci. Technol.*, vol. 10, no. 01, pp. 125–156, Aug. 2019, doi: 10.1142/S1793626819300081.

[71] C. Benvenuti, D. Bloess, E. Chiaveri, N. Hilleret, M. Minestrini, and W. Weingarten,

"Superconducting Cavities Produced By Magnetron Sputtering of Niobium on Copper," in *Proceedings of 3rd Workshop on RF Superconductivity (SRF 1987)*, 1987, pp. 445–468.

[72] S. Calatroni, "20 Years of experience with the Nb/Cu technology for superconducting cavities and perspectives for future developments," *Phys. C Supercond. its Appl.*, vol. 441, no. 1–2, pp. 95–101, 2006, doi: 10.1016/j.physc.2006.03.044.

[73] G. Lanza *et al.*, "The HIE-ISOLDE Superconducting Cavities : Surface Treatment and Niobium Thin Film Coating," in *Proceedings of 14th International Conference on RF Superconductivity (SRF 2009)*, 2009, no. 227579, pp. 801–805.

[74] N. Jecklin *et al.*, "Niobium Coatings for The HIE-ISOLDE QWR Superconducting Accelerating Cavities," *Proceedings of 16th International Conference on RF Superconductivity (SRF 2013)*, p. tup073, 2013.

[75] S. Stark *et al.*, "Niobium sputter-coated QWRs," in *Proceedings of 8th Workshop on RF Superconductivity (SRF 1997)*, 1997, pp. 1156–1163.

[76] D. B. Beringer, W. M. Roach, C. Clavero, C. E. Reece, and R. A. Lukaszew, "Characterization of two different orientations of epitaxial niobium thin films grown on MgO(001) surfaces," *Journal of Applied Physics*, vol. 114, no. 22. 2013, doi: 10.1063/1.4837595.

[77] G. K. White, "The thermal and electrical conductivity of copper," *Proc. R. Soc. London. Ser. A Math. Phys. Sci.*, vol. 211, no. 1104, pp. 122–125, 1953.

[78] F. Koechlin and B. Bonin, "Parametrisation of the niobium thermal conductivity in the superconducting state," in *Proceedings of 7th Workshop on RF Superconductivity (SRF 1995)*, 1995, pp. 665–669.

[79] V. Palmieri *et al.*, "The Way of Thick Films toward a Flat Q-curve in Sputtered Cavities," in *Proceedings of 18th International Conference on RF Superconductivity (SRF 2017)*, 2017, pp. 378–381, doi: 10.18429/JACoW-SRF2017-TUYBA03.

[80] J. Halbritter, "Granular superconductors and their intrinsic and extrinsic surface impedance," *J. Supercond.*, vol. 8, no. 6, pp. 691–703, 1995, doi: 10.1007/BF00727492.

[81] G. Terenziani, S. Calatroni, and A. Ehiasarian, "Niobium coatings for superconducting rf applications by HiPIMS," *Proceedings of 4th HIPIMS Conference*, 2012.

[82] G. Terenziani, S. Calatroni, T. Junginger, I. A. Santillana, and S. Sheffield, "Nb Coating Developments With HiPIMS for SRF Applications," in *Proceedings of 16th International Conference on RF Superconductivity (SRF 2013)*, 2013, pp. 621–624.

[83] M. Burton *et al.*, "RF results of Nb coated srf accelerator cavities via HiPIMS," in *Proceedings of 18th International Conference on RF Superconductivity (SRF 2017)*, 2017, pp. 535–538, doi: 10.18429/JACoW-SRF2017-TUPB066.

[84] A. Anders *et al.*, "Deposition of niobium and other superconducting materials with high power impulse magnetron sputtering: Concept and first results," *Proceedings of 15th International Conference on RF superconductivity (SRF 2011)*, pp. 302–308, 2011.

[85] S. Wilde *et al.*, "DC magnetism of Niobium thin films," in *Proceedings of 18th International Conference on RF Superconductivity (SRF 2017)*, 2017, pp. 3–7, doi: 10.18429/JACoW-SRF2017-TUPB103.

[86] F. Avino *et al.*, "Improved film density for coatings at grazing angle of incidence in high power impulse magnetron sputtering with positive pulse," *Thin Solid Films*, vol. 706, p. 138058, Jul. 2020, doi: 10.1016/j.tsf.2020.138058.

[87] G. Rosaz, "Nb/Cu studies at CERN," *FCC Week 2018*, 2018.

[88] R. Russo, "Quality measurement of niobium thin films for Nb/Cu superconducting RF cavities," *Meas. Sci. Technol.*, vol. 18, no. 8, pp. 2299–2313, Aug. 2007, doi: 10.1088/0957-

0233/18/8/003.

[89] K. M. Velas, S. F. Chapman, I. Irfan, and M. Krishnan, "Energetic condensation growth of Nb on Cu SRF cavities," in *Proceedings of 17th International Conference on RF Superconductivity (SRF 2015)*, 2015, pp. 629–632.

[90] A. M. Valente-Feliciano *et al.*, "ECR Nb films grown on Cu substrates: Influence of ion energy and interface," *Proceedings of 16th International Conference on RF Superconductivity (SRF 2013)*, 2013.

[91] A. M. Valente-Feliciano, G. Eremeev, C. Reece, J. Spardlin, S. Aull, and T. Proslier, "Material Quality & SRF Performance of Nb Films Grown on Cu via ECR Plasma Energetic Condensation," in *Proceedings of 17th International Conference on RF Superconductivity (SRF 2015)*, 2015, pp. 622–625.

[92] V. García, E. Chyhyrynets, F. Stivanello, L. Zanotto, and C. Pira, "Update in Deposition of Nb Thick Films on Cu for 6 GHz Cavities.," *FCC Week 2019*, 2019.

[93] A.-M. Valente-Feliciano, "SRF Materials other than Niobium," *Proceedings of 13th International Workshop on RF Superconductivity (SRF 2007)*, 2007.

[94] A. Sublet *et al.*, "Developments on SRF Coatings at CERN," in *Proceedings of 17th International Conference on RF Superconductivity (SRF 2015)*, 2015, pp. 617–621.

[95] W. Lengauer, M. Bohn, B. Wollein, and K. Lisak, "Phase reactions in the Nb–N system below 1400°C," *Acta Mater.*, vol. 48, no. 10, pp. 2633–2638, Jun. 2000, doi: 10.1016/S1359-6454(00)00056-2.

[96] G. Brauer, "Nitrides, Carbonitrides and oxynitrides of niobium," *J. less-common Met.*, vol. 2, pp. 131–137, 1960.

[97] Y. Zou *et al.*, "Discovery of Superconductivity in Hard Hexagonal ε-NbN," *Sci. Rep.*, vol. 6, no. 1, p. 22330, Apr. 2016, doi: 10.1038/srep22330.

[98] G. Eremeev, "Review of rf properties of NbN and MgB2 thin coating on Nb samples and cavities," in *Proceedings of 14th International Conference on RF Superconductivity (SRF 2009)*, 2009, pp. 159–163.

[99] K. S. Keskar, T. Yamashita, and Y. Onodera, "Superconducting transition temperatures of RF sputtered NbN films," *Jpn. J. Appl. Phys.*, vol. 10, no. 3, pp. 370–374, 1971.

[100] K. L. Westra, "Properties of reactively sputtered NbN films," *J. Vac. Sci. Technol. A Vacuum, Surfaces, Film.*, vol. 8, no. 3, p. 1288, 1990, doi: 10.1116/1.576913.

[101] J. Tyan and J. T. Lue, "Grain boundary scattering in the normal state resistivity of superconducting NbN thin films," *J. Appl. Phys.*, vol. 75, no. 1, pp. 325–331, Jan. 1994, doi: 10.1063/1.355853.

[102] R. W. Guard, J. W. Savage, and D. G. Swarthout, "Constitution of a Portion of the Niobium(Columbium)- Nitrogen System," *Trans. Metall. Soc. AIME*, vol. 239, pp. 643–649, 1967.

[103] G. Oya and Y. Onodera, "Transition temperatures and crystal structures of single-crystal and polycrystalline NbN x films," *J. Appl. Phys.*, vol. 45, no. 3, pp. 1389–1397, Mar. 1974, doi: 10.1063/1.1663418.

[104] E. I. Isaev *et al.*, "Phonon related properties of transition metals, their carbides, and nitrides: A first-principles study," *J. Appl. Phys.*, vol. 101, no. 12, p. 123519, Jun. 2007, doi: 10.1063/1.2747230.

[105] F. Mercier *et al.*, "Niobium nitride thin films deposited by high temperature chemical vapor deposition," *Surf. Coatings Technol.*, vol. 260, pp. 126–132, 2014, doi: 10.1016/j.surfcoat.2014.08.084.

[106] C. Benvenuti, P. Chiggiato, L. Parrini, and R. Russo, "Reactive diffusion produced niobium nitride films for superconducting cavity applications," *Nucl. Inst. Methods*

Phys. Res. A, vol. 336, no. 1–2, pp. 16–22, 1993, doi: 10.1016/0168-9002(93)91077-Z.

[107] D. W. Capone II, K. E. Gray, and R. T. Kampwirth, "New scaling relation for sputtered NbN films," *J. Appl. Phys.*, vol. 65, no. 1, pp. 258–261, Jan. 1989, doi: 10.1063/1.342582.

[108] J. R. Gavaler, A. I. Braginski, M. Ashkin, and A. T. Santhanam, "Thin films and metastable phases," in *Superconductivity in D- and F-Band Metals*, Elsevier, 1980, pp. 25–36.

[109] M. Bhushan, "Analysis of reactive sputtering mechanisms for NbN film deposition," *J. Vac. Sci. Technol. A*, vol. 5, no. 5, p. 2829, 1987, doi: 10.1116/1.574316.

[110] S. Isagawa, "rf superconducting properties of reactively sputtered NbN," *J. Appl. Phys.*, vol. 52, no. 2, pp. 921–927, Feb. 1981, doi: 10.1063/1.328846.

[111] A. Nigro, G. Nobile, V. Palmieri, G. Rubino, and R. Vaglio, "Superconducting and normal state properties of niobium-nitride thin films," *Phys. Scr.*, vol. 38, no. 3, pp. 483–485, Sep. 1988, doi: 10.1088/0031-8949/38/3/027.

[112] C. Z. Antoine, "Influence of crystalline structure on rf dissipation in superconducting niobium," *Phys. Rev. Accel. Beams*, vol. 22, no. 3, p. 034801, Mar. 2019, doi: 10.1103/PhysRevAccelBeams.22.034801.

[113] M. R. Beebe, D. B. Beringer, M. C. Burton, K. Yang, and R. A. Lukaszew, "Stoichiometry and thickness dependence of superconducting properties of niobium nitride thin films," *J. Vac. Sci. Technol. A Vacuum, Surfaces, Film.*, vol. 34, no. 2, p. 021510, Mar. 2016, doi: 10.1116/1.4940132.

[114] I. L. Singer, R. N. Bolster, S. A. Wolf, E. F. Skelton, and R. A. Jeffries, "Abrasion resistance, microhardness and microstructures of single-phase niobium nitride films," *Thin Solid Films*, vol. 107, no. 2, pp. 207–215, 1983, doi: 10.1016/0040-6090(83)90023-8.

[115] N. N. Iosad, B. D. Jackson, S. N. Polyakov, P. N. Dmitriev, and T. M. Klapwijk, "Reactive magnetron sputter-deposition of NbN and (Nb, Ti)N films related to sputtering source characterization and optimization," *J. Vac. Sci. Technol. A Vacuum, Surfaces, Film.*, vol. 19, no. 4, pp. 1840–1845, Jul. 2001, doi: 10.1116/1.1349189.

[116] A. C. Anderson, D. J. Lichtenwalner, and W. T. Brogan, "Process control for the low temperature deposition of niobium-nitride thin films," *IEEE Trans. Magn.*, vol. 25, no. 2, pp. 2084–2088, Mar. 1989, doi: 10.1109/20.92718.

[117] W. M. Roach, J. R. Skuza, D. B. Beringer, Z. Li, C. Clavero, and R. A. Lukaszew, "NbN thin films for superconducting radio frequency cavities," *Supercond. Sci. Technol.*, vol. 25, no. 12, p. 125016, Dec. 2012, doi: 10.1088/0953-2048/25/12/125016.

[118] D. D. Bacon *et al.*, "Properties of NbN thin films deposited on ambient temperature substrates," *J. Appl. Phys.*, vol. 54, no. 11, pp. 6509–6515, 1983.

[119] Z. Wang, A. Kawakami, Y. Uzawa, and B. Komiyama, "Superconducting properties and crystal structures of single-crystal niobium nitride thin films deposited at ambient substrate temperature," *J. Appl. Phys.*, vol. 79, no. 10, pp. 7837–7842, 1996.

[120] M. J. Deen, D. Landheer, J. D. Wade, G. I. Sproule, and M. D. Denhoff, "NbN thin films reactively sputtered with a high-field direct-current magnetron," *J. Vac. Sci. Technol. A Vacuum, Surfaces, Film.*, vol. 6, no. 4, pp. 2299–2303, Jul. 1988, doi: 10.1116/1.575579.

[121] Y. M. Shy, L. E. Toth, and R. Somasundaram, "Superconducting properties, electrical resistivities, and structure of NbN thin films," *J. Appl. Phys.*, vol. 44, no. 12, pp. 5539–5545, 1973, doi: 10.1063/1.1662193.

[122] K. Makise, H. Terai, M. Takeda, Y. Uzawa, and Z. Wang, "Characterization of NbTiN Thin Films Deposited on Various Substrates," *IEEE Trans. Appl. Supercond.*, vol. 21, no. 3, pp. 139–142, Jun. 2011, doi: 10.1109/TASC.2010.2088350.

[123] A. Nigro, G. Nobile, M. G. Rubino, and R. Vaglio, "Electrical resistivity of

polycrystalline niobium nitride films," *Phys. Rev. B*, vol. 37, no. 8, pp. 3970–3972, Mar. 1988, doi: 10.1103/PhysRevB.37.3970.

[124] S. Kubo, M. Hikita, and M. Igarashi, "Magnetic penetration depths in superconducting NbN films prepared by reactive dc magnetron sputtering," *Appl. Phys. Lett.*, vol. 44, no. 2, pp. 258–260, 1984.

[125] N. N. Iosad, T. M. Klapwijk, S. N. Polyakov, V. V. Roddatis, E. K. Kov'ev, and P. N. Dmitriev, "Properties of DC magnetron sputtered Nb and NbN films for different source conditions," *IEEE Trans. Appiled Supercond.*, vol. 9, no. 2, pp. 1720–1723, Jun. 1999, doi: 10.1109/77.784785.

[126] T. Kubo, "Optimum multilayer coating of superconducting particle accelerator cavities and effects of thickness dependent material properties of thin films," *Jpn. J. Appl. Phys.*, vol. 58, no. 8, p. 088001, Aug. 2019, doi: 10.7567/1347-4065/ab2f0a.

[127] A. A. Abrikosov, "On the lower critical field of thin layers of superconductors of the second group," *J. Exp. Theor. Phys.*, vol. 19, no. 4, pp. 988–991, 1964.

[128] C. Z. Antoine *et al.*, "Characterization of superconducting nanometric multilayer samples for superconducting rf applications: First evidence of magnetic screening effect," *Phys. Rev. Spec. Top. - Accel. Beams*, vol. 13, no. 12, pp. 1–6, 2010, doi: 10.1103/PhysRevSTAB.13.121001.

[129] T. Kubo, Y. Iwashita, and T. Saeki, "Radio-frequency electromagnetic field and vortex penetration in multilayered superconductors," *Appl. Phys. Lett.*, vol. 104, no. 3, p. 032603, Jan. 2014, doi: 10.1063/1.4862892.

[130] A. Gurevich, "Maximum screening fields of superconducting multilayer structures," *AIP Adv.*, vol. 5, 2015.

[131] C. Z. Antoine *et al.*, "Progress on characterisation and optimisation of miltilayers," in *Proceedings of 18th International Conference on RF Superconductivity (SRF 2017)*, 2017, pp. 368–373, doi: 10.18429/JACoW-SRF2017-TUYBA01.

[132] T. Junginger, "Review of muSR studies for SRF applications," *7th Int. Work. Thin Film. New Ideas Push. Limits RF Supercond.*, 2016.

[133] W. M. Roach, D. B. Beringer, Z. Li, C. Clavero, and R. A. Lukaszew, "Magnetic shielding larger than the lower critical field of niobium in multilayers," *IEEE Trans. Appl. Supercond.*, vol. 23, no. 3, pp. 2012–2014, 2013, doi: 10.1109/TASC.2012.2234956.

[134] M. C. Burton *et al.*, "Superconducting NbN-based multilayer and NbTiN thin films for the enhancement of srf accelerator cavities," in *Proceedings of 17th International Conference on RF Superconductivity (SRF 2015)*, 2015, pp. 638–642.

[135] R. A. Lukaszew *et al.*, "Proof of concept thin films and multilayers toward enhanced field gradients in srf cavities," in *Proceedings of 16th International Conference on RF Superconductivity (SRF 2013)*, 2013, pp. 782–784.

[136] R. Katayama *et al.*, "Evaluation of the superconducting characteristics of multi-layer thin-film structures of NbN and SiO2 on pure Nb substrate," in *Proceedings of 19th International Conference on RF Superconductivity (SRF 2019)*, 2019, pp. 809–811, doi: 10.18429/JACoW-SRF2019-THFUA2.

[137] "Electric glow discharge." https://www.plasma-universe.com/Electric-glow-discharge (accessed May 13, 2019).

[138] J. E. Mahan, *Physical Vapor Deposition of Thin Films*. Wiley-Interscience, 2000.

[139] M. Ohring, *Materials Science of Thin Films: Deposition and Structure*, Second Edi. Academic Press, 2002.

[140] G. Lanza, "New magnetron configurations or sputtering niobium thin films into copper tesla-type superconducting cavities," Ph.D. Thesis, Università degli Studi di

Padova, 2008.
[141] J. Faber, G. Hötzsch, and C. Metzner, "Sputter etching of steel substrates using DC and MF pulsed magnetron discharges," *Vacuum*, vol. 64, no. 1, pp. 55–63, Nov. 2001, doi: 10.1016/S0042-207X(01)00375-X.
[142] Y. Yamamura and H. Tawara, "Energy dependence of ion-induced sputtering yields from monatomic solids at normal incidence," *At. Data Nucl. Data Tables*, vol. 62, no. 2, pp. 149–253, 1996, doi: 10.1006/adnd.1996.0005.
[143] D. Depla and S. Mahieu, Eds., *Reactive Sputter Deposition*. Springer, 2008.
[144] A. Anders, "Tutorial: Reactive high power impulse magnetron sputtering," *J. Appl. Phys.*, vol. 121, no. 171101, 2017, doi: 10.1063/1.4978350.
[145] E. Shidoji, M. Nemoto, and T. Nomura, "An anomalous erosion of a rectangular magnetron system," *J. Vac. Sci. Technol. A Vacuum, Surfaces, Film.*, vol. 18, no. 6, pp. 2858–2863, Nov. 2000, doi: 10.1116/1.1312376.
[146] Q. H. Fan, L. Q. Zhou, and J. J. Gracio, "A cross-corner effect in a rectangular sputtering magnetron," *J. Phys. D. Appl. Phys.*, vol. 36, no. 3, pp. 244–251, Feb. 2003, doi: 10.1088/0022-3727/36/3/305.
[147] S. M. Rossnagel, "Gas density reduction effects in magnetrons," *J. Vac. Sci. Technol. A Vacuum, Surfaces, Film.*, vol. 6, no. 1, pp. 19–24, Jan. 1988, doi: 10.1116/1.574988.
[148] A. Anders, "Discharge physics of high power impulse magnetron sputtering," *Surf. Coatings Technol.*, vol. 205, pp. S1–S9, Jul. 2011, doi: 10.1016/j.surfcoat.2011.03.081.
[149] D. Depla and R. De Gryse, "Target poisoning during reactive magnetron sputtering: Part II: the influence of chemisorption and gettering," *Surf. Coatings Technol.*, vol. 183, no. 2–3, pp. 190–195, May 2004, doi: 10.1016/j.surfcoat.2003.10.007.
[150] D. Depla and R. De Gryse, "Target poisoning during reactive magnetron sputtering: Part I: the influence of ion implantation," *Surf. Coatings Technol.*, vol. 183, no. 2–3, pp. 184–189, May 2004, doi: 10.1016/j.surfcoat.2003.10.006.
[151] I. Safi, "Recent aspects concerning DC reactive magnetron sputtering of thin films: A review," *Surf. Coatings Technol.*, vol. 127, no. 2–3, pp. 203–219, 2000.
[152] W. D. Sproul, D. J. Christie, and D. C. Carter, "Control of reactive sputtering processes," *Thin Solid Films*, vol. 491, no. 1–2, pp. 1–17, 2005, doi: 10.1016/j.tsf.2005.05.022.
[153] S. Berg and T. Nyberg, "Fundamental understanding and modeling of reactive sputtering processes," *Thin Solid Films*, vol. 476, no. 2, pp. 215–230, 2005, doi: 10.1016/j.tsf.2004.10.051.
[154] V. Kouznetsov, K. Macák, J. M. Schneider, U. Helmersson, and I. Petrov, "A novel pulsed magnetron sputter technique utilizing very high target power densities," *Surf. Coatings Technol.*, vol. 122, no. 2–3, pp. 290–293, Dec. 1999, doi: 10.1016/S0257-8972(99)00292-3.
[155] J. Bohlmark, J. Alami, C. Christou, A. P. Ehiasarian, and U. Helmersson, "Ionization of sputtered metals in high power pulsed magnetron sputtering," *J. Vac. Sci. Technol. A Vacuum, Surfaces, Film.*, vol. 23, no. 1, pp. 18–22, Jan. 2005, doi: 10.1116/1.1818135.
[156] N. Hosokawa, T. Tsukada, and H. Kitahara, ".," in *Proceedings of the 8th International Vacuum Congress*, 1980, pp. 11–14.
[157] A. Anders, J. Andersson, and A. Ehiasarian, "High power impulse magnetron sputtering: Current-voltage-time characteristics indicate the onset of sustained self-sputtering," *J. Appl. Phys.*, vol. 102, no. 11, p. 113303, Dec. 2007, doi: 10.1063/1.2817812.
[158] A. Anders, "Self-sputtering runaway in high power impulse magnetron sputtering: The role of secondary electrons and multiply charged metal ions," *Appl. Phys. Lett.*, vol.

92, no. 20, p. 201501, May 2008, doi: 10.1063/1.2936307.
[159] S. Wilde, "Development of superconducting thin films for use in SRF cavity applications," Ph.D. Thesis, Loughborough University, 2017.
[160] A. Anders, "Deposition rates of high power impulse magnetron sputtering: Physics and economics," *J. Vac. Sci. Technol. A Vacuum, Surfaces, Film.*, vol. 28, no. 4, pp. 783–790, Jul. 2010, doi: 10.1116/1.3299267.
[161] S. Konstantinidis, J. P. Dauchot, and M. Hecq, "Titanium oxide thin films deposited by high-power impulse magnetron sputtering," *Thin Solid Films*, vol. 515, no. 3, pp. 1182–1186, Nov. 2006, doi: 10.1016/j.tsf.2006.07.089.
[162] A. P. Ehiasarian, Y. A. Gonzalvo, and T. D. Whitmore, "Time-Resolved Ionisation Studies of the High Power Impulse Magnetron Discharge in Mixed Argon and Nitrogen Atmosphere," *Plasma Process. Polym.*, vol. 4, no. S1, pp. S309–S313, Apr. 2007, doi: 10.1002/ppap.200730806.
[163] A. P. Ehiasarian, W. D. Münz, L. Hultman, U. Helmersson, and I. Petrov, "High power pulsed magnetron sputtered CrNx films," *Surf. Coatings Technol.*, vol. 163–164, pp. 267–272, 2003.
[164] J. Andersson and A. Anders, "Self-Sputtering Far above the Runaway Threshold: An Extraordinary Metal-Ion Generator," *Phys. Rev. Lett.*, vol. 102, no. 4, p. 045003, Jan. 2009, doi: 10.1103/PhysRevLett.102.045003.
[165] J. T. Gudmundsson, D. Lundin, N. Brenning, M. A. Raadu, C. Huo, and T. M. Minea, "An ionization region model of the reactive Ar/O 2 high power impulse magnetron sputtering discharge," *Plasma Sources Sci. Technol.*, vol. 25, no. 6, p. 065004, Oct. 2016, doi: 10.1088/0963-0252/25/6/065004.
[166] K. Sarakinos, J. Alami, and M. Wuttig, "Process characteristics and film properties upon growth of TiO x films by high power pulsed magnetron sputtering," *J. Phys. D. Appl. Phys.*, vol. 40, no. 7, pp. 2108–2114, Apr. 2007, doi: 10.1088/0022-3727/40/7/037.
[167] E. Wallin and U. Helmersson, "Hysteresis-free reactive high power impulse magnetron sputtering," *Thin Solid Films*, vol. 516, no. 18, pp. 6398–6401, Jul. 2008, doi: 10.1016/j.tsf.2007.08.123.
[168] M. Audronis and V. Bellido-Gonzalez, "Hysteresis behaviour of reactive high power impulse magnetron sputtering," *Thin Solid Films*, vol. 518, no. 8, pp. 1962–1965, Feb. 2010, doi: 10.1016/j.tsf.2009.12.011.
[169] R. Ganesan *et al.*, "The role of pulse length in target poisoning during reactive HiPIMS: application to amorphous HfO 2," *Plasma Sources Sci. Technol.*, vol. 24, no. 3, p. 035015, May 2015, doi: 10.1088/0963-0252/24/3/035015.
[170] R. Ganesan *et al.*, "Duty cycle control in reactive high-power impulse magnetron sputtering of hafnium and niobium," *J. Phys. D. Appl. Phys.*, vol. 49, no. 24, p. 245201, Jun. 2016, doi: 10.1088/0022-3727/49/24/245201.
[171] I. Petrov, P. B. Barna, L. Hultman, and J. E. Greene, "Microstructural evolution during film growth," *J. Vac. Sci. Technol. A Vacuum, Surfaces, Film.*, vol. 21, no. 5, pp. S117–S128, 2003, doi: 10.1116/1.1601610.
[172] M. C. Burton, "Superconducting Thin Films for the Enhancement of Superconducting Radio Frequency Accelerator Cavities," Ph.D. Thesis, The College of William & Mary, 2017.
[173] A. Anders, "A structure zone diagram including plasma-based deposition and ion etching," *Thin Solid Films*, vol. 518, no. 15, pp. 4087–4090, 2010, doi: 10.1016/j.tsf.2009.10.145.
[174] J. M. Seeman, "Bias sputtering: its techniques and applications," *Vacuum*, vol. 17, no.

3, pp. 129–137, Mar. 1967, doi: 10.1016/0042-207X(67)93141-7.

[175] J. A. Thornton and D. W. Hoffman, "Stress-related effects in thin films," *Thin Solid Films*, vol. 171, no. 1, pp. 5–31, 1989, doi: 10.1016/0040-6090(89)90030-8.

[176] D. Tonini *et al.*, "Morphology of niobium films sputtered at different target–substrate angle," in *Proceedings of 11th Workshop on RF Superconductivity (SRF 2003)*, 2003, pp. 614–621.

[177] J. Alami, P. O. Å. Persson, D. Music, J. T. Gudmundsson, J. Bohlmark, and U. Helmersson, "Ion-assisted physical vapor deposition for enhanced film properties on nonflat surfaces," *J. Vac. Sci. Technol. A Vacuum, Surfaces, Film.*, vol. 23, no. 2, pp. 278–280, Mar. 2005, doi: 10.1116/1.1861049.

[178] H. Windischmann, "Intrinsic stress in sputter-deposited thin films," *Crit. Rev. Solid State Mater. Sci.*, vol. 17, no. 6, pp. 547–596, Jan. 1992, doi: 10.1080/10408439208244586.

[179] C. T. Wu, "Intrinsic stress of magnetron-sputtered niobium films," *Thin Solid Films*, vol. 64, no. 1, pp. 103–110, Nov. 1979, doi: 10.1016/0040-6090(79)90549-2.

[180] D. W. Hoffman, "Perspective on stresses in magnetron-sputtered thin films," *J. Vac. Sci. Technol. A Vacuum, Surfaces, Film.*, vol. 12, no. 4, pp. 953–961, 1994, doi: 10.1116/1.579073.

[181] A. Materne, H. Moriceau, B. Blanchard, and J. Florestan, "Changes in stress and coercivity after annealing of amorphous {Co}({Zr}, {Nb}) thin films deposited by {RF} sputtering," *IEEE Trans. Magn.*, 1988, doi: 10.1109/20.11591.

[182] V. Palmieri, "Fundamentals of electrochemistry - The electrolytic polishing of metals: Application to copper and niobium," in *Proceedings of 11th Workshop on RF Superconductivity (SRF 2003)*, 2003, pp. 579–587.

[183] D. M. Turley and L. E. Samuels, "The Nature of Mechanically Polished Surfaces of Copper," *Metallography*, vol. 14, no. 4, pp. 275–294, 1981, doi: 10.1016/0026-0800(81)90001-X.

[184] S. Calatroni *et al.*, "Influence of copper substrate treatments on properties of niobium coatings," in *Proceedings of 6th Workshop on RF Superconductivity (SRF 1993)*, 1993, pp. 687–695.

[185] P. Kneisel, K. Saito, R. Parodi, T. Jefferson, N. Accelerator, and N. News, "Performance of 1300MHz KEK-type single cell niobium cavities," in *Proceedings of 8th Workshop on RF Superconductivity (SRF 1997)*, 1997, pp. 463–471.

[186] L. Lilje *et al.*, "Improved surface treatment of the superconducting TESLA cavities," *Nucl. Instruments Methods Phys. Res. Sect. A Accel. Spectrometers, Detect. Assoc. Equip.*, vol. 516, no. 2–3, pp. 213–227, 2004, doi: 10.1016/j.nima.2003.08.116.

[187] J. Knobloch, R. L. Geng, M. Liepe, and H. Padamsee, "High-Field Q Slope in Superconducting Cavities Due to Magnetic Field Enhancement at Grain Boundaries," in *Proceedings of 9th Workshop on RF Superconductivity (SRF 1999)*, 1999, pp. 77–91.

[188] G. Ciovati, P. Dhakal, and A. Gurevich, "Decrease of the surface resistance in superconducting niobium resonator cavities by the microwave field," *Appl. Phys. Lett.*, vol. 104, no. 9, p. 092601, Mar. 2014, doi: 10.1063/1.4867339.

[189] S. Calatroni, E. Barbero-Soto, C. Benvenuti, L. Ferreira, and H. Neupert, "Progress of Nb/Cu technology with 1.5 GHz cavities," in *Proceedings of 11th Workshop on RF Superconductivity (SRF 2003)*, 2003, pp. 544–550.

[190] A. Pautrat *et al.*, "Quantitative analysis of the critical current due to vortex pinning by surface corrugation," *Phys. Rev. B*, vol. 69, no. 22, p. 224504, Jun. 2004, doi: 10.1103/PhysRevB.69.224504.

[191] J. D. Adam, J. P. Birabeau, J. Guerin, and S. Pousse, "Procedes de preparation de

surface de cuivre compatibles avec un depot de niobium realise par pulverisation cathodique," 1985.

[192] J. Halbritter, "Transport in superconducting niobium films for radio frequency applications," *J. Appl. Phys.*, vol. 97, no. 8, p. 083904, Apr. 2005, doi: 10.1063/1.1874292.

[193] C. Pira *et al.*, "ARIES Deliverable Report D15.1: Evaluation of cleaning process," 2018. [Online]. Available: https://edms.cern.ch/document/1820617/1.0%0A.

[194] C. Cooper, K. Saito, B. Bullock, S. Joshi, and A. Palczewski, "Centrifugal barrel polishing of cavities worldwide," in *Proceedings of 15th International Conference on RF superconductivity (SRF 2011)*, 2011, pp. 571–575.

[195] A. P. Rodríguez, L. M. A. Ferreira, and A. Sublet, "Subu Characterisation : Bath Fluid Dynamics Vs Etching Rate," in *Proceedings of 18th International Conference on RF Superconductivity (SRF 2017)*, 2017, pp. 575–579, doi: 10.18429/JACoW-SRF2017-TUPB078.

[196] S.-C. Chang, J.-M. Shieh, C.-C. Huang, B.-T. Dai, Y.-H. Li, and M.-S. Feng, "Microlevelling mechanisms and applications of electropolishing on planarisation of copper metallisation.pdf," *J. Vac. Sci. Technol. B Microelectron. Nanom. Struct.*, vol. 20, no. 5, pp. 2149–2153, 2002, doi: 10.1116/1.1511218.

[197] P. Pendyala, M. S. Bobji, and G. Madras, "Evolution of Surface Roughness During Electropolishing," *Tribol. Lett.*, vol. 55, no. 1, pp. 93–101, Jul. 2014, doi: 10.1007/s11249-014-0336-x.

[198] J. Edwards, "Feature Section The Mechanism of Electropolishing of Copper in," *J. Electrochem. Soc.*, vol. 100, no. 8, pp. 223C-230C, 1953, doi: 10.1149/1.2781129.

[199] D. Landolt, "Fundamental aspects of electropolishing," *Electrochim. Acta*, vol. 32, no. 1, pp. 1–11, Jan. 1987, doi: 10.1016/0013-4686(87)87001-9.

[200] G. Yang, B. Wang, K. Tawfiq, H. Wei, S. Zhou, and G. Chen, "Electropolishing of surfaces: theory and applications," *Surf. Eng.*, vol. 33, no. 2, pp. 149–166, Feb. 2017, doi: 10.1080/02670844.2016.1198452.

[201] G. P. Rothwell and T. P. Hoar, "The influence of solution flow on anodic polishing. Copper in aqueous o-phosphoric acid," *Electrochim. Acta*, vol. 9, no. September 1962, pp. 135–150, 1965, doi: 10.1016/0013-4686(65)80056-1.

[202] P. A. Jacquet, "Electrolytic Method for obtaining Bright Copper Surfaces," *Nature*, vol. 135, no. 3426, pp. 1076–1076, Jun. 1935, doi: 10.1038/1351076c0.

[203] S.-C. Chang and Y.-L. Wang, "Effects of applied voltages on planarization efficiency of Cu electropolishing," *J. Vac. Sci. Technol. B Microelectron. Nanom. Struct.*, vol. 22, no. 6, p. 2754, 2004, doi: 10.1116/1.1819898.

[204] I. I. Suni and B. Du, "Cu planarization for ULSI processing by electrochemical methods: A review," *IEEE Trans. Semicond. Manuf.*, vol. 18, no. 3, pp. 341–349, 2005, doi: 10.1109/TSM.2005.852091.

[205] R. Vidal and A. C. West, "Copper Electropolishing in Concentrated Phosphoric Acid 1. Experimental Findings," *J. Electrochem. Soc.*, vol. 142, no. 8, pp. 2682–2689, 1995.

[206] A. M. Awad, N. A. A. Ghany, and T. M. Dahy, "Removal of tarnishing and roughness of copper surface by electropolishing treatment," *Appl. Surf. Sci.*, vol. 256, no. 13, pp. 4370–4375, 2010, doi: 10.1016/j.apsusc.2010.02.033.

[207] B. Du and I. I. Suni, "Mechanistic Studies of Cu Electropolishing in Phosphoric Acid Electrolytes," *J. Electrochem. Soc.*, vol. 151, no. 6, p. C375, 2004, doi: 10.1149/1.1740783.

[208] A. A. Taha, A. M. Ahmed, H. H. A. Rahman, and F. M. Abouzeid, "The effect of surfactants on the electropolishing behavior of copper in orthophosphoric acid," *Appl. Surf. Sci.*, vol. 277, pp. 155–166, 2013, doi: 10.1016/j.apsusc.2013.04.017.

[209] D. Li *et al.*, "An in-situ study of copper electropolishing in phosphoric acid solution," *Int. J. Electrochem. Sci.*, vol. 8, no. 1, pp. 1041–1046, 2013.
[210] V. Palmieri *et al.*, "Besides the Standard Niobium Bath Chemical Polishing," in *Proceedings of 10th Workshop on RF Superconductivity (SRF 2001)*, 2001, pp. 408–412.
[211] V. Palmieri, V. L. Ruzinov, S. Y. Stark, and F. Stivanello, "Electropolishing of seamless 1.5 ghz ofhc copper cavities," in *Proceedings of 7th Workshop on RF Superconductivity (SRF 1995)*, 1995, pp. 605–609.
[212] C. Pira, "ARIES Milestone Report: First sample substrates cleaned at INFN for depositing at partners," 2017.
[213] C. Pira *et al.*, "Impact of the Cu substrate surface preparation on the morphological, superconductive and rf properties of the Nb superconductive coatings," in *Proceedings of 19th International Conference on RF Superconductivity (SRF 2019)*, 2019, pp. 937–942, doi: 10.18429/JACoW-SRF2019-THP041.
[214] D. Tikhonov, S. Keckert, J. Knobloch, O. Kugeler, Y. Tamashevich, and · A.-M Valente-Feliciano, "Superconducting Thin Films Characterization at HZB with the Quadrupole Resonator," in *Proceedings of 19th International Conference on RF Superconductivity (SRF 2019)*, 2019, pp. 616–620, doi: 10.18429/JACoW-SRF2019-TUP073.
[215] E. Chyhyrynets, "Cu/Nb QPR surface preparation protocol in the framework of ARIES project," To be published.
[216] R. Kleindienst, "Radio Frequency Characterization of Superconductors for Particle Accelerators," Ph.D. Thesis, Universität Siegen, 2017.
[217] S. Keckert, "Advanced Radio-Frequency Characterization of Thin-Film Superconducting Samples," Ph.D. Thesis, Universität Siegen, 2019.
[218] D. Tikhonov, "Ph.D. thesis, to be published," Universität Siegen.
[219] "ICSD File 52256." Inorganic Crystal Structure Database, 2003.
[220] W. Wisniewski, S. Saager, A. Böbenroth, and C. Rüssel, "Experimental evidence concerning the significant information depth of electron backscatter diffraction (EBSD)," *Ultramicroscopy*, vol. 173, no. July 2016, pp. 1–9, Feb. 2017, doi: 10.1016/j.ultramic.2016.11.004.
[221] M. A. Peck, "Structural and superconducting properties of sputter-deposited niobium films for applications in rf accelerating cavities," Ph.D. Thesis, Technische Universität Wien, 1999.
[222] A. R. Stokes and A. J. C. Wilson, "The diffraction of X rays by distorted crystal aggregates - I," *Proc. Phys. Soc.*, vol. 56, no. 3, pp. 174–181, May 1944, doi: 10.1088/0959-5309/56/3/303.
[223] J. I. Langford and A. J. C. Wilson, "Scherrer after sixty years: A survey and some new results in the determination of crystallite size," *J. Appl. Crystallogr.*, vol. 11, no. 2, pp. 102–113, Apr. 1978, doi: 10.1107/S0021889878012844.
[224] B. Gale and D. Griffiths, "Influence of instrumental aberrations on the schultz technique for the measurement of pole figures," *Br. J. Appl. Phys.*, vol. 11, no. 3, pp. 96–102, Mar. 1960, doi: 10.1088/0508-3443/11/3/302.
[225] S. Foner, "Versatile and Sensitive Vibrating-Sample Magnetometer," *Rev. Sci. Instrum.*, vol. 30, no. 7, pp. 548–557, Jul. 1959, doi: 10.1063/1.1716679.
[226] E. Seiler, "Private Discussion." 2019.
[227] "R0oland, CC BY-SA 3.0 <https://creativecommons.org/licenses/by-sa/3.0>, via Wikimedia Commons," 2011. https://commons.wikimedia.org/wiki/File:VSM_en.svg.
[228] Quantum Design, "Vibrating Sample Magnetometer (VSM) Option User's Manual," San Diego, 2011.

[229] D.-X. Chen, C. Prados, E. Pardo, A. Sanchez, and A. Hernando, "Transverse demagnetizing factors of long rectangular bars: I. Analytical expressions for extreme values of susceptibility," *J. Appl. Phys.*, vol. 91, no. 8, pp. 5254–5259, Apr. 2002, doi: 10.1063/1.1459745.

[230] D. M. Gokhfeld, "Analysis of Superconductor Magnetization Hysteresis," *J. Sib. Fed. Univ. Math. Phys.*, vol. 11, no. 2, pp. 219–221, May 2018, doi: 10.17516/1997-1397-2018-11-2-219-221.

[231] E. Chiaveri, E. Haebel, E. Mahner, and J. M. Tessier, "The quadrupole resonator: construction, rf system, field calculations and first applications," in *Proceedings of EPAC 1998*, 1998, no. June 1998, pp. 1852–1854.

[232] P. Goudket, T. Junginger, and B. P. Xiao, "Devices for SRF material characterization," *Supercond. Sci. Technol.*, vol. 30, no. 1, p. 013001, Jan. 2017, doi: 10.1088/0953-2048/30/1/013001.

[233] T. Junginger, W. Weingarten, and C. Welsch, "Extension of the measurement capabilities of the quadrupole resonator," *Rev. Sci. Instrum.*, vol. 83, no. 6, p. 063902, Jun. 2012, doi: 10.1063/1.4725521.

[234] R. Kleindienst, O. Kugeler, and J. Knobloch, "Development of an Optimized Quadrupole Resonator At HZB," *Proceedings of 16th International Conference on RF Superconductivity (SRF 2013)*, pp. 614–616, 2013.

[235] O. Kugeler, S. Keckert, R. Kleindienst, and J. Knobloch, "Activities with the quadrupole resonator at HZB," *Proceedings of EuCARD-2 3rd Annual WP12 Meeting*, 2016.

[236] T. Junginger, "Investigations of the surface resistance of superconducting materials," Ph.D. Thesis, Ruperto-Carola University of Heidelberg, 2012.

[237] R. Kleindienst, A. Burrill, S. Keckert, J. Knobloch, and O. Kugeler, "Commissioning results of the HZB quadrupole resonator," *Proceedings of 17th International Conference on RF Superconductivity (SRF 2015)*, 2015.

[238] S. Aull, S. Doebert, T. Junginger, and J. Knobloch, "High Resolution Surface Resistance Studies," in *Proceedings of 16th International Conference on RF Superconductivity (SRF 2013)*, 2013, pp. 785–788.

[239] S. Wilde *et al.*, "Physical vapour deposition of NbTiN thin films for superconducting rf cavities," in *Proceedings of 8th International Particle Accelerator Conference*, 2017, pp. 1102–1104, doi: 10.18429/JACoW-IPAC2017-MOPVA104.

[240] G. Jouve, C. Séverac, and S. Cantacuzène, "XPS study of NbN and (NbTi)N superconducting coatings," *Thin Solid Films*, vol. 287, no. 1–2, pp. 146–153, Oct. 1996, doi: 10.1016/S0040-6090(96)08776-7.

[241] K. S. Havey, J. S. Zabinski, and S. D. Walck, "The chemistry, structure, and resulting wear properties of magnetron-sputtered NbN thin films," *Thin Solid Films*, vol. 303, no. 1–2, pp. 238–245, Jul. 1997, doi: 10.1016/S0040-6090(96)09529-6.

[242] J. Halbritter and A. Darlinski, "Angle resolved XPS studies of oxides at NbB, NbC, and Nb surfaces," *Surf. Interface Anal.*, vol. 10, no. May 1986, pp. 223–237, 1987, doi: 0142-2421/87/050223-15.

[243] M. Benkahoul, E. Martinez, A. Karimi, R. Sanjinés, and F. Lévy, "Structural and mechanical properties of sputtered cubic and hexagonal NbNxthin films," *Surf. Coatings Technol.*, vol. 180–181, pp. 178–183, 2004, doi: 10.1016/j.surfcoat.2003.10.040.

[244] "ICSD File 982." Inorganic Crystal Structure Database, 1980.

[245] "ICSD File 76011." Inorganic Crystal Structure Database, 2000.

[246] "ICSD File 26252." Inorganic Crystal Structure Database, 1980.

[247] G. Brauer and H. Kirner, "Drucksynthese von Niobnitriden und Konstitution von delta-NbN," *Zeitschrift für Anorg. und Allg. Chemie*, vol. 328, no. 1–2, pp. 34–43, Apr. 1964, doi: 10.1002/zaac.19643280105.

[248] F. Ying, R. W. Smith, and D. J. Srolovitz, "The mechanism of texture formation during film growth: The roles of preferential sputtering and shadowing," *Appl. Phys. Lett.*, vol. 69, no. 20, pp. 3007–3009, Nov. 1996, doi: 10.1063/1.116821.

[249] "ICSD File 76384." Inorganic Crystal Structure Database, 2000.

[250] J. Alami, S. Bolz, and K. Sarakinos, "High power pulsed magnetron sputtering: Fundamentals and applications," *J. Alloys Compd.*, vol. 483, no. 1–2, pp. 530–534, Aug. 2009, doi: 10.1016/j.jallcom.2008.08.104.

[251] J. Ding *et al.*, "Effects of Negative Bias Voltage and Ratio of Nitrogen and Argon on the Structure and Properties of NbN Coatings Deposited by HiPIMS Deposition System," *Coatings*, vol. 8, no. 1, p. 10, Dec. 2017, doi: 10.3390/coatings8010010.

[252] Y. P. Purandare, A. P. Ehiasarian, and P. Eh Hovsepian, "Target poisoning during CrN deposition by mixed high power impulse magnetron sputtering and unbalanced magnetron sputtering technique," *J. Vac. Sci. Technol. A Vacuum, Surfaces, Film.*, vol. 34, no. 4, p. 041502, Jul. 2016, doi: 10.1116/1.4950886.

[253] O. Kugeler *et al.*, "ARIES Deliverable Report D15.3: Evaluation of system 3 and SIS," 2020. [Online]. Available: https://edms.cern.ch/document/1820619/1.0%0A.

[254] S. Wilde, R. Valizadeh, O. B. Malyshev, G. B. G. Stenning, T. Sian, and B. Chesca, "dc magnetometry of niobium thin film superconductors deposited using high power impulse magnetron sputtering," *Phys. Rev. Accel. Beams*, vol. 21, no. 7, p. 073101, Jul. 2018, doi: 10.1103/PhysRevAccelBeams.21.073101.

[255] W. M. Roach *et al.*, "Niobium thin film deposition studies on copper surfaces for superconducting radio frequency cavity applications," *Phys. Rev. Spec. Top. - Accel. Beams*, vol. 15, no. 6, pp. 1–6, 2012, doi: 10.1103/PhysRevSTAB.15.062002.

[256] "ICSD File 645059," 2008.

[257] L. S. Yu, J. M. E. Harper, J. J. Cuomo, and D. A. Smith, "Control of thin film orientation by glancing angle ion bombardment during growth," *J. Vac. Sci. Technol. A Vacuum, Surfaces, Film.*, vol. 4, no. 3, pp. 443–447, May 1986, doi: 10.1116/1.573902.

[258] J. Spradlin *et al.*, "Structural Properties of Niobium Thin Films Deposited on Metallic Substrates," in *Proceedings of 15th International Conference on RF superconductivity (SRF 2011)*, 2011, pp. 877–882.

[259] H. Ji, G. S. Was, J. W. Jones, and N. R. Moody, "Effect of ion bombardment on in-plane texture, surface morphology, and microstructure of vapor deposited Nb thin films," *J. Appl. Phys.*, vol. 81, no. 10, pp. 6754–6761, May 1997, doi: 10.1063/1.365217.

[260] X. Zhao *et al.*, "Large crystal grain niobium thin films deposited by energetic condensation in vacuum arc," *J. Vac. Sci. Technol. A Vacuum, Surfaces, Film.*, vol. 27, no. 4, pp. 620–625, Jul. 2009, doi: 10.1116/1.3131725.

[261] M. Burton, A. Palczewski, A. M. Valente-Feliciano, and C. E. Reece, "Progress with Nb HiPIMS films on 1.3GHz Cu cavities," in *Proceedings of 19th International Conference on RF Superconductivity (SRF 2019)*, 2019, pp. 823–827, doi: 10.18429/JACoW-SRF2019-THFUB2.

[262] S. Wilde, R. Valizadeh, O. Malyshev, and B. Chesca, "Superconducting Thin Films for SRF Cavities," *7th Int. Work. Thin Film. New Ideas Push. Limits RF Supercond.*, 2016.

[263] A. van der Drift, "Evolutionary selection, a principle governing growth orientation in vapour-deposited layers," *Philips Res. Reports*, vol. 22, no. 3, pp. 267–288, 1967.

[264] J. Alami, K. Sarakinos, G. Mark, and M. Wuttig, "On the deposition rate in a high

power pulsed magnetron sputtering discharge," *Appl. Phys. Lett.*, vol. 89, no. 15, p. 154104, Oct. 2006, doi: 10.1063/1.2362575.

[265] S. B. Roy, G. R. Myneni, and V. C. Sahni, "On the reliable determination of the magnetic field for first flux-line penetration in technical niobium material," *Supercond. Sci. Technol.*, vol. 21, no. 6, p. 065002, Jun. 2008, doi: 10.1088/0953-2048/21/6/065002.

[266] M. a. Mantenieks, "Sputtering Threshold Energies of Heavy Ions," *NASA Tech. Memo.*, vol. 2, no. June, p. 209273, 1999.

[267] J. T. Gudmundsson, N. Brenning, D. Lundin, and U. Helmersson, "High power impulse magnetron sputtering discharge," *J. Vac. Sci. Technol. A Vacuum, Surfaces, Film.*, vol. 30, no. 3, p. 030801, May 2012, doi: 10.1116/1.3691832.

[268] J. H. Goldsmith *et al.*, "Influence of nitride buffer layers on superconducting properties of niobium nitride," *J. Vac. Sci. Technol. A*, vol. 36, no. 6, p. 061502, Nov. 2018, doi: 10.1116/1.5044276.

[269] A. Iqbal and F. Mohd-Yasin, "Reactive Sputtering of Aluminum Nitride (002) Thin Films for Piezoelectric Applications: A Review," *Sensors*, vol. 18, no. 6, p. 1797, Jun. 2018, doi: 10.3390/s18061797.

[270] K.-H. Chiu, J.-H. Chen, H.-R. Chen, and R.-S. Huang, "Deposition and characterization of reactive magnetron sputtered aluminum nitride thin films for film bulk acoustic wave resonator," *Thin Solid Films*, vol. 515, no. 11, pp. 4819–4825, Apr. 2007, doi: 10.1016/j.tsf.2006.12.181.

[271] M. B. Assouar, O. Elmazria, L. Le Brizoual, and P. Alnot, "Reactive DC magnetron sputtering of aluminum nitride films for surface acoustic wave devices," *Diam. Relat. Mater.*, vol. 11, no. 3–6, pp. 413–417, Mar. 2002, doi: 10.1016/S0925-9635(01)00708-7.

[272] M. Vogel, "Herstellung von Aluminiumnitrid Dünnschichten mittels Magnetron Sputtern auf Diamant für potentielle Pseudo-Surface-Acoustic- Wave-Anwendungen," Ph.D. Thesis, Universität Siegen, 2016.

[273] "ICSD File 54697." Inorganic Crystal Structure Database, 2004.

[274] M. Wen *et al.*, "The AlN layer thickness dependent coherent epitaxial growth, stress and hardness in NbN/AlN nanostructured multilayer films," *Surf. Coatings Technol.*, vol. 235, pp. 367–375, Nov. 2013, doi: 10.1016/j.surfcoat.2013.08.004.

Appendix A Supplementary Information

Appendix A.1 DC MS NbN Screening Study Sample List

Run Order	Substrate Temperature ($°C$)	Deposition Pressure (mbar)	Substrate Bias (V)	N_2%	Process Gas	Cathode Power (W)
1	270	8.0×10^{-3}	-80	10	Kr	300
2	115	8.0×10^{-3}	0	30	Ar	300
3	270	1.6×10^{-2}	-80	30	Kr	300
4	270	1.6×10^{-2}	-80	10	Ar	300
5	115	1.6×10^{-2}	0	10	Ar	300
6	180	1.2×10^{-2}	-40	20	Kr	400
7	115	8.0×10^{-3}	-80	10	Kr	500
8	270	1.6×10^{-2}	-80	30	Ar	500
9	270	1.6×10^{-2}	-80	10	Kr	500
10	115	1.6×10^{-2}	-80	10	Kr	300
11	115	1.6×10^{-2}	0	30	Ar	500
12	180	1.2×10^{-2}	-40	20	Ar	400
13	180	1.2×10^{-2}	-40	20	Kr	400
14	115	8.0×10^{-3}	-80	30	Ar	500
15	270	8.0×10^{-3}	0	10	Ar	300
16	270	8.0×10^{-3}	-80	30	Ar	300
17	115	1.6×10^{-2}	-80	30	Ar	300
18	115	8.0×10^{-3}	-80	10	Ar	300
19	115	8.0×10^{-3}	0	30	Kr	500
20	115	8.0×10^{-3}	-80	30	Kr	300
21	115	8.0×10^{-3}	0	10	Ar	500
22	115	1.6×10^{-2}	0	30	Kr	300
23	270	8.0×10^{-3}	0	10	Kr	500
24	115	1.6×10^{-2}	0	10	Kr	500
25	115	1.6×10^{-2}	-80	30	Kr	500
26	270	8.0×10^{-3}	0	30	Kr	300
27	270	1.6×10^{-2}	0	30	Kr	500
28	270	1.6×10^{-2}	0	10	Kr	300
29	180	1.2×10^{-2}	-40	20	Ar	400
30	115	8.0×10^{-3}	0	10	Kr	300
31	115	1.6×10^{-2}	-80	10	Ar	500
32	270	8.0×10^{-3}	-80	30	Kr	500
33	270	1.6×10^{-2}	0	30	Ar	300
34	270	8.0×10^{-3}	-80	10	Ar	500
35	270	8.0×10^{-3}	0	30	Ar	500
36	270	1.6×10^{-2}	0	10	Ar	500

Appendix A.2 DC MS NbN Deposition Parameter Study Sample List

Sample ID	Deposition Pressure (mbar)	Nitrogen Content (%)	Substrate Bias (V)	Cathode Power (W)	Substrate Temperature (°C)	Film Thickness (μm)
			Nitrogen Percentage			
811	8.0×10^{-3}	4	0	500	270	1.13
789	8.0×10^{-3}	6	0	500	270	1.09
790	8.0×10^{-3}	8	0	500	270	1.18
793	8.0×10^{-3}	10	0	500	270	1.12
810	8.0×10^{-3}	12	0	500	270	1.16
797	8.0×10^{-3}	14	0	500	270	1.17
799	8.0×10^{-3}	16	0	500	270	1.14
808	8.0×10^{-3}	18	0	500	270	1.14
809	8.0×10^{-3}	20	0	500	270	1.36
814	8.0×10^{-3}	30	0	500	270	1.48
			Substrate Bias			
821	8.0×10^{-3}	10	25	500	270	1.22
815	8.0×10^{-3}	10	50	500	270	1.15
820	8.0×10^{-3}	10	75	500	270	1.13
816	8.0×10^{-3}	10	100	500	270	1.2
817	8.0×10^{-3}	10	150	500	270	1.17
818	8.0×10^{-3}	10	200	500	270	1.34
819	8.0×10^{-3}	10	300	500	270	1.37
			Deposition Pressure			
822	6.0×10^{-3}	10	0	500	270	1.16
823	1.0×10^{-2}	10	0	500	270	1.17
824	1.4×10^{-2}	10	0	500	270	1.09
825	1.8×10^{-2}	10	0	500	270	1.12
			Optimised Samples			
889	8.0×10^{-3}	6	0	400	270	1.27
891	8.0×10^{-3}	8	0	400	270	1.48
892	6.0×10^{-3}	10	0	400	270	0.9
893	6.0×10^{-3}	8	75	400	270	1.34
897	1.2×10^{-2}	8	0	400	290	1.34
898	1.4×10^{-2}	8	0	500	290	1.9
899	1.4×10^{-2}	8	75	500	290	1.06
900	1.2×10^{-2}	6	75	500	270	1.41
902	1.2×10^{-2}	8	50	400	270	1.12

Appendix A.3 HiPIMS NbN Sample List

Sample ID	Deposition Pressure (mbar)	Nitrogen Content (%)	Substrate Bias (V)	Cathode Power (W)	Substrate Temperature (°C)	Film Thickness (μm)
5 % N_2 – 1.4 x 10^{-2} - Power Variation						
1187	1.4 x 10^{-2}	5	50	300	180	0.69
1189	1.4 x 10^{-2}	5	50	400	180	0.98
1190	1.4 x 10^{-2}	5	50	500	180	1.14
1191	1.4 x 10^{-2}	5	50	600	180	1.24
5 % N_2 – 400 W - Pressure Variation						
1196	1.2 x 10^{-2}	5	50	400	180	0.59
1197	1.8 x 10^{-2}	5	50	400	180	0.98
1199	2.2 x 10^{-2}	5	50	400	180	0.98
1285	2.2 x 10^{-2}	5	50	400	180	1.43
1287	2.4 x 10^{-2}	5	50	400	180	1.41
8 % N_2 – 400 W - Pressure Variation						
1200	1.4 x 10^{-2}	8	50	400	180	-
1215	1.4 x 10^{-2}	8	50	400	180	-
1202	1.8 x 10^{-2}	8	50	400	180	0.87
1203	2.2 x 10^{-2}	8	50	400	180	0.87
1288	2.4 x 10^{-2}	8	50	400	180	1.44
8 % N_2 – 2.2 x 10^{-2} – Power Variation						
1205	2.2 x 10^{-2}	8	50	500	180	1.16
1206	2.2 x 10^{-2}	8	50	300	180	0.68
1207	2.2 x 10^{-2}	8	50	400	180	0.89
8 % N_2 - 2.2 x 10^{-2} – 300 W – Bias Variation						
1213	2.2 x 10^{-2}	8	50	300	180	-
1284	2.2 x 10^{-2}	8	50	300	180	1.38
1209	2.2 x 10^{-2}	8	100	300	180	-
1375	2.2 x 10^{-2}	8	100	300	180	0.56
1445	2.2 x 10^{-2}	8	75	300	180	0.92
1455	2.2 x 10^{-2}	8	60	300	180	1.15
1467	2.2 x 10^{-2}	8	30	300	180	1.09
1208	2.2 x 10^{-2}	8	100	400	180	0.79
10 % N_2 – 400 W - Pressure Variation						
1291	1.4 x 10^{-2}	10	50	400	180	1.20
1295	1.8 x 10^{-2}	10	50	400	180	1.59
1296	2.2 x 10^{-2}	10	50	400	180	1.63
1325	2.4 x 10^{-2}	10	50	400	180	1.61
400 W – 2.2 x 10^{-2} - N_2% Variation-						
1556	2.2 x 10^{-2}	8	50	400	180	1.25
1327	2.2 x 10^{-2}	14	50	400	180	-
1441	2.2 x 10^{-2}	14	50	400	180	1.46
1341	2.2 x 10^{-2}	18	50	400	180	1.73
1448	2.2 x 10^{-2}	22	50	400	180	1.55
300 W – 2.2 x 10^{-2} - N_2% Variation-						
1468	2.2 x 10^{-2}	10	50	300	180	1.61
1472	2.2 x 10^{-2}	14	50	300	180	1.59
1475	2.2 x 10^{-2}	18	50	300	180	1.39

1550	2.8×10^{-2}	22	50	300	180	-
1553	2.2×10^{-2}	22	50	300	180	1.46
			8 % N_2 -300 W - Pressure Variation			
1552	1.8×10^{-2}	8	50	300	180	1.24
1554	1.4×10^{-2}	8	50	300	180	1.16
1555	2.4×10^{-2}	8	50	300	180	1.26
			Extreme Values			
1359	2.2×10^{-2}	8	100	600	290	0.73
1362	2.2×10^{-2}	8	100	600	90	0.76
1377	2.2×10^{-2}	8	0	600	90	1.91
1379	2.2×10^{-2}	8	0	263	90	1.38
1381	2.2×10^{-2}	8	0	600	290	1.72
1404	2.2×10^{-2}	8	0	263	290	1.31
1410	2.2×10^{-2}	8	100	263	290	0.96
1412	2.2×10^{-2}	8	100	263	90	0.42
1477	2.2×10^{-2}	8	50	600	90	1.10
1551	2.2×10^{-2}	8	50	300	290	1.40

Appendix A.4 Nb Target Processing Procedure

Run Number	Substrate Temperature ($°C$)	Deposition Pressure (mbar)	Process Gas	Cathode Power (W)	Time (min)
1	290	1.5×10^{-2}	Ar	400	120
2	270	1.5×10^{-2}	Ar	400	120
3	270	1.5×10^{-2}	Ar	400	120
4	270	8.0×10^{-3}	Ar	500	60
5	270	8.0×10^{-3}	Ar	600	60
6	270	8.0×10^{-3}	Ar	500	60
7	270	8.0×10^{-3}	Ar	500	60

Appendix A.5 HiPIMS Nb Plasma Stability Testing

Pulse length (μs)	Cathode Average Current (A)				Cathode Average Voltage (V)			
	6×10^{-3}	8×10^{-3}	1.0×10^{-2}	1.2×10^{-2}	6×10^{-3}	8×10^{-3}	1.0×10^{-2}	1.2×10^{-2}
40	unstable	unstable	unstable	unstable	unstable	unstable	unstable	unstable
60	unstable	0.5	0.6	0.6	unstable	477	450	426
80	0.5	0.6	0.7	0.7	475	406	389	374
100	0.6	0.7	0.7	0.75	419	374	360	346
120	0.7	0.7	0.8	0.8	393	355	340	326
140	0.7	0.8	0.8	0.8	378	339	326	313
160	0.7	0.8	0.9	0.9	365	328	309	303
180	0.75	0.8	0.9	0.9	353	320	302	295
200	0.8	0.8	0.9	0.9	346	314	296	290